ESPOO 2005 VTT RESEARCH NOTES 2286

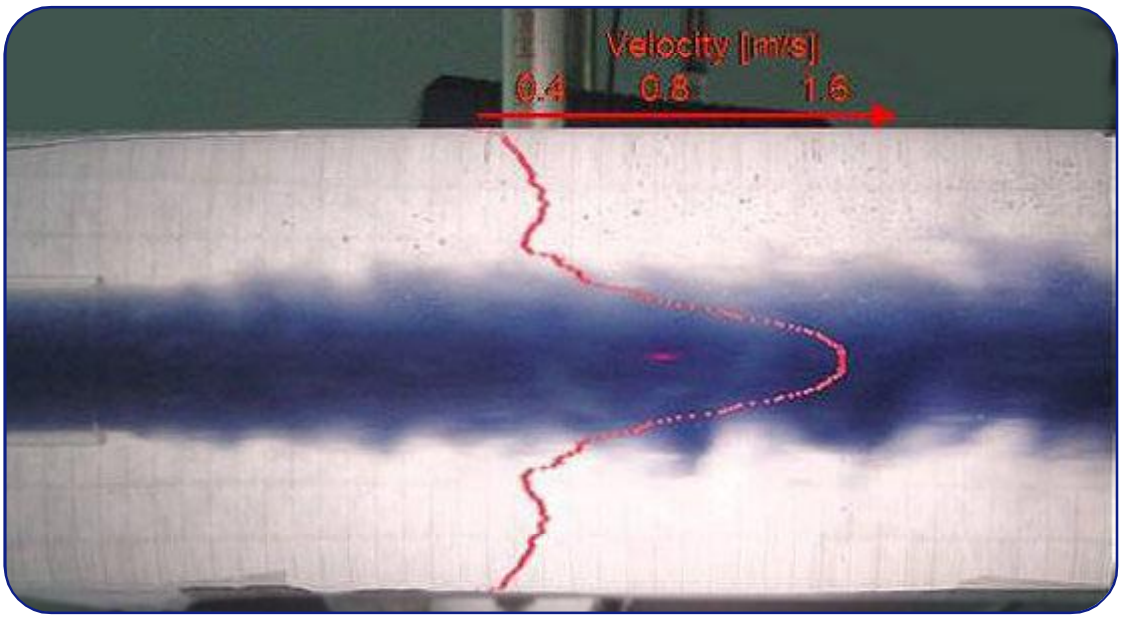

Multiphase flows in process industry

ProMoni

Multiphase flows in process industry

ProMoni

Markku Kataja[1] (ed.)

Antti Koponen, Veli-Matti Luukkainen, Mikko Manninen, Ulla Ojaniemi, Janne Poranen, Juha Salmela & Pasi Selenius[1]

Hannu Eloranta, Jouko Halttunen, Markus Honkanen, Tero Pärssinen, Pentti Saarenrinne & Shaomin Zhou[2]

Markus Engblom, Kim Fagerudd, Manuel Flores Geant, Alf Hermanson & Sirpa Kallio[3]

Jari P. Kaipio, Ville Kolehmainen, Katja Markkanen, Tanja Tarvainen, Antti Vanne & Marko Vauhkonen[4]

Sanna Haavisto, Markko Myllys & Esa Rehn[5]

[1] VTT Processes
[2] Tampere University of Technology
[3] Åbo Akademi University
[4] University of Kuopio
[5] University of Jyväskylä

ISBN 951–38–6536–3 (soft back ed.)
ISSN 1235–0605 (soft back ed.)

ISBN 951–38–6537–1 (URL: http://www.vtt.fi/inf/pdf/)
ISSN 1455–0865 (URL: http://www.vtt.fi/inf/pdf/)

Copyright © VTT 2005

JULKAISIJA – UTGIVARE – PUBLISHER

VTT, Vuorimiehentie 5, PL 2000, 02044 VTT
puh. vaihde 020 722 111, faksi 020 722 4374

VTT, Bergsmansvägen 5, PB 2000, 02044 VTT
tel. växel 020 722 111, fax 020 722 4374

VTT Technical Research Centre of Finland, Vuorimiehentie 5, P.O.Box 2000, FI–02044 VTT, Finland
phone internat. +358 20 722 111, fax +358 20 722 4374

VTT Prosessit, Koivurannantie 1, PL 1603, 40101 JYVÄSKYLÄ
puh. vaihde 020 722 111, faksi 020 722 2596

VTT Processer, Koivurannantie 1, PB 1603, 40101 JYVÄSKYLÄ
tel. växel 020 722 111, fax 020 722 2596

VTT Processes, Koivurannantie 1, P.O.Box 1603, FI–40101 JYVÄSKYLÄ, Finland
phone internat. +358 20 722 111, fax +358 20 722 2596

Technical editing Marja Kettunen

Valopaino Oy, Helsinki 2005

Multiphase flows in process industry. ProMoni. Kataja, Markku (ed.). Espoo 2005. VTT Tiedotteita – Research Notes 2286. 177 p. + app. 4 p.

Keywords process industry, process measurements, flow measurement, multiphase flow, fluidized bed reactors, bubbling fluidized beds, computational methods, fibre suspensions, particle image velocimetry, digital imaging

Synopsis

The project "Multiphase flows in process industry (ProMoni)" 1.1.2001–30.4.2004 was a research consortium carried out jointly by seven research groups from VTT Technical Research Centre of Finland, University of Jyväskylä, Tampere University of Technology, Åbo Akademi University and University of Kuopio. It included modeling, development and validation of numerical methods as well as development of new experimental techniques for multiphase flows found in process industry. The primary fields of application are in fluidized beds and in various processes found in the paper and pulp industry. The total extent of the project was approximately 25 person years and it was funded by the National Technology Agency of Finland, Foster Wheeler Energia Oy, Metso Oyj and Fortum Oyj.

The main results reported in this final report of the ProMoni project include:

- Results from experimental and numerical research of bubbling fluidized beds indicating that modelling produces the bed behaviour realistically and the simulations can be used in developing approximative macroscopic two-phase models.

- A new gas-solid drag correlation model was successfully used within Fluent CFD code to simulate the typical flow structures in a circulating fluidized bed riser.

- Several new or newly adapted experimental methods and measuring devices for fibre suspension flows were developed and brought in regular use in laboratory or pilot scale environments.

- Particle Image Velocimetry and Digital Imaging measurement were developed and used in two-phase flows to measure hydrodynamical interaction and morphology of the dispersed phase.

- Optical and electrical impedance tomographic devices and related image reconstruction algorithms were developed for non-intrusive measurement of consistency profiles and flow velocity in flows of diffusive fluids such as wood fibre suspensions.

More detailed information can be found in numerous publications and reports issued by the participating groups, and referred to in this report.

Contents

1 Introduction

Flows found in many industrial processes are intrinsically multiphase flows where the flowing material is composed of two or more distinct components or 'phases', which themselves may be fluids or solids. Common examples of industrial multiphase flows are those found in a fluidized bed, bubbly flow in nuclear reactors, gas-particle flow in combustion reactors and fiber suspension flows within pulp and paper industry. Compared to flows of simple liquids and gases, controlling and understanding the behaviour of these flows is considerably more difficult. One important reason for this is that many of the methods, experimental methods in particular, that are commonly used in other branches of fluid mechanics are not as such applicable in complex multiphase flows. Consequently, also the theoretical background and numerical methods for multiphase flows are not as well established as for the more conventional flows of simple fluids. Development of new methods and techniques therefore is and will long remain as an essential feature of multiphase flows research and its applications.

The ProMoni project was initiated in 2001 after an extensive pilot survey of on-going research activities and needs in the field of industrial multiphase flows[1)]. In agreement with the experience gathered during previous research programs in fluid dynamcis, e.g. the Computational Fluid Dynamics (CFD) Programme[2)], this survey indicated a clear demand for such a research, experimental research, in particular. The potential research topics were many ranging from computational multiphase flow dynamics related to various unit processes and development of sensors for control and automation, to basic research of flow phenomena relevant in such processes. The problems associated with modeling, measurement and computation required in effective process development and control seem to be similar in many process industries. Perhaps the most important hindrance for accurate measurement, modeling and computation of those processes is the obvious lack in experimental methods and equipment applicable for industrial multiphase flows. Compared to its predecessor, the project "Dynamcis of industrial multiphase flows (MonDy)" that was a part of the CFD programme and devoted primarily to theoretical and numerical issues of multiphase flows, the present consortium project was thereby directed more towards experimental research by development of new experimental techniques. Numerical methods and applications remain, however, an important part of also the ProMoni project.

[1)] Kataja, M., Luukkainen, V.-M. & Saarenrinne, P. Monifaasivirtausten mittaukset. Esiselvitys. VTT Tutkimusraportti, ENE22/T0096/99. (In Finnish)

[2)] Häkkinen, R.J., Hirsch, C., Krause, E. & Kytömaa, H.K. Computational Fluid Dynamics Programme 1995–1999. Mid-term evaluation report, Technology Programme Report 1/97, Tekes, Helsinki, 1997.

In order to maximize the potential for industrial applications and technology transfer of the projected results, the particular research topics for ProMoni -project were selected in a close cooperation with the industries involved, and utilizing the results of the pilot survey[1)]. The general goals of the project were to enhance the skills and capabilities of the participating research groups for their applied research, to support their ongoing and planned industry-related research projects and, ultimately, to advance and intensify the dicipline of industrial multiphase flow research in Finland.

[1)] M. Kataja, V.-M. Luukkainen & P. Saarenrinne. Monifaasivirtausten mittaukset. Esiselvitys. VTT Tutkimusraportti, ENE22/T0096/99.

2 Project overview

ProMoni project was carried out as a consortium of seven research groups from VTT Technical Research Centre of Finland (coordinator), University of Jyväskylä, Tampere University of Technology, Åbo Akademi University and University of Kuopio. It was funded by Tekes, VTT and industry. The project organization including contact information to participating research groups and the members of the project committee are given in Appendix 1.

The project includes two main parts, namely development and validation of computational models and development of experimental methods. Both parts include also applications to selected industrial processes. Applications are, however, primarily carried out in parallel industrial projects. According to the research plan (updated for years 2002 and 2003), the main parts of the project consist of several subtopics as follows.

I DEVELOPMENT AND VALIDATION OF COMPUTATIONAL MODELS

I.1 Fluidized bed reactors
a) Bubbling fluidized bed
b) Computational methods for circulating fluidized bed reactors

I.2 Filtration of fibre suspensions

II DEVELOPMENT OF EXPERIMENTAL METHODS

II.1 Process tomography
a) Optical tomography
b) Impedance tomography

II.2 PIV -methods

II.3 Process measurements of fibre suspensions
a) Fast pressure measurements
b) Conduction measurement in stratified flows
c) Acoustic measurement of air content in fibre suspensions
d) Optical methods for fibre suspension flows

II.4 Flow rate measurement of fibre suspensions

Some of the topics include several subtopics. The item II.3.c) was abandoned after a short preliminary study showing no useful results. Otherwise, the main results of each topic are given below.

3 Results

3.1 Experimental study and CFD modeling of bubble formation in a bubbling fluidized bed

Sirpa Kallio, Alf Hermanson, Kim Fagerudd, Markus Engblom and Manuel Flores Geant
Åbo Akademi University, Heat Engineering Laboratory

Ulla Ojaniemi and Mikko Manninen
VTT Processes, Pulp and Paper Industry, Process simulation

3.1.1 Background

Bubbling fluidized beds (BFB) are used in a large number of applications in the chemical and process industries and in energy production. Modeling of bubbling fluidized beds was earlier based entirely on empirical and half-empirical correlations and different versions of the two phase theory of bubbling fluidization. Today computational fluid dynamics (CFD) offers a new approach to BFB modeling. The main problems in the CFD models are the uncertainties in the formulation of the transfer equations for momentum and in the closure relations used. To validate the CFD models for BFB research, detailed measurements are necessary from simple and well-defined conditions.

One of the first comparisons between CFD modeling and measurement data was presented by Syamlal & O'Brien **[1]**. For further comparisons, Kuipers **[2]** conducted experiments in a two-dimensional fluidized bed, where a single bubble was introduced by a gas flow through an orifice. The bed was otherwise in minimum fluidization conditions. Boemer **[3]** calculated bubble formation with the Fluent CFD code in the conditions of Kuipers' experiments and compared simulated and measured bubble behaviour. A similar wider experimental and theoretical study was conducted by Taivassalo et al **[4].** In present study, their work is continued using a different 2D BFB, where two orifices can be used simultaneously to introduce two chains of bubbles. A similar test arrangement has been used in Hong et al **[6].**

3.1.2 The experimental unit and instrumentation

The two-dimensional bubbling fluidized bed cold model used in this work is illustrated in Figure 1. The transparent walls of the bed are 0.9 m wide and 1.25 m high. The distance between the walls is 15 mm. The air distributor is made of 1 mm thick perforated aluminium plate. Three orifices of 12.1 mm by 12.1 mm are taken through the plate at 25 cm, 40 cm and 65 cm distance from the left edge. The bed is equipped

with air flow meters and controllers, and pressure meters. CO_2, used as a tracer, was detected by means of Datex Multicap^R system. Sony Handycam was used as video grabber. More detailed information on the equipment and the instrumentation used is given in Kallio et al **[5].**

Glass particles were used as bed material. The material density of glass particles was 2480 kg/m^3 and the Sauter mean diameter was 0.385 mm. According to Geldart's classification, these particles belong to class B. The minimum fluidization velocity was 0.152 m/s.

For comparison, some experiments were conducted using lighter polymer resin particles. The material density was 1050 kg/m^3 and the Sauter mean diameter 0.457 mm. Also these particles belong to Geldart's group B.

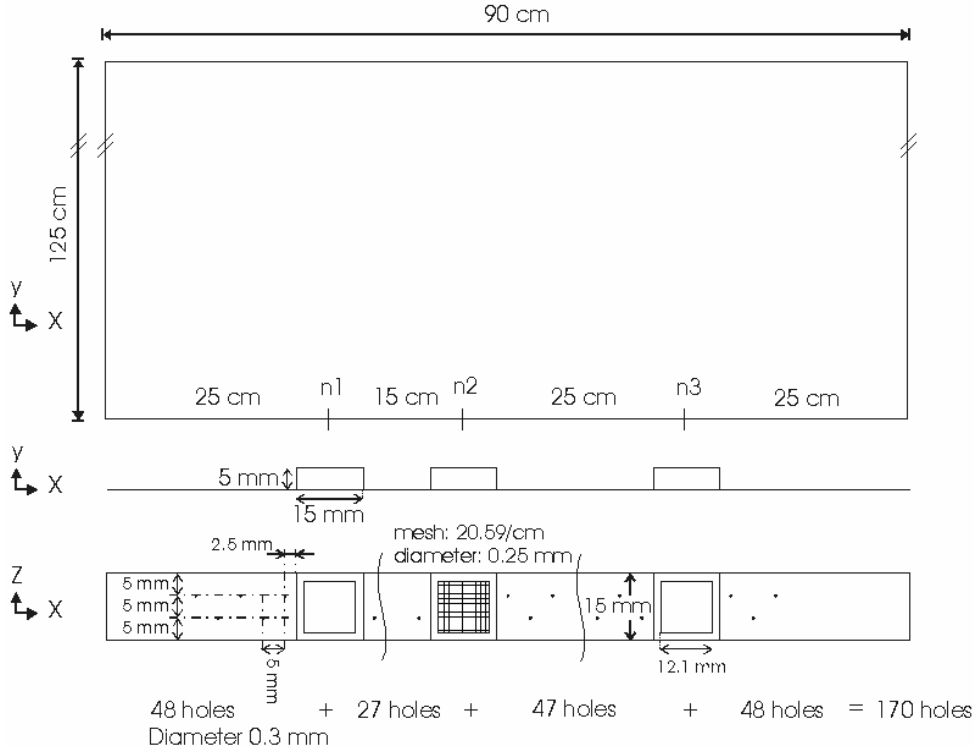

Figure 1. Side view of the bubbling bed cold model (top), side view of the bottom plate with orifices for gas (middle), and top view of the bottom plate (bottom).

3.1.3 Experimental method

For analysis of bubble behavior totally 52 experiments were video recorded, 42 with glass particles and 10 with polymer resin particles. In some of the experiments all air was introduced through the bottom plate and spontaneous bubble formation in the freely bubbling bed was studied. In other experiments, one or two air flows were injected

through the orifices at the bottom plate to a bed that was otherwise kept in minimum fluidization state by introducing a sufficient amount of air through the bottom plate.

The sensitivity of the results to the fluid dynamic conditions was studied in detail and it was observed that bubble behaviour is not extremely sensitive to the fluidization conditions in the surrounding bed. Some experiments were done at very low superficial velocities and formation of stagnant voids close to the orifice was observed. The effect of bed height was studied in some tests by using a shallow glass particle bed.

About 40 s of each experiment was recorded on video at 25 Hz and the video images were analysed by an in-house Visual Basic code. By analysing the video images quantitative information on bubble behaviour was obtained. For each of the bubbles, the image processing code calculated bubble location, shape and velocity. The length of the bed surface and the highest and lowest points of the freeboard were also recorded. The total area identified as emulsion phase was calculated, similarly the coordinates of the midpoint of the emulsion phase. The dark areas in the freeboard were assumed splashes of ejected particles and their total area was calculated.

The division of the air flow into visible bubble flow, flow required to fluidize the bed and throughflow was determined in a freely bubbling bed and in situations with one and two introduced bubble chains. The local concentration of particles was estimated from a number of images using the relation between light intensity and particle concentration. Additional experiments were done with the glass particle bed using dark sand particles as tracers, the velocity of which was determined from video images. Spreading of gas from the bubbles was studied using CO_2 as tracer. Bubbling frequency was determined from measured CO_2 time series.

The number of experiments was much larger than what was needed directly for CFD validation runs. A larger number was needed since the type of bubble interaction in different conditions was not known a priori. It was easier to choose suitable cases for validation, when a large number of alternatives were tested in practice. The large set of experiments gave valuable information on the sensitivity of different fluidization phenomena on fluidization parameters. This additional information was helpful in comparisons with simulations. It was also used for comparisons with literature data and confirmed that the equipment was functioning in a reliable way.

3.1.4 CFD modeling of experiments in the 2D bubbling fluidized bed

In order to validate the present CFD models, the measured two bubble chain cases were simulated by means of the Eulerian multiphase models of Fluent 4.52 CFD software **[7]**.

In the case selected for the validation, the two leftmost orifices 15 cm apart were used to introduce two chains of bubbles at gas flow rates 45.6 l/min and 20.1 l/min.

The calculations were carried out as 2D time dependent laminar flow by using several combinations of the models for kinetic viscosity $\mu_{s,kin}$ and for momentum exchange coefficient K_{sf}. Results are presented for the combinations applying the model for kinetic viscosity of solid particles $\mu_{s,kin}$ according to Gidaspow et al. and for momentum exchange coefficient K_{sf} model of Gidaspow or Syamlal & O'Brien. The models are presented in detail in the project report **[15]** and in the references **[8–10].** In following, the results are presented for the air flow rate 45.6 l/min.

A number of simulation tests were carried out for evaluating the relevance of calculation parameters for the results. In the study, the possibility to simplify the present models of Fluent was investigated. The simulations of the bubbling bed based on Gidaspow model above were carried out using constant values for the solids viscosity or the granular temperature. The effect of turbulence models was examined, too. For predicting the solids pressure, a simple model assuming the pressure to be relative to the solids volume fraction was tested. The model is applied by CFX and was studied both by CFX and Fluent. These tests are explained in detail in the project report **[15]**.

The statistical analysis of the results of the simulations was carried out with the image processing code used also for the video images. The predicted bubble interaction patterns were compared to the measured ones.

3.1.5 CFD modeling of turbulent bed

The simulation of turbulent bed was carried out on the basis of the bubbling bed modeling experiences. The aim of the simulations has been the validation of the present models for simulation of turbulent bed. In addition, the applicability of the results for development of macroscopic models was studied. The real boilers are too large to be modeled with the grid density needed in modeling of physical phenomena in detail. One way to model the real boilers is to use macroscopic models that take into account the size of the cells in averaging the closure models.

In the simulations, the conditions typical of turbulent beds were achieved by increasing the fluidizing air flow rate significantly above the minimum fluidizing flow rate but keeping it below the rate required for transportation of bed solids out from the riser. The setup of the simulation was mainly the same as used in bubbling bed simulations. The simulations are presented in detail in the project report **[16].**

The ways to realize the air inlet, the effect of air flow rate and the ways to calculate the turbulence were tested. The results presented here are for the system where the air into the bed was introduced through a grate with pressure drop. The air both for fluidizing and bubble forming was fed to a space below the grate, from where the air spread into the bed by a varying number of openings in the grate. The air feed into the bed varied slightly with time and location, because the pressure drop over the air distributor is determined by the air velocity in the openings.

The simulations were carried out with Fluent 6.1.18 applying the model combination for kinetic viscosity $\mu_{s,kin}$ and momentum exchange coefficient K_{sf} that predicted best the experiment of bubbling fluidized bed. Thus, the Gidaspow et al. model was applied for the kinetic viscosity of solid particles $\mu_{s,kin}$ and for momentum exchange coefficient K_{sf} the model of Gidaspow**.** The mixture and dispersed phase turbulence models in Fluent **[12]** were tested**.**

3.1.6 Experimental results

Experimental results are presented in detail in **[5]** and **[14]**. Here some selected results are shown from experiments with a bed of glass particles. The velocity of the gas introduced through the bottom plate to fluidize the bed was 0.152 m/s. Experiments were done at different gas flow rates through the middle orifice. The obtained average properties of bubble flow are plotted in Figure 2. Average bubble size gets smaller and consequently average bubble velocity goes down as the gas flow rate is reduced. The measured bubble sizes and velocities were in good agreement with empirical correlations given in literature.

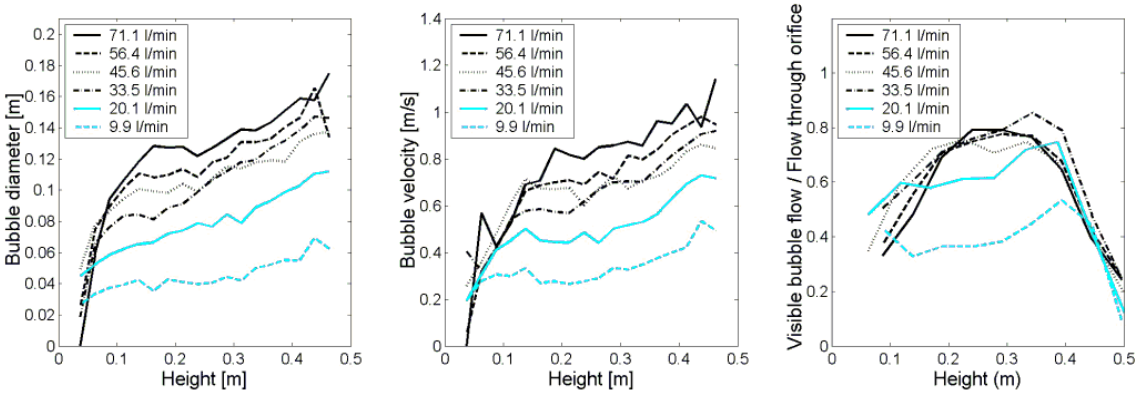

Figure 2. Average bubble diameter and velocity, and visible bubble flow rate as a function of height at varying gas flow rates through the middle orifice.

The measurement of CO_2 allowed us to study the bubbling frequency by analysing the time series taken from above the bed. The analysis of an experiment with 20.1 l/min gas

flow rate through the orifice showed no single bubbling frequency although a maximum was seen around 1 Hz. With gas flow rate 45.6 l/min it was even more difficult to see a clear bubbling frequency. The dominating frequencies are in both cases below 2 Hz. Also this fits well literature data.

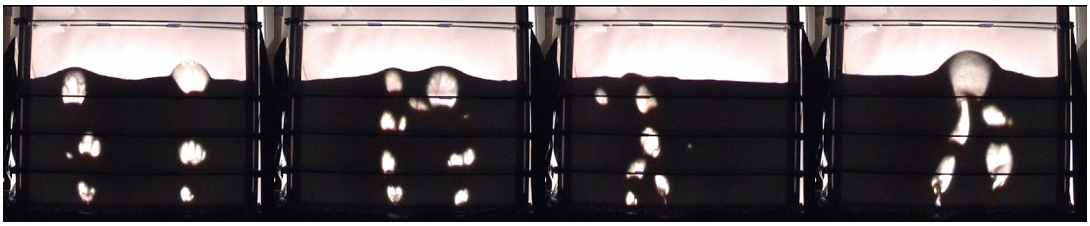

Figure 3. Bubble behaviour in experiments with two chains of bubbles. Gas flow rate through each orifice 20.1 l/min in the three first photographs and 45.6 l/min in the last. Orifice locations: a) (25,65), b) (40,65), c) (25,40), d) (40,65).

The main goal of the experiments was to study bubble interaction. Six experiments were done with two bubble chains, three with the gas flow rate 20.1 l/min and three with 45.6 l/min through each orifice. Figure 3 shows examples of bubble behaviour and Figure 4 the locations of the bubble midpoints and the lowest and highest points of the bed surface in each video frame of the six experiments.

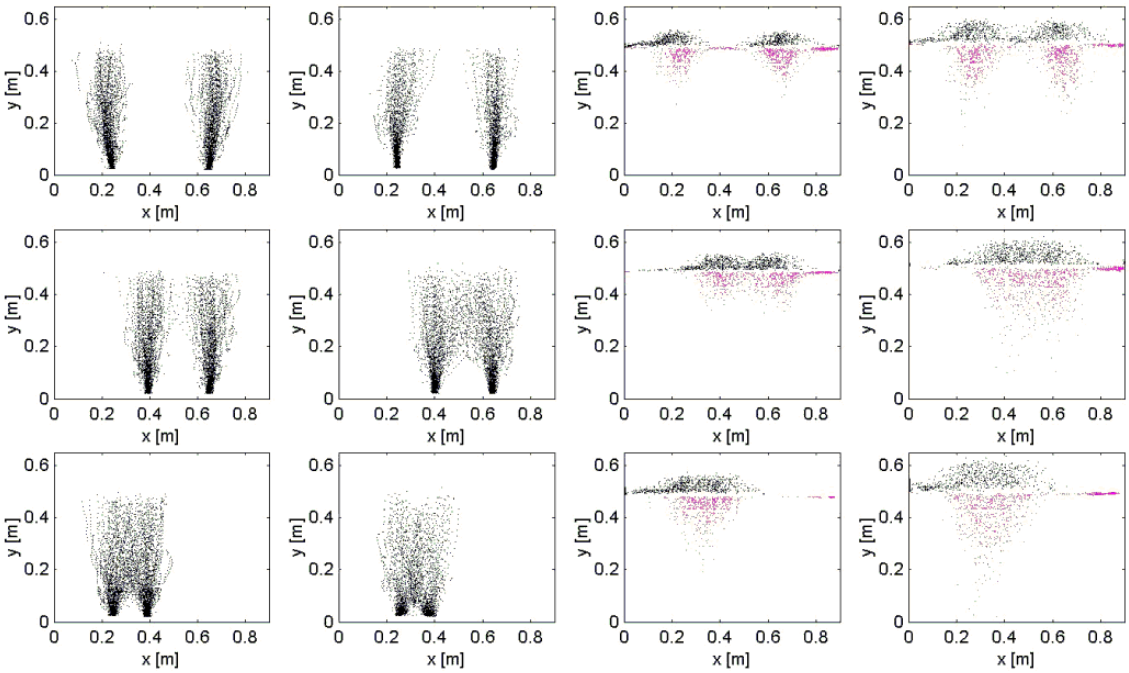

Figure 4. Midpoints of the bubbles (first column with 20.1 l/min, second with 45.6 l/min) and locations of the lowest ($y < 0.5$m) and highest ($y > 0.5$m) points of the bed surface (third column with 20.1 l/min, fourth with 45.6 l/min). Distance between orifices on the first, second and third rows 0.4 m, 0.25 m and 0.15 m, respectively.

The height at which bubbles interact and coalesce got lower as the distance between bubble chains was reduced or the gas flow rate was increased. When the gas flow rate through the left and right orifices located 40 cm apart was 20.1 l/min, no clear interaction between the two chains of bubbles could be seen other than in the bending of the bubble paths. When the distance between the orifices was reduced to 25 cm, interaction between bubbles and coalescence took place occasionally after 0.3 m above the bottom plate and some bubbles moved to the middle region. No big change in the average bubble size was seen. When the distance between orifices was 15 cm, bubble chains clearly interacted above 0.1 m. At the higher gas flow rate of 45.6 l/min, when the distance between the orifices was the maximum 40 cm, the interaction between the two streams of bubbles was seen only in the increased tendency of the bubbles to move towards the center of the bed. As the distance between bubble chains was reduced to 15 cm, very strong interaction took place above 0.1 m height.

There is no simple way to measure gas flow patterns and velocities inside the bed. Some indirect information on the gas flows can still be obtained. Some experiments were conducted to study the loss of tracer gas from bubbles. Air with small amount of CO_2 was fed through the middle orifice and CO_2 concentration profile at bed surface was measured. The minimum and maximum concentrations at different gas flow rates are shown in Figure 5 as function of lateral position. The maximum concentrations reflect the concentration in the bubbles. The minimum concentrations reflect the lowest concentration in the emulsion phase. The maximum concentration in the figures, 3.9%, corresponds to the concentration at the orifice. At highest gas velocities, some air from the bubbles occasionally spreads over the whole bed width. The concentration in the bubbles increases as the gas velocity increases. The minimum concentration at the orifice centreline is always at least about one third of the concentration in the bubble. This non-zero concentration in the emulsion phase is caused by the throughflow of gas through bubbles and the re-circulation through the cloud phase. The lateral spread of CO_2 should be compared with average bubble diameters at bed surface (see Figure 2) and with maximum bubble diameters that are about 40% bigger.

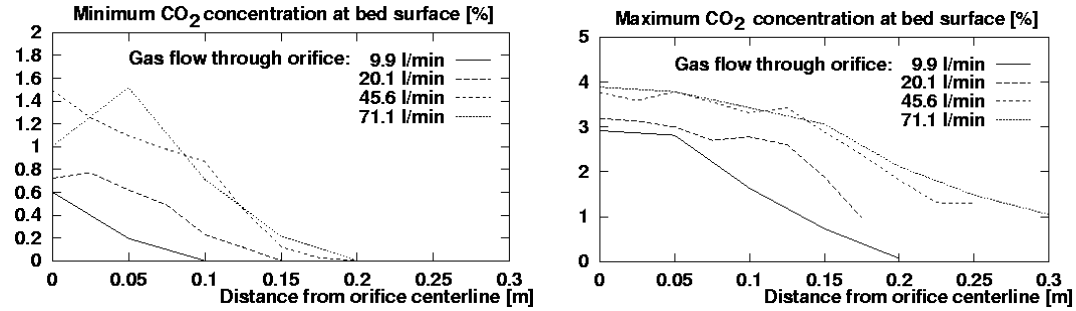

Figure 5. Minimum and maximum CO_2-percentage profiles at bed surface.

The particle velocities were tracked by adding a small amount of colored quartz sand to the bed and by following the movement of the quartz particles. Three different methods were used to determine particle velocities in the bubbling bed: two video cameras and one digital camera for still photography. With an ordinary video camera it was possible to capture single particles in fairly slow motion around the bubbles. By following the particles in several images both the magnitude and the direction of their velocities could be determined. Another video camera with an adjustable exposure time was used successfully to detect particle movement both inside and outside bubbles. Velocities were determined from black streaks formed in the images by the black particles as they moved during the exposure time. A digital camera was used in the same manner to measure particle velocities from the streaks the particles form.

Examples of measured velocities are shown in Figure 6. The highest velocities that could be measured were of the order of 2 m/s. Particles flow away from bubble around the upper part of the bubble and down along sides around the lower half of the bubble. In the wake phase below the bubble they move upwards at a high velocity. This happens more clearly in case of coalescing bubbles in the wake regions of both the bubbles. Single slower bubbles have less pronounced wake regions. The highest downflow velocities outside a bubble are found at about 1 cm distance from a bubble and the velocity increases towards the rear portion of the bubble. The highest upflow velocities are found at the nose of the bubble.

Inside the bubbles particles fall and especially in slower bubbles falling particle streams and curtains were observed. Between two bubbles, particles flow from the nose of the trailing bubble towards the wake of the leading bubble (Figure 6b). The velocities are higher than in a similar single bubble case. The video shows that particles get trapped in the region between two bubble chains for long time periods and the net flux out from this region is small.

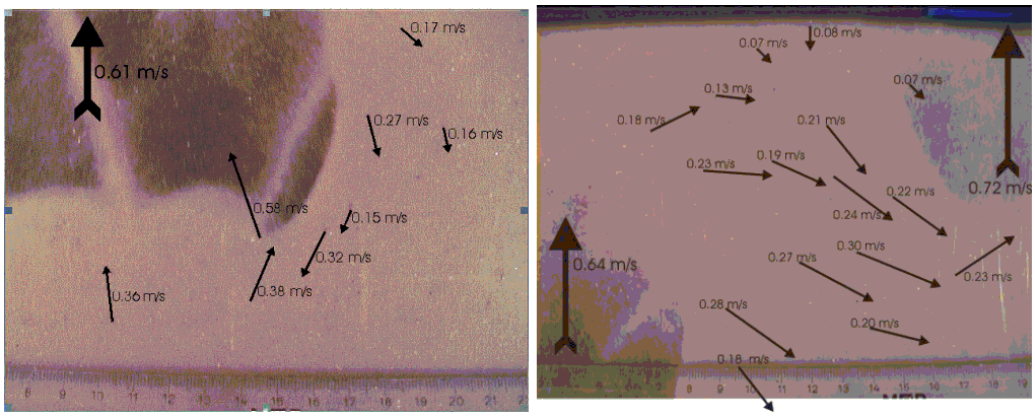

Figure 6. Bubble and particle velocities a) close to the bottom of a bubble and b) between two bubbles (Kallio et al. (5)).

Figure 7a shows the general solids flow patterns inside the bed when gas flows through a single orifice to a bed that is at minimum fluidization conditions. The typical solids flow pattern around a single bubble is illustrated in figure 7b.

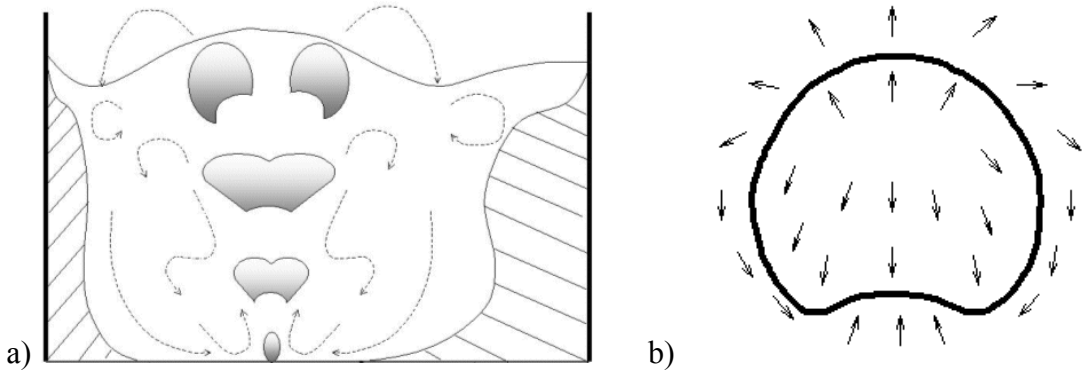

Figure 7. a) The general solids flow patterns inside the bed when gas flows through a single orifice to a bed that is at minimum fluidization conditions. b) Typical solids flow pattern around a single bubble.

The detected light intensity depends on the local particle concentration according to the Beer-Lambert law when passing through the suspension. The grey scale values in the video frames were converted to corresponding volume fractions.

Figure 8 shows a bubble that is suffering a roof collapse. According to the analysis of grey scale values, the particle concentration is 10–20 vol% in the region, from which the instability starts to fall. The concentration goes down to 6–7 vol% as the particles fall through the bubble. About 3–4 cm wide layers with slightly thinned suspension are observed in the wake and cloud regions around the 12 cm wide bubble.

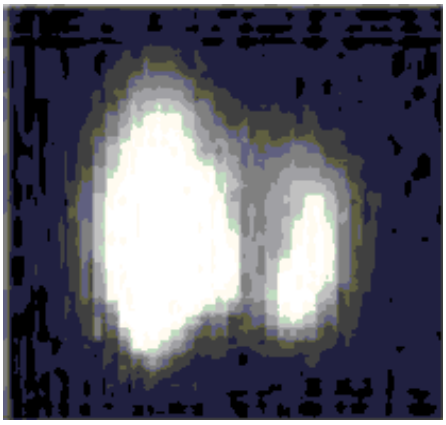

Figure 8. A bubble with a falling particle curtain.

3.1.7 Simulation results of bubbling bed

The computational grid consisted of 15200 cells sized 5.92 mm X 10 mm. First order discretization for time stepping and power law interpolation for spatial discretization were employed. A finer grid tested did not change the results significantly. Thus, the resolution is considered sufficient to provide grid-independent solutions, cf. Guenther and Syamlal **[11].** The time step was 1 ms, and 50 iterations per time step were performed. Typically, under-relaxation factor 0.5 was applied for pressure and 0.2 for other parameters. The simulations were carried out with Fluent version 4.5.2. The unstructured version 6.0.20 was also tested, but the results with identical physical models were qualitatively different with a poorer agreement with the measurements.

The minimum velocity needed for fluidizing the experimental bed was calculated by both models of momentum exchange coefficient K_{sf} presented above. The minimum fluidization velocity calculated by Gidaspow model, 0.14 m/s, is in accordance with the cold model experiment. The Syamlal & O'Brien model for K_{sf} predicts a significantly higher minimum fluidization velocity, 0.22 m/s. In the simulations, fluidization velocity was 0.152 m/s as in the experiments.

The aim of the simulation was to study the continuous bubbling of the bed. Statistical analyses, similar to those for the experimental results, were carried out. Figure 9 shows a comparison of measurements and simulation results. Examples of instantaneous bubble frames are shown together with the locations of the bubbles, bubble diameters vs. height, and the bubble rise velocities vs. height.

Although both combinations of models predict qualitatively correct bubble formation and interaction, some deviations from measurements are observed. Figure 9 shows that thinned areas in the suspension and even bubbles develop spontaneously inside the bed close to the surface with both models. This phenomenon was more typical with the Gidaspow model for K_{sf}. However, the size of the bubbles was larger compared to the results of Syamlal model, hence the results were more like the experimental ones. In general, both models yield smaller and faster bubbles than were typical in the experiment. A similar result was obtained in simulation based on 20.1 l/min air flow.

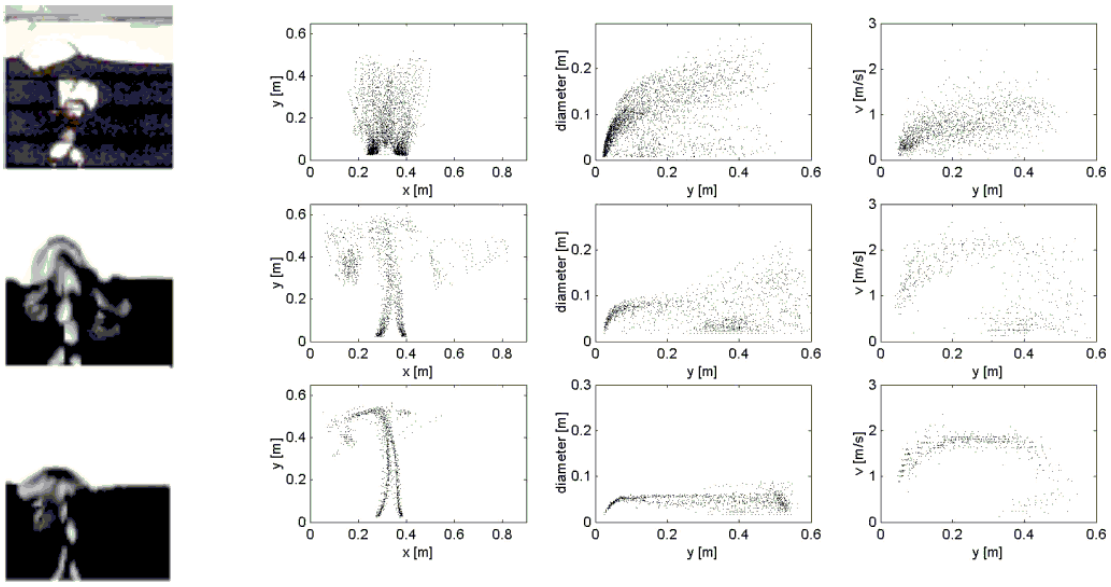

Figure 9. Comparison of the measurements (top) and simulations with the model of Gidaspow et al (middle) and with the model of Syamlal & O'Brien (below) with air flow rate of 45.6 l/min. The figure shows examples of instantaneous bubble frames, the locations of the bubbles, bubble diameters vs. height, and the bubble rise velocities vs. height.

The results of both model combinations show a more obvious interaction between the two bubble columns than the experimental results. According to the simulations, the bubble columns from the two orifices tend to join together to a single trail of bubbles. In the measurements, the average bubble size was larger and, consequently, bubble coalescence took place already at a lower elevation. Lateral movement of the bubbles was more extensive in the experiment. The behaviour of the bed surface was vigorous in both simulations and in the experiments, with big waves rising high and crossing the whole bed width.

The predicted flow fields of solids and air in the bed were examined. The general solids flow pattern is similar to the one shown in Figure 7a. However, close to the bubbles there are discrepancies in the solids flow field. In the simulations, downflow of solids takes place at a significantly longer distance from the bubbles than was seen in the velocity measurements, where solids are moving down along the sides of the bubbles. In the simulations, solids were heading upwards inside the bubbles whereas in the experiments particles were observed to fall down inside most bubbles. This discrepancy is caused by the smaller size and higher velocity of the bubbles in the simulations.

A good measure of the bed behaviour is the ratio between the visible bubble flow and the air flow in excess of minimum fluidization conditions, see e.g. Kunii & Levenspiel **[13].** Figure 10 shows a comparison of measurements and simulations. The result of the Gidaspow model is closer to the measurements. In the simulation using the model of

Syamlal & O'Brien, part of the gas is needed to fluidize the bed, which could explain the smaller bubbles and visible bubble flow.

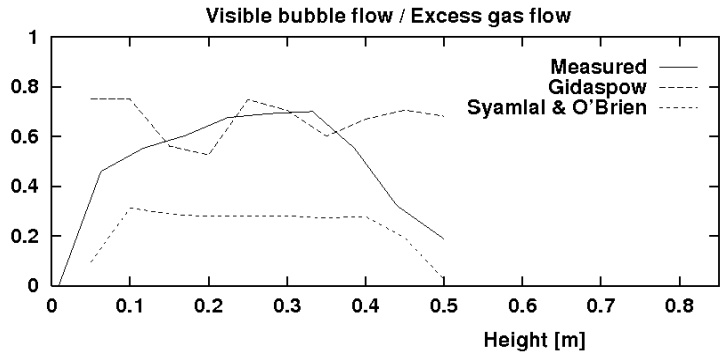

Figure 10. Visible bubble flow divided by air flow through the orifice vs. height.

3.1.8 Simulation results of turbulent bed

The computational grid consisted of about 10000 cells sized 10 mm X 20 mm. First order discretization for time stepping and second order spatial discretization were employed. Also coarse grid consisting about 1700 cells and dense grid consisting of about 30000 cells were tested. During the calculation, the dense grid led in convergence problems more often. The time step was 1 ms, and 50 iterations per time step were performed. Typically, under-relaxation factor 0.3 was applied for pressure, 0.7 for momentum and 0.2 for volume of fraction. For the air feed in the simulations, the velocities of 0.77 m/s, 1.5 m/s and 2.0 m/s were tested.

The aim of the simulation was to study the applicability of the models for calculation of turbulent bed. The simulations are examined as animations of the calculation results. The simulation results of turbulent bed have not been validated in the same way as the results of bubbling fluidized bed calculation due to the lack of experimental data. However, the results seemed to be qualitatively acceptable. Examples of instantaneous frames are shown in the Figure 11.

Simulations by the mixture turbulence model seemed to be blurred compared to the results by the dispersed turbulence model, see Figure 11. By both models, the clusters and strings of solid particles were formed inside the bed by the bigger air flow rate used. By the air flow rate 0.77 m/s, bubbles appeared clearly inside the bed. The figures were cleaner by the model of dispersed phases. The time-averaged solid volume fraction from 3 seconds calculation period showed that the solid particles were laterally located near to the walls of the grid. At the center of the bed, the time-averaged volume fraction of particles was smaller. Thus the models were assumed to predict the turbulent bed behaviour correctly.

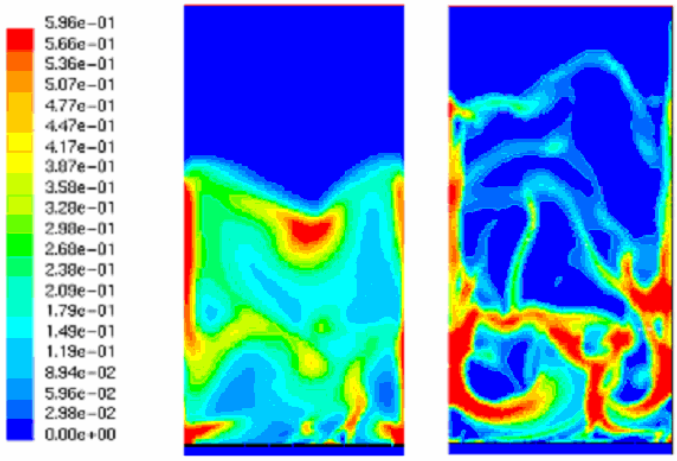

Figure 11. Examples of the solid volume fraction obtained from turbulent bed simulation. Left: mixture turbulence model, air flow velocity 1.5 m/s; right: dispersed turbulence model, air flow velocity 2.0 m/s.

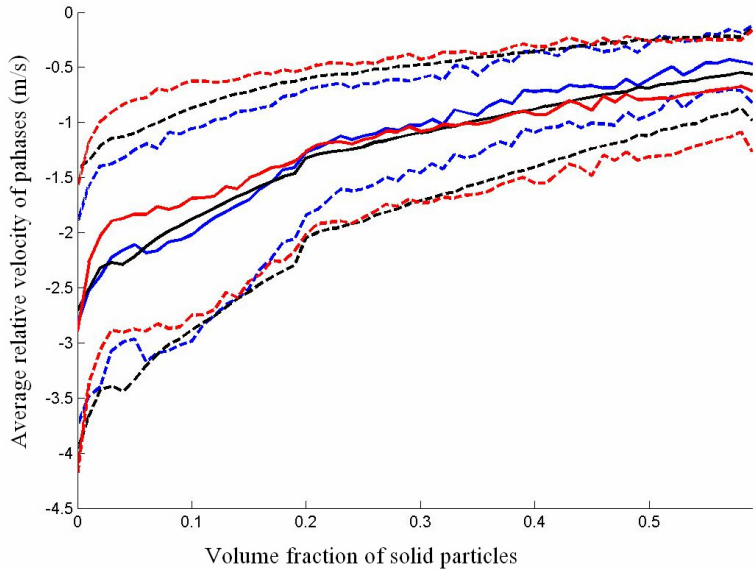

Figure 12. Average relative velocity (solid line) of phases as a function of solid volume fraction calculated by different grid densities. The standard deviation of the average is described by dash line. Black line: basic grid density, red line: dense grid, blue line: coarse grid, air flow velocity: 2.0 m/s.

In order to study the applicability of the simulations for the development of macroscopic models, the averaging method was studied. Essentially, drag force depends on the relative velocity of the phases and volume fraction of solid particles. The dependence of relative velocity of the phases on the solid particles volume fraction was examined in the following way. The volume fraction was discretized in 61 intervals from zero to the maximum packing. Utilizing a large number of instantaneous images,

the relative velocity values corresponding to each volume fraction interval were extracted from the simulation results. The average and standard deviation of the relative velocity of the phases were then calculated vs. the solids volume fraction. The procedure was carried out for the three different grid densities used in simulations. The comparison of the results showed that the relative velocity of the phases as a function of the solids volume fraction seemed to be slightly dependent on the grid density, as shown in Figure 12. The dense grid yielded a smaller average relative velocity than the coarse grid in regions of small volume fraction of solid particles. At dense suspension regions, the average of relative velocity produced by the coarse grid was smaller.

In the design of physical and chemical processes in fluidized beds, the understanding of solids mixing behaviour is important. A knowledge of the particle movement in fluidized beds assists in the understanding of solids mixing in fluidized beds. Here the solids mixing in the fluidized bed is studied by tracer technique. Part of the solid phase in the bed is changed locally to another phase with identical properties and while continuing the calculation by time the mixing of the solids is studied. Figure 13 shows the mixing of solid particles inside the turbulent bed to be both vertical and horizontal.

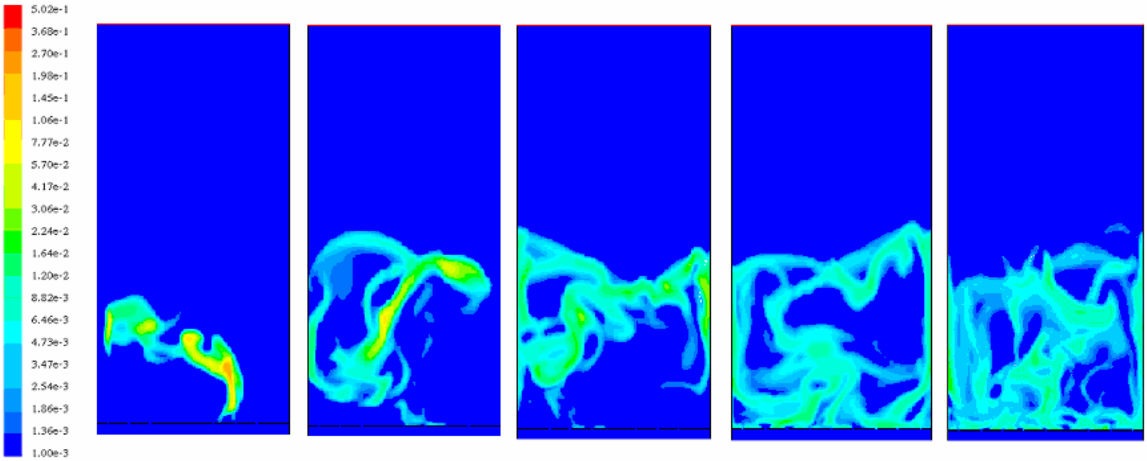

Figure 13. Mixing of the solid particles inside the turbulent bed using the air flow velocity of 0.77 m/s. Time period for the presented mixing is about 2.5 seconds. The volume fraction of tracer phase is presented by logarithmic scale.

3.1.9 Applications

In the study, the experimental results give good opportunities to validate CFD models of gas-solids flow and to evaluate their applicability in bubbling fluidized bed research and development. The multiphase calculation of industrial processes is more challenging than the one phase simulation due to the long computing times and limitations of the models. The results of the simulations are valuable in modeling the multiphase

processes. Sub-phenomena, like solids particles mixing offers knowledge, which can be used in development of simple mixing models. The results of the simulations have been directly used in development of models for combustion processes.

Although the study has been close to the fundamental research, the results can be adapted for industrial projects involving multiphase modeling. Most of the validation was for bubbling fluidized beds, but fundamentally the same models are applied to turbulent and circulating fluidized beds, too. In all these processes, lateral mixing is most efficient in the dense bottom region. In many processes, such as fluidized bed combustors, a major part of the chemical reactions also take place in this region. Because of the importance of the dense bottom zone, a better understanding of mixing of gas and solids in the dense suspension conditions is extremely important for process improvements. Thus, the results and experience gained by the study are valuable for future studies of fluidization processes. The results have already significantly contributed to the development of models for circulating fluidized beds (see next section). In addition to the process industry, the most important appliances of the fluidization processes are found in energy production, metallurgy and oil refining industries.

3.1.10 References

[1] Syamlal, M. & O'Brien, T.J. Computer Simulation of Bubbles in Fluidized Beds, AIChE Symposium Series, No. 270, 85, 22–31, 1989.

[2] Kuipers, J.A. A two-fluid micro balance model of fluidized beds. PhD thesis, University of Twente, The Netherlands, 1990.

[3] Boemer, A. Euler/Euler-Simulation der Fluid dynamik blasenbildender Wirbelschichten. PhD Thesis, Aachen, Germany, 1996.

[4] Taivassalo, V., Koskinen, K., Jacobson, T., Korhonen, S., Manninen, M. & Parmes, E. Two- and Three-Dimensional CFD Modelling of a Bubbling Bed Experiment, The 4th Int. Conf. on Multiphase Flow, New Orleans, 2001.

[5] Kallio, S., Hermanson, A., Fagerudd, K. & Engblom, M. Experimental study of bubble interaction in a 2D bubbling fluidized bed cold model. Report 2003 - 01, Åbo Akademi University, Heat Engineering Laboratory, 2003.

[6] Hong, R.Y.,Guo, Q.J.,Luo, G.H.,Zhang, J.Y. & Ding, J.M. On the jet penetration height in fluidized beds with two vertical jets. Powder Tech., Vol. 133, pp. 216–227, 2003.

[7] Fluent., Fluent Users' Guide – Release 4.4 2nd Ed. Fluent Inc., Lebanon, 1997.

[8] Gidaspow, D., Bezburuah, R. & Ding., J. Hydrodynamics of circulating fluidized beds, kinetic theory approach. Fluidization VII, Proceedings of the 7th Engineering Foundation Conference on Fluidization. Pp. 75–82, 1992.

[9] Ding, J. & Gidaspow, D. A Bubbling fluidization model using kinetic theory of granular flow. AIChE Journal, Vol. 36, No. 4, 1990.

[10] Syamlal, M. & O'Brien, T.J. Simulation of granular layer inversion in liquid fluidized beds. Int. J. Multiphase Flow, Vol. 14, No. 4, pp. 473–481, 1988.

[11] Guenther, C. & Syamlal, M. The effect of numerical diffusion on isolated bubbles in a gas-solid fluidized bed. Powder Technol., Vol. 116, pp.142–154, 2001.

[12] Fluent, Fluent Users' guide – Release 6.0, Fluent Inc., 2001.

[13] Kunii, D. & Levenspiel, O. Fluidization Engineering. Butterworth-Heinemann, second edition, 1991.

[14] Kallio, S., Flores Geant, M. & Hermanson, A. Experimental study of local flow structures in a 2D bubbling fluidized bed cold model.

[15] Ojaniemi, U. & Manninen, M. Kuplivan leijupedin laskenta. VTT Prosessit, PRO5/P7526/03, 2003.

[16] Ojaniemi, U. & Manninen, M. Turbulentin pedin CFD-mallinnus. VTT Prosessit, PRO5/P7505/04, 2004.

3.2 CFD modeling of circulating fluidized bed risers

Sirpa Kallio
Åbo Akademi University, Heat Engineering Laboratory

3.2.1 Background

Circulating fluidized bed (CFB) processes are used e.g. in energy production and in petrochemical and metallurgical industries. In all these processes, heterogeneous and/or catalytic reactions take place. Thus understanding the mixing processes of gas and solids is necessary for further improvement of the processes. As an example of CFB's, Figure 1 illustrates the principle according to which a circulating fluidized bed combustor operates.

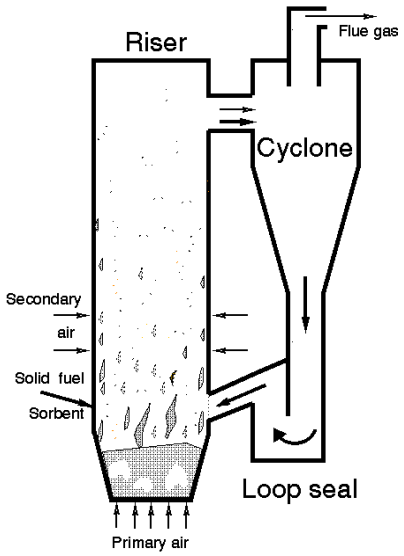

Figure 1. A circulating fluidized bed combustor.

Gas blown from the bottom at a high velocity fluidizes the solids in the riser. Solid fuel and secondary air streams enter the furnace higher up at different elevations. Solid particles are transported out off the riser and get separated in a cyclone and return to the furnace bottom. In the riser, the vertical distribution of solid material shows a separation into a dense bottom region, a dilute upper region and an intermediate transition region. A denser zone with down-flow of solids is observed at the walls.

The dense bottom region resembles a bubbling bed but is much more vigorously mixed. Bubbles are replaced by voids of varying shapes. In the upper dilute part of the riser, the gas-particle suspension is separated in a dilute suspension and dense regions described as clusters. Clusters form, grow, change shape and disintegrate in a continuously fluctuating process, when the solid particles are transported up by the carrying gas. Clusters tend to move, on average, upwards and from the inner part of the riser towards the walls. There their upward momentum is reduced and they tend to fall down along the wall. This process creates the denser wall region.

Although circulating fluidized beds have been used in the industry for decades, serious problems still remain in the empirical knowledge and in the theoretical and numerical description of turbulent flow of the dense, non-homogeneous gas-solid suspension inside a CFB.

In numerical calculation of gas-solid flows, the limited computational resources and long computation times restrict the number of mesh points that can be used. Table 1 shows the relationship between the number of computational cells and the element size, when the computational domain inside a large CFB boiler is divided into cells of equal size. The problem of large element sizes in practical CFB simulations has been taken up by Hyppänen **[1]**, Poikolainen **[2],** Kallio et al **[3],** Sundaresan **[4]**, and Kashiwa & Yang **[5]**.

Table 1. Relationship between the number of elements and element size.

3D simulation, furnace volume 10 x 30 x 40 m^3	
Elements	Element size
20 000	0.85^3 m^3
100 000	0.5^3 m^3
100 000 000	0.05^3 m^3
2D simulation, furnace area 30 x 40 m^2	
Elements	Element size
20 000	0.25^2 m^2
100 000	0.11^2 m^2
500 000	0.05^2 m^2

To properly describe the varying voidage and velocity conditions, fluidization would have to be simulated as a time-dependent process. This is true especially in case of bubbling beds. To yield representative average properties the calculated time period should be several seconds, preferably tens of seconds. At the same time, the time step should be very short to guarantee numerical convergence. Proper description of bubbling and cluster formation requires that a fair number of mesh points in each direction is located inside the bubble/cluster to avoid mesh-dependent results. As a result of these requirements, computation times on today's computers are often too long especially in the case of industrial beds and 3D simulations.

The problem caused by coarse meshes required for 3D calculations of large industrial furnaces was considered by Hyppänen **[1],** who derived balance equations for gas-solid flow at two different levels. First, local equations were written for the description of the fine structure of the flow; the control volume size was assumed to be an order of magnitude smaller than the length scale of inhomogeneities such as clusters. From the

local equations he derived macroscopic equations in which the local flow structure must be accounted for by closure relations. Poikolainen **[2]** and Kallio et al **[3]** continued this work and presented macroscopic equations and simulation results from steady state calculations in two and three dimensions.

The problem with macroscopic equations is that since fluctuation terms dominate momentum transfer, as is shown in the measurements presented in Kallio **[6]**, closure relations have a dominating role in the modeling. Thus a significant amount of experimental data would be needed to close the equation system. In Kallio **[6]**, the fluctuation terms in macroscopic solid phase equations in the vertical direction were determined from measurements for one flow situation and one particle size. No information on the lateral velocities could be obtained from the measurements. Since measurements are time-consuming and difficult, one alternative way to obtain closure relations for macroscopic equations would be to perform simulations using a more detailed description of the time-dependent behavior of the gas-solid suspension in smaller processes and in 2D and to estimate from the results the macroscopic fluctuation terms. One goal of the present work is to develop this type of more detailed models.

The most common approach used today for CFD modeling of fluidization processes is based on the kinetic theory of granular flow. A simplified version of the model is implemented in Fluent 6 **[7]**. In the derivation and closure of the equations, it is assumed that inside the averaging domain, particles are distributed quite randomly and their velocities fluctuate in a random way. The distances between mesh points should be of the order of a couple of centimeters, or preferably less, in order to keep the assumptions used in the averaging procedures still valid in the numerical treatment. Unfortunately, in practical calculations this requirement is usually not met.

Results of this mismatch are easily seen in many numerical simulations of gas-solid flows in CFB risers. Too low solid concentrations and too low slip velocities in the bottom region indicate that the gas-solid drag forces are overestimated. Often, the opposite phenomenon is observed in the upper part of the riser: the predicted solid concentration is too high. This is a result of the drag correlation used. Not only the drag forces are wrong but also the other terms in the momentum equations suffer from the mismatch between modeling assumptions and mesh size. However, since the largest terms in the equation system are due to gas-solid drag forces in the vertical direction, correction of this term is of greater importance than modification of the other, smaller terms.

Although the main source of errors is easily seen, finding a good remedy is difficult. The corrections to the drag forces must be some function of the inhomogeneity inside each control volume. The inhomogeneity is dependent on the size of the control volume: the maximum inhomogeneity is observed, when we assume a control volume encompassing

the whole flow domain and, in addition, we assume that the equations are valid for steady state (a time average over a long time step is applied). In all steady state calculations, big corrections are necessary if there is any clustering tendency in the solids flow. Another difficulty in the determination of the necessary corrections is that clustering behaviour is strongly dependent on the properties of the fluid and the particles and on the average velocities and the solids loading. In the case of small, light particles (e.g. FCC particles) a much larger correction is needed than in the case of coarse, heavy particles (e.g. sand). Hence careful comparison of simulation results with empirical data is absolutely necessary.

The goal in this work has been to create a model that would describe the typical features of gas-solids flow in a CFB, including the large scale fluctuations of voidage and velocities. This model could then be used to simulate smaller CFB's and large ones in 2D. It could even be used to provide information on fluctuations to derive closure relations for macroscopic equations.

What are then the characteristics of fluidization processes we wish to produce through this type of numerical simulations? Fluidization processes are typically reactors (cracking reactors, combustion chambers etc) and any features relevant to the description of the chemical processes will be of interest. Thus the residence times of gas and solids, and hence the average velocities and velocity fluctuations, should be close to real ones. In a circulating fluidized bed, it is especially important to have correct solids circulation rate through the cyclone and a correct residence time at all levels of the riser since the chemical processes taking place at different elevations can differ significantly. This means that circulation inside the riser has also to be correctly presented. Moreover, the axial distribution of solids should be correct: at the bottom there is typically a dense bed, from which splashes of solids emerge to the region above and fall back causing efficient mixing and long solids residence times in this bottom zone. At the walls, the suspension density should be high and particles should move on average downwards.

3.2.2 Discussion on the gas-solid drag force

In most CFD simulations of fluidization processes, the model of Gidaspow **[8]** that combines the equation of Ergun **[9]** and the model of Wen & Yu **[10]** has been used for description of gas-solid drag. Especially in CFB simulations, the results have been poor and the concentration of solids at the bottom of the riser has been too low, and as a consequence, the pressure profile has significantly differed from the measured one (see e.g. Peirano et al **[11]**). There are several reasons for this discrepancy. One factor enhancing formation of a dense bottom bed is the interaction between the pressure fluctuations in the riser itself and in the wind box. Another factor is the particle size

distribution. In a typical CFB, particle sizes vary inside a wide range and the terminal velocity of the largest particles is typically below the superficial gas velocity.

Although these factors are significant, they alone are not sufficient to explain the large discrepancy between measurements and simulations. The main reason for the discrepancies seems to be particle clustering. A counterargument often given is that if we reduce the size of the computational cells sufficiently, the model itself should produce clusters and no correction to the drag laws for homogeneous flows is necessary. Thus we should compare the length scales of clusters and the element sizes used in the calculations. To correctly describe a region, which differs from its surroundings in terms of solids concentration, several mesh points should be located inside each clearly separate dense or dilute domain. For small risers, it has shown to be possible to correctly predict cluster formation and realistic slip velocities. One example is found in Sundaresan **[4]**. Another example is shown in Zhang & VanderHeyden **[12]**, who employed a simplified set of Eulerian-Eulerian multiphase equations that disregarded particle-particle interactions and used the single phase drag law for gas-particle drag.

One additional complicating factor is the effect a cluster has on the gas flow field around the cluster. Moran & Glicksman **[13]** showed that clusters induce large scale fluctuations in the surrounding gas flow. The interaction of the clusters with the surrounding gas can be difficult to account for in Eulerian-Eulerian simulations.

Cluster sizes and shapes have been determined in a large number of studies. Clusters/aggregates are long and narrow, with thicknesses often below 1 cm. Gas pockets surrounded by horseshoe shaped clusters heading upwards and falling clusters of similar shape but of opposite direction have been detected (Van den Moortel et al **[14]**). The 3D laser sheet study of Horio & Kuroki **[15]** showed in a similar way that a typical cluster has a paraboloid shape with the nose facing downwards.

The experimental findings indicate that the dimensions of clusters and the gas velocity gradients around the clusters in CFB risers are at least partly too small to be properly described in Eulerian-Eulerian simulations. They have to be included in the closure equations representing the subgrid scale phenomena. This conclusion is the same as drawn by Kashiwa & Yang **[5]**. Several researchers have corrected the drag force written for homogeneous suspensions to account for formation of clusters and the increased average slip velocities caused by clustering. However, no general and user-friendly model has so far been presented. The models presented either have limited validity (models of Niewland et al **[16]**, O'Brien & Syamlal **[17]**, and Poikolainen **[2]**) or are complicated (EMSS based models **[18]**).

Cluster corrections to drag forces have been derived from two directions: either from local flow structures (EMSS **[18]**) or from global, macroscopic behavior of gas-solids suspensions (e.g. Poikolainen **[2]**). Some authors have suggested that local Lagrangian simulations should serve as a basis for deriving closure relations. This is a tedious process although otherwise attractive. The other alternative would be to use macroscopic information as in Poikolainen **[2]** (see also Kallio et al **[3]**).

Poikolainen's model was developed originally for one-dimensional steady state simulations and its use in calculation of time-dependant gas-solids flow in 2 and 3 dimensions sounds questionable. The basic question is, how big a part of the fluctuations in velocities and voidage is of a smaller scale than typical mesh size and does this part behave in a similar way as the large scale fluctuations described by the 1D model so that a similar functional form could be used. From a literature review it became obvious that at least a significant part of the fluctuations is of a smaller dimension (thin clusters surrounded by steep velocity gradients in the gas phase) so that a model of similar structure sounds at least to be a feasible starting point for model development. This approach is chosen in the present work.

When the drag force correlations are derived on the basis of models for special cases of fluidization, as was done in **[2]**, it guarantees that the models yield right or at least qualitatively reasonable results for the special well known (one-dimensional) cases. The drag force correlations for homogeneous flows determined from empirical data from packed beds, dilute suspensions, liquid-solid fluidization and gas-solid flow at incipient fluidization state are also valid for non-homogeneous flows (e.g. bubbling and fast fluidized beds) locally inside any homogeneous region. In the same way as for homogeneous flows we can derive special macroscopic models for non-homogeneous aggregative gas-solid flows on the basis of empirical information. One way to formulate the correlations, which is also used in this work, is to apply a correction to the particulate flow models.

3.2.3 The CFD model

The kinetic theory model of granular flow in Fluent 6.1.22 **[7]** is used for testing and comparisons of different models. Fluent allows division of the solid phase into a number of computational granular solid phases. In the present study, solids are, however, described as one phase characterized by a single particle diameter and material density. In the simulations, the solid phase kinetic viscosity was calculated from the model by Syamlal et al **[19]**. Granular temperature is calculated in Fluent from an algebraic equation obtained from the original transport equation by neglecting convection and diffusion

terms. For the gas phase, k-ε model of turbulence is used in the simulations to calculate the effective gas viscosity.

For a single solid particle moving in a fluid, the drag force is proportional to the velocity difference between the particle and the fluid, the slip velocity. In a similar way, the interphase drag forces in a gas-solid suspension can be expressed as a function of the average slip velocity. For a dense gas-solid suspension, we must multiply the single particle drag force by a correction function to account for the effects of the void fraction.

Before we start model development we should set up the basic requirements the drag model should fulfill. One obvious requirement is that at very low solids concentrations the drag force should be equal to the single phase drag. Another requirement is that the model should produce the correct minimum fluidization conditions. In practically all fluidization processes there are regions, which can temporarily become de-fluidized. In the kinetic theory model implemented in Fluent there is a packing limit for the solids, which prevents the bed from collapsing beyond reasonable solids concentrations. If the drag force is overestimated dense regions can not form and as a result, the maximum solids concentration in a simulation is far below minimum fluidization conditions. Especially in bubbling bed simulations errors in the predicted minimum fluidization velocity would lead to serious problems and to erroneous bubble flow rates (see section 3.1).

When the solids concentration increases from very dilute, the drag force should first reduce and at some point start to increase again. This requirement comes from the observed cluster behavior and measured average slip velocities. A further requirement is that the drag force should change continuously as a function of voidage and other relevant parameters.

All types of fluidization processes and particle sizes should be accommodated in a single model. Even other particle properties than size and material density have significant effects on clustering tendency. These factors (restitution coefficient, shape, surface structure etc) are difficult to include in the model a priory. Hence the model should be easy to adapt to measured conditions. One important factor, which we also ignore in this first attempt, is the particle size distribution.

There is no simple way to determine the best way to formulate the voidage function in the region between very dense and very dilute conditions. Thus twelve alternative ways, numbered in the following from 1 to 12, were tested and sensitivity analyses were performed. Examples of tested voidage functions, by which the single particle drag force is multiplied, are shown in Figure 2 for the slip velocity 1 m/s (d_p=230 μm and ρ_s=1800 kg/m^3).

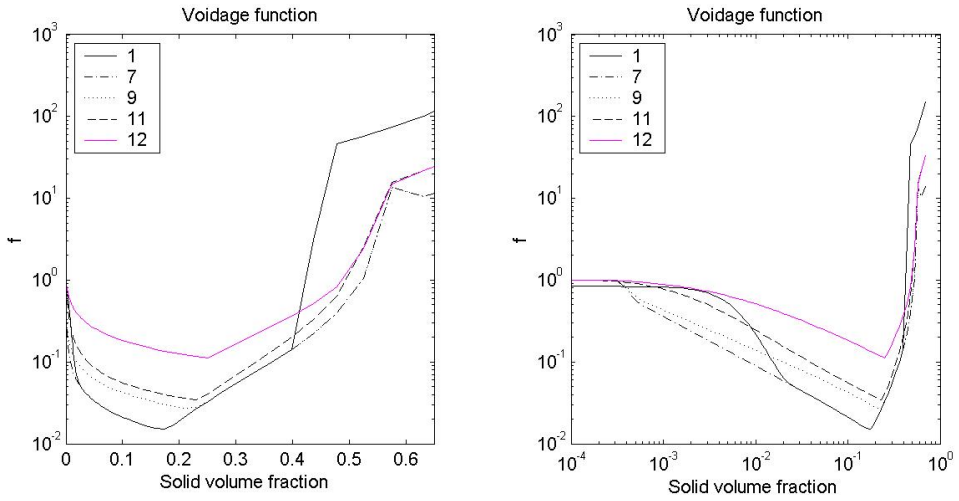

Figure 2. Examples of voidage functions used for Geldart B particles (d_p=230 μm and ρ_s=1800 kg/m^3) at slip velocity 1 m/s plotted in two different scales.

3.2.4 Simulation results

A large number of test runs were performed. These included three different particle suspensions, all characterized by a single particle size and solid material density. One of the suspensions belonged to Geldart A and two to Geldart B. Fluidization conditions in the simulations varied from bubbling to turbulent and circulating beds. The effect of mesh refinement was also tested. Different CFB sizes were studied.

The major part of the simulations were done for the cold model experiment conducted at Foster Wheeler Energia Oy, the results of which were presented in Kallio **[6]**. The purpose of these test simulations was to validate the chosen drag laws in simple, well-defined conditions, from which measurement data was available. Since a large number of runs was necessary, the simulations were performed in a simplified manner in 2D. No exit effects were taken into account. The initial conditions used in the simulations were created by using drag law 1. The bed was filled with particles up to 0.4 m height and fluidization air flow was switched on. After 7.5 s fluidization, the simulations were interrupted and the result was stored and used as initial state in the further simulations conducted for different comparisons.

It is a normal practice to calculate the solids flux at the outlet and to feed the same amount to the bottom bed e.g. as a mass source term. The calculations are then continued till convergence and a time-integration is performed to obtain average values at steady state. This procedure was not, however, followed in the comparisons of the present work. In 2D simulations there is a risk that the results are somewhat distorted by the solids added to the bottom. In addition, the solids flux at the outlet should be, if the model works correctly, fairly low so that some kind of pseudo steady-state is anyway obtained during the

simulation. By letting the bed slowly empty, a single simulation gives thus information on the existence and character of the bottom bed at different solids loads. Moreover, time is saved since it is not necessary to wait till the process has reached steady state. Although the conditions in the simulations of this model comparison study differ thus slightly from steady state, they were estimated to be close enough to allow comparisons between different drag models and between simulation results and measurements.

Particle size in the simulated case was 230 μm and the material density was 1800 kg/m^3. Riser height was 7.3 m and width 1 m. The average superficial gas velocity above the air distributor was 4 m/s. The local gas inflow velocities were described by means of a function, the value of which fluctuated as a function of place and time (with 0.8 s frequency). The function was based on the 2D approximation of the air distributor used in the experiment. Three different computational mesh sizes were used: 4400 elements, 17600 elements and 70400 elements. In all these meshes, the mesh was refined close to the right wall in order to observe, how the model resolves the wall layer in different meshes. Thus there is no symmetry in the results.

First some initial tests were conducted with the models implemented in Fluent 6 (the model of Gidaspow **[8]** and the model of Syamlal & O'Brien **[20]**). In these simulations no dense bottom bed was formed and the bed got emptied fast. After this, the drag correlations developed in this work were implemented in Fluent and tested. With all the drag models developed in this work, a bottom bed was created. In all simulations, clusters with u-shaped bottoms were also formed.

Figure 3 shows examples of the simulations. The comparison of drag models in Figure 3a illustrates the differences in bottom bed height and density obtained in the different cases. Also the concentration of solids in the dilute region varies significantly in the simulations. In Figure 3b, results obtained using a finer mesh with drag model 12 show how the bed slowly empties in about one minute, when there is no feed of solids to the riser bottom. Figure 3c shows a comparison of the three meshes. The basic structure in the results obtained with all the three meshes is the same but more fine structures become visible as the element sizes are reduced.

Figure 4 shows the changes in solids outflow rate at the top of the riser and the fluctuations in the pressure drop over the riser as functions of time in a simulation where the riser slowly gets emptied. Solids flux remains almost constant although the pressure drop, which correlates linearly with the solids load, is reduced. Typical measured solids circulation rates in combustors are of a similar order as obtained in the simulations, in which they have on average varied between 5 kg/(s m) and 10 kg/(s m). In the pressure curve we see the fluctuating changes as the gas velocity changes. This result is expected and desirable, since experimental observations have confirmed that the main fluctuation frequency in a CFB originates from the air distributor and the air feeding system.

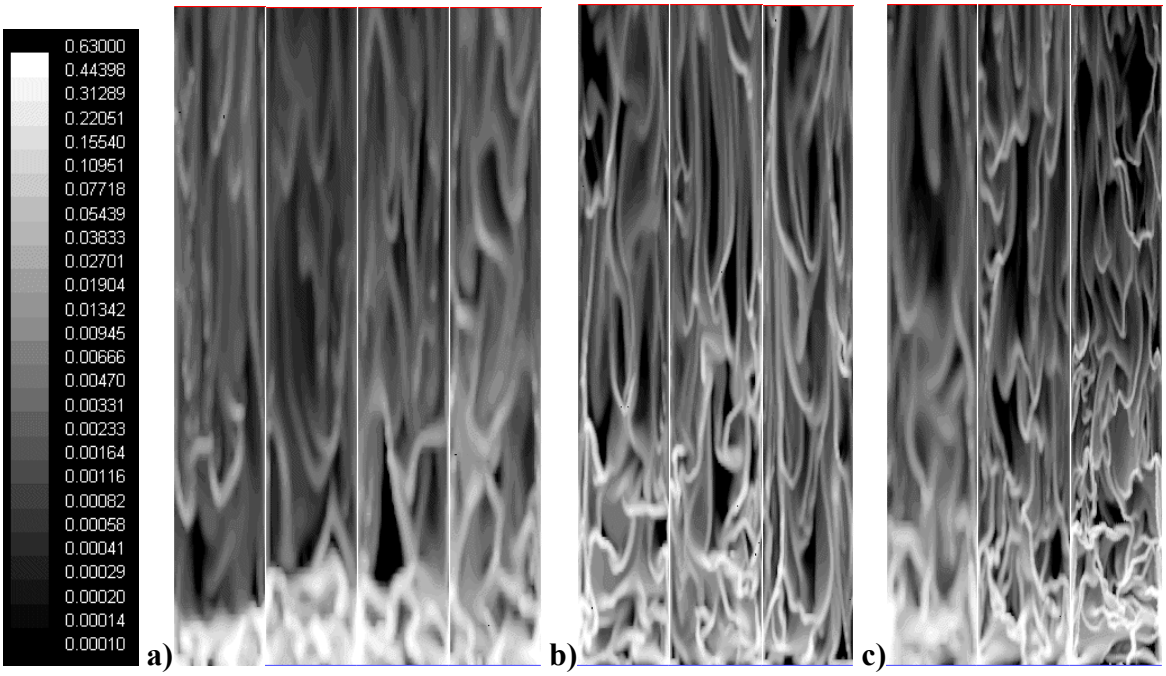

Figure 3. a) Solids volume fraction at 10 s obtained with the coarse mesh and, from the left, drag models 1, 7, 9, and 12. b) The situation in the riser after 5 s, 10 s, and 20 s calculation using drag model 12 in a finer grid with 17600 elements. c) Comparison of results after 10 s simulation obtained with drag model 11 in the three different meshes used in the study.

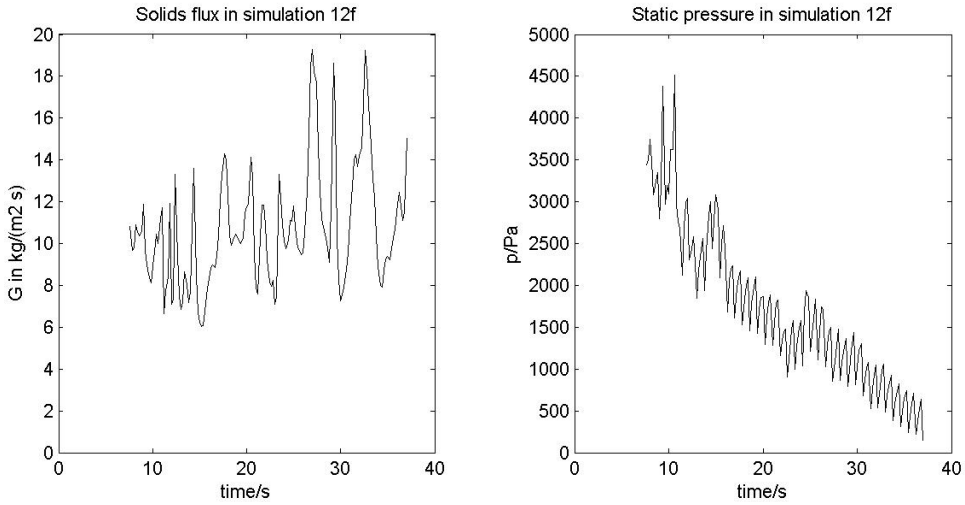

Figure 4. Solid flux at riser outlet and pressure drop over the riser as functions of time simulated with drag model 12 in a coarse mesh.

In Figure 5, a comparison of the pressure profiles and solid volume fraction profiles obtained with different models is shown. The curves show the average between 5 and 10 s of the simulation, during which time the solids load roughly corresponds the one in the

experiments. Average solids concentration at the bottom varies in the different simulations between 15 and 30 volume %. In general the behavior is as expected.

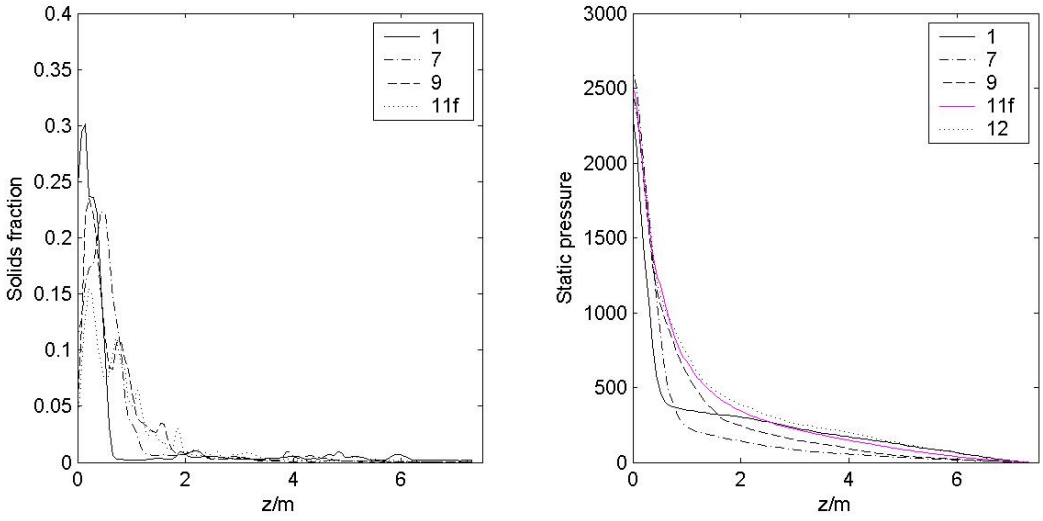

Figure 5. Comparison of vertical solids volume fraction profiles and pressure profiles obtained with different drag models (f refers to a mesh with 17600 elements; other simulations were conducted in a coarse mesh with 4400 elements).

Unfortunately no accurate measurement of the pressure profile was available in Kallio **[6]**. The total pressure drop is close to the one estimated from the measurements and the structure of the profile with steep drop at riser bottom fits well the observations presented in literature. The average solids densities measured in the bottom bed in similar conditions have been in literature data between 20% and 40%. The highest estimates are typically obtained from pressure measurements, which can reflect the high solid concentration and higher static pressure close to the walls. Figure 6 shows the average lateral pressure profiles from a simulation with drag model 12. A clear increase in static pressure is observed in the corners. Some models gave even higher pressures in the corners, up to 4 kPa.

Figure 7 shows the average solids volume fraction, average gas velocity and average solids velocity between 5 and 10 s in a simulation with drag model 12. The correct structure of the flow is clearly visible. At the walls, a denser region is created with solids flowing on average down along the wall. Both the solids velocity and volume fraction are of the same order of magnitude as measured (see **[6]**). On the right side, where the mesh is refined, solids velocity and density at the wall are higher and even the gas flows down. Downflow of gas has been observed also in practice in real furnaces.

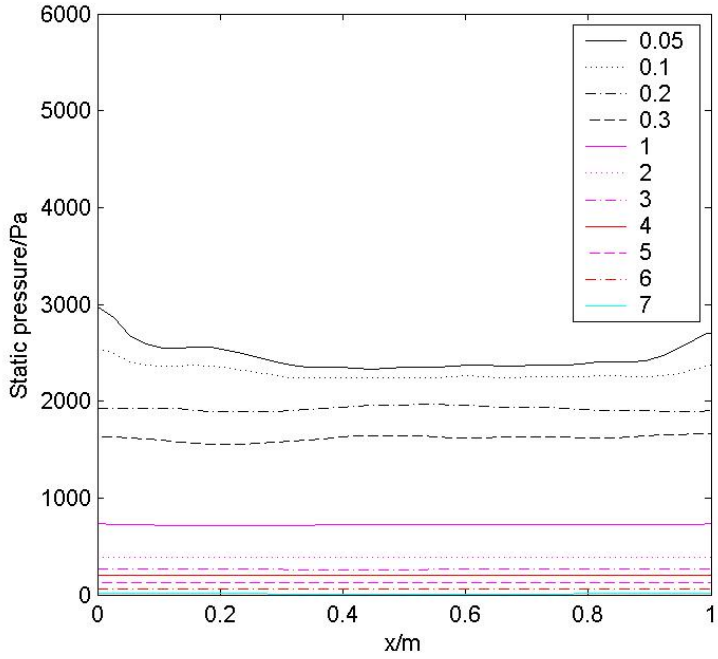

Figure 6. Lateral profiles of average static pressure at heights between 0.05 m and 7 m above air distributor. Drag model 12 was used in this simulation.

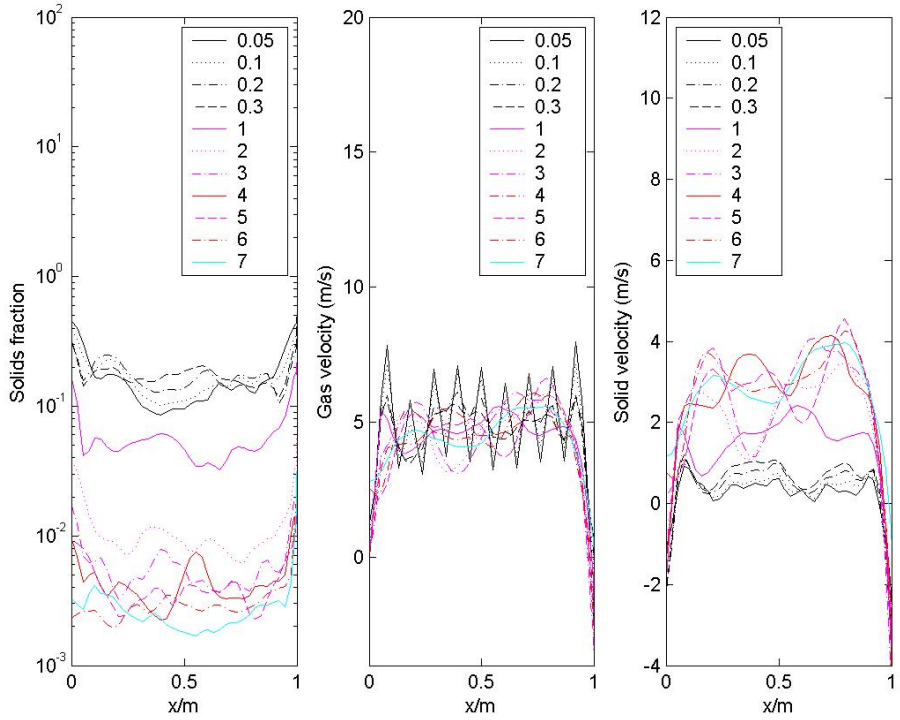

Figure 7. Lateral profiles of average solids volume fraction and average gas and solids velocities at different heights in simulation 12.

Figure 8 shows the fluctuations in the solids volume fraction and gas and solids velocities between 5 and 10 s. For comparison, measurements taken from Kallio **[6]** are also depicted. The scatter in the measured and simulated values is quite similar. At the bottom, the solids fractions above 40% are less common than in the measurements in **[21],** which were from similar fluidization conditions.

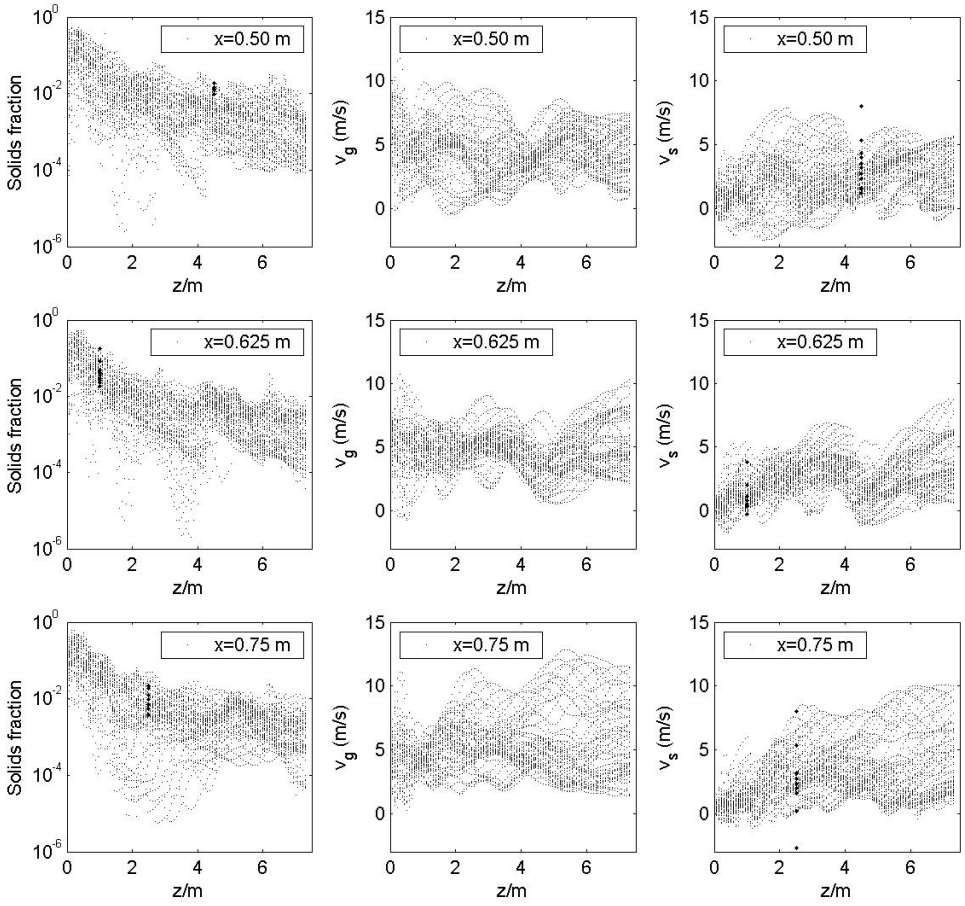

Figure 8. Measured (darker points) and simulated values of solids volume fraction and gas and solids velocities between 5 s and 10 s in a simulation of the cold model experiment performed in the coarse mesh with drag model 12.

The simulations of the cold model experiments presented in Kallio **[6]** gave satisfactory results and showed correctly the main features of the gas solid flow structure in a CFB riser. The biggest control volumes used in these simulations were in the coarse mesh 2.6 cm X 7.3 cm and the smallest in the fine mesh 0.65 cm X 1.8 cm (the elements at the right wall were even smaller). The size of the riser was smaller than used in commercial fluidized beds.

To see, whether the model works well for bigger risers, some tests were conducted for a riser with 5 m width and 18.5 m height. The results illustrated in Figure 9 show that the typical division in a dense bottom bed and a dilute upper zone is obtained even in this case. The element size was 6.9 cm X 9 cm in the coarsest mesh. Bigger risers and element sizes gave, however, less satisfactory results.

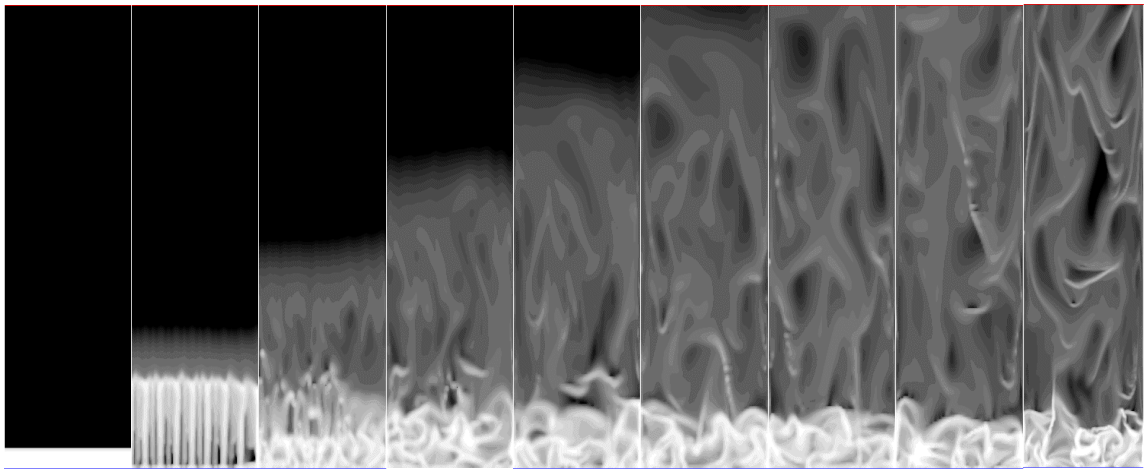

Figure 9. Solids volume fraction at 0 s, 1 s, 2 s, 3 s, 4 s, 5 s, 6 s, 10 s, and 12 s, respectively, in a riser with height 18.25 m and width 5 m. The mesh is changed from the coarse mesh to the finer mesh at 6 s and to the finest mesh at 10 s.

The behavior of the drag correlation was also tested in the case of a freely bubbling bed. No serious, unexpected problems were encountered although the concentration of solids inside the bubbles was clearly higher than experimentally observed and what was obtained in simulations in section 3.1. Results from a bubbling bed simulation are shown in Figure 10.

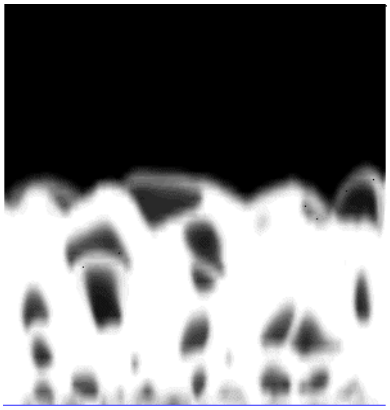

Figure 10. Spontaneous bubbling simulated with drag model 9 plotted using a linear color scale.

3.2.5 Conclusions

In the present work, a new simple drag model is written, implemented in Fluent6.1.22 and tested in simple 2D simulations. Test cases include both Geldart A and Geldart B particles and the fluidization conditions vary from bubbling beds to CFB risers. Runs with different mesh spacings and riser sizes have also been included in the tests. Simulation results are described in detail in **[22]**.

The general fluidization characteristics shown by the simulations are qualitatively correct. At low velocities bubbles are formed and at higher velocities in CFB conditions there is a dense bed above which the more dilute suspension shows clustering tendency. Axial pressure and density profiles in CFB simulations are similar to the measured ones and the solids mass flow rate at the top of the riser is also reasonable. Fluctuations in solids velocity and concentration are as expected on basis of measurements. Simulations show formation and disintegration of U-shaped clusters in the middle of the CFB riser and clusters falling at the wall.

Although there are still several unresolved problems and there is a need for improvements, already this simple first model version looks promising and could be used to improve the predictive capabilities of today's commercial codes.

3.2.6 Applications

The model developed in the present work gives reasonably good results for small risers in 2D simulations. It improves our understanding of the mixing phenomena in the riser and can be used to improve the processes. Although it cannot, due to the long computation times, be used for simulation of large industrial furnaces in 3D, it will yield the missing information on fluctuating motion that is needed for closure of the macroscopic equations used for simulation of large furnaces.

Most of the cases simulated and all validation data used were from combustion processes, where particles of Geldart's group B are typically used. In other industrial processes, such as catalytic crackers, particles are smaller Geldart A particles and gas velocities higher. Some tests were done to study the behavior of the model in case of fine particles. It seems possible to use the same model also for these processes, although further validation tests will be necessary. The model is easily modified when necessary and when measurement data of solids velocities and concentrations from new conditions are available.

3.2.7 References

[1] Hyppänen, T. An experimental and theoretical study of multiphase flow in a circulating fluidized bed. Lappeenranta University of Technology, Department of Energy Technology, Dissertation, 1989.

[2] Poikolainen, V. Mathematical modeling of gas-solid fluidization with a one-dimensional hydrodynamical model. Lappeenranta University of Technology, Master of Science Thesis, 1992. (In Finnish)

[3] Kallio, S., Poikolainen, V. & Hyppänen, T. Mathematical modeling of multiphase flow in a circulating fluidized bed. Report 96-4. Heat Engineering Laboratory, Åbo Akademi University, 1996.

[4] Sundaresan, S. Modeling the hydrodynamics of multiphase flow reactors: current status and challenges. AIChE J., Vol. 46, No. 6, pp. 1102–1105, 2000.

[5] Kashiwa, B.A. & Yang, W.-C. Computational fluid dynamics for the CFBR: challenges that lie ahead, Circulating Fluidized bed Technology VII. Proceedings of the 7th Int. Conf. in CFBs, Niagara Falls, Canada, 2002.

[6] Kallio, S. An experimental and numerical study of the velocity and voidage distribution in a circulating fluidized bed cold model. Report 95-7. Heat Engineering Laboratory, Åbo Akademi University, 1995.

[7] Fluent, Fluent Users' guide – Release 6.0. Fluent Inc., 2001.

[8] Gidaspow, D., Bezburuah, R. & Ding., J. Hydrodynamics of circulating fluidized beds, kinetic theory approach. Fluidization VII, Proceedings of the 7th Engineering Foundation Conference on Fluidization. Pp. 75–82, 1992.

[9] Ergun, S. Fluid flow through packed columns. Chemical Engineering Progress, 48, pp. 89–94, 1952.

[10] Wen, C.Y. & Yu, Y.H. Mechanics of fluidization. Chemical Engineering Progress Symposium Series, Vol. 66, No. 62, pp. 100–111, 1966.

[11] Peirano, E., Begis, J., Johnsson, F., Leckner, B. & Balzer, G. Gas-solid computations of a circulating fluidized bed. Circulating fluidized bed technology VI. Proceedings of the 6th int. conf. on CFBs, Wűrzburg, Germany, 1999.

[12] Zhang, D.Z. & VanderHeyden, W.B. High-resolution three-dimensional numerical simulation of a circulating fluidized bed. Powder Technology, 116, pp. 133–141, 2001.

[13] Moran, J.C. & Glicksman, L.R. Experimental and numerical studies on the gas flow surrounding a single cluster applied to a circulating fluidized bed. Chemical engineering science, 58, pp. 1879–1886, 2003.

[14] Van den Moortel, T., Santini, R., Tadrist, L. & Pantaloni, J. Experimental analysis of the gas-particles flow structure in the dilute zone of a circulating fluidized bed by image processing. In: Fluidization IX. Fan, L.-S. & Knowlton, T.M. (Eds.). Proceedings of the 9th Engineering Foundation Conference on Fluidization, Durango, USA, 1998.

[15] Horio, M. & Kuroki, H. Three-dimensional flow visualization of dilutely dispersed solids in bubbling and circulating fluidized beds. Chemical Engineering Science, 49, pp. 2413–2421, 1994.

[16] Niewland, J.J., Huizenga, P., Kuipers, J.A.M. & van Swaaij, W.P.M. Hydrodynamic modeling of circulating fluidized beds. Chemical Engineering Science, Vol. 49, No. 24B, pp. 5803–5811, 1994.

[17] O'Brien, T.J. & Syamlal, M. Particle cluster effects in the numerical simulation of a circulating fluidized bed. Preprint volume, 4th International Conference on CFB, Somerset, USA. Pp. 430–435, 1993.

[18] Yang, N., Wang, W., Ge, W. & Li, J. Choosing sreucture-dependent drag coefficient in modeling gas-solid two-phase flow. China Particuology, Vol. 1, pp. 38–41, 2003.

[19] Syamlal, M., Rogers, W. & O'Brien, T.J. MFIX Documentation. Volume 1, Theory Guide. National Technical Information Service, Springfield, VA, DOE/METC-9411004, NTIS/DE9400087, 1993. (Referenced in [16])

[20] Syamlal, M. & O'Brien, T.J. Computer Simulation of Bubbles in Fluidized Beds. AIChE Symposium Series, No. 270, 85, pp. 22–31, 1989.

[21] Peirano, E., Bégis, J., Johnsson, F., Leckner, B. & Balzer, G. Gas-solid flow computation of a circulating fluidized bed. Proceedings of the 6th Int. Conf. on CFBs, Würzburg, Germany, 1999.

[22] Kallio, S. The role of the gas-solid drag force in CFB modeling of fluidization. Heat Engineering Laboratory, Åbo Akademi University, 2004. (Manuscript under preparation)

3.3 Filtration of fibre suspension

Markku Kataja
VTT Processes, Pulp and paper Industry, Multiphase flows

Sanna Haavisto
University of Jyväskylä, Department of Physics

3.3.1 Introduction

A novel method and device for measuring local velocity field of fibres during filtration of dilute liquid-fibre suspension was developed earlier at VTT flow laboratory [1]. The original device consisted of a simple gravity driven hand-sheet mould equipped with a pulsed ultrasound-Doppler anemometer (PUDA) for measuring the local time-dependent velocity field of the fibre phase during vertical filtration. The total flux of the suspension is measured using a separate ultrasound transducer to detect the position of the free surface of the suspension in the mould. Pressure loss caused by the consolidating fibre layer is measured by a pressure sensor located under the filtration wire. Using the two-phase flow equations appropriate for the present two-phase system, the other relevant flow quantities (fields) such as fluid velocity and pressure, consistency, flow resistance and structural stress of the fibre network can be computed based on the measured data. The method can thus provide detailed information on the dynamics of filtration and material properties of the consolidating fibre layer that has not been previously available.

In this project, the device was further developed to allow for more accurate measurement of various quantities and for better control of the filtration procedure. In addition, the data acquisition and processing methods were developed to reduce uncertainties arising from the noise inherent to PUDA device. The purpose of this developments was to make it possible to measure rheological properties of consolidating fibre network in more dynamical conditions. For example, by interrupting the filtration for a certain time, one can extract information on relaxation behaviour and on the intricate rheological properties of fibre structure, such as viscoelasticity, plasticity etc.

3.3.2 Theoretical background

A vertical (z -directional) time dependent filtration flow of a suspension that contains a continuous fluid phase ('water') and a particulate solid phase ('fibres') is governed by the following continuity and momentum equations

$$\frac{\partial}{\partial t}\phi_f + \frac{\partial}{\partial z}(\phi_f \widetilde{u}_f) = 0 \tag{1}$$

$$\frac{\partial}{\partial t}\phi_s + \frac{\partial}{\partial z}(\phi_s \widetilde{u}_s) = 0 \tag{2}$$

$$\phi_f \frac{\partial}{\partial z}\widetilde{p}_f = D - \phi_f \widetilde{\rho}_f g \tag{3}$$

$$\phi_f \frac{\partial}{\partial z} p_s = -D - \phi_f \phi_s (\widetilde{\rho}_s - \widetilde{\rho}_f) g\,. \tag{4}$$

Here, subscripts f and s refer to the fluid phase and the solid phase, respectively, ϕ_α is the volume fraction, $\widetilde{u}_\alpha$ is the flow velocity in z -direction, p_α is the pressure, $\widetilde{\rho}_\alpha$ is the density for phase $\alpha = f, s$, D is the momentum transfer term between phases and g is the acceleration due to gravity. The notation $\widetilde{x}_\alpha$ denotes an intrinsic average of quantity x_α, *i.e.* an average taken over the volume ΔV_α occupied by phase α in a general averaging volume ΔV (such that $\phi_\alpha = \Delta V_\alpha / \Delta V$). Adding the continuity equations (1) and (2) and using the identity $\phi_f + \phi_s = 1$ gives

$$\frac{\partial}{\partial z} q_T = 0\,, \tag{5}$$

where

$$q_T = \phi_f \widetilde{u}_f + \phi_s \widetilde{u}_s \tag{6}$$

is the total flux of the suspension. According to Eqn. (5) the total flux does not depend on the spatial coordinate z, and $q_T = q_T(t)$. Similarly, adding the momentum equations (3) and (4) leads to

$$\frac{\partial}{\partial z} p_T = -\rho g\,, \tag{7}$$

where $p_T = p_s + \widetilde{p}_f$ is the total pressure and $\rho = \phi_f \widetilde{\rho}_f + \phi_s \widetilde{\rho}_s$ is the density of the suspension.

3.3.3 Experimental set-up

An overview of the filtration device is shown in Fig. 1. The device consists of a sealed tank and a riser tube of diameter 160 mm with a plastic wire and a wire support grid. Fluid can be driven up and down in the riser tube by adjusting air pressure in the tank. The fluid motion and the measuring procedure is controlled by a programmable logic unit.

a)

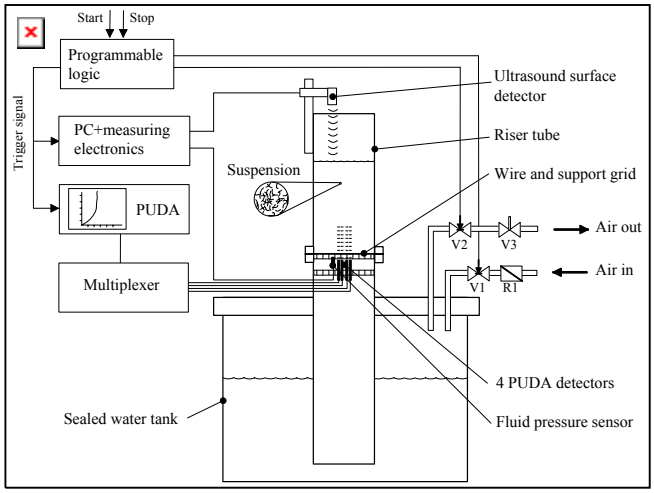

b)

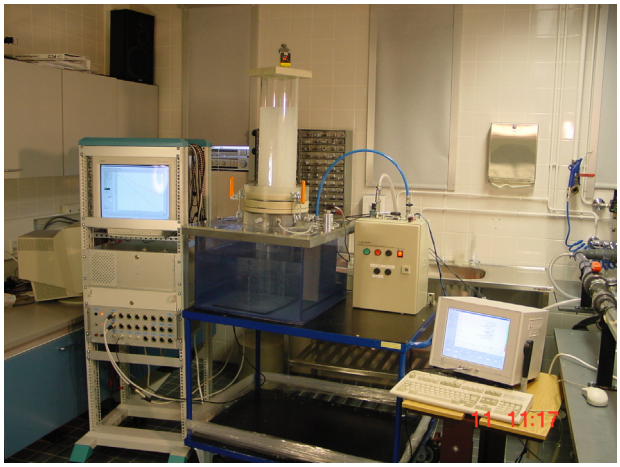

Figure 1 a) Schematic illustration and b) laboratory set-up of the filtration device based on pulsed ultrasound-Doppler anemometry.

The vertical velocity of fibres is measured through the wire by a commercial pulsed ultrasound-Doppler anemometer (PUDA) (DOP 2000 -device by Signal-Processing S.A., Lausanne, Switzerland). Four ultrasonic probes of diameter 5 mm are assembled in upright position symmetrically around the centerline of the riser tube and about 10 mm below the wire. The probes are connected to PUDA through a multiplexer. The probes can detect the local vertical velocity of fibres through the wire and up to the

distance of approximately 80 mm above the wire. The spatial resolution is approximately 0.3 mm in the z -direction. A typical measuring rate is about 4 profiles per second, each profile being an average of four profiles from different multiplexed probes and measured using 15 ultrasound pulse emissions. As a result, we get the experimental vertical velocity field $\widetilde{u}_S = \widetilde{u}_S(t,z)$ (see Eqn. (2)) during the filtration process in a layer that ranges from the surface of the wire about 80 mm upwards near the center of the wire.

The instantaneous location of the free surface of the fibre suspension in the riser tube is detected by an ultrasound position sensor. Differentiating the surface position data with respect to time gives the surface velocity that equals the total flux $q_T = q_T(t)$ of the suspension (see Eqns. (5) and (6)).

Fluid pressure at the wire is measured by a pressure detector placed immediately under the wire. The offset value of the sensor is adjusted such that the reading corresponds to fluid pressure at the upper surface of the wire.

The measurement is initiated by filling the tank by distilled water at room temperature. Water is compelled in the riser tube by opening valve V1. A weighed amount of fibres is then carefully mixed in the riser tube. After mixing, suspension is allowed to settle for a few seconds. The measurement is started by a computer command which triggers all the measurements simultaneously. The experiment is controlled by a pre-programmed sequence which opens and closes the proportional adjustable valve V2 at given levels of fluid in the raiser tube. The experiment can be repeated for a number of times using the same sample of fibres by raising the fluid level and remixing the fibres.

3.3.4 Data analysis

The data analysis of filtration experiment is based on Eqns. (1) through (4) with an assumption that the solid velocity field $\widetilde{u}_S(t,z)$ is given by the experiment in the entire flow region above the wire. One recent objective in filtration studies has been the improvement of data analysis, the fibre velocity data obtained by the PUDA device, in particular. Prior to flow calculations, the measured velocity data must be appropriately filtered in order to remove the residual spurious noise inherent in the PUDA techniques. The filtering of velocity data should be carried out without a significant loss of essential information. Finding an effective way to filter the velocity data is quite challenging, because the data may contain both rapid and slow changes – especially when dynamical properties of fibre network are of interest.

In order to find an appropriate filtering method for velocity data, different common filters and their effects in final results were tested. So far, the best results were obtained using a simple 2D median filter with a sliding-window. Such a median filter effectively removes impulse noise *i.e.* clearly outlying values from the velocity data, but preserves rapid mean velocity changes in the case of *e.g.* suddenly interrupted filtration.

Using the measured and properly filtered solid velocity field $\tilde{u}_s(t,z)$ we can then solve the solid phase pathlines $z_s(t)$ in the *t-z* -plane using the equation

$$\frac{d\,z_s}{d\,t} = \tilde{u}_s(t, z_s)\,. \tag{8}$$

The solid volume fraction ϕ_s is proportional to the mass consistency of dry fibres C_m. Writing the solid phase continuity equation (2) in terms of C_m, and applying it along a pathline determined by Eqn. (8) yields

$$\frac{d\,C_m}{d\,t} = C_m \frac{\partial}{\partial z}\tilde{u}_s(t, z_s)\,, \tag{9}$$

where the derivative with respect to time denotes the convective derivative along solid pathlines. Given the initial consistency $C_{m0}(z)$, we can thus solve the dry fibre consistency $C_m(t,z)$ in the entire flow region.

3.3.5 Results

The new method was first applied in a suspension made of unbeaten bleached softwood fibres mixed in water with an initial consistency $C_{m0} \approx 0.2\%$. An example of typical measured solid phase pathlines in the *t-z* -plane are shown in Fig 2 a) together with the measured position of the free surface. A more detailed flow pattern in the filtration zone near the wire is shown in Fig. 2 b) together with contours of constant C_m as solved using Eqn. (9).

In the free sedimentation region well above the filtration region, the solid pathlines are nearly parallel to each other. At this region, consistency C_m is constant and equals the initial consistency. The upper thick line indicates measured position of the surface. Sedimentation is visible as increasing distance between the surface line and the uppermost solid pathline. At the end of experiment, $t = 30\,\mathrm{s}$, the distance between the two lines is approximately 25 mm which corresponds the visually observed thickness of the clear water layer next to the surface.

The filtration region near the wire is indicated by the marked bending of pathlines towards horizontal as the solid velocity $\widetilde{u}_s$ approaches zero (and the fluid velocity $\widetilde{u}_f$ slightly increases). The consistency increases as the fibre network is compressed against the wire by the fluid flow. As shown by Fig. 2 b), the slowing down of the solid phase starts approximately at a consistency of 0.4%, which indeed is near the theoretical sedimentation consistency of the present fibres, *i.e.* the consistency in which the fibres have enough contacts such that the network can carry structural stress. The data does not however show any clear boundary between the filtrated layer and the free sedimentation layer.

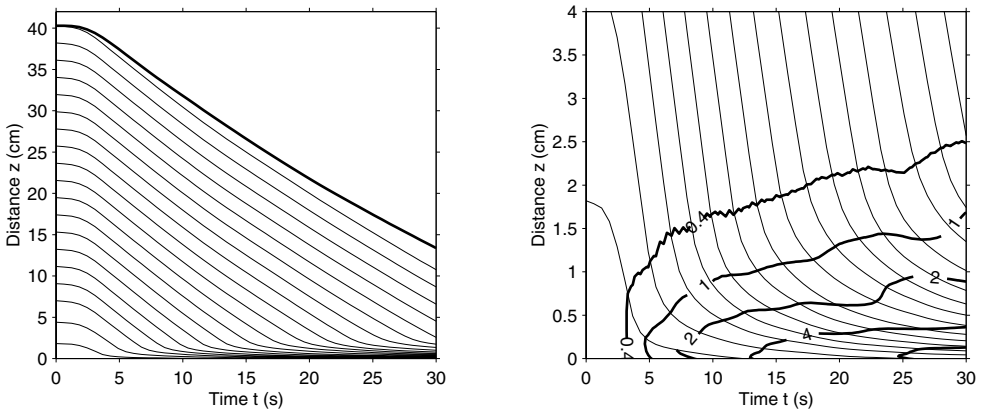

Figure 2 a) Measured solid pathlines in t-z -plane in the riser tube. The uppermost thick line shows the location of the fluid surface as measured by ultrasound surface detector. The wire is located at z = 0. b) Solid pathlines (thin lines) and contours of constant consistency (thick lines) near the wire. Labeling indicates consistency in (%).

Utilizing also the momentum equations (3) and (4), the experimental data given by the present new method can be used to infer information on also the material properties such as flow resistance and stress-strain relation of the consolidating network. In order to accomplish such an analysis the interaction term D that appears in the momentum equations and the volume fractions ϕ_α for the two phases must be known. In what follows we assume that the interaction (momentum transfer) between phases is given by a Darcy -type drag force density of the form

$$D = -\frac{\mu}{k}(\widetilde{u}_f - \widetilde{u}_s)\,, \tag{10}$$

where μ is the dynamic viscosity of the fluid phase and k is the permeability coefficient of the fibre network that depends on volume fractions. Several permeability

functions, applicable for porous materials with qualitatively different structure, can be found in the literature. Here, we shall consider only three examples, namely equations by Kozeny-Carman [2], Kuwabara [2] and Koponen et al. [3].

$$\frac{k}{k_0} = \frac{(1-\phi_s)}{\phi_s^2}, \qquad \text{(Kozeny Carman)} \qquad (11\text{ a})$$

$$\frac{k}{a^2} = \frac{1}{8\phi_s(1-\phi_s)^2}\left(-\ln\phi_s - \frac{3}{2} + 2\phi_s\right) \qquad \text{(Kuwabara)} \qquad (11\text{ b})$$

$$\frac{k}{a^2} = 5.55\left((1-\phi_s)^2\,(e^{10.1\phi_s} - 1)\right)^{-1} \qquad \text{(Koponen et al.)} \qquad (11\text{ c})$$

Here, k_0 is the specific permeability (in Kozeny-Carman relation) and a is the radius of fibres.

Figure 3 shows the measured fluid pressure at screen (at $z = 0$) as a function of time for softwood fibres. Also shown are the total pressure and the fluid pressure at $z = 0$ as calculated utilizing the velocity data and the momentum equations with the three different permeability functions. In each case, the value of the unknown parameter (k_0 or a) was found by fitting the calculated function $p_f(t,z=0)$ with the measured pressure data. As shown in Fig. 3, all of the three permeability functions give a resonably good fit to the measured data for softwood fibres. In Table I given are the corresponding fitted values of the unknown parameters that appear in each permeability function, Eqn. (11). For the formulas (11 b) and (11 c), especially derived for fibrous structures, the free parameter is the fibre radius a. As shown by the table, the fitted diameter is of a correct order of magnitude for all cases (for pine fibres $2a \sim 30$ μm). The most accurate result in this respect is given by the result by Koponen et al. Notice however, that the analytical and numerical results used here, excluding Kozeny-Carman, are obtained for smooth regular fibres, while wood fibres are irregular in shape and have fine structured surface. Consequently, real wood fibres have higher specific surface area. We may thus expect the effective diameter of fibres, as calculated from the measured value of permeability, to be less than the geometrical mean radius of fibres.

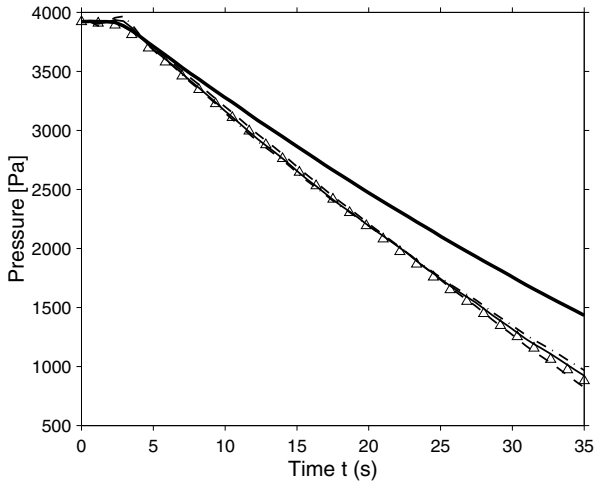

Figure 3. The measured and the calculated pressure values at screen (z = 0) during filtration for unbeaten softwood fibres. The solid thick line is the calculated total pressure. The measured values of fluid pressure are given by open triangles. Also shown are the fluid pressure values calculated using the permeability model by Kozeny-Carman (dashed line), by Kuwabara (thin solid line) and by Koponen et al. (dash-dotted line).

Table 1. Fitted values of the free parameters and the fit residual for various permeability functions for unbeaten softwood fibres.

Perm. model	**Fitted values**	**Fit residual**
	k_0 (m^2)	
Kozeny-Carman	$1.4 \cdot 10^{-12}$	$3.8 \cdot 10^{-4}$
	$2a$ (μm)	
Kuwabara	20.4	$1.6 \cdot 10^{-4}$
Koponen et al.	32.9	$2.0 \cdot 10^{-4}$

Also given in the Table 1 are the fit residuals for each permeability function. A small value of the residual indicates good agreement between measured and calculated pressure values. For softwood fibres the best fit is achieved by using the permeability function of Kuwabara while the worst fit is given by the Kozeny-Carman result.

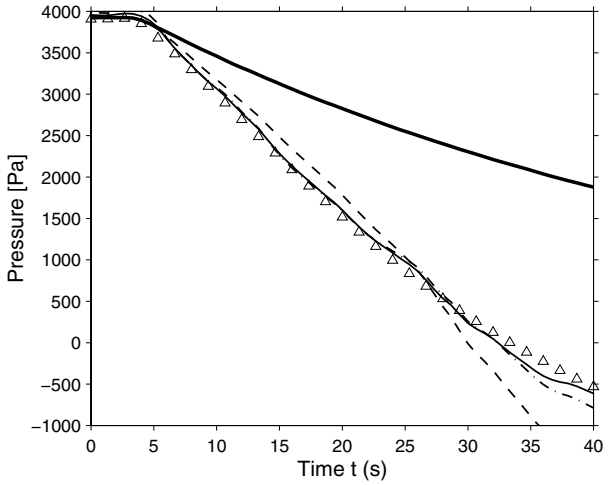

Figure 4. Same as Fig. 3, but for unbeaten hardwood fibres.

In Fig. 4 and in the Table 2, show is the same data as in Fig. 3 and Table 1, but for hardwood fibres (birch). Also in this case the best agreement with measured data is obtained by the Kuwabara result, while the result corresponding to Kozeny-Carman formula is clearly off the measured data. The fitted values of fibre diameter are again of a correct order of magnitude (for birch fibres $2a \sim 20$ μm).

Table 2. Same as Table 1, but for unbeaten hardwood fibres.

Perm. model	**Fitted values**	**Fit residual**
	k_0 (m^2)	
Kozeny-Carman	$0.75 \cdot 10^{-12}$	$72 \cdot 10^{-4}$
	$2a$ (μm)	
Kuwabara	12.0	$9.4 \cdot 10^{-4}$
Koponen et al.	18.1	$21 \cdot 10^{-4}$

Figure 5 shows the calculated solid pressure p_s as a function of solid mass consistency C_m along a number of solid pathlines for softwood fibres and for hardwood fibres. The most remarkable feature of this result is that the data points for all pathlines fall quite closely on a single curve in C_m-p_s -plane (for softwood and for hardwood fibres separately). The two results are both well fitted by a power law of the form $p_s = p_{s0} \cdot (C_m / C_{m0} - 1)^{1.75}$ with $p_{s0} \approx 1.6$ Pa and 2.8 Pa, and the initial consistency $C_{m0} =$ 0.2% and 0.4% for softwood and hardwood, respectively. (Notice, that both

initial consistencies correspond to the same growding number of approximately 15.) This result indicates, that the measured behaviour indeed reflects a true material property, namely the stress-strain behaviour of the consolidating fibre network during filtration! As expected, the network formed by birch fibres appears softer than that formed by pine fibres. Notice however, that the measured stress-strain correlation depends on the permeability function used in data analysis. Here, the formula by Kuwabara was used.

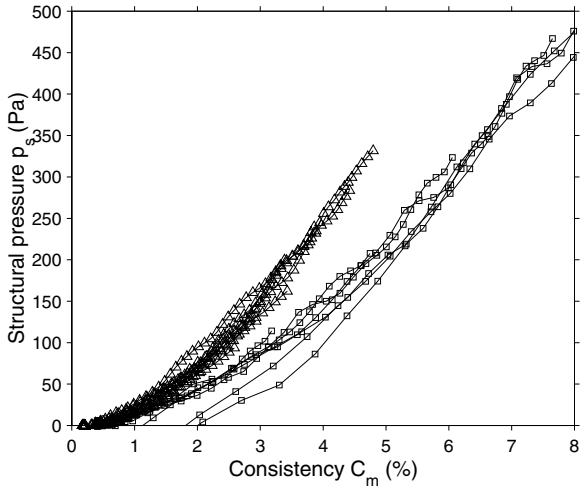

Figure 5. Solid pressure as a function of consistency along pathlines for unbeaten softwood fibres (triangles) for unbeaten hardwood fibres (squares).

In addition to the continuous consolidation discussed above, the device can now, after improvements in data-analysis of the PUDA device, be used to study more complicated filtration processes. For example, by interrupting the filtration for a certain time, one can extract information on relaxation behaviour and on the intricate rheological properties of fibre structure, such as viscoelasticity, plasticity etc. Figure 6 a) shows the pressures measured at $z = 0$ in such an experiment for unbeaten softwood fibres. Here, filtration is interrupted by closing the air valve approximately 6 seconds after the beginning and then opened after 10 seconds. This causes the total pressure to level off and the fluid pressure on screen surface to increase and approach the total pressure from below as the flow ceases. Figure 6 b) shows the structural pressure of a single fibre layer as a function of consistency in interrupted filtration. The figure allows us to follow the compression-relaxation behaviour of a particular fibre layer during interrupted filtration.

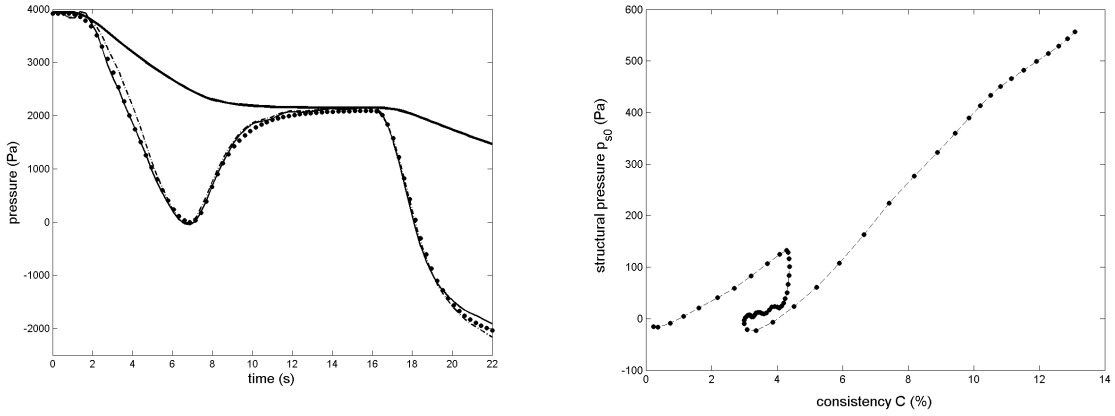

a) b)

Figure 6. a) Measured and calculated pressures at the wire (z=0) for interrupted filtration. The thick solid line gives the total pressure $p_T(t,0)$ *and the solid symbols give the measured values of fluid pressure* $\tilde{p}_f(t,0)$*. Thin solid line corresponds to the model by Kuwabara, with the fitted fibre diameter* $2a = 12.5\,\mu m$*. Dashed line corresponds to Kozeny – Carman model with the fitted value of specific permeability constant* $k_0 = 7.9 \cdot 10^{-13}$ *m2. b) Structural pressure of a single fibre layer as a function of consistency.*

Figure 6 b) shows the stress-strain history of fibres along a single solid pathline during interrupted foltration. The curve first follows a path similar to those shown in Fig. 5 for continuous consolidation. After the flow is stopped, fibre network undergoes relaxation which is indicated by a rapid decrease of solid pressure towards zero associated with a slight decrease of also consistency as the fibre network expands. Obviously, the behaviour of the network at this stage is highly non-elastic. As the flow is resumed, the stress-strain curves again approach the curve of continuous consolidation. The time required to approach the original curve gives a rough estimate of the magnitude of the time constant associated to viscoelastic behaviour of the network. (The time interval between the data points indicated by solid symbols on the curve is approximately 0.6 s.) A more detailed analysis of the stress-strain behaviour of the consolidating fibre network is left in a future work.

3.3.6 Conclusions

Filtration measurement based on pulsed ultrasound Doppler anemometry facilitates detailed experimental study of slow one-dimensional filtration of fibre suspensions. Essential material properties, such as the permeability to fluid flow and the stress-strain

behaviour of the consolidating fibre network can be studied by utilizing the general two-phase flow equations in the data analysis.

A clear and plausible difference in the flow resistance and stress-strain properties was observed for unbeaten softwood and hardwood fibres. Of the various possibilites tested in this preliminary study, the best compatibility of measured data was obtained using the permeability correlation by Kuwabara.

The recent development in measured data processing now allow dynamic measurements whereby also viscoelastic properties of the consolidating fibre network can be studied. The filtration measurement developed here is presently applied at VTT flow laboratory as and advanced method for fibre property characterization in research projects involving fibre suspension flows and their industrial applications.

3.3.7 References

1. Kataja, M. & Hirsilä, P. Application of ultrasound anemometry for measuring filtration of fibre suspension. The Science of Papermaking, Transactions of the 12th fundamental research symposium. Vol. 1. Baker, C.F. (ed.). Oxford, September 2001, The Pulp and Paper funcamental Research Society, UK, 2001. Pp. 591–604.

2. Jackson, G.W. & James, D.F. The permeability of fibrous porous media. Can. J. Chem. Eng., 64, 364, 1986.

3. Koponen, A., Kandhai, D., Hellén, E., Alava, M., Hoekstra, A., Kataja, M., Niskanen, K., Sloot, P. & Timonen, J. Permeability of Three-Dimensional Random Fiber Webs. Phys. Rev. Lett., 80, 716, 1998.

3.4 Optical process tomography

Tanja Tarvainen, Ville Kolehmainen, Jari P. Kaipio, Antti Vanne, Katja Markkanen, and Marko Vauhkonen
University of Kuopio, Department of Applied Physics

Markko Myllys and Esa Rehn
University of Jyväskylä, Department of Physics

3.4.1 Background

Optical (diffusion) tomography (OT) is an imaging method in which the absorption and scattering coefficients within the object are estimated based on light transmission measurements that are made on the exterior boundary of the object. The estimated image parameters carry different relevant information in different applications. In industrial process imaging OT can be used, for example, for monitoring of flows in industrial process pipelines and to estimate particle distributions in vessels. Medical applications include e.g. detection and classification of breast cancer, monitoring of infant brain tissue oxygenation levels and functional brain activation studies.

From the mathematical point of view, the image reconstruction in OT is an ill-posed inverse problem. In practice, this means that the problem is extremely instable in the sense that even small errors in measured data can cause arbitrarily large errors in the estimated images. Due to these properties, the development of mathematical models, computational methods and hardware for optical tomography is a challenging task.

The goal of the research project was to develop computational methods for optical tomography. Especially, the emphasis was on the development of computational methods that can be utilized in industrial applications of OT. A typical feature in industrial applications is the non-stationary nature of the optical properties within the target medium (e.g., process vessel). By non-stationary we mean that the optical properties of the object change so fast that the data needed for one "classical" OT image cannot be collected fast enough. During the measurements the optical properties of the target have exhibited significant changes. To avoid errors in the reconstructed images, the time-varying nature of the target needs to be taken into account. Due to ill-posed nature of the problem, other crucial issues in optical tomography in general are accurate and efficient modelling of the light transport in the media, minimizing measurement errors and accurate calibration of the measurement setup. Therefore, during the project issues concerning light transport models, image reconstruction, system calibration, and non-stationary imaging were considered.

3.4.1.1 Forward problem

The forward problem in optical tomography is to compute the intensity of the transmitted light when the optical properties of the object and the intensities of the light sources are known. The most relevant currently approved physical model for OT measurements is the radiative transfer equation (RTE) model. This is an extremely hard computational problem in general bounded domains and for spatially varying absorption and scattering coefficients. The RTE can be solved, in principle, by either stochastic Monte Carlo techniques or finite element (FE) based approaches. However, both of these approaches lead to computationally very demanding solutions that are too slow for most practical situations.

The state of the art approaches to OT inverse problem are typically based on regularized output least squares methods. An iterative solution of these optimization problems requires repetitive solutions of the forward problem. The number of forward solutions needed is especially large in the non-stationary applications in which the goal is to estimate a sequence of states given the OT data from a time-varying object. Thus, to make the computational load feasible, approximate forward models are typically employed. The most usual approach to date has been to use the diffusion approximation (DA) to the RTE as the forward model.

However, the DA is a good approximation in such sub-domains in which the angular distribution of the propagating light can be well approximated by a smooth cosine function. These conditions are generally met in scattering dominated media whenever the point of interest is not close to the highly collimated light sources at the object boundary. Thus, one of the main problems with the DA is the difficulty to accommodate accurate models for the light sources. Currently, the most usual source model in the DA has been to approximate the collimated sources on the boundary by isotropic point sources that are placed one mean free path inside the boundary.

3.4.1.2 Calibration

As mentioned above, the OT image reconstruction is an ill-posed inverse problem, and thus the measurement system needs to be calibrated accurately. In OT measurements, the optic fibres that are used to guide the light from the source to the object surface and to guide the transmitted light from the object surface to detectors, cause unknown attenuation losses and phase shifts. In addition, the output of the laser sources and the responses of the detector elements may have small variations. Unless these systematic errors are modelled or calibrated properly they can cause severe distortions in reconstructed images.

3.4.1.3 Non-stationary inverse problems

Traditional algorithms for the solution of the OT inverse problem assume at least implicitly that all measurements correspond to the same target (solution). As explained above, the optical properties of the target may vary significantly during the time that is needed to acquire the set of measurements for one classical OT-image. If the temporal variation in the object is very slow compared to the data acquisition speed, the use of traditional stationary algorithms for the difference reconstruction between states may yield useful information. However, in most non-stationary applications the time that is needed to acquire all necessary intensity measurements is too long to be able to assume that the target exhibit time-invariant properties during this interval. The use of traditional stationary inversion algorithms leads to useless results in these cases.

3.4.1.4 Camera tomography

The idea in optical camera-tomography is to illuminate the object from one side and to use a CCD-camera to "measure" the light intensity on the other side. With several different light-camera placements, approximations for the optical properties inside the object can be computed. This can be done in a similar way as in standard optical tomography.

In this project, the main application in mind was imaging of cylindrically symmetric mixing in a pipe. If the liquid in the pipe is transparent, then it is fairly easy to "see" how the mixing process works. However, if the liquid is opaque, then we have to use the same approaches as in the optical tomography in order to estimate what happens inside the pipe.

3.4.2 Methods

3.4.2.1 Forward problem

In this project, new models for the forward problem have been developed. The models are based on combining the RTE and DA: the main idea is to utilize the RTE near the sources and in sub-domains where the DA fails, and to utilize the computationally more feasible DA elsewhere. Two different RTE/DA-based combined models were developed: 1) a hybrid radiative transfer – diffusion model and 2) a finite element based coupled RTE-DA model. The combined models combine the accuracy of the RTE and the computational efficiency of the DA.

The hybrid radiative transfer – diffusion approach consists of two parts: constructing the RTE based source model for the DA and solving the DA. First, the RTE is solved in a small area in the proximity of the light source where the DA is not valid. The solution of the RTE is used to construct a Dirichlet boundary condition for the DA on a fictitious interface that is chosen far enough from the source so that the assumptions of the DA are valid. The DA is then solved in the remaining area using the RTE based Dirichlet boundary data at the fictitious interface boundary within the domain. The RTE based Dirichlet boundary condition at the interface boundary can be considered as a distributed source model for the DA. The computation of the source model is extensive but can be done off-line.

In the coupled model, the RTE and the DA are linked together as a coupled system of equations. The computational domain is separated into two disjoint subdomains: one in which the RTE is used as the forward model, and other in which the DA is used as the forward model. The RTE and DA interact through their boundary conditions on the interface between the RTE and DA subdomains.

Both of the models were implemented by the finite element (FE) methods.

3.4.2.2 Inverse problem: stationary case

Image reconstruction algorithms were developed for 2D and 3D cases. The algorithms are based on the total variation regularized output least squares approach. The current versions of the reconstruction algorithms employ the diffusion approximation as the forward model. To optimize the use of computer resources, a method that is based on pre computed finite element matrices was developed. Currently, parallel computing versions of these algorithms are being implemented in C-code for a PC-cluster environment. This is essential for enabling 3D computations in large object volumes.

3.4.2.3 Computational calibration method

The calibration of the unknown fibre losses may not be feasible at the hardware level. Thus, a computational calibration method for optical tomography was developed. The model of the calibration scheme is based on the rotational symmetry of the traditional cylindrical measurement setup. This is the measurement setup in most applications of OT and, therefore, specific calibration tools are not needed. In the calibration model, the amplitude loss and phase shift at each of the optic fibres are modelled by multiplicative coupling coefficients. The relative source and detector coupling coefficients can be estimated when a dataset from a homogeneous and isotropic object is given. Once the

relative coupling coefficients have been estimated, any dataset measured with the same measurement setup can be calibrated. Thus, the coupling coefficients do not need to be redefined as long as the measurement setup remains unchanged.

3.4.2.4 Non-stationary inverse problems

A state-estimation approach to the non-stationary optical tomography problem was developed. In the state estimation approach the optical properties of the target are modelled as a multivariate stochastic process. The known or assumed time-varying properties of the target are described in terms of a state evolution model. The measurements from the object are modelled by an observation model, which is based on physical model of light transport and assumed properties of the observation noise. Given this pair of equations and the OT measurements, the objective is to estimate a sequence of states for the time-varying optical parameters. Under certain conditions, the estimation of the states can be carried out by recursive estimators. In this work, the estimates are computed by the extended Kalman recursion algorithms. Modelling of the time-dependence of the target can also be interpreted as temporal regularization for the problem.

3.4.2.5 Camera-tomography

In this project a 3D approach, based on diffusion approximation and finite element method, was developed for estimating optical properties inside a (rectangular) pipe in cylindrically symmetric mixing **[2].** The proposed approach was tested with computer simulations. Only difference reconstructions were used due to the computational complexity of the problem. In difference reconstruction, two data sets are needed; one for homogeneous distribution and the other for inhomogeneous distribution. The non-iterative reconstruction is based on the difference in the measured camera images.

3.4.3 Results

3.4.3.1 Forward problem

The finite element based hybrid radiative transfer – diffusion model was implemented and tested with 2D simulations. The simulation results were compared with finite element solutions of the RTE and the DA and with Monte Carlo simulations. The size of the computational domain was chosen such that the RTE and Monte Carlo solutions can be computed in the whole domain for comparison purposes. Examples of simulation results are shown in Figs. 1 and 2, in which the photon densities are shown in the left

column and the absolute values of relative errors of the finite element solutions with respect to Monte Carlo simulation in the right column. The results show that the computationally less expensive hybrid model gives almost as accurate results as the FEM solution of the RTE. Notable feature is also that the DA solution differs significantly from the RTE and hybrid solutions, and has significantly larger errors with respect the Monte Carlo simulation. This is due to the fact that the collimated light source cannot be modelled accurately within the DA. The developed model is expected to lead accurate and computationally efficient algorithms in 3D OT.

A publication about the hybrid model has been submitted **[10]**. In addition, the results have been presented at domestic and international conferences, e.g. **[8]**, **[9]**.

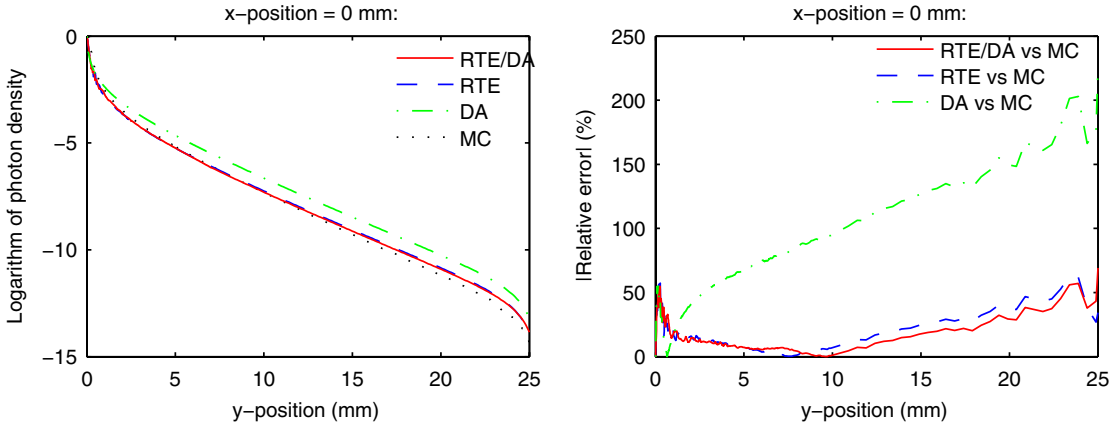

Figure 1. Logarithms of the photon densities (left column) and the absolute values of the relative errors with respect to Monte Carlo simulation (right column) on a vertical line downward from the source (x-position=0mm).

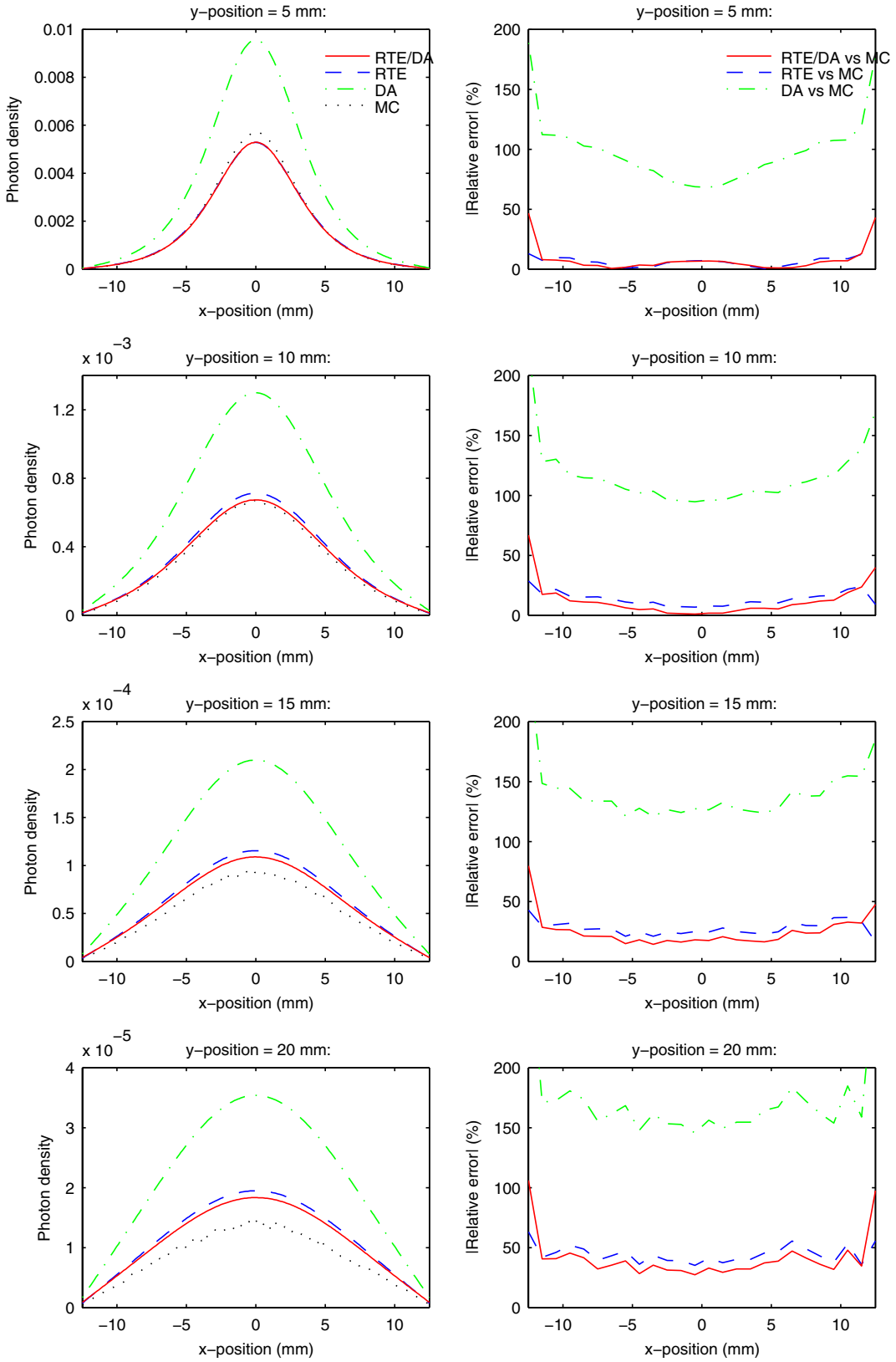

Figure 2. Photon densities (left column) and the absolute values of relative errors with respect to Monte Carlo simulation (right column) on horizontal lines within the domain (from top to bottom: y-position= 5mm, 10mm, 15mm, and 20mm).

The FEM based coupled RTE/DA model was tested with 2D simulations in different domains. The results were compared with finite element solutions of the RTE and the DA. An example of simulation results is illustrated in Fig. 3. Amplitudes and phase shifts of the photon densities are shown in the left column and the corresponding relative errors with respect to the RTE solution are shown in the right column of Fig. 3. The results show that the coupled RTE-DA model gives almost as accurate results as the RTE in the whole domain. Thus, the coupled model offers tools for accurate physical modelling in OT with significantly decreased computational load compared to solving the RTE over the whole domain.

A manuscript about the coupled RTE-DA model is under preparation **[6]** and the results have been presented in **[7]**.

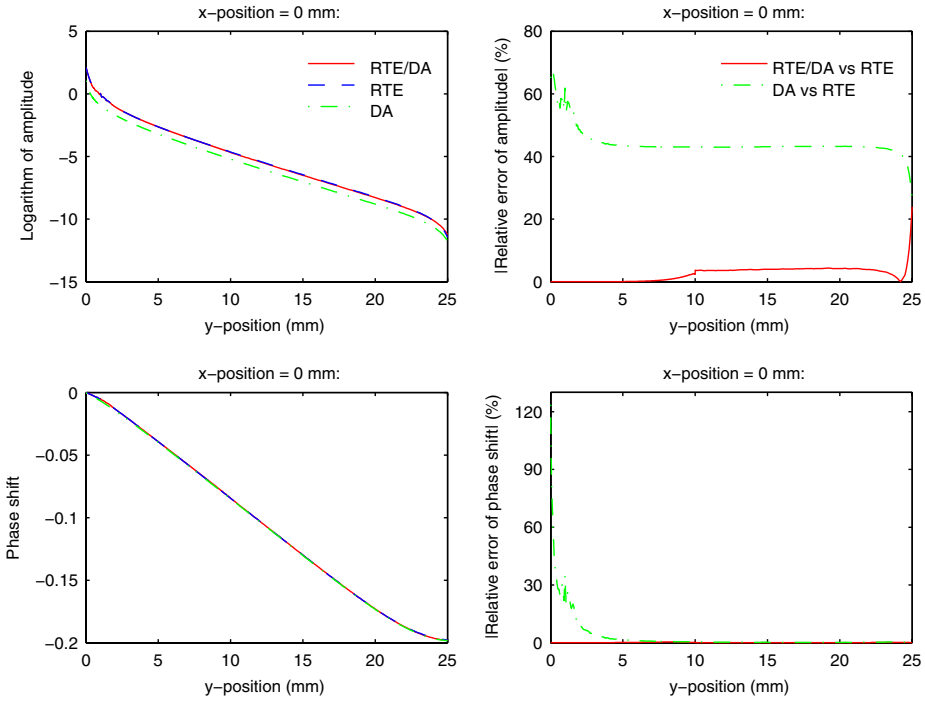

Figure 3. Top row: Amplitudes of photon densities (left column) and the absolute values of the relative errors with respect to RTE solution (right column) on a vertical line downward from the source. Bottom row: Phase shifts of photon densities (left column) and the absolute values of the relative errors with respect to RTE solution (right column) on a vertical line downward from the source.'

3.4.3.2 Inverse problem

The stationary inversion algorithms have been tested for both simulated and measured data. An example of simulation reconstructions is illustrated in middle column of Fig. 6.

As it can be seen, the reconstructed images are sharp and the inclusions are well distinguished. An example of reconstructions from real data is illustrated in Fig. 4. The data was measured with the measurement device that was built during the project in the Physics Department at University of Jyväskylä. During the measurements, a plastic rod was placed in different places in a tank containing diffusive fluid. Images were reconstructed from the measured datasets. As can be seen, the absorption images are sharp and the rod is well distinguished. The scattering images contain more artefacts than the absorption images.

The results have been presented in publications and at domestic and international conferences, e.g. **[5]** and **[11]**.

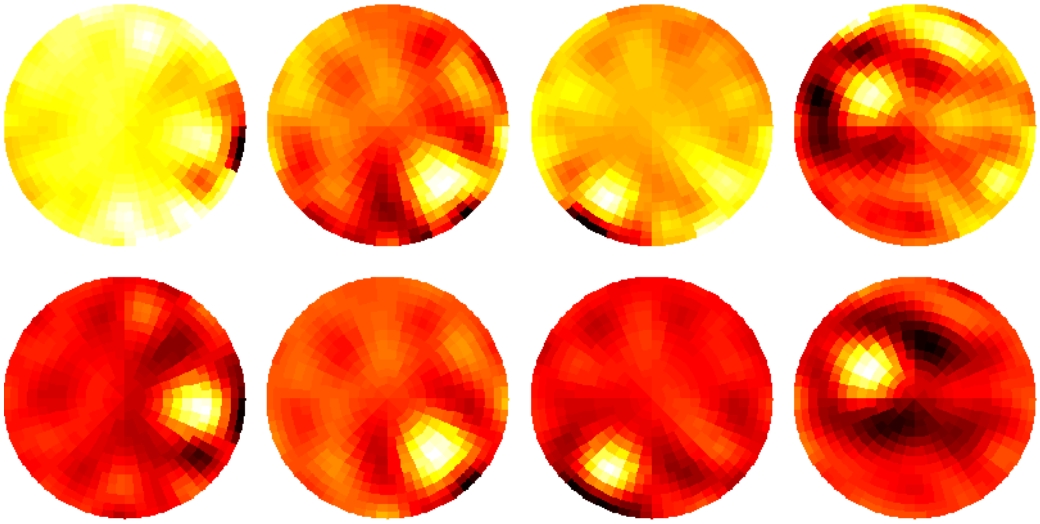

Figure 4. Measurement reconstructions: scattering coefficients (top row) and absorption coefficients (bottom row).

3.4.3.3 Computational calibration method

The computational calibration method was tested with simulations and measurements. An example of simulation results is illustrated in Figs. 5 and 6. In the simulation, a two dimensional case was considered. Dataset for simulation was generated with an extended FE-model for the diffusion approximation. The dataset was calibrated with the computational calibration approach. The amplitude and phase shift of the dataset as a function of source-detector angle index before and after calibration are shown in Fig. 5. To test the effect of the calibration on reconstructed images, another dataset was generated. The simulated absorption and scattering distributions are shown in the left column of Fig. 6. The reconstructed absorption and scattering coefficients from the calibrated data and raw data are shown in the middle and right columns of Fig. 6, respectively.

The results show that the computational calibration method can be used to estimate the relative coupling coefficients accurately, and that the calibration improves the quality of the reconstructed images by reducing the effect of the systematic attenuation losses caused by the measurement equipment.

A publication about the computational calibration method has been submitted **[5]** and the results have been presented at conferences, e.g. **[11]**.

In addition, the Biomedical Optics Research Laboratory in the University College London is considering attaching the calibration method as a part of their imaging software. Furthermore, the calibration method has already been utilized in calibrating measured data from measurement device of Medical Optical Imaging Group of Laboratory of Biomedical Engineering in Helsinki University of Technology **[3]**.

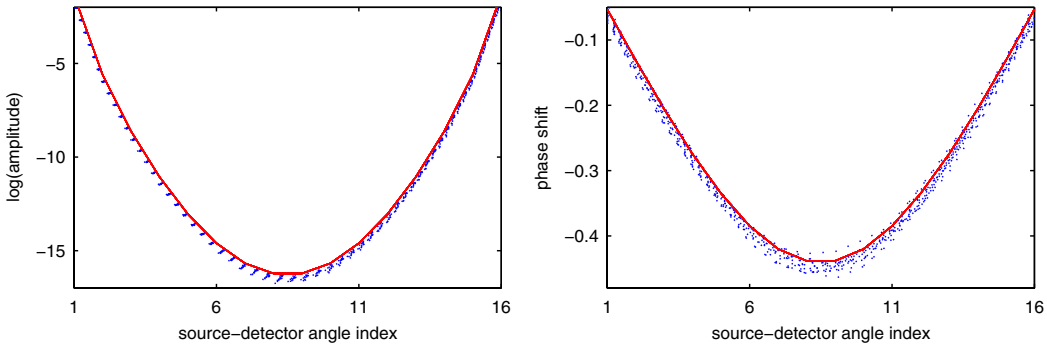

Figure 5. Left column: logarithm of amplitude as a function of source-detector angle index before calibration (dotted line) and after calibration (solid line). Right column: phase shift as a function of source-detector angle index before calibration (dotted line) and after calibration (solid line).

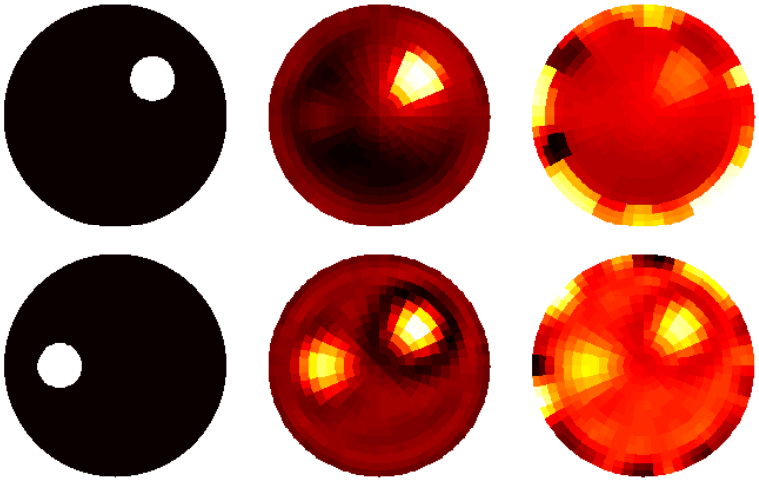

Figure 6. Scattering coefficients (top row) and absorption coefficients (bottom row). From left to right: simulated distributions, reconstructions from calibrated data, and reconstructions from raw uncalibrated data.

3.4.3.4 Non-stationary inverse problems: state estimation approach

The performance of the state-estimation approach was tested with simulated 2D data. The observation model was based on the diffusion approximation. The temporal evolution of the target was modelled by the Brownian random walk process. Fig. 7 shows results for one test case.

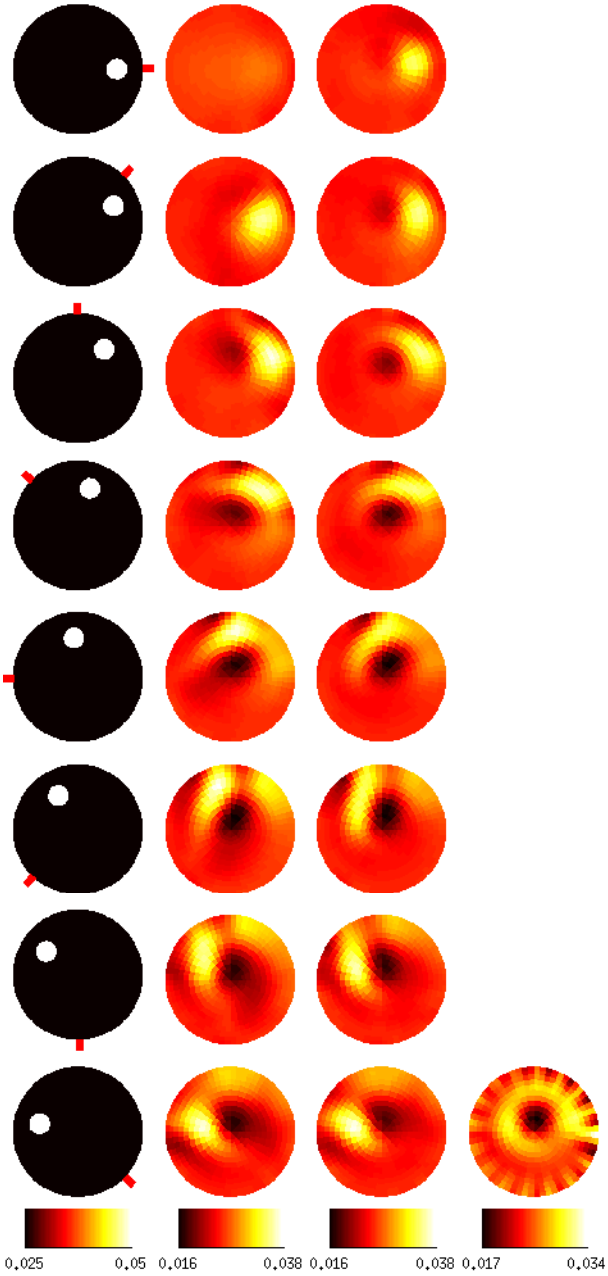

Figure 7. State estimation approach to OT. Colums from left to right: Absorption distribution at 8 time instants, extended Kalman filter estimates, Kalman smoother estimates and traditional, stationary reconstruction.

The left column shows the absorption distribution within the target at 8 time instants. The red line at the surface of the object indicates the location of the illuminated light source at each instant. The image in the bottom row of the fourth column shows the reconstruction that is obtained by the classical stationary reconstruction method (acquisition of data takes16 time instants). The second column shows the extended Kalman filter estimates and the third column the Kalman smoother estimates for the time varying absorption process at the respective time instants. As can be seen, the state estimation approach produces good estimates and captures most of the temporal evolution of the optical properties. The method and the results were published in **[1]**.

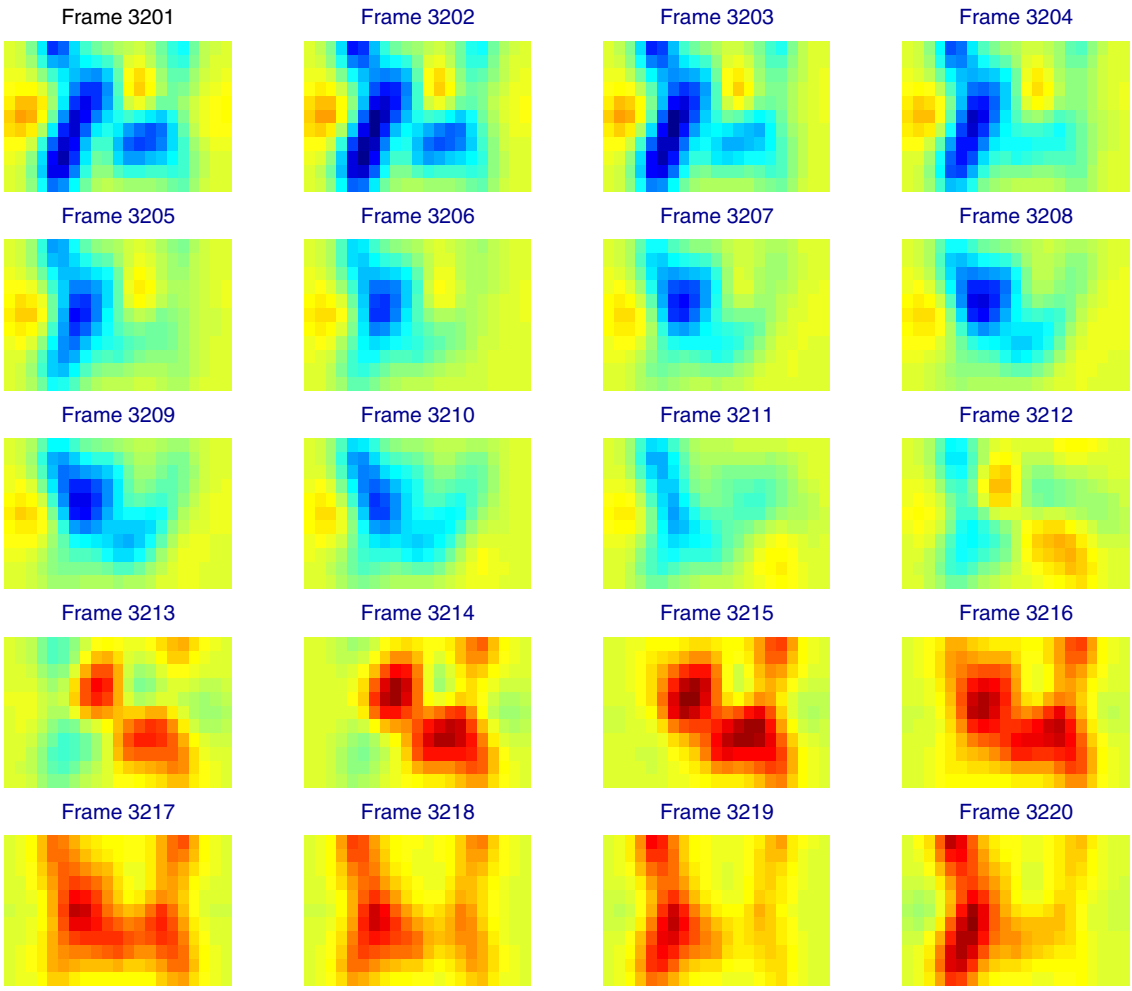

Figure 8. Reconstructions from data collected by a sensor array on human head. The data is by the research group in Tufts University and the figure from the joint publication [4]. The variation is presumably principally due to arterial pulsation. Reconstructions with classical methods are meaningless.

The state estimation model was later extended to medical applications and applied to real data from functional brain activation studies. Results from this collaboration study **[4]** are shown in Fig. 8. The results have also been presented in international conferences.

The future topics in the state estimation include e.g., the development of more realistic evolution models for industrial imaging and the integration of the light propagation models that have been developed in the project into the state estimation algorithms.

3.4.3.5 Camera-tomography

For testing the camera-tomography approach, a 3D rectangular domain was constructed for computer simulations. This presented a piece of a process pipe. For the mixing simulations the optical properties at the centre of the pipe were changed and simulated data was computed. The optical properties inside the pipe, assuming cylindrical symmetry, were estimated. An example of simulated camera data (difference between homogeneous and inhomogeneous) is shown in Fig. 9. The results of the estimated diffusion coefficients inside the pipe and also the true distribution are shown in Figs. 10 and 11. The results are for difference reconstructions in which also data for homogeneous distribution was used in the reconstruction.

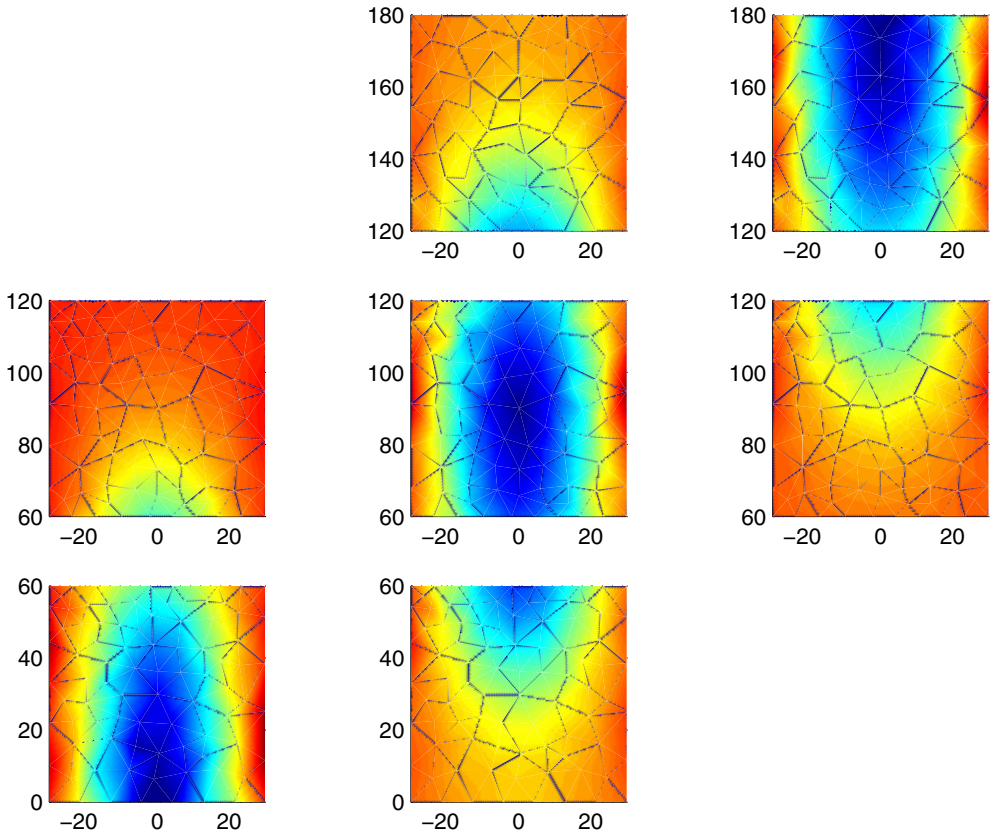

Figure 9. Simulated camera-data for three different illumination positions. In the first column, the illumination has been in the lowermost part, in the second column in the centre and in the third column on the uppermost part of the pipe.

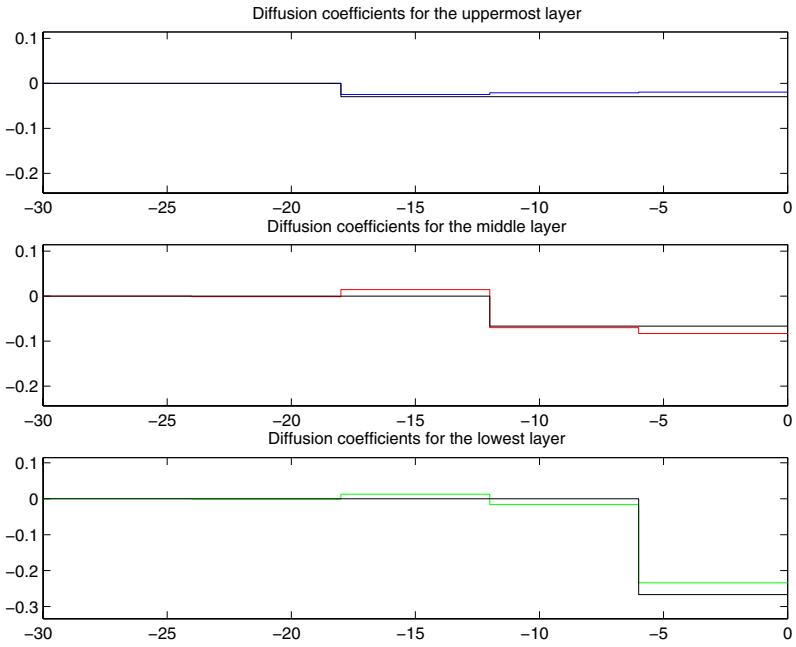

Figure 10. The estimated radial distributions (differences) of the diffusion coefficient. Black line in each figure corresponds to the true difference distribution and coloured lines to the estimated distributions.

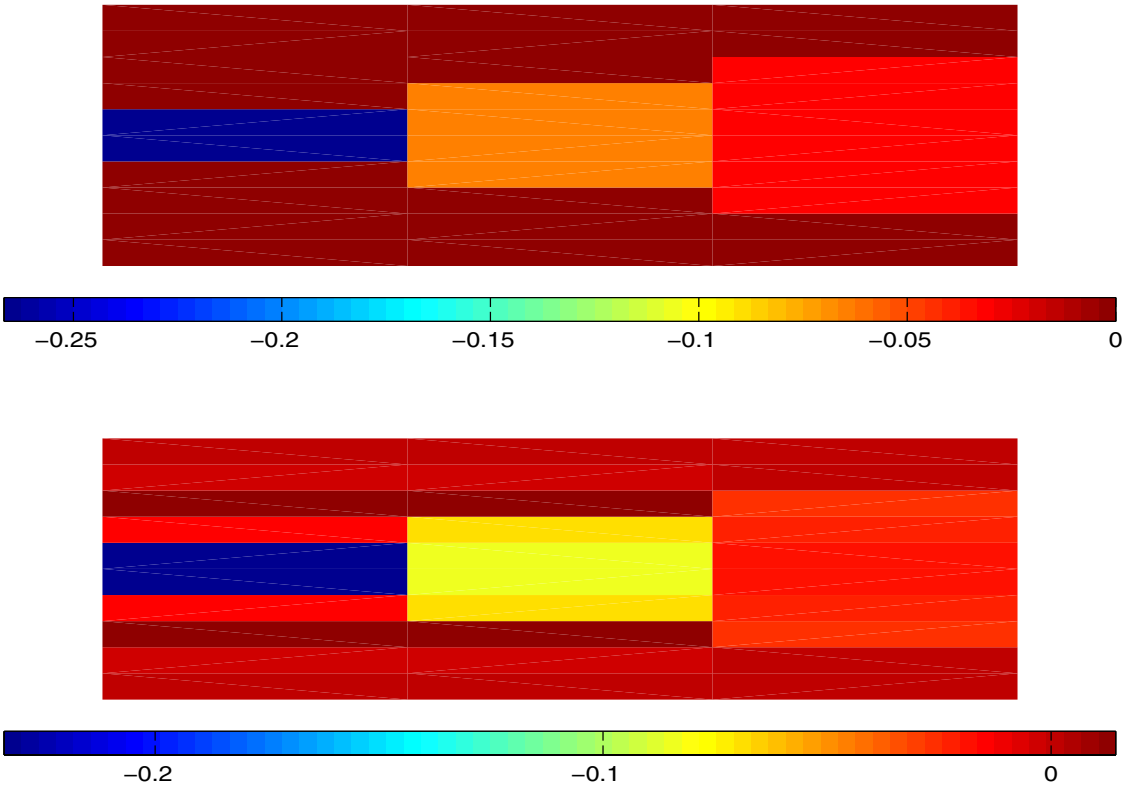

Figure 11. The true difference diffusion coefficient distribution (upper) and the estimated one (lower).

3.4.4 Experimental set-up

We have developed a device for optical tomographic 2D and 3D imaging of highly diffusive multiphase fluids such as paper pulp. The device can be used in on-line imaging of *e.g.* mixing flows. The present measurement system includes two circular measurement collars with inner diameter 100 mm and height 50 mm (see Fig 12). Each collar includes eight 25 mW/690 nm lasers and eight avalanche photodiode light detectors mounted evenly around the inner surface of the collars. A single measurement cycle involves illuminating the sample with one laser at a time and, for each laser, detecting the intensity of light at all detectors. One measurement cycle (exposure) thus results in image reconstruction from 64 or 256 light intensity values for one collar (2D imaging) and two collar (3D imaging) operation modes, respectively. With the present device version, the exposure time is 1/16 seconds for 2D imaging and 1/8 seconds for 3D imaging. The laser light is guided in the fluid through a plastic diffuser which provides a non-pointlike light source preferred by the image reconstruction algorithm based on diffusion approximation (see above). Each exposure results in two images represent the distribution of absorption coefficient and of scattering coefficient in the reconstructed volume.

The reconstruction procedure is relatively sensitive to errors in measured light intensity. In order to reduce such errors, the measurement was implemented by phase sensitive lock-in amplifier techniques, which can detect signals well below the average noise level. This is achieved by modulating the lasers with a 650 kHz sine wave and locking the instrumental amplifiers into the modulating signal that is created by a TTi TGI 550 function generator and distributed to each laser via a 16-channel multiplexer. Exposure time for each laser is typically from 50 down to 7 ms. The photodiode detectors are connected to Becker-Hickl LIM-100 analog single phase lock-in amplifier modules which detect the amplitude of the modulated output of the light detectors and feed it to the data acquisition system. The DAQ system consists of National Instruments PXI based controller with two 8-channel DAQ-cards that are configured for simultaneous sampling. The 24-bit resolution enables accurate measurements for large dynamical range of light intensity. The maximum sampling rate is 100 kS/s. The number of images taken in a given time is limited by the amount of memory of the measurement computer and by the length of modulated laser pulses that is needed for accurate amplitude detection.

3.4.5 Benchmarking results

The device was first tested in stationary conditions. The two collars were assembled on top of a horizontal plate to form a sealed bowl as shown in Fig. 12. The bowl was filled with diffusive latex fluid (not present in Fig. 12). White plastic rods of different length

were then placed in the bowl to form a simple 3D phantom object. The experiment was done using a difference method where the reference signal was first obtained for pure latex in the bowl. The image reconstruction was based on the difference of signals with and without the phantom object present in the bowl. The advantage of such a method is to avoid the need of calibration of absolute laser power and detector sensitivity. Both 2D and 3D methods were used. The first results indicate that the performance of the experimental system and image reconstruction method is very good in 2-D measurements whereas the image obtained by the 3D method still appear somewhat blurred (see Figs. 13 and 14).

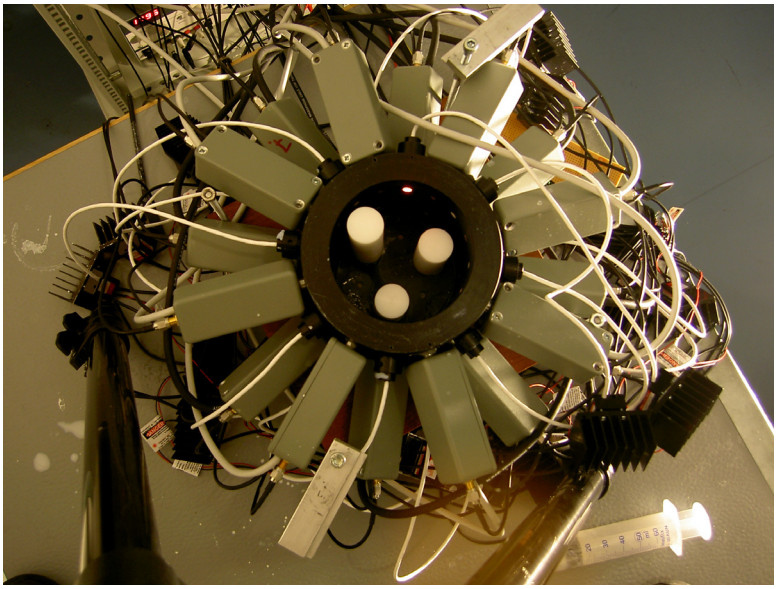

Figure 12. The current prototype version of the 16-channel optical tomography device. Three plastic rods inside the bowl as a 3D phantom object and no diffusive latex added to the bowl.

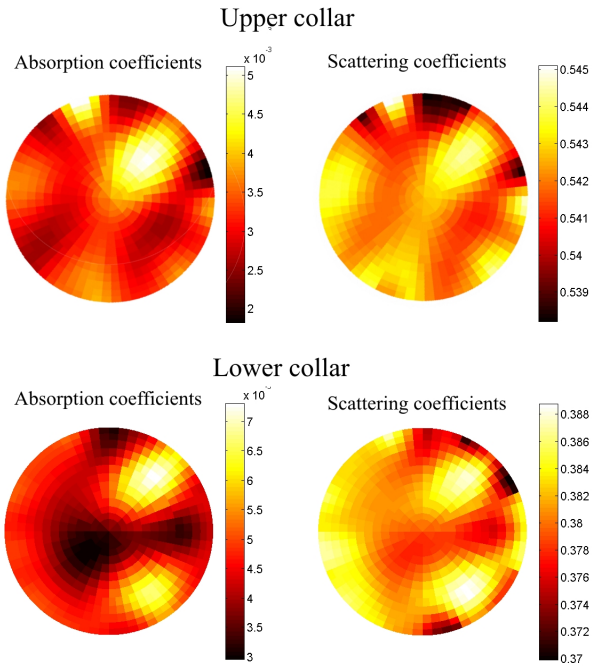

Figure 13. 2D- reconstructions of two stationary plastic rods in the measurement bowl for upper and lower collar.

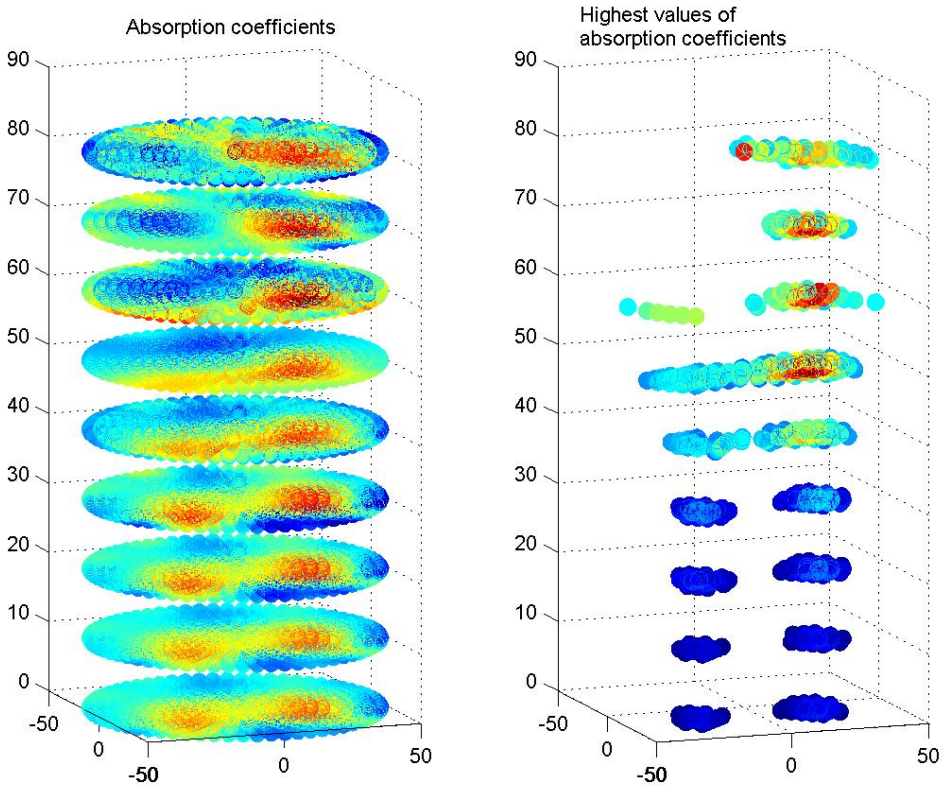

Figure 14. 3D-reconstruction of two stationary plastic rods in measurement bowl.

In order to test the measurement techniques in non-stationary mixing flow conditions, the two collars were assembled in a horizontal tube of inner diameter 100 mm in VTT flow laboratory (see Fig. 15). A shorter tube of inner diameter 25 mm was mounted concentrically in the larger tube. Mixing flow was generated by pumping diffusive latex fluid in the larger tube and paper pulp in the central tube (see Fig. 16). The tomographic imaging collars were located in the mixing zone downstream of the end point of the central tube. The mixing rate could be adjusted by controlling the velocity difference between the two flows. In order to achieve better contrast between the two fluids, the fibers were dyed blue. The measurements were done varying pulp and latex consistency, velocity difference and exposure time. Examples of reconstructed images of cross sections at different locations along the concentric mixing flow region are shown in Fig. 17.

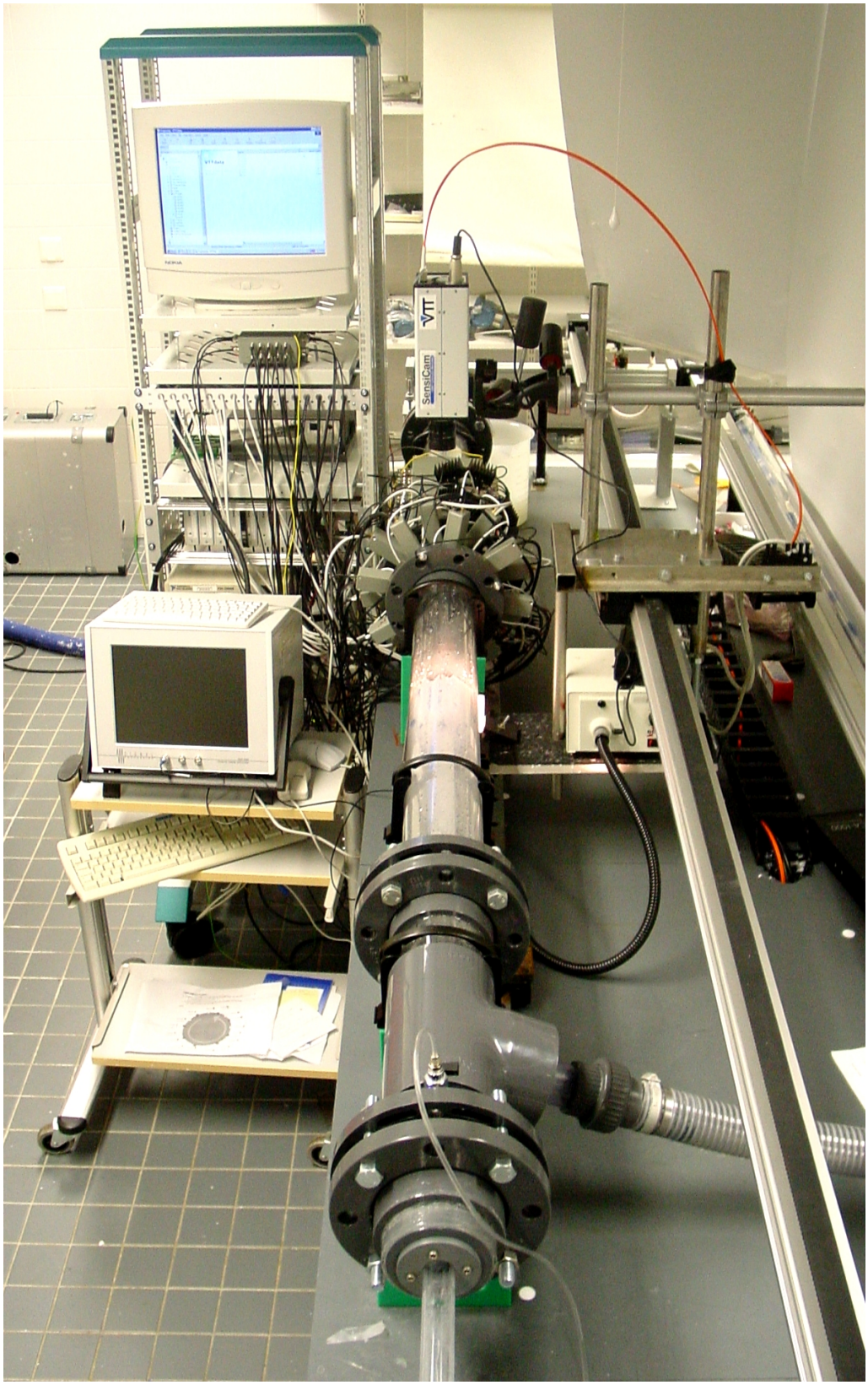

Figure 15. Overview of the experimental set-up with the mixing line at VTT flow laboratory.

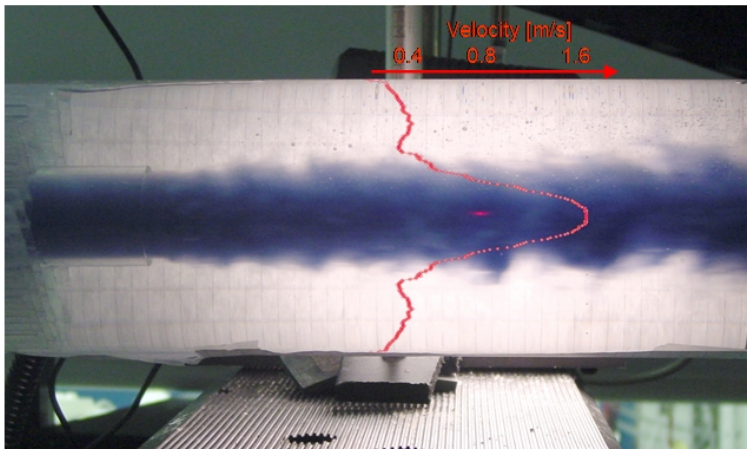

Figure 16. Mixing of water (no latex added) and suspension of fibres dyed blue at consistency 0.5%. Also shown is the mean longitudinal velocity profile in the mixing zone measured using a pulsed ultrasound Doppler-velocimeter.

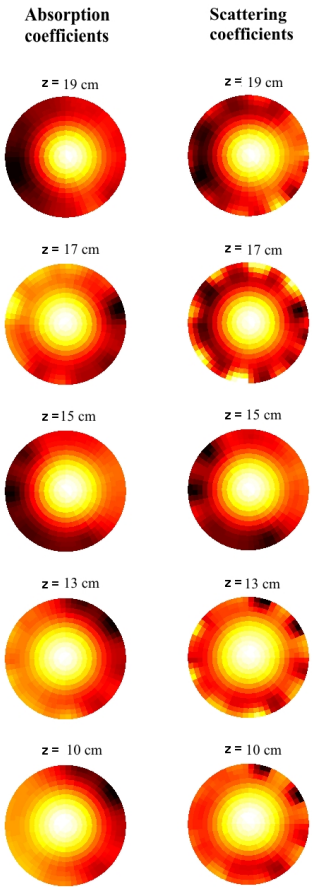

Figure 17. Reconstructed images based on the distribution of absorption and scattering coefficients for different cross sections in concentric mixing flow. The labels above individual images indicate distance from the beginning of the mixing zone (end of the central tube).

3.4.6 Conclusions

The developed computational methods can be utilized both in industrial and medical applications of OT. The new light transport models improve the accuracy of the forward solution with respect to the DA. In addition, with the hybrid model the computational load (mesh size) can be decreased by using a pre computed library of smooth, RTE based sources. This is crucial for many 3D applications. On the other hand, the coupled model offers an efficient forward model for more general domains containing low-scattering regions. The computational calibration method has already been successfully utilized in calibrating optical tomography measurements. It has proven to be an efficient and convenient alternative for difficult and time consuming hardware calibrations. The state estimation approach has been tested with simulated and real data, and it shows good performance for imaging of time varying objects. It can be used as an algorithmic framework for the development of computational methods for dynamic OT. As a conclusion, in this project we have improved the performance of OT in several ways which can help to improve the applicability of OT in industry, especially in time-varying cases and with low scattering medium.

Optical tomography device that we have developed for industrial purposes is a combination of advanced low signal measurement technique and sophisticated mathematics of inverse problems. This new measurement technique is powerful and have great advantages like non-intrusive, fast and capable to 3D measurements. With these properties OT is far ahead from traditional measuring technics used in industrial processes. Only limitation for OT device is that imaging media have to be scattering dominated, because image reconstruction assumes diffusion approximation for light transport in the media. Another disadvantage of OT is that output data needs extensive processing and resolution is limited. But despite of these limitations OT device is new and promising technique for imaging dense particle suspensions like paints, coating/sizing colours and water-wood fibre suspension in real process applications.

Conferences in which the results have been presented

1) Mathematical Days (8–9.1.2002, Joensuu)

2) Physics Days (14–16.3.2002, Joensuu)

3) OSA Biomedical Topical Meetings (7–10.4.2002, Miami Beach, Florida)

4) ProMoni-MANDI seminar (22–23.10.2002, Lappeenranta)

5) Applied Inverse Problems (18–23.5.2003, Lake Arrowhead, California)

6) International Congress in Industrial and Applied Mathematics (7–11.7.2003, Sydney, Australia)

7) 3rd World Congress on Industrial Process Tomography (2–5.9.2003, Banff, Canada)

8) ProMoni-MANDI seminar (17–18.11.2003, Espoo)

9) OSA Biomedical Topical Meetings (14–17.4.2004, Miami Beach, Florida).

3.4.7 References

[1] Kolehmainen, V., Prince, S., Arridge, S.R. & Kaipio, J.P. State-estimation approach to the nonstationary optical tomography problem. J. Opt. Soc. Am. A., 20(5), pp. 876–889, 2003.

[2] Markkanen, K. Optinen diffuusiotomografia – kuvantaminen sylinterisymmetrisessä sekoittumisessa kolmessa dimensiossa", Master's thesis, University of Kuopio, Department of Applied Physics, 2003.

[3] Nissilä, I., Noponen, T., Kotilahti, K., Tarvainen, T., Lipiäinen, L., Järvenpää, S. & Katila, T. Techniques and instrumentation for the multichannel measurement of phase and amplitude in optical tomography. (In preparation)

[4] Prince, S., Kolehmainen, V., Kaipio, J.P., Franceschini, M.A., Boas, D. & Arridge, S.R. Time-series estimation of biological factors in optical diffusion tomography. Phys. Med. Biol., 48, pp. 1491–1504, 2003.

[5] Tarvainen, T., Kolehmainen, V., Vauhkonen, M., Vanne, A., Gibson, A.P., Schweiger, M., Arridge, S.R. & Kaipio, J.P. Computational calibration method for optical tomography. Appl. Opt., 2004. (Submitted)

[6] Tarvainen, T., Vauhkonen, M., Kolehmainen, V. & Kaipio, J.P. Finite element model for the coupled radiative transfer equation and diffusion approximation. (In preparation)

[7] Vauhkonen, M., Vilhunen, T., Kolehmainen, V. & Kaipio, J.P. Utilizing radiative transfer equation in optical tomography. In: Biomedical Topical Meetings CD-ROM, (The Optical Society of America, Washington, DC), WF48, 2004.

[8] Vilhunen, T., Vauhkonen, M., Kolehmainen, V. & Kaipio, J.P. Linking the radiative transfer equation and the diffusion approximation. In: Biomedical Topical Meetings, (The Optical Society of America, Washington, CD), SuB1-1, 2002.

[9] Vilhunen, T., Kolehmainen, V., Vauhkonen, M. & Kaipio, J.P. A source model for optical diffusion tomography. In: Proceedings of 3rd World Congress on Industrial Process Tomography, Banff, Canada, 2.–5.9.2003, The Virtual Centre for Industrial Process Tomography, 2003.

[10] Vilhunen, T., Vauhkonen, M., Kolehmainen, V. & Kaipio, J.P. A hybrid radiative transfer – diffusion model for optical tomography. Appl. Opt., 2003. (Submitted)

[11] Vilhunen, T., Kolehmainen, V., Vauhkonen, M., Vanne, A., Gibson, A.P., Schweiger, M., Arridge, S.R. & Kaipio, J.P. Computational calibration method for optical tomography. In: Biomedical Topical Meetings CD-ROM, (The Optical Society of America, Washington, DC), ThD3, 2004.

3.5 Impedance Tomography

Shaomin Zhou and Jouko Halttunen
Tampere University of Technology, Measurement and Information Technology

3.5.1 Background

Electrical Impedance Tomography (EIT) is an imaging method that can profile the resistivity distribution within a domain. The pulp flow mixes with suspension, air bubbles and so on, which materials have different conductivity. Therefore, it is possible to identify them from resistivity measurement. The advantage of such a technique over many other measurement methods is that it provides a non-intrusive and sensitive method of measuring the pulp flow using non-ionising radiation. The relative low cost and its suitability to perform long term monitoring are also very desirable features. The EIT imaging is not affected by the opacity of suspensions. Thus, it can be used for dense or coloured suspensions. Also, the measurements can be made without perturbing the flow of the suspension.

Unfortunately, a severe limitation of EIT is its poor spatial resolution which is related to the number of electrodes used (Seagar et al. [**1**]). However, it is not a case of simply increasing the number of electrodes to overcome this problem. This is due to the practical difficulties of applying large number of electrodes to the object, the associated complexity of the electronics, which can accurately measure signals with large dynamic range, and the computational difficulties of processing vast quantities of data. For these reasons, the majority of EIT systems that have been developed only incorporate 16 electrodes, leading to a resolution limit of about 12% of the image diameter (Sinton et al. [**2**]).

During the past three years, three prototype systems were developed in the Institute of Measurement and Information Technology, Tampere University of Technology. The first prototype system included a 16-electrode sensor, a signal conditioning board, an A/D card and a host computer. Both the data sampling and image reconstruction were completed by the host computer. The Newton-Rahpson algorithm, coded in Matlab, was applied to reconstruct the cross sectional image.

In order to improve the performance of the measurement system, a separate data sampling system (DAS) was designed in the second prototype system. The host computer was only used to reconstruct the images. The collected data was transmitted from the DAS to host computer via serial port.

In the first and the second prototype systems, the sensor had one set of electrodes. Therefore, the flow velocity cannot be measured. In the third prototype system, a dual-plane sensor was applied. Two sets of cross sectional images were collected from the dual-plane sensor, and then applied the cross correlation algorithm to calculate the velocity. The software was coded in Delphi.

3.5.2 Physical model of impedance tomography

The basic idea of process tomography is to install a number of sensors around the pipe or vessel to be imaged, see Fig. 1. The distribution function of conductivity is σ. A current is injected via a pair of electrodes and the response voltages are measured from the other electrodes. The response voltages depend on the position of the component boundaries within their sensing zones.

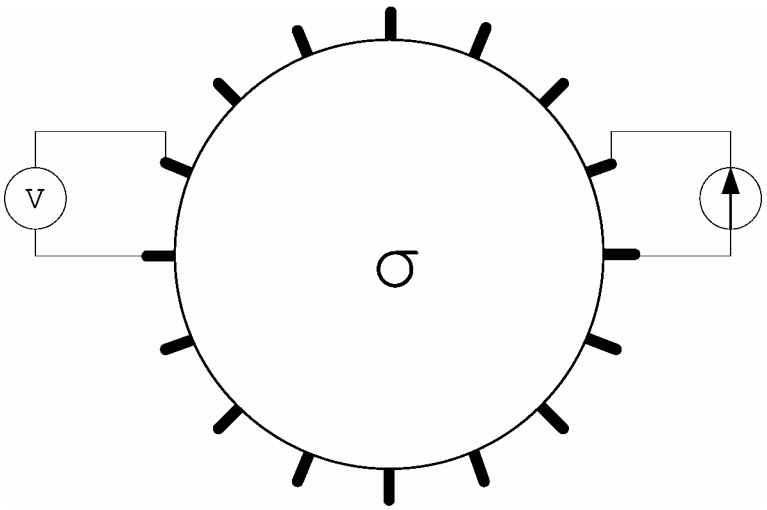

Figure 1. Physical mode of EIT.

The underlying relationships, which govern the interaction of electricity and magnetism are summarised by Maxwell's equations. For the case of EIT, several simplifying assumptions can be applied to reduce the complexity of the problem. The frequency of the applied currents is assumed to be low enough such that the displacement current can be ignored. The region can therefore be considered as an ionic conductor, and thus the quasi-steady equations of Maxwell can be used in which the electric and magnetic inter-relationships can be written as (Duffin [**3**]):

Electric:

$$\nabla \cdot \mathbf{E} = \rho / \varepsilon_r \varepsilon_0 \tag{1}$$

$$\nabla \times \mathbf{E} = 0 \tag{2}$$

Magnetic:

$$\nabla \cdot \mathbf{B} = 0 \tag{3}$$

$$\nabla \times \mathbf{B} = \mu_r \mu_0 \mathbf{J} \tag{4}$$

where ∇ is the gradient operator
$\mathbf{E}$ is the electric field strength
$\mathbf{B}$ is the magnetic flux density
ρ is the charge density
ε_r, ε_0 is the relative and free space permittivity
μ_r, μ_0 is the relative and free space permeability
$\mathbf{J}$ is the current density

For EIT application, the magnetic permeability of the objects is very low, and we are therefore only concerned with the electrical properties of the medium. The electric field in terms of the electric potential ϕ can be expressed as:

$$\mathbf{E} = -\nabla \phi \tag{5}$$

Combining Eqn. (**1**) and (**5**) gives Poisson's equation:

$$\nabla^2 \phi = -\rho / \varepsilon_r \varepsilon_0 \tag{6}$$

and if there are no free charges, ρ=0, and thus Eqn. (**6**) becomes Laplace's equation:

$$\nabla^2 \phi = 0 \tag{7}$$

This partial differential equation has an infinite number of solutions, each giving a distribution of ϕ. To limit these solutions, boundary conditions can be applied, which specify the value of certain parameters on the surface. These may be either: Dirichlet conditions, in which the potential on the surface is specified; Neumann conditions, in which the current density crossing the boundary is specified; or mixed conditions, which are a combination of Dirichlet and Neumann conditions.

3.5.3 Image reconstruction algorithm

EIT image reconstruction can generally be classified into two distinct types: those which seek a full reconstruction of the conductivity distribution, using iterative methods to take account of the non-linearity of the inverse problem; and those which linearise the reconstruction and therefore result in a less accurate, but faster solution.

A number of reconstruction algorithms have been proposed up till now. Two common algorithms used in this project will be introduced in the section below.

Sensitivity method

The sensitivity method was based on sensitivity theorem of Geselowitz [**4**]. Fig. 2 shows a bounded domain with uniform conductivity σ. A current I is injected via a pair of adjacent surface electrodes a-b, and the response voltage U is measured between the pair of electrodes c-d.

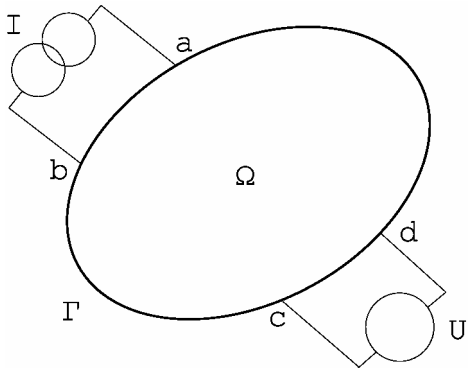

Figure 2. Sensitivity method for image reconstruction.

Assume that the unit current (I = 1) is applied, the response voltage U is given by

$$U = \int_{\Omega} \sigma \nabla \Phi \cdot \nabla \Psi dv \tag{8}$$

where Φ is the potential field when current is applied through electrodes a-b
ψ is the potential field when current is applied through electrodes c-d
Ω is a bounded domain with uniform conductivity σ

Now we consider the general conductivity distribution and associated voltage measurements in terms of uniform and perturbed conductivity distributions, such that:

$$\sigma = \sigma_u + \sigma_p \tag{9}$$

$$U = U_u + U_p \tag{10}$$

$$\nabla \Phi = \nabla \Phi_u + \nabla \Phi_p \tag{11}$$

$$\nabla \Psi = \nabla \Psi_u + \nabla \Psi_p \tag{12}$$

where subscripts u and p are the uniform and perturbed equivalents respectively. Expanding Eqn. (**8**) gives:

$$U = \int_{\Omega} (\sigma_u + \sigma_p)(\nabla\Phi_u + \nabla\Phi_p) \cdot (\nabla\Psi_u + \nabla\Psi_p) dv \tag{13}$$

Simplifying Eqn. (**13**) (refer to [**5**] for detail), we obtain

$$U_p = -\int_{\Omega} \sigma_p \nabla\Phi_u \cdot \nabla\Psi_u dv \tag{14}$$

which is known as the linearised sensitivity relationship. The integration is over the bounded domain Ω. Normally, it is very difficult to get an analytical solution. Therefore, the finite element method is often applied to solve this problem.

The domain Ω is split into N elements Ω_e (e=1,2, …, N) and in each element Ω_e, the conductivity change is σ_p^e, then

$$U_p = -\sum_{e=1}^{N} \int_{\Omega_e} \sigma_p^e \nabla\Phi_u^e \cdot \nabla\Psi_u^e dv \tag{15}$$

We can write Eqn. (**15**) in matrix form

$$U_p = \mathbf{S}\boldsymbol{\sigma}_p \tag{16}$$

where U_p is the vector of response voltage change
$\boldsymbol{\sigma}_p$ is the vector of conductivity change
$\mathbf{S}$ is the sensitivity matrix

The value in matrix **S** is given by

$$S_{ij} = -\int_{\Omega_e} \sigma_p \nabla\Phi_u \cdot \nabla\Psi_u dv \tag{17}$$

According to Eqn. (**16**), the conductivity distribution $\boldsymbol{\sigma}_p$ can be calculated by inversion of the sensitivity matrix:

$$\boldsymbol{\sigma}_p = \mathbf{S}^{-1}\mathbf{g}_p \tag{18}$$

Therefore, given the boundary measurements $\mathbf{g}_p$, the perturbed conductivity image $\boldsymbol{\sigma}_p$ can be computed. But the sensitivity coefficient matrix is often ill-conditioned, hence the inversion of matrix is not stable and the image reconstruction performance is affected.

Some algorithms have been developed to avoid inversion procedure. For example, Barber [**6**] proposed a back-projection algorithm, which performs a linearised back-projection between two equipotential lines. That is, the potential difference, calculated by the forward solver, between two equipotential lines on the boundary was back-projected to a resistivity value in the area enclosed by the two lines for all possible injection/measurement combinations.

Kotre [**7**] developed enhanced back-projection algorithm utilizing all the image pixel sensitivity, not only those on the diagonal, of the sensitivity matrix. In his method, the grey-scale value of each pixel $P(x, y)$ is related to the set of normalized voltage gradient changes by

$$P(x,y) = \frac{\sum_{m=1}^{M}\sum_{n=1}^{N} S_{m,n,x,y} \ln \dfrac{V'(m,n)}{V(m.n)}}{\sum_{m=1}^{M}\sum_{n=1}^{N} S_{m,n,x,y}} \tag{19}$$

where m is the current drive electrode pair
n is the response voltage electrode pair
$V(m,n)$ is the reference voltage measurement
$V'(m,n)$ is the perturbed voltage measurement
$S_{m,n,x,y}$ is the sensitivity coefficient

$S_{m,n,x,y}$ is the sensitivity coefficient at point (x, y) for a current-driving electrode pair m and a voltage measurement electrode pair n. it can be pre-calculated according to Eqn. (**17**).

The main advantage of the sensitivity algorithm is that it can be performed in a single step using a pre-calculated pixel sensitivity matrix. The image is simply reconstructed via a matrix/vector multiplication. Therefore, the image reconstruction rate is very high.

Modified Newton-Raphson Method

This method implements a FEM solver and a modified Newton-Raphson iterative method (Yorkey [**8**]) to compute the conductivity distribution. A forward transform **F** to describe the relationship between the boundary voltages **V** and the resistivity **r** is given by:

$$\mathbf{V} = \mathbf{F}(\mathbf{r}) \tag{20}$$

The quadratic error $\mathbf{e}(\mathbf{r})$ between the computed voltages of the previous equation and the measured voltages $\mathbf{V}_0$ is defined by:

$$\mathbf{e}(\mathbf{r}) = \frac{1}{2}\left[\mathbf{F}(\mathbf{r}) - \mathbf{V}_0\right]^T \left[\mathbf{F}(\mathbf{r}) - \mathbf{V}_0\right] \tag{21}$$

Here T represents the matrix transpose. Minimisation of this error with respect to the resistivity gives:

$$\mathbf{e}'(\mathbf{r}) = \left[\mathbf{F}'(\mathbf{r})\right]^T \left[\mathbf{F}(\mathbf{r}) - \mathbf{V}_0\right] = 0 \tag{22}$$

where $\left[\mathbf{F}'(\mathbf{r})\right]_{ij} = \dfrac{\partial \mathbf{F}_i}{\partial \mathbf{r}_j}$ and is called the Jacobian matrix.

Finding the Taylor expansion of Eqn. (**22**) and ignoring the non-linear terms, Yorkey [**8**] obtained a correction factor for the conductivity at the k^{th} iteration as:

$$\Delta \mathbf{r}^k = -\left\{\left[\mathbf{F}'(\mathbf{r}^k)\right]^T \mathbf{F}'(\mathbf{r}^k)\right\}^{-1} \left[\mathbf{F}'(\mathbf{r}^k)\right]^T \left[\mathbf{F}(\mathbf{r}^k) - \mathbf{V}_0\right] \tag{23}$$

The updated conductivity distribution becomes:

$$\mathbf{r}^{k+1} = \mathbf{r}^k + \Delta \mathbf{r}^k \tag{24}$$

The Jacobian is recalculated at each iteration and thus an efficient FEM implementation is required to compute the forward transformation and Jacobian. The principle problem associated with this algorithm however, is the inversion of the matrix:

$$\mathbf{A} = \left[\mathbf{F}'(\mathbf{r}^k)\right]^T \mathbf{F}'(\mathbf{r}^k) \tag{25}$$

This matrix **A** is often ill-conditioned and thus regularisation techniques are required if images are to be reconstructed from real data which will inevitably include measurement noise. Yorkey [**8**], implemented the Marquardt [**9**] method to achieve the regularisation, whilst Hua et al. [**10]** modified the term to be minimised (Eqn. (**21)**, by adding a penalty term such that:

$$\mathbf{e}(\mathbf{r}) = \frac{1}{2}\left[\mathbf{F}(\mathbf{r}) - \mathbf{V}_0\right]^T \left[\mathbf{F}(\mathbf{r}) - \mathbf{V}_0\right] + \lambda \mathbf{r}^T \mathbf{P}\mathbf{r} \tag{26}$$

where λ is a scalar and **P** is a positive definite matrix, depending on the form of prior information. Generally, **P** can be a simple diagonal matrix. The correction factor in Eqn. (23) becomes:

$$\Delta \mathbf{r}^k = -\left\{\left[\mathbf{F}'(\mathbf{r}^k)\right]^T \mathbf{F}'(\mathbf{r}^k) + 2\lambda \mathbf{P}\right\}^{-1} \left[\mathbf{F}'(\mathbf{r}^k)\right]^T \left[\mathbf{F}(\mathbf{r}^k) - \mathbf{V}_0\right] \tag{27}$$

The matrix **A** now includes an additional term and this tends to improve the matrix condition. However, the value of these regularisation terms can greatly alter the performance of the algorithm. If λ is too high, the smoothing may result in severely degraded image resolution, whilst a small λ will have little effect on the conditioning of the matrix.

Several groups have adopted a single step strategy based on the iterative Newton-Raphson method. Cheney et al. [**11]** developed the NOSER (Newton One-Step Error Reconstruction) algorithm in which the Jacobian matrix is calculated prior to reconstruction and stored. This results in a much faster image reconstruction but at the expense of accuracy.

In our study, the number of electrodes is 16. In order to avoid electrode contact impedance problem, the voltages are not measured at those current-injecting electrodes. Therefore, if we use adjacent measurement strategy, the total number of independent measurements is 16×(16-3)/2=104. If the opposite measurement strategy is used, then the number of independent measurements is 8×(16-4)=96 (Dickin et al. [**12**]).

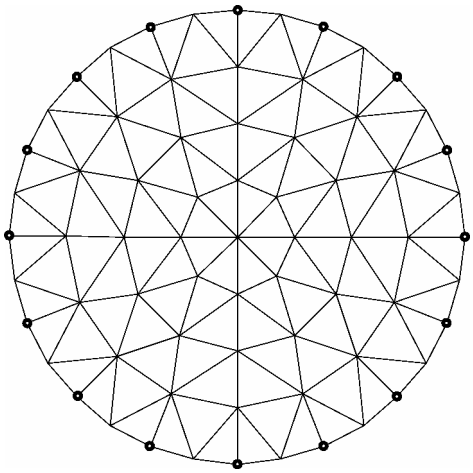

Figure 3. Finite element mesh.

To estimate the voltage **U** for a resistivity distribution ρ, a finite element mesh of 66 nodes and 104 triangular elements is used, see Fig. 3. The black dots are the places of electrodes. The basic steps of calculation are as follows:

(a) Forward problem: guess initial **r**, apply finite elements to estimate the potential distribution, and then calculate the boundary voltage.

(b) Calculate the error sum according to Eqn. (**21**), if it is less than the prescribed error limits, then stop iteration, otherwise, go to (c).

(c) Inverse problem: calculate Δ**r** according to Eqn. (**27**), update **r**, and then go to (a) for next iteration.

3.5.4 Prototype system design

The basic idea of process tomography is to install a number of sensors around the pipe or vessel to be imaged. This reveals information on the nature and distribution of components within the sensing zone. The sensor output signals depend on the position of the component boundaries within their sensing zones. Most tomographic techniques are concerned with abstracting information to form a cross-sectional image. A computer is used to reconstruct a tomographic image of the cross-section being observed by the sensors. This will provide, for instance, identification of the distribution of mixing zones in stirred reactors, interface measurement in complex separation processes and measurements of two-phase flow boundaries in pipes with applications to multiphase flow measurement. The image data can also be analysed quantitatively for subsequent use to improve process control or to develop models to describe individual processes.

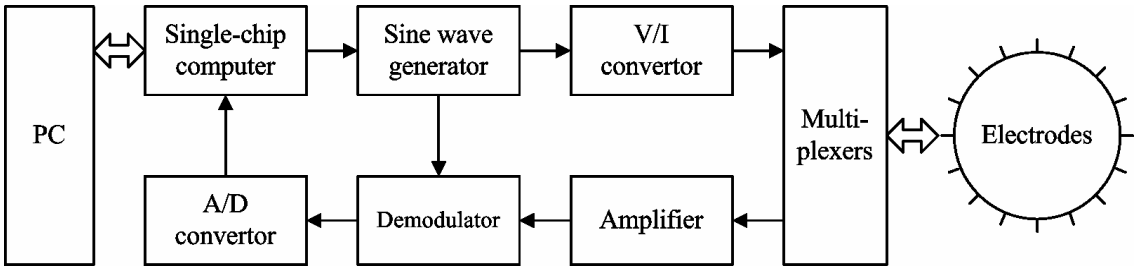

Figure 4. EIT measurement system.

In our project, a 16-electrode EIT system is used to measure the resistivity distribution of pulp in a pipe, then the consistency and consistency profile can be analysed. The schematic diagram of the system is shown in Fig. 4.

Sine wave/DC pulse is generated by an EPROM-based function generator, see Fig. 5. A synchronous signal is also generated for demodulation purpose. The output frequency can be selected among 153 Hz, 200 Hz, 300 Hz … 19.5 kHz by different factor of frequency divider. The amplitude of the output wave is controlled by the reference voltage of DAC1. Therefore, we can change the output voltage of DAC2 to obtain the desired amplitude of the output wave.

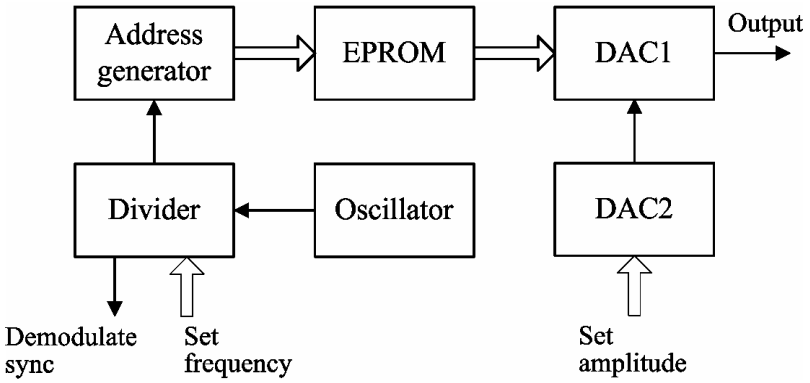

Figure 5. Sine wave/DC pulse generator.

The electrode signals are first amplified by programmable gain amplifier, which provides gains of 1, 10, 100 and 1000. Resistivity signal is demodulated by a phase-sensitive demodulator AD630 and digitized by a 12-bit A/D converter, see Fig. 6. The single-chip computer accepts commands from host computer to initialize the hardware (gain of amplifier, amplitude of injected current, sample interval and so on), selects electrodes for injecting current and electrodes for collecting voltage signals, controls the A/D converter to acquire data and sends the sampled data to host computer via serial port. The whole system is simple, flexible and relatively low cost.

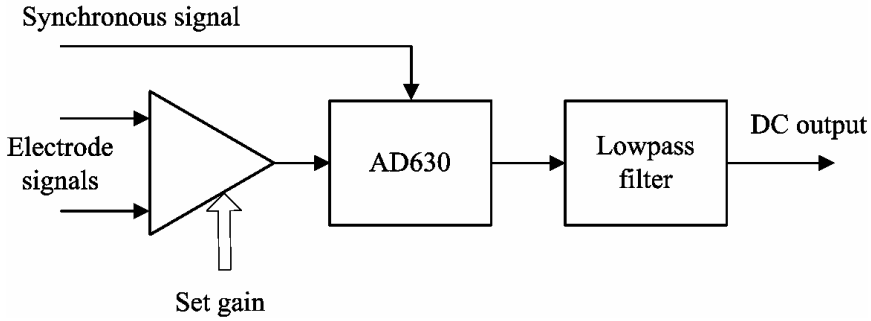

Figure 6. Signal demodulator.

3.5.5 Monitoring consistency in pulp flow

In pulp and paper making, the control of the pulp slurry consistency is especially important. Without uniform consistency the process is practically impossible to control. Whether the uniformity is achieved with instrumentation or by other means, it must be measured. The manual method of measuring consistency consists of selecting and weighing a representative sample, removing the water, and weighing the reminder. This method is satisfactory for spot checking but it is not acceptable for continuous control. Changes in consistency must be monitored continuously and online if satisfactory control is to be achieved. For control purposes, it is important to be able to sense the

variations in consistency rather than to determine the absolute value of consistency (Lavigne [**13**]).

The conventional measuring instruments are unsuitable for this purpose, because they may not work in the difficult internal conditions of the process, or disturb the operation of the process. The measuring instruments for such applications must use robust, non-invasive sensors. Since 1990s, tomography has been applied to multiphase flow measurement in order to get a more illustrative and accurate result. The image data can be analysed quantitatively for subsequent use to actuate process control strategies or to develop models to describe individual processes (Williams et al. [**14**]).

The experiments were carried out in a cylindrical tank of 60 mm diameter with 16 circular stainless steel electrodes of 6 mm diameter, see Fig. 7. Four kinds of pulp in different consistency were used and Newton-Raphson algorithm was applied to reconstruct images. The results are shown in Fig. 8. The colour bars show the resistivity of the pulp. These images indicate that the resistivity of the pulp increases as the consistency increases.

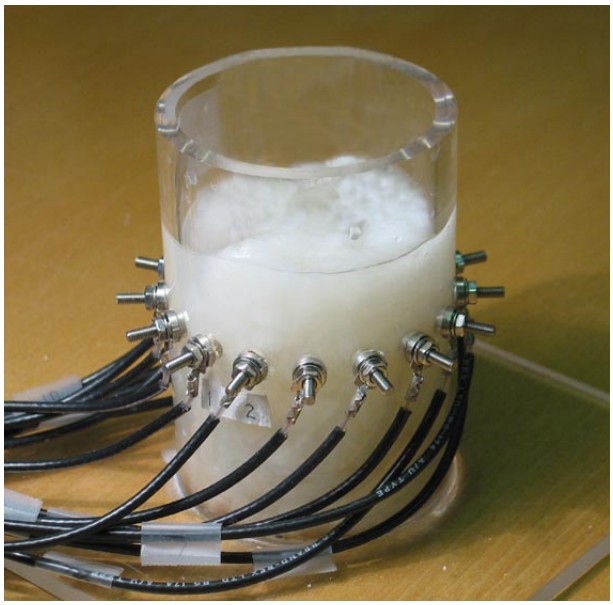

Figure 7. Experimental setup.

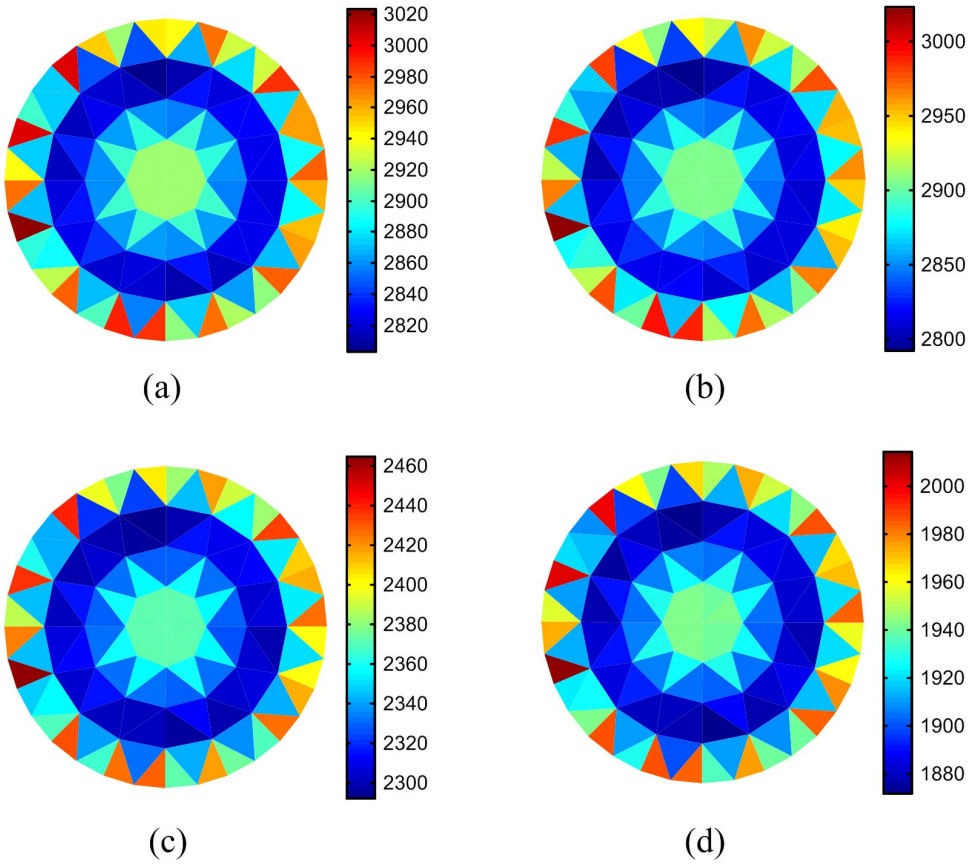

Figure 8. Consistency measurement: (a) Consistency higher; (b) Consistency high; (c) Consistency medium; (d) Consistency low.

3.5.6 Monitoring air bubbles in pulp flow

It is obvious that there is a difference in conductivity between air bubble and pulp. Therefore, it is possible to identify air bubbles from resistivity measurements. In our experiment, the same device was used as shown in Fig. 7. The tank was full of pulp (consistency about 3.5%) and some plastic rods were used to form several different areas of resistivity, see Fig. 9. The injected current was set to 2.0 mA/1kHz.

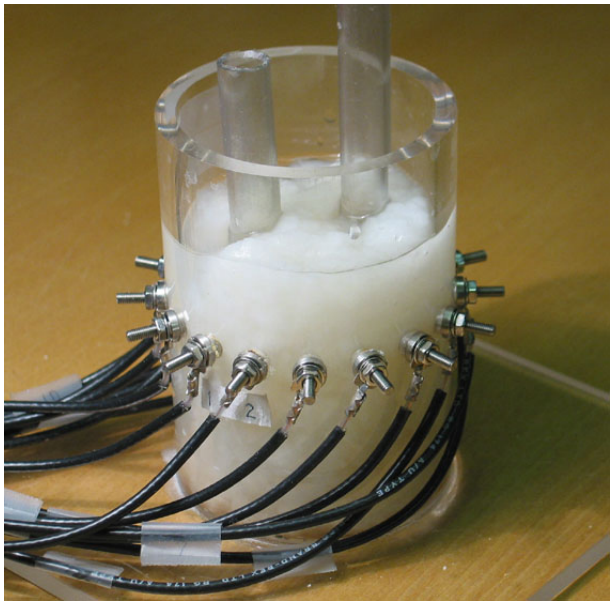

Figure 9. The plastic rods were used to simulate air bubbles.

The pictures in Fig. 10 show the results when a plastic rod with diameter of 20 mm diameter was placed in different positions.

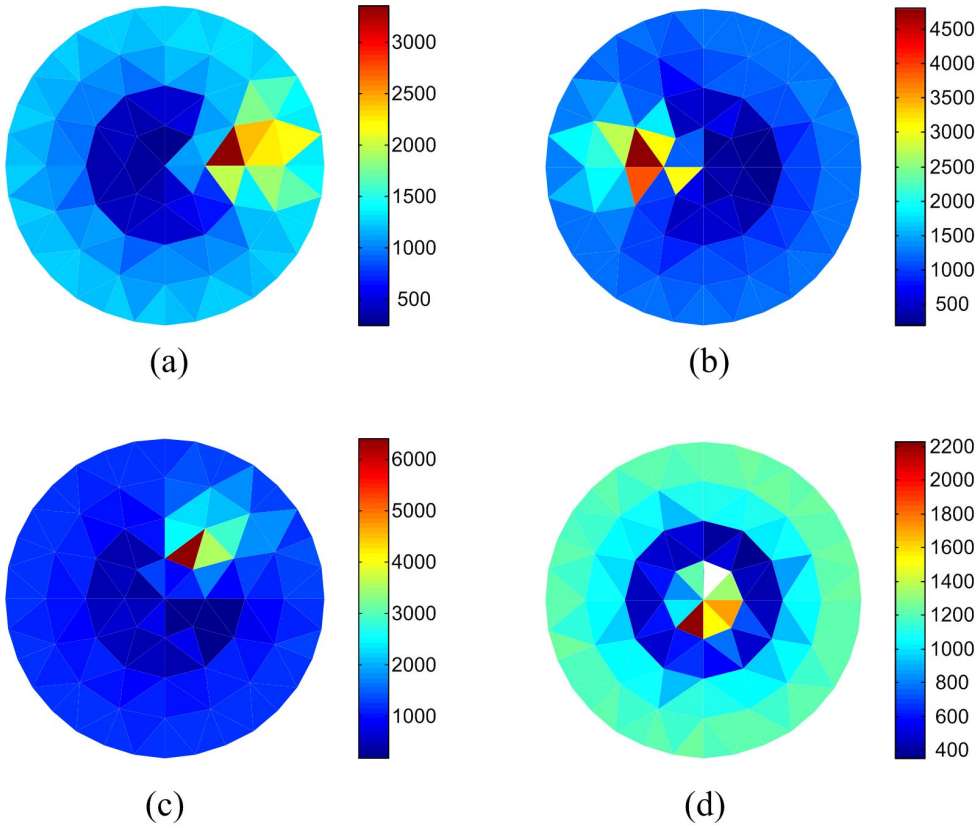

Figure 10. Experimental results: (a) Plastic rod on the right; (b) Rod on the left; (c) Rod near centre; (d) Rod at the centre.

3.5.7 Measuring velocity in pulp flow

The basic idea is to apply the process tomography to obtain the images containing the distribution information about each phase and calculate the cross correlation of the images to get the velocity information, then the volume flow rate or mass flow rate can be calculated.

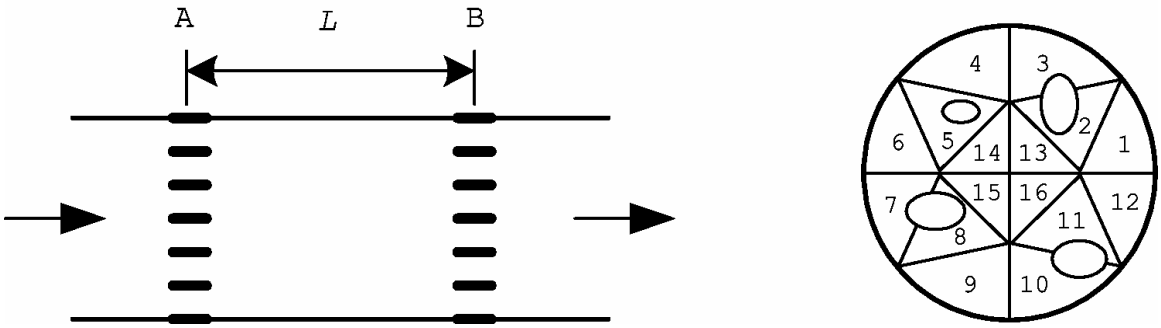

Figure 11. Flow velocity measurement.

In this research, the velocity was measured by pixel-pixel cross correlation. Fig. 11 shows a dual 16-electrode sensor for this system. The cross section was divided into 16 pixels. If the flow pattern can be considered 'frozen' during passing from plane A to plane B, the time that the k^{th} pixel moves from plane A to plane B can be determined by following cross-correlation function,

$$R_k(j) = \frac{1}{N}\sum_{i=1}^{N} x_k(i) y_k(i+j) \qquad j = 0,1,2,...,M \;\; k = 1,2,...,16 \tag{28}$$

where $x_k(i)$ and $y_k(i)$ are the up-stream and down-stream signals, N is the number of samples in cross correlation calculation, j is the number of delayed samples, and k is the pixel index. When the time delay equals to the flow transit time τ^*, the cross correlation function produces the maximum value. The flow velocity can be calculated $V=L / \tau^*$, where L is the distance between the sensors. In total, 16 velocities can be calculated.

After the fraction profile and the velocity profile have been obtained, the volumetric flowrate can be derived

$$Q = \sum_{i=1}^{m} \beta_i V_i A_i \tag{29}$$

where A_i is the area of i^{th} pixel, β_i is the modifying factor of flowrate.

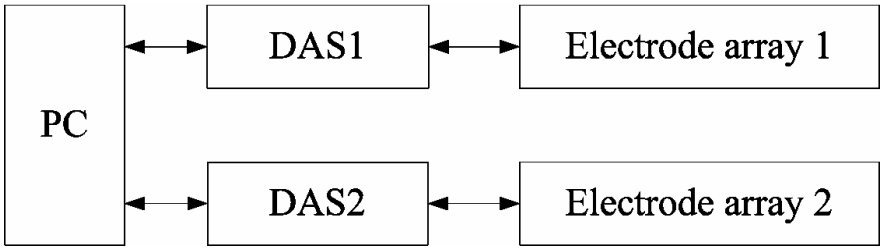

Figure 12. System block diagram.

In order to implement the measurement of flow velocity, two independent data acquisition systems DAS1 and DAS2 are connected to the two electrode arrays as shown in Fig. 12. The dual-plane electrodes are shown in Fig. 13.

Figure 13. Dual-plane electrodes.

To simulate the air bubble motion, a plastic rod was put into the tank, and then pulled from the bottom to top. In Fig. 14, the first curve is signal from the 7^{th} pixel in up-plane; the second curve is the signal from the 7^{th} pixel in down-plane and the third curve is the cross correlation curve.

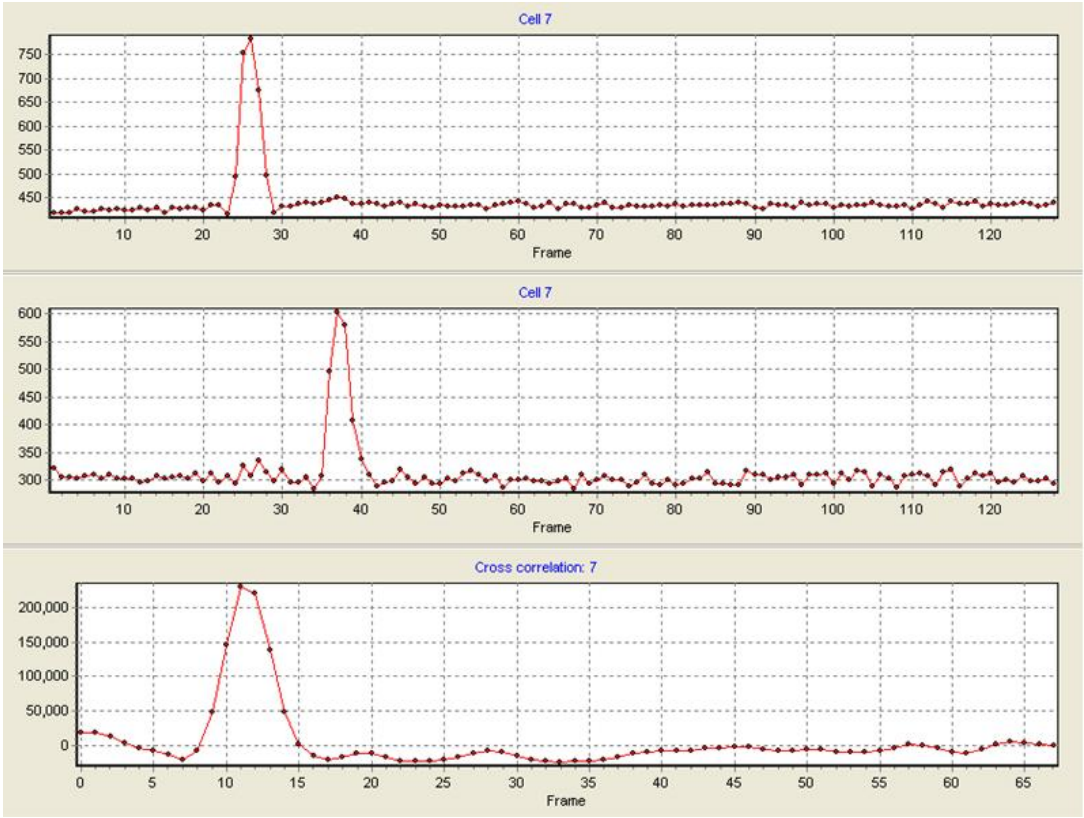

Figure 14. Cross correlation curve.

3.5.8 Summary

Process tomography provides a novel method for multiphase flow measurement, including solids fraction profile, flow regime, velocity profile and volumetric flowrate. As our first stage, we created a simple and relatively low cost flow measurement system. The two independent data acquisition systems give a flexible solution for the measurement system. The host computer reconstructs images, calculates cross correlation function and parameters of flow. At the same time, the two data acquisition systems acquire data from electrode arrays. In order to realize online measurement, the real-time performance of DAS needs to be improved further.

3.5.9 References

[1] Seagar, A.D., Baber D.C. & Brown, B.H. Theoretical Limits to Sensitivity and Resolution in Impedance Imaging. Clin. Phys. Physiol. Meas., 8 (Suppl. A), pp. 13–31, 1987.

[2] Sinton, A.M., Brown, B.H., Barber, D.C., McArdle F.J. & Leathard, A.D. Noise and Spatial Resolution of a Real-time Electrical Impedance Tomograph. Clin. Phys. Physiol. Meas., 13 (Suppl. A), pp. 125–130, 1992.

[3] Duffin W.J. Electricity and Magnetism (3rd Ed). McGraw Hill, London,1980.

[4] Geselowitz, D.B. An Application of Electrocardiographic Lead Theory to Impedance Plethysmography. IEEE Trans. Biomed. Eng., 18, pp. 38–41, 1971.

[5] Metherall, P. Three Dimensional Electrical Impedance Tomography of the Human Thorax. PhD Thesis, University of Sheffield, 1998.

[6] Barber, D.C. & Brown, B.H. Applied Potential Tomography (Review Article). J. Phys. E: Sci. Instrum, 17, pp. 723–733, 1984.

[7] Kotre, C.J. A Sensitivity Coefficient Method for the reconstruction of Electrical Impedance Tomograms. Clin. Phys. Physiol. Meas., 10, pp. 275–281, 1989.

[8] Yorkey, T.J., Webster, J.G. & Tompkins, W.J. Comparing Reconstruction Algorithms for Electrical Impedance Tomography. IEEE Trans. Biomed. Eng., Vol. 11, pp. 843–852, 1987.

[9] Marquardt, D.W. An Algorithm for Least-Squares Estimation of Nonlinear Parameters. SIAM J. Appl. Math., 11, pp. 431–441, 1963.

[10] Hua, P., Webster J.G. & Tompkins, W.J. Iterative Reconstruction Methods Using Regularization and Optimal Current Patterns in Electrical Impedance Tomography. IEEE Trans. Medical Image, Vol. 10, pp. 624–628, 1991.

[11] Cheney, M., Isaacson, D., Newell, J.C., Simake S. & Goble, J. NOSER: An Algorithm for Solving the Inverse Conductivity Problem. Int. J. Imag. Sys. Technol., 2, pp. 66–75, 1990.

[12] Dickin, F. & Wang, M. Electrical resistance tomography for process applications. Meas. Sci. Technol., 7, pp. 247–260, 1996.

[13] Lavigne,J.R. Instrumentation Application for the Pulp and Paper Industry. Miller Freeman Books, San Francisco. Pp. 176–182, 1979.

[14] Williams, R.A., Beck, M.S. Process Tomography-Principles, Techniques and Applications. Butterworth-Heinemann, Oxford, 1995.

3.6 PIV-methods

Markus Honkanen, Tero Pärssinen, Hannu Eloranta and Pentti Saarenrinne
Tampere University of Technology, Energy and Process Engineering

3.6.1 Background

Particle Image Velocimetry (PIV) is a relatively new optical fluid velocity measurement method. This set of instruments was acquired to TUT 1997 in Virtausdynamiikan teknologiaohjelma -project supported by TEKES. PIV gives two or three instantaneous velocity components at specific grid points on the measurement plane of the investigated flow field. In PIV technique, flow is seeded with tracer particles and illuminated by a laser light sheet. An image of the illuminated flow is acquired with a digital camera. Image pairs are acquired with a very small time delay, so the correlation analysis of consecutive images yields the two-dimensional velocity field of the flow. In the case of multiphase flow, the acquired image consists of tracer particles seeded to the continuous phase and particles of the dispersed phase. Both phases of the flow can be studied separately in order to provide reliable information of local, instantaneous fluid dynamics of the continuous phase and the properties of individual dispersed particles.

The goal of this sub-project was to develop the PIV-method in multiphase flow measurements. In many industrial projects, as also in review Kataja et al. **[1]**, it was noted the need for multiphase measurements and also the lack of suitable measurement and analysis methods. The interest in industry was directed to the properties of the dispersed phase and especially to the interaction of the dispersed phase with the flow turbulence. The quantitative connection between these two phenomena was pointed out as an area were knowledge would be valuable. Originally the PIV-method was developed for single-phase measurements and there were no tools for image grabbing, pre- and post-processing for multiphase flows. Also methods for the flow and turbulence structure analysis were lacking. Main problems arise with (1) the optical imaging of the flow, (2) the discrimination between two phases, (3) the removal noise due to the disturbed optical access to the flow, (4) the correct measurement of the properties of the dispersed particle images and (5) relating these measures to real particle size distribution in the flow, (6) the correct measurement of particle velocity and (7) the correct comparison between the measured fluid flow field and the particle velocity. The task was divided to four sub tasks:

First subtask develops and tests image grabbing and illumination techniques for the PIV. Secondly methods are developed to evaluate the properties of the dispersed phase simultaneous with flow field of the continuous phase. This sub-task concerns

multiphase-PIV measurement methods to measure dispersed particle's size, concentration and velocity, and the fluid flow field simultaneously in multiphase flows. The applications include, in bubbly flow, sprays, wood fiber-water suspensions and the flow of solid particles in fluid. In the case of bubbly flows, the interaction between the tracer particles and bubbles in the fluid has also to be taken into account.

The third task was to apply the developed methods to the needs of the other ongoing projects. This task concerns the application of Particle Image Velocimetry (PIV) – technique to study the dynamics of turbulent, multiphase flows in industrial processes.

The fourth sub task was to develop methods for analysis coherent and periodic structures of turbulence. Additionally two new research environments were tested **[2]**, **[3]**.

Measurement methods developed in this work allow the utilization of PIV in denser and more challenging multiphase flows acquiring more reliable and more accurate measurement results than before. In spite of that they were mostly developed and tested for bubble flows, these methods are easily applicable for other particles, like solid particles, flocs, wood fibers.etc. As an outcome, the flow dynamics and the morphology of the individual dispersed particles can be quantitatively analysed.

In the following are the methods developed for multiphase flow measurement first described. After this follows a section for dispersed phase object analysis methods. Applications for multiphase flow cases are described third and finally are explained and applied the developed velocity field post processing methods. This is a shortened version of the original report **[21]** which is available at website: www.tut.fi, from which to >Yksiköt>Laitokset>Energia- ja prosessitekniikka >Tutkimus> Virtaustekniikka.

3.6.2 Optical measurement methods for multiphase flows

The dispersed multiphase flow dynamics is studied with PIV and DI by measuring (a) simultaneously velocity fields of all phases; (b) mean, fluctuating and relative velocities of the continuous and dispersed phases; (c) the concentration of the dispersed phase; and (d) sizes, shapes and orientation of the dispersed phase objects. For example the bubble shape and dimensions play an important role in heat and mass transfer between the continuous and dispersed phases, since they determine the interfacial area available for such phenomena. In addition, the measured velocity fields of the both phases reveal fundamental phenomena of turbulent bubbly flow (e.g. bubble induced turbulence, momentum transfer between the phases, bubble slip velocities as a function of bubble size, and the interaction of bubbles in a bubble swarm).

Imaging of two-phase flows

Direct Imaging (DI, include PIV) technique is able to measure all irregularly shaped objects accurately. Also a very wide dynamic range of object sizes can be measured with the DI technique. The dynamic range depends on the optics used. With a micro-objective with an image size 3x4 mm^2 **[4]** the size range from 10 μm to 2000 μm is achieved. The DI technique is limited to measuring multiphase flows with low dispersed phase concentrations (in bubbly flows the gas void-fractions should not exceed 2%).

Several illumination techniques are studied to capture images of multiphase flow with minimum amount of distortions and background noise. The backlight illumination method for measuring sizes and shapes of objects is introduced and the combination of light sheet illumination and back lighting is developed. Also the Laser Induced Fluorescence (LIF) technique is adopted. At present, the PIV/LIF/back lighting method has the best capabilities to capture both the fluid flow and the dispersed phase with high accuracy.

Several diode laser configurations were tested as the illumination source together with TUT Applied Optics laboratory and Oseir Oy. The use of diode lasers in PIV and related applications was long hampered by their low peak power and pulse energy compared to solid-state lasers. This is countered by arranging several diode laser bars in a row, in total 184 individual emitters (Figure 1). Two different emitting diode types were tested with wavelengths 590 and 808 nm. Using micro-optics, this configuration

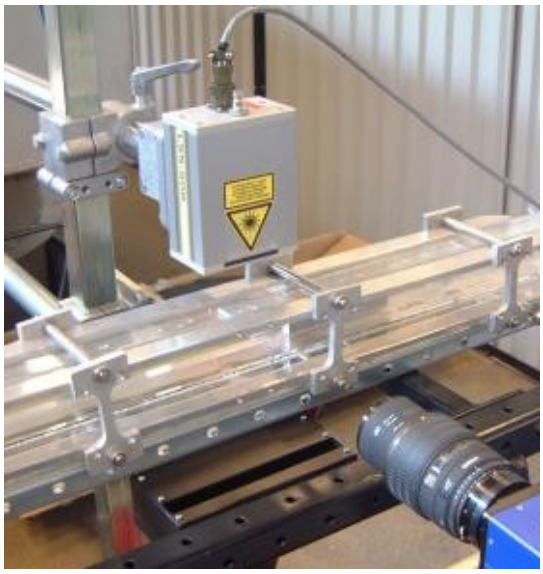

Figure 1. Diode laser as light source in digital imaging.

can be used to provide either sheet illumination or a near-uniform backlight. This system can be freely modulated by simply applying current. The peak power is still weaker than that of a typical Nd:YAG laser, but the pulse energy can be increased by using longer pulses.

When a bubbly flow is illuminated with a light sheet and a back-light produced by diode lasers, the reflections of bubbles have to be removed from images by geometrical alignment of the camera and by digital image processing methods. When backlight is used, the reflections usually exist inside the bubble shadows, thus making the digital removal of reflections relatively easy.

In **[5]**, the bubbly flow measurements have been carried out with different measurement methods using only a Nd-YAG laser light sheet illumination. The most efficient method for that type of illumination is using two cameras at different viewing angles, with optical filters to discriminate the signals of bubbles and fluorescent particles **[5, 6]**. It is often referred as PIV/LIF technique.

Some bubbly flow measurements have been done using only back lighting and one camera perpendicular to the measurement plane. The bubbles in the flow are visualized well and their dimensions and velocities are measured accurately (Figure 2).

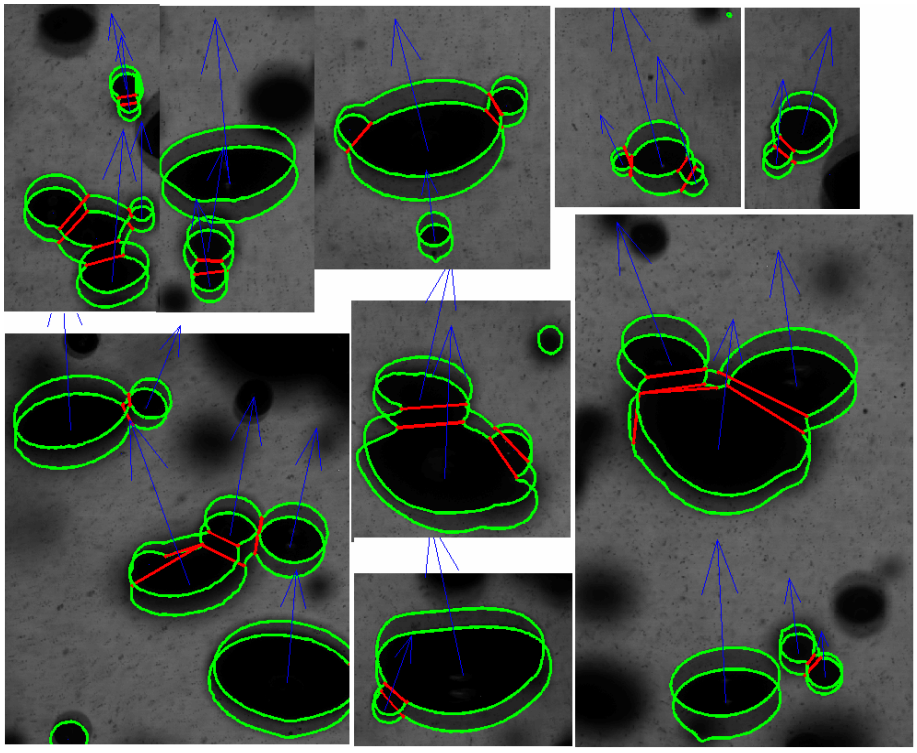

Figure 2. a) Rising bubbles in a stagnant water.

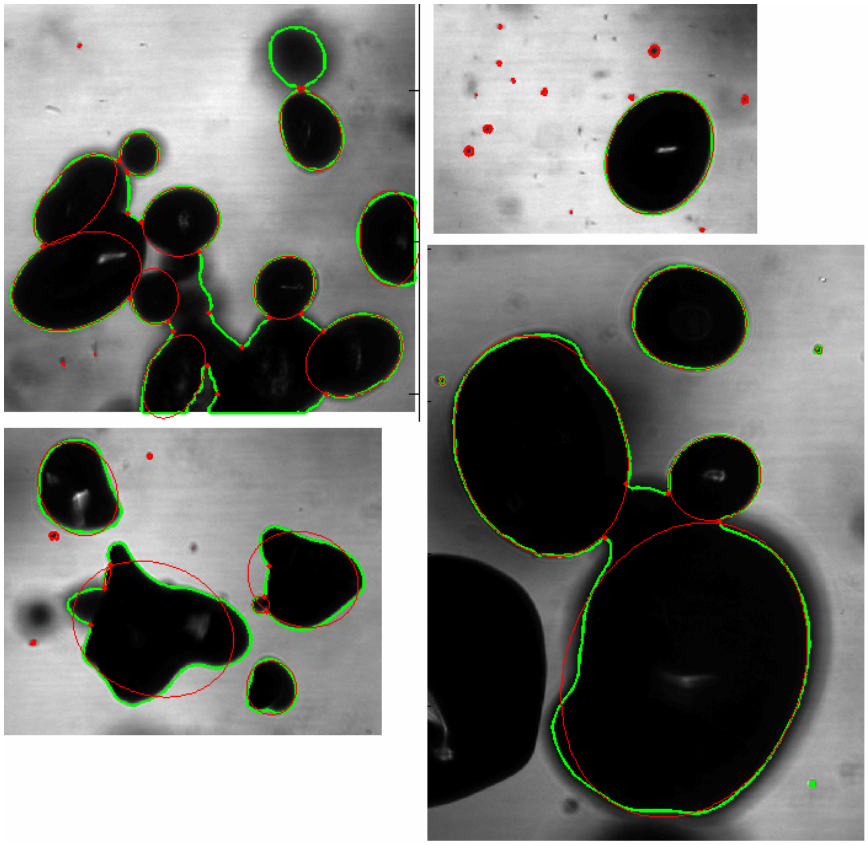

Figure 2. b) Turbulent bubbly flow in an outlet pipe of a centrifugal pump.

The back lighting method and PIV technique using two cameras perpendicular to each other is the most promising approach. In this set-up the two-phase PIV measurement technique combines the PIV/LIF technique with a back lighting method. The pulsed back lighting (with a diode-laser, 808 nm) is used to detect bubble outlines and the (Nd-YAG) laser light sheet is produced to illuminate the tracer particles. Images are recorded with only one camera. The fluid is seeded with tracer particles, which have a fluorescent dye that can be excited by the illumination source. The camera is equipped with an optical edge filter (>570 nm). Therefore, the camera records only the light scattered by fluorescent tracer particles and the shadows of the bubbles. The minimization of reflections on the bubbles enables the visualization of the second-order refraction on the bubble surface as seen in Figure 3. This improves the detection accuracy of bubbles.

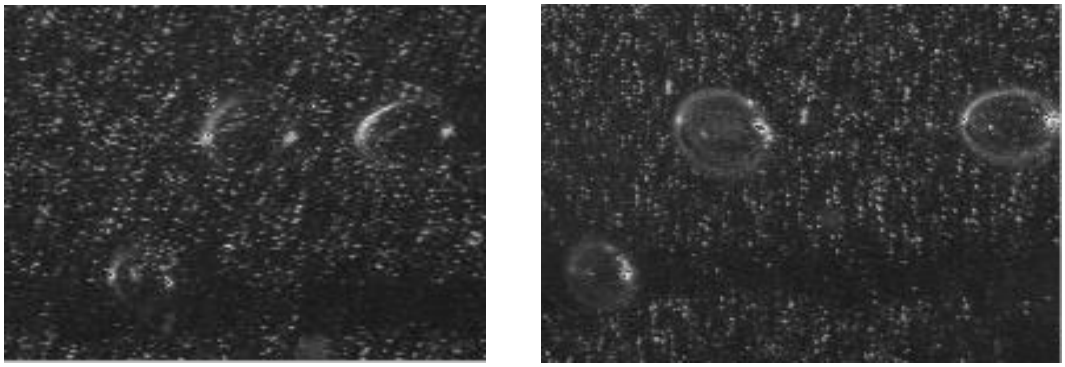

Figure 3. Two overlaid bubble image pairs simultaneously recorded with two cameras at Brewster angle on the opposite sides of the laser light sheet

The discrimination of the phases

Before computing the velocity map of the two-phase flow, the phases have to be separated using optical or digital image processing methods. The fluid phases may differ in particle image size and brightness, the wavelength of the scattered light or the flow dynamics.

Optical method: If the laser induced fluorescence (LIF) method is used with PIV (=PIV/LIF), the continuous phase is seeded with fluorescent tracer particles. Fluorescent particles absorb the light around the wavelength of 532 nm and emit light due to the fluorescence phenomenon at higher wavelengths. With the aid of optical filters and two monochrome cameras, one may separate the radiation scattered by fluorescent and neutral particles.

Digital image processing methods: A digital two-dimensional median filtering method utilizes the difference in particle image size as a discrimination parameter. Scattering intensity discrimination method is used to separate large particulate phase from tracer particles with a diameter of the order of 1 μm. In the phase discrimination method the inherent differences in the motion of the two phases is used to discriminate between them. In addition to the application of the masking techniques, threshold and size discrimination is used to establish digital masks.

The noise removal due to the disturbed optical access to the flow

In order to decrease the noise level of images they are pre-processed by proper filtering procedures. The background noise of the image is mainly increased by objects outside the measurement plane, which cause distortions of the image and damp the light intensity in the image **[7]**.

Another used pre-processing approach is to convert an image taking a natural logarithm of the image. A non-homogenous dispersed phase density in the flow causes large

changes in the background intensity of the image. The changes in the background intensity of the image are equalized effectively by subtracting the sliding background of the logarithmic image.

The sizing of the dispersed particle images

When the multiphase flow images are segmented by gray scale threshold, all the shadow images (in-focus and out-of-focus images) are detected as dispersed particles. Only the in-focus objects should be recognized in order to minimize the bias errors caused by the particle size sensitive effective thickness of the measurement volume, and because the detection accuracy of un-focused object images is much weaker than the accuracy for sharp images.

The size of a single, noiseless object image can be measured with high accuracy. The accuracy decreases when noise increases and the percentage of overlapping object images increases. Measuring a larger sample of objects can increase the accuracy of measured object size distribution **[10]**.

Relating particle image size to real particle size distribution in the flow

The larger particles appear to be in focus over a thicker measurement volume than smaller particles. This will result in the measured size distribution becoming biased towards larger particles. In addition, the images of large particles have higher probability to overlap with other particle images, so the measured sizes of large particles are often also overestimated. On the other hand, the large particles have higher probability to fall partly behind the un-focused objects that locate in front of the measurement plane. Thus, image's effective measurement area for detecting the large particles is smaller than for small particles. In addition, for very small objects, the size of the object image does not directly relate to the real object size.

Not only dispersed phase object size distributions, but also number- and mass-averaged object diameters, number of detected objects and the dispersed phase concentration are derived from the measurement results. All the results are biased upwards, if a constant value for thickness of the measurement volume is used. Instead, the thickness of the measurement volume should be defined as a function of the detected object diameter.

The measurement of particle velocity

The accuracy of different velocity calculation methods of a dispersed particle image (PTV methods) is studied with simulated multiphase flow images consisting of a dispersed particle shadow and bright tracer particles on top of it. The methods under study are a cross correlation based FFT-CC method and centroiding methods combined with particle tracking (simple centroiding SC, intensity weighted centroiding IWC and

fitted ellipse centroiding FE). Cross correlation based FFT-CC method is also referred as Individual Particle Correlation (IPC) and it is described in **[6, 9]**.

The used velocity measurement methods attain sub-pixel accuracy. Four main features that affect the measured velocity accuracy are background noise i.e. tracer particle images, object size, object displacement and object image contrast. Figure 4 shows that for images without background noise the error of FFT-CC method remains under 0.015 pixels for all object sizes and displacements, the error of IWC method remains under 0.02 pixels and the error of simple centroiding remains under 0.07 pixels. Due to the discretized information of the digital image the measured object displacements are biased towards nearest integer values (i.e. peak locking effect). The bias error is large for SC method, but IWC method gives already much better results. Only very small peak locking effect occurs for FFT-CC method.

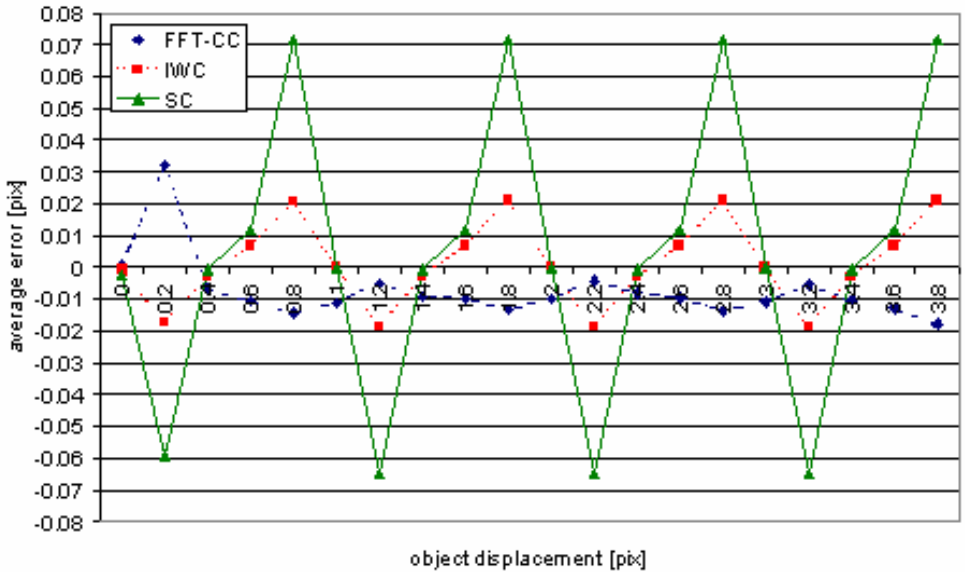

Figure 4. The average errors in the measurement of object's velocity in an image without background noise relative to the varying object displacement.

The comparison between the measured fluid flow field and the particle velocity

In order to measure a correct relative velocity for an object, the object must locate centrally in the direction of depth in the measurement plane. When back lighting is used, the depth of field of the image is controlled by camera aperture.

The fluid flow field is measured from the tracer particle image, which is produced by subtracting the sliding background of the multiphase flow image. The fluid velocity information is transferred as an initial predictor to the PTV algorithm that calculates the object velocity. The linear interpolation seems to be an accurate interpolation method. The Figure 13 in the applications-Chapter shows that the two velocity PDF's of the

interpolated fluid flow velocities and of all the other fluid flow velocities are very similar revealing a good interpolation scheme. All the turbulence quantities are measured only in the areas outside the digital mask, so their accuracy does not depend on the interpolation scheme **[12]**.

3.6.3 Overlapping object separation methods

The images of dense multiphase flow consist of in-focus and out-of-focus dispersed phase objects. The density of objects in each image is so high that the individual separate objects are seldom detected. Most of the objects are overlapping with other objects in the image. A robust algorithm is developed to separate and individually detect the overlapping objects in the image. The development work is done in co-operation with a PIV hardware/software manufacturer, LaVision GmbH **[11]**. The developed algorithm calculates the overall perimeter of a segment, finds the points at the perimeter that represent the connecting points of overlapping objects and fits ellipses on the separated arcs of the perimeter. In literature the connecting point is also referred as a "breakpoint". If the segment that consists of overlapping objects, is too complex, the segment is rejected in order to avoid false recognitions.

Performance of the methods

By comparing four digital overlapping object separation methods, we found out that the Curvature-profile method locates the connecting points most accurately and most reliably. It is also least sensitive to noise. Shen's method is the best approach if spherical bubbles are studied. The Probability-of-centre method performed the worst. If the studied bubbles are larger than few millimeters, it is recommended to pair the connecting points and separate the segments instead of fitting a sphere or an ellipse to the separated arcs of the perimeter. For small, ellipse-like bubbles the ellipse-fitting procedure gives very accurate results. The presented methods have a good tolerance against noise, brightness deviations and bright regions inside the shadow, but grey scale threshold value should be selected carefully, so that the out-of-focus images are left out from the analysis.

A small sample of PIV-images of bubbles rising in a stagnant water are studied. 25% of detected bubbles are overlapping in the images. The overlapping object separation method has detected 83% of the groups, none of the individual bubbles are falsely detected as a group of bubbles and it has correctly separated 30 groups *i.e.* 68% of the bubble groups. Figure 5 shows the results for the sample images, *i.e.* the size distribution of bubbles and average velocities of bubbles in different size classes.

Figure 6 shows the results of the same set of images, calculated with a basic bubble recognition method, but more images are analyzed. The same computation time is consumed in the both analysis. The basic bubble recognition method can analyze much more samples and increase its accuracy by statistical approach, but still some errors remain. The axial velocities of bubbles in Figure 5 correspond to the values from literature, while the axial velocities analyzed with the basic bubble recognition method (in Figure 6) deviate much more **[14]**.

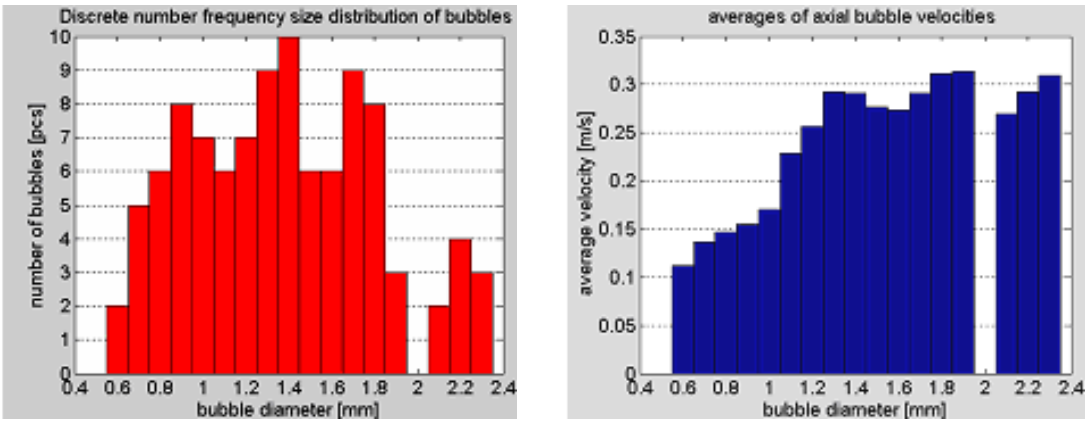

Figure 5. The size distribution and average axial velocities of bubbles in different size classes calculated with the overlapping object separation method.

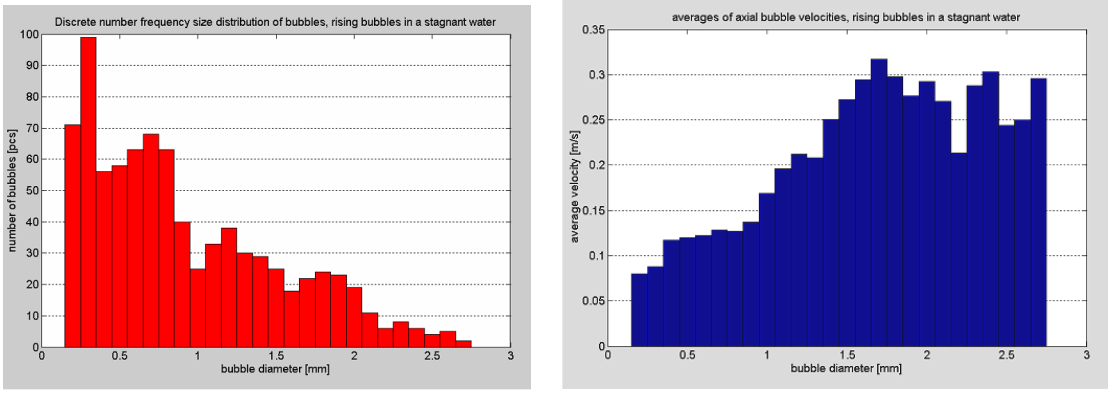

Figure 6. The size distribution and average axial velocities of bubbles in different size classes calculated with the basic bubble recognition method, with more samples than in Figure 5.

Data handling

After detecting the objects with a object recognition method and finding the object pairs with a PTV algorithm, the object properties can be averaged over two images and a rotation parameter can be calculated, defined as the difference of object orientation angles between the image frames. The remaining objects, which lack a proper pair, and objects on the edges of the field of view are also included in the analysis but without any velocity information.

The analysis records the following properties of the dispersed phase objects: object label, area (mm^2), centre point coordinates (mm), projected area diameter (mm), object's absolute velocity u/v/U (m/s), the instant fluid velocity at the centre of object u/v/U (m/s), object's relative (i.e. slip) velocity u/v/U (m/s), object's relative Reynolds number (-), slip angle (rad), the properties of an ellipse fitted to the object: major and minor axis (mm), orientation angle and aspect ratio. Also Eötvös number, Froude number and the Weber number can be measured for each object. Notes: Every property is calculated in sub-pixel accuracy, so the results are not restricted to discrete image pixel values. The projected area diameter of the object is the diameter of the circle whose area equals the projected area of the object.

3.6.4 Estimation of the fiber orientation

Orientation distribution of non-spherical particles is crucial in many applications of multi-phase flows **[15]**. Anisotropic orientation distribution may result from particle-fluid interaction or external forces. Also the consequences of particle orientation are many folds ranging from turbulence modulation to particle deposition efficiency. This part deals with the orientation of wood fibers in pulp-suspension flow, which has an application in paper manufacturing. Initial stages in the process of paper manufacturing are governed by the fluid mechanics of wood fiber - water suspension, which is non-Newtonian in nature. Fiber orientation in the flow proceeding the formation of the paper web has direct effect on the properties of the final product. Thus the fluid mechanical control of fiber orientation is important. A method for direct estimation of local orientation distribution of non-spherical particles is described here. Experiments are conducted in a converging channel, which creates a constantly accelerating base flow **[16]**. The flow is illuminated with back lightning by a halogen light source and a CCD-camera is used to record fibers in the flow. An image processing algorithm is used to determine the orientation of fibers in each part of the image. Typically several hundred fiber images are exposed in one position after which the camera –system is transferred to another position. The fiber concentration in present measurements is 0.01% and four streamwise locations are measured. From the image analysis point of view, there are two classes of fiber images which need different kind of treatment when estimating the orientation. In the first class, each fiber can be identified individually and the orientation determined for each fiber. This condition is related to very low fiber concentrations or application of so-called tracer fibers, which can be optically filtered from the other fibers. Two fibers falling on top of each other always produce some ambiguity in this type the analysis.

In the other class, several fibers can cross each other and the aim is not to look at individual fibers, but to estimate the orientation function over specific spatial area. Fiber

images are analyzed block-wise with Hough-transform resulting local orientation distributions. The idea of applying Hough-transform is that when the direction of the line of integration matches with the orientation of a fiber, large value for the integral is expected. Resulting Hough-transform plane is processed into a more compact form in which one can find peaks corresponding to individual fibers. The procedure is repeated for each block in one image after which next image is analyzed. As a result one obtains a matrix of local orientation distributions over a 2D region of interest. This is the method used in following examples.

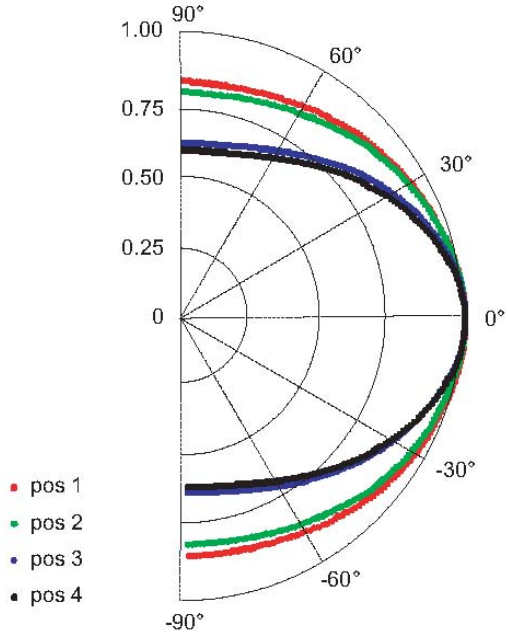

Figure 7. Development of mean orientation function in accelerating suspension flow.

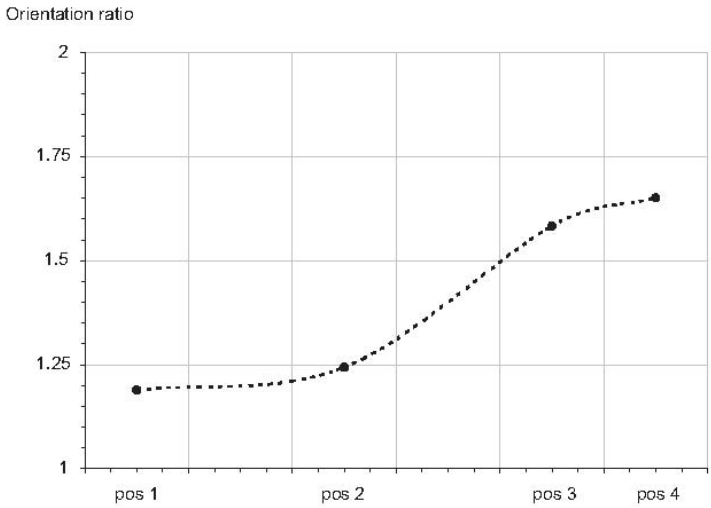

Figure 8. The ratio between the streamwise and transverse orientation at different locations in accelerating flow. Position 1 (Pos 1) is in the beginning and the position 4 at the end of the contraction.

Figure 7 presents the development of the mean orientation function as the suspension flows through the accelerating section. These mean orientation functions result from averaging both in space and time, i.e. over the entire image area and set of 500 images, respectively. Functions are normalized by the value in the main orientation direction. The ratio between the magnitude of the streamwise, which is now the main orientation direction, and transverse orientation as a function of the streamwise location is plotted in Figure 8. These results clearly show that the fibers align in the streamwise direction as the flow passes through the contraction. Also the standard deviation of the main orientation angle, i.e. the angle with maximum magnitude of

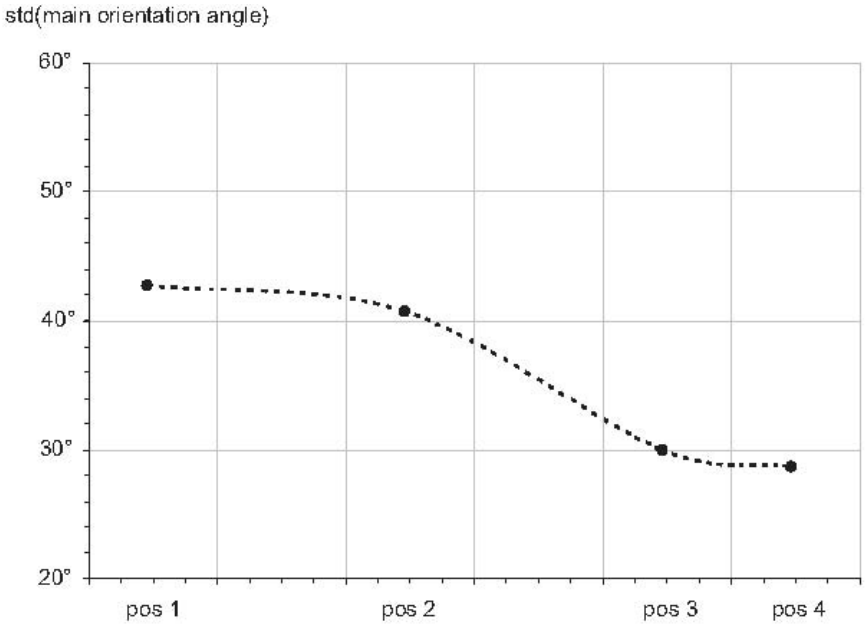

Figure 9. The standard deviation of the main orientation angle at different locations in accelerating flow.

orientation, can be computed from the instantaneous orientation maps. This value plotted as a function of the streamwise position is presented in figure 9. As the orientation ratio increases also the variation in the orientation angle decreases.

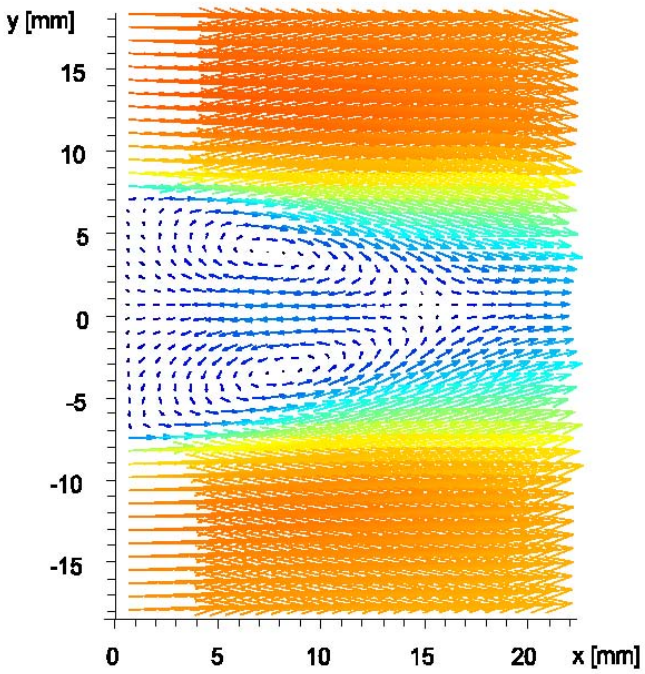

Figure 10. The mean flow pattern after the trailing edge of a flat plate.

The second case is used to study the effect of strong shear on the orientation function. The mean flow pattern around the trailing edge of a plate is presented in figure 10. A recirculation region is developed after the body. The mean velocity field is measured by particle image velocimetry. Figure 11 shows the main orientation angles in the wake.

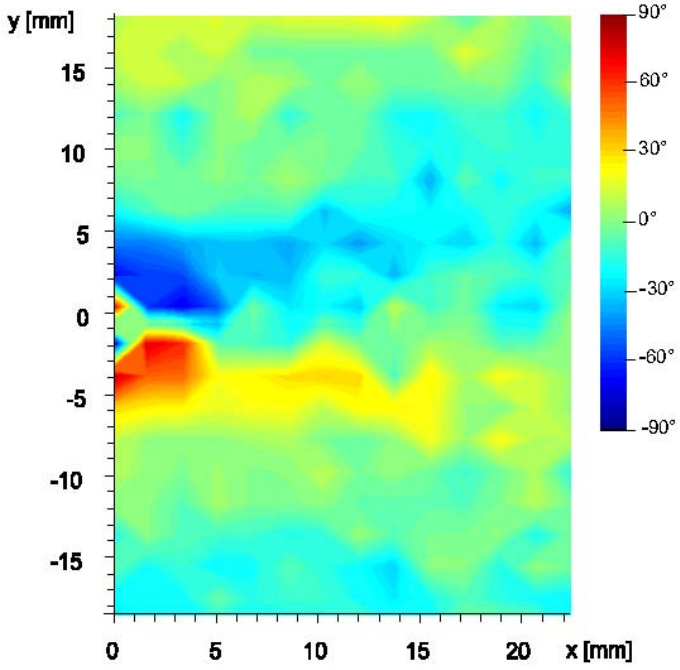

Figure 11. Main orientation angles in the wake.

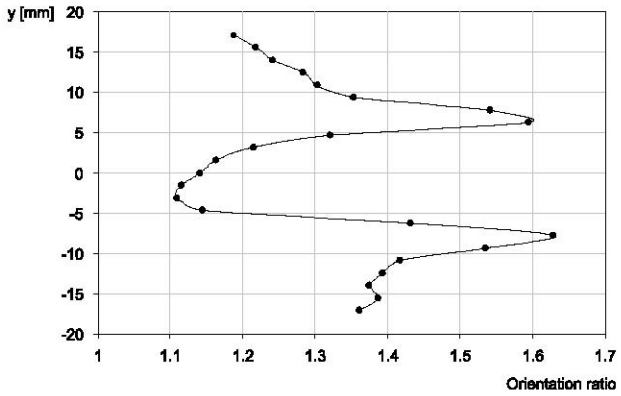

Figure 12. The orientation ratio profile in the y-direction along a line just behind the trailing edge.

Both shear layers are high-lighted by orientation deviating from the mean flow direction. Right behind the trailing edge the fibers are mainly transversely oriented, but this result should be considered together with figure 12. This figure presents the orientation ratio profile in the y-direction along a line just behind the trailing edge. Now, the orientation ratio is computed between the maximum and minimum values in the mean orientation function. The angle of the maximum orientation is the angle indicated in figure 11. The shear layers are obvious also from the orientation ratio. Surfaces of the body and associated shear layers result in a narrow orientation distribution. Close to the center line of the wake, the orientation is rather isotropic, even if the main orientation angle is close to the transverse direction.

3.6.5 Some applications

3.6.5.1 Turbulent bubbly flow measurements in a mixing vessel with PIV

The turbulent bubbly flow in air-water and CO_2-butanol dispersions in a cylindrical mixing vessel is studied in **[13]**. The highly three-dimensional turbulent flow field and the long optical paths to the measurement plane lead to challenging measurement conditions. The results reveal good agreement with the measured quantities and reality **[8, 9]**. The results point out valuable information of the studied process. Further studies are done in a same mixing vessel equipped with a Rushton turbine **[9]**. The results shown here are 5 mm above the Rushton turbine, where the flow accelerates downwards to the turbine. The results with two rotation speeds: 400 rpm and 250 rpm, are compared. The turbulence intensity of the fluid flow is about 60% in both cases. A set of 500 images is recorded in both cases, in which 18000 bubbles are detected with 400 rpm and 5000 bubbles with 250 rpm. The velocity PDFs of bubbles and fluid flow are shown in Figures 13 and 14. Positive directions are axially downwards and radially to the center of the vessel.

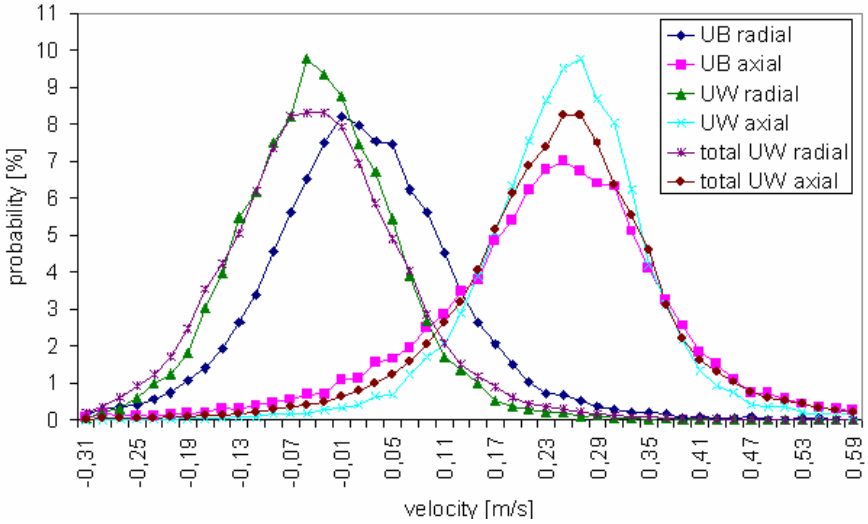

Figure 13. The velocity PDFs of bubbles and fluid flow with a rotation speed of 400 rpm.

There is a clear slip velocity between bubble-phase (UB) and liquid-phase (UW) in radial direction due to virtual mass effects caused by centrifugal acceleration. The axial velocities match well, because the pressure drop in the turbine region defeats the buoyancy force of small bubbles. There are two velocities for fluid flow: one is measured from the whole fluid flow field (total UW) and the other is the PDF of interpolated velocities on the center points of the bubbles (UW). Figure 15 shows the average axial and radial relative velocities of bubbles versus bubble size. Average bubble size is about 0.6 mm. Measurement results show clear correlation between the average relative velocities of bubbles and the rotation speed. Axial relative velocity of the bubbles is also highly dependent on the bubble size.

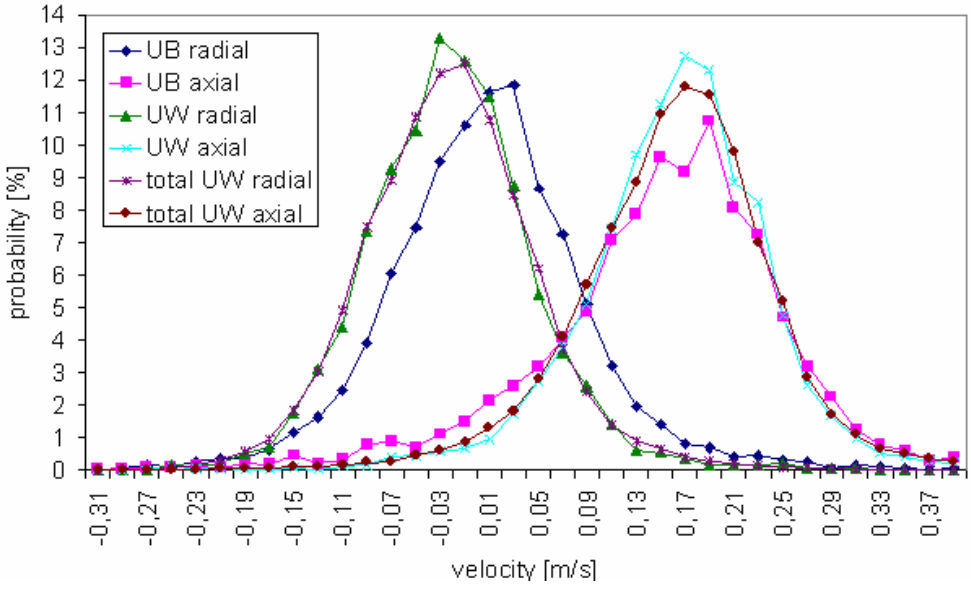

Figure 14. The velocity PDFs of bubbles and fluid flow with a rotation speed of 250 rpm.

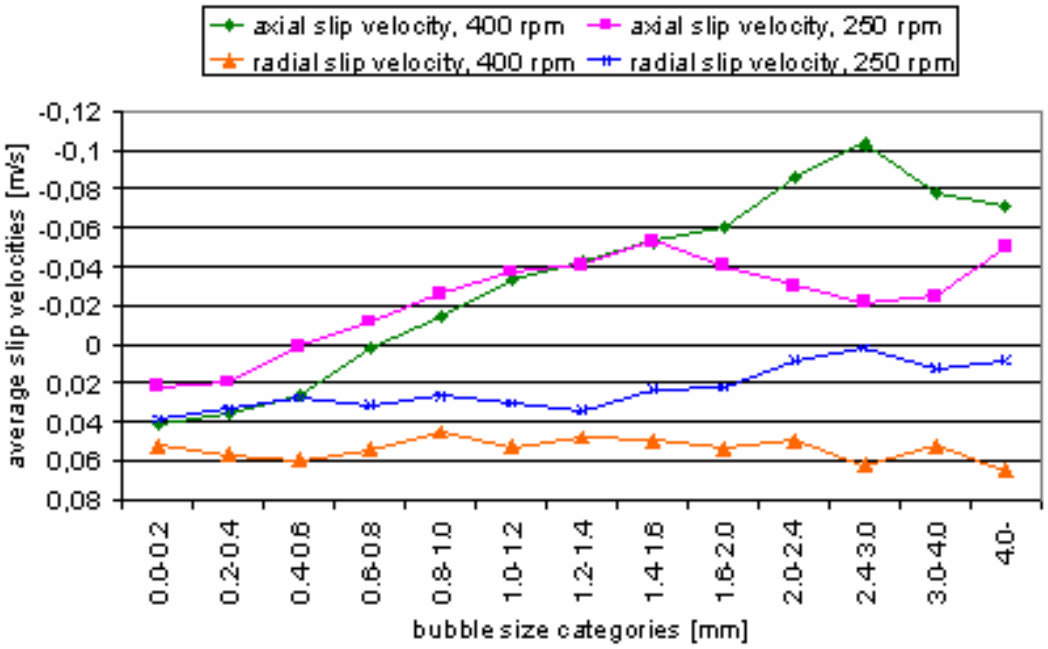

Figure 15. The average axial and radial slip velocities of bubbles versus bubble size.

3.6.5.2 Turbulent bubbly flow in the outlet pipe of a centrifugal pump

The aim of the study is to use the Direct Imaging method to study dense bubbly flows and to measure bubble size distributions in a turbulent bubbly flow in the outlet pipe of a centrifugal pump **[4]**. A digital camera and a pulsed back-light are used to detect bubble outlines. Algorithm employs an overlapping object separation method and an ellipse-fitting method. This technique finds only the sharp, in-focus, individual bubble images and detects their size with high accuracy. The three-dimensional volume of a bubble is approximated from two-dimensional images and the local gas void fraction is derived considering the effective thickness of the measurement volume. The void-fractions measured by DI technique are compared with the results of a microwave concentration measurement device providing good correspondence of results until the gas void-fraction of 0.5%. For larger gas void- fractions, the DI method clearly underestimates the gas void-fraction. This is due to overlapping of bubbles in the image, which leads to the decrease of the effective bubble detection area in the image.

3.6.5.3 Characterization of turbulent flow and floc morphology in a flocculation process: PIV/Digital imaging experiments

This study concerns the flocculation of an untreated lake water in a mixing vessel using an iron-salt as a hydrolyzing coagulant **[13]**. The aim of this study is related to three

topics: 1.) Measuring the flow field in the vessel and studying its mixing properties and turbulence quantities. 2.) Studying the flocculation and disintegration of organic

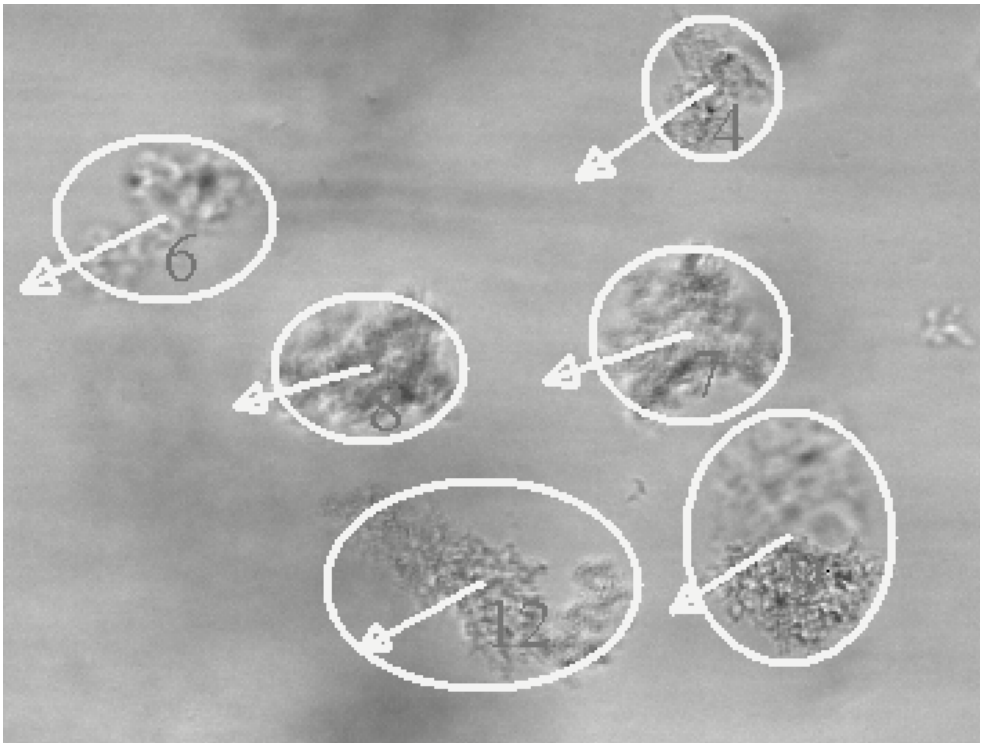

Figure 16. The image of flocculate particles with white arrows showing their measured velocities.

contaminants. 3.) Relating the flow dynamics to the growth rate and disintegration rate of flocs. An extensive single phase 2D-PIV analysis is carried out to determine the inhomogeneous turbulent flow fields in the whole mixing vessel with various turbine rotation speeds (30–400 rpm). The velocity fields and turbulence quantities are resolved for various turbine phase angles by synchronizing measurements with the turbine. Digital imaging with a pulsed back-light is used to detect the particle outlines. A typical image of flocculate particles can be seen in Figure 16.

The sizes and velocities of the flocculent particles are measured and the growth rate, disintegration rate and the time-wise change of the size distribution of flocs are derived. The velocity Probability Density Functions are plotted for each floc size category in order to determine the dynamic behavior of flocs in a turbulent flow. The interaction between turbulence and break-up of flocs is derived finding a clear correlation between the change of maximum Reynolds stresses in the turbine discharge zone and the change of characteristic floc size in the flow.

3.6.6 Velocity field post-processing methods

The flow velocity measurements before the arise of the PIV-technique were restricted only to a few individual simultaneously sampled points in space. Only during the last few years, studies on instantaneous and time-mean 2D velocity fields acquired with PIV have realized different novel methods to understand the structure and the phenomena of turbulence. In many industrial applications there is a growing need for more and more detailed information of the flow. The instantaneous values of various flow quantities, as well as their distribution and transient variation, are essential in order to understand and evaluate the role of turbulence in diverse processes, including single and multi-phase flows (applications related to combustion, mixing and flocculation are particularly interesting).

Despite the usefulness of the information obtained by examining individual momentary fields for different quantities computed from PIV-fields or the time-mean turbulence quantities (TMTQ) based on measurements, these solutions do not satisfy all the needs. In this part few examples of detection and statistical analysis of turbulent structures and instabilities are presented.

3.6.6.1 Spectral and correlation analysis on the characterization of vortex shedding

The estimation of vortex shedding frequency and energy are demonstrated in a wake of flat plate, which is subjected to mechanical vibration **[19]**. Due to a fluid-structure interaction resulting from the plate vibration, vortex shedding at the plate trailing edge occurs in cells. This cell structure is analyzed by SPIV (x-z -plane) and conventional PIV (x-y -plane) techniques. The coordinate-system and measurement planes are presented in figure 17.

Many fundamental features of the shedding process controlling the wake of a flat plate can be derived from the time-mean statistics. However, much of the potential of the PIV-technique lies in other tasks than determination of the mean-flow pattern and turbulence level. A natural extension to this is the estimation of frequency and amplitude of the vortex shedding.

Figure 17. The location of the measurement planes after the plate tip.

2D-velocity fields allow – with some limitations – the estimation of space-correlation functions and spectra. Already a visual examination of 2D PIV-data lets certain deductions of the spatial scales and nature of the flow to be made. Three examples of instantaneous velocity fields in the x-z –plane are presented in figure 18.

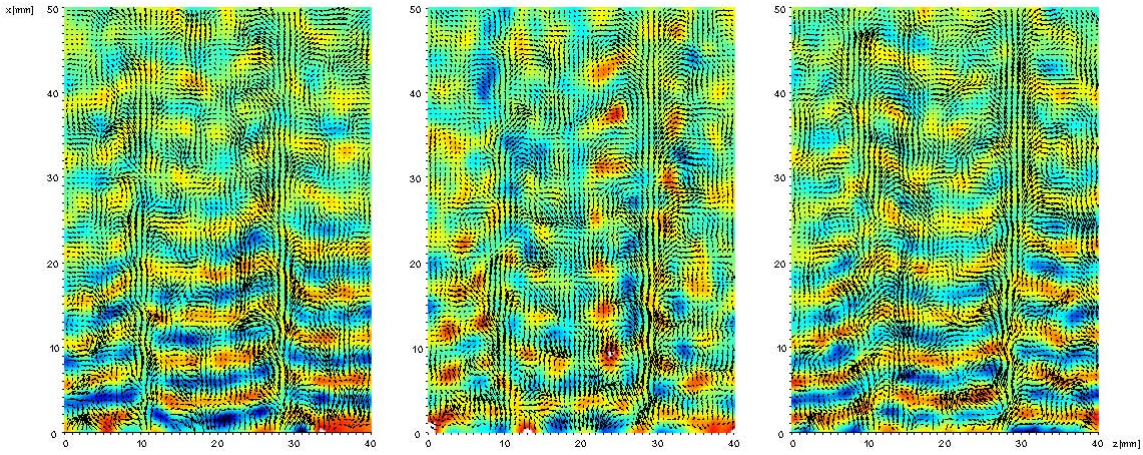

Figure 18. Examples of instantaneous velocity fields in the x-z-plane.

Vectors indicate the in-plane components (u_x and u_z) and the contours on the background correspond to the u_y-component. Working in the spatial domain compensates poor time-resolution inherent in standard PIV-technique. By choosing appropriate measurement resolution, the spectral analysis proves to be an efficient tool to estimate periodic phenomena, for example vortex shedding after the plate. Spectral and space-correlation analysis can be performed for any velocity component. The requirement of data stationariness is not strictly fulfilled in the wake of the plate, since the flow is accelerating and the wake is developing to the downstream direction. This may broaden the spectral and correlation peaks slightly, but does not invalidate the methods, because these trends are not too severe.

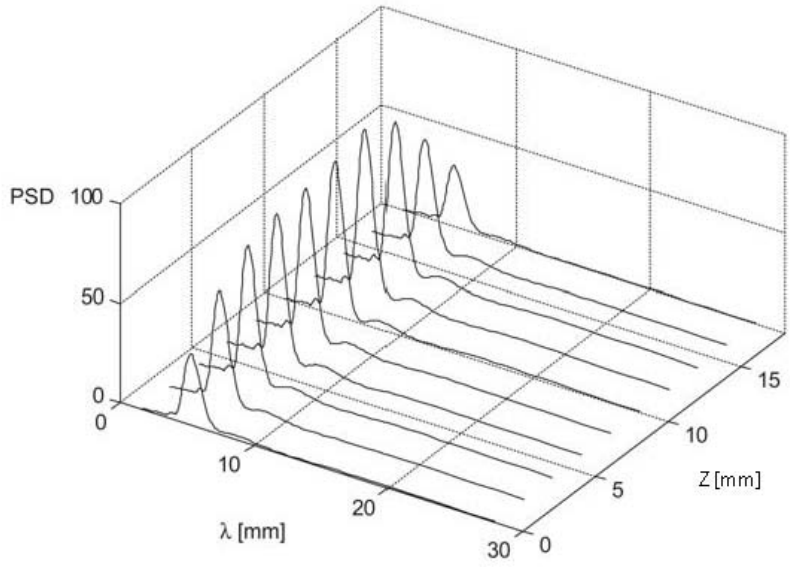

Figure 19. Spanwise variation of streamwise spectra for u_y computed from the data measured in the x-y-plane.

The basis for the analysis is an instantaneous velocity field. The Power Spectral Density (PSD) can be computed for each column or row in the vector field. Now primarily the stream wise (x) spectra as a function of the span wise (z) location are of interest. For the data measured in the x-y-plane, this simply means that each measured z-location is processed individually. First instantaneous spectra for each velocity field are computed and then all the instantaneous spectra are averaged to establish the mean-spectra for that particular location. Next the results from separate data sets are gathered to the same plot depicting the spanwise variation. This kind of plot is presented in figure 19. The variation of the spectrum over one cell for u_y-component is shown. Remarkably lower energy of shedding is detected on the edges of the cell compared to the energy levels inside the cell (profiles in the middle of the plot). The edges of this cell structure, or actually the areas between the cells, are referred as nodes in the following and the locations in the middle of the cell are called as anti-nodes.

For the SPIV-data there is another way to proceed. The spectra are computed for each streamwise column in an instantaneous field resulting instantaneous spectra at different spanwise locations. This is done for all the instantaneous fields and finally the mean-spectra is computed as an average for the set of 500 instantaneous spectra. Columns are analyzed separately and thus it is possible to plot directly the spanwise variation of the spectra. Figure 20 portrays the spectra for each velocity component in the wake symmetry plane. The first picture contains spectra for u_x, the second one for u_z and the last one for u_y. Spanwise variation of energy related to the vortex shedding is evident. The dominant shedding wave-length is clear for all the components and there is no remarkable variation of the shedding frequency across the span. The energy of the u_z

component is associated to the shedding on the borders of the cells. Similar conclusion can be drawn for the u_x- and u_y -components, even though the energy is more homogeneous distributed over the cell.

To further scrutiny the differences of vortex shedding in the node and anti-node positions, instantaneous peaks of the spectra (i.e. peak energy and the wave-length related to the peak) are plotted in figure 21. This analysis is carried out to support the conclusion made

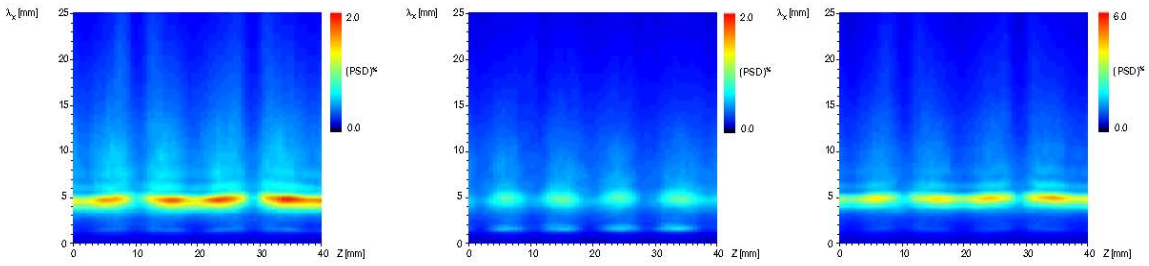

Figure 20. Spanwise variation of the streamwise spectra for all the velocity components (from left to right: ux, yz and uy). Computed for the SPIV-data.

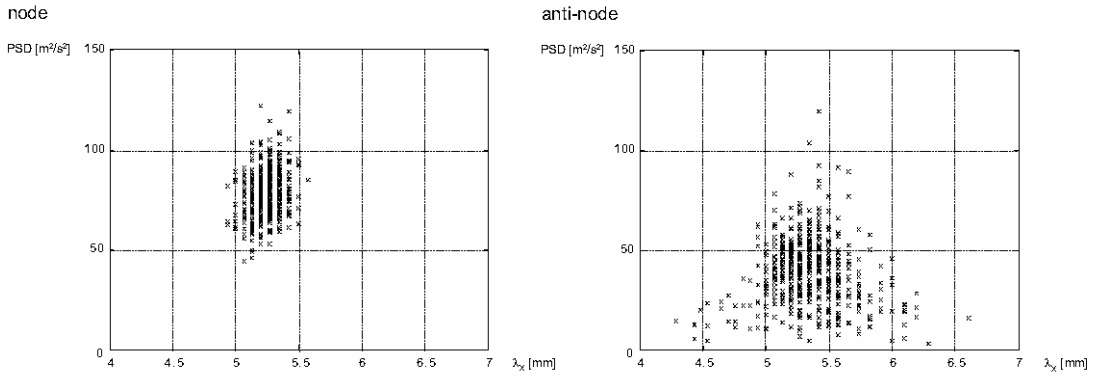

Figure 21. Distribution of energy vs. wavelength of instantaneous spectra for u_y in an anti-node (left) and node (right).

from instantaneous example fields presented in figure 18. The scatter plots show that in the anti-node, the energy or frequency of the vortex shedding do not vary much from time to time. This is not the case in the node, where instantaneous energies and wavelengths are spread out to a larger area. The shedding is not totally absent, since some spectra show rather high energy at about 5mm wavelength. But in most cases the energy is less than half of the typical value in the anti-node. Another conclusion from these plots is that there is some variation in the instantaneous shedding frequency, but it does not show for example intermittent switching between two separate frequencies, which is sometimes observed in forced vibration. In the computation of the 2D space-

correlation function, the information about the span wise location is neglected. The auto-correlation maps presented in figure 22 are not normalized at the zero-lag and thus the correlation maxim also indicates the energy of shedding. However, more interesting is the pattern found in the correlation maps, which is produced by instantaneous flow structures. Maximum correlation in the stream wise direction is achieved at the distance of 5mm

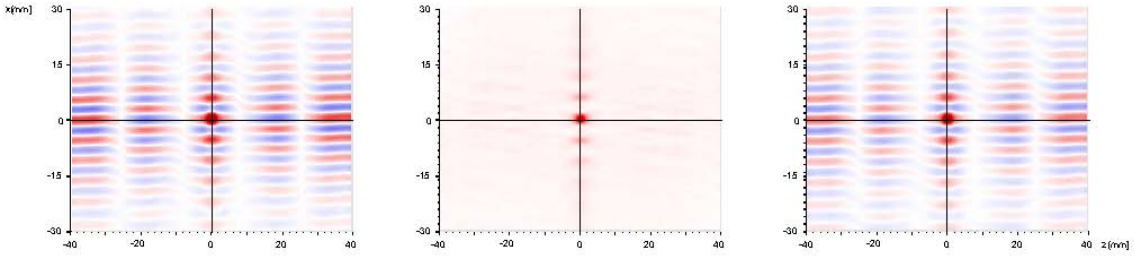

Figure 22. 2D-space auto-correlation maps for all the velocity components (from left to right: ux, yz and uy) computed from the SPIV-data.

(distance from red to red). This is naturally the wavelength produced also by the spectral estimation. In span wise direction, maximum correlation is found at the distance 38mm, which corresponds to the distance over two cells. There is actually a negative correlation at the distance of 19mm, which indicates that two neighboring cells shed vortices with 180 degree phase shift. This issue is identified already from the examples provided in figure 5, but the fact that correlation map shows such a clear pattern, proves that this is a very well organized structure and not just an incident captured in some example fields.

3.6.6.2 Detection and analysis of coherent flow structures

Next, methods are developed to detect and analyze coherent flow structures from the PIV-data. These methods can be used for a wide range of problems, where the appearance of for example vortices, their scale, magnitude and other properties are of interest.

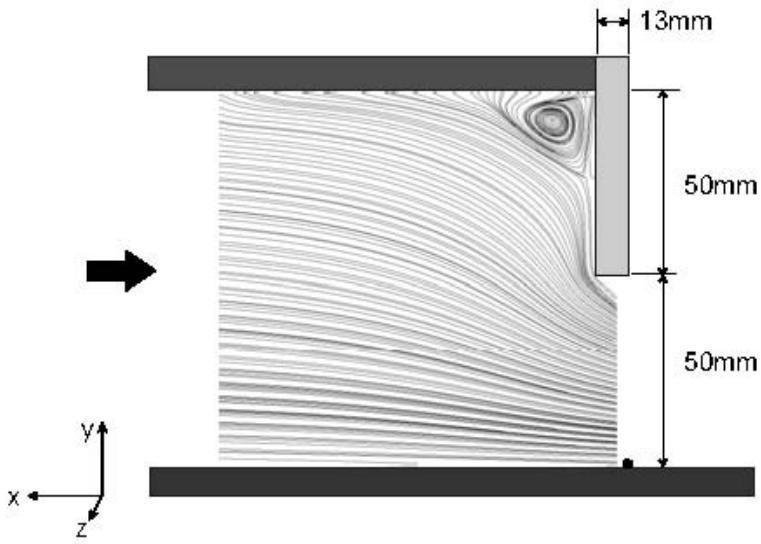

Figure 23. Design, dimensions and coordinate system of the experimental setup.

Now one example of using the detection of a vortex pair and subsequent conditional averaging based on vortex location is presented **[17], [18], [20]**. The flow inside a headbox nozzle is studied by reproducing the fundamental fluid dynamics in a very simplified geometry. The design, dimensions and the coordinate system related to the experimental setup are shown in figure 23. Experiments are performed only inside the nozzle to understand the role of flow instabilities and large-scale flow structures to the jet quality.

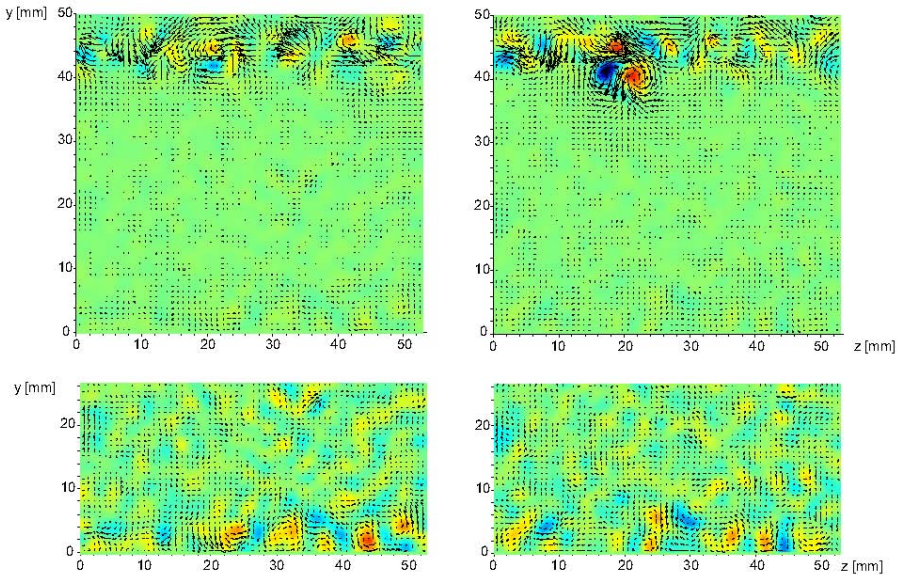

Figure 24. Two examples of instantaneous flow fields in the y-z-plane just under the step. Small windows represent the lower part of the field re-scaled to adduce the boundary layer structures.

Two instantaneous flow fields in the y-z – plane are presented in figure 24. Both fields are measured just under the downstream edge of the step. The uppermost frames cover the entire channel height under the step. The small frames on the bottom are cropped from the wall-region and re-scaled. This is done to visualize the boundary layer structures, which are almost an order of magnitude weaker than those present in the step shear layer. The contours on the background represent stream wise vorticity ω_x and the vectors velocity fluctuations according to the Reynolds decomposition. In the large frame the scale of vorticity is set to ±300 1/s and in the small frame to ±100 1/s. The first pair shows only weak activity beneath the edge of the step. On the bottom wall, the flow field appears to be quite smooth with some stream wise vortices. The second pair portrays a strong vortex pair in the step-shear layer and again rather weak vortex structures in the boundary layer.

To address the questions of the vortex generation and their time-scales in the step shear layer, PIV-data is used to produce a time-sequence of vorticity. This is performed by extracting one row of data in each velocity field and combining consecutive rows into a new plot with z-location on the x-axis and time on the y-axis. The camera frequency is only 10Hz, but since strong vortices remain at fixed positions over the period of several frames, estimation of the scale of the largest vortices can be deduced. Figure 25 presents three this kind of vorticity time-sequences. Time resolution is 0.1s and by using the mean convective velocity of 2.0m/s this corresponds to a spatial resolution of 0.2m. Even though it is not clear if vorticity that remains at a fixed location over several frames indicates a single vortex pair or a sequence of individual vortex pairs, which are triggered and born one after another, the vorticity forms extremely large-scale structures. In the figures the spanwise wandering of the vortices seems to be remarkable, but it has to be emphasized that it is only in the order of 20mm. On the other hand, the time-scale of the structures may be as large as 10 frames (1 second), which corresponds to 2m in length. Similar analysis in the boundary layer does not indicate any large-scale vortices.

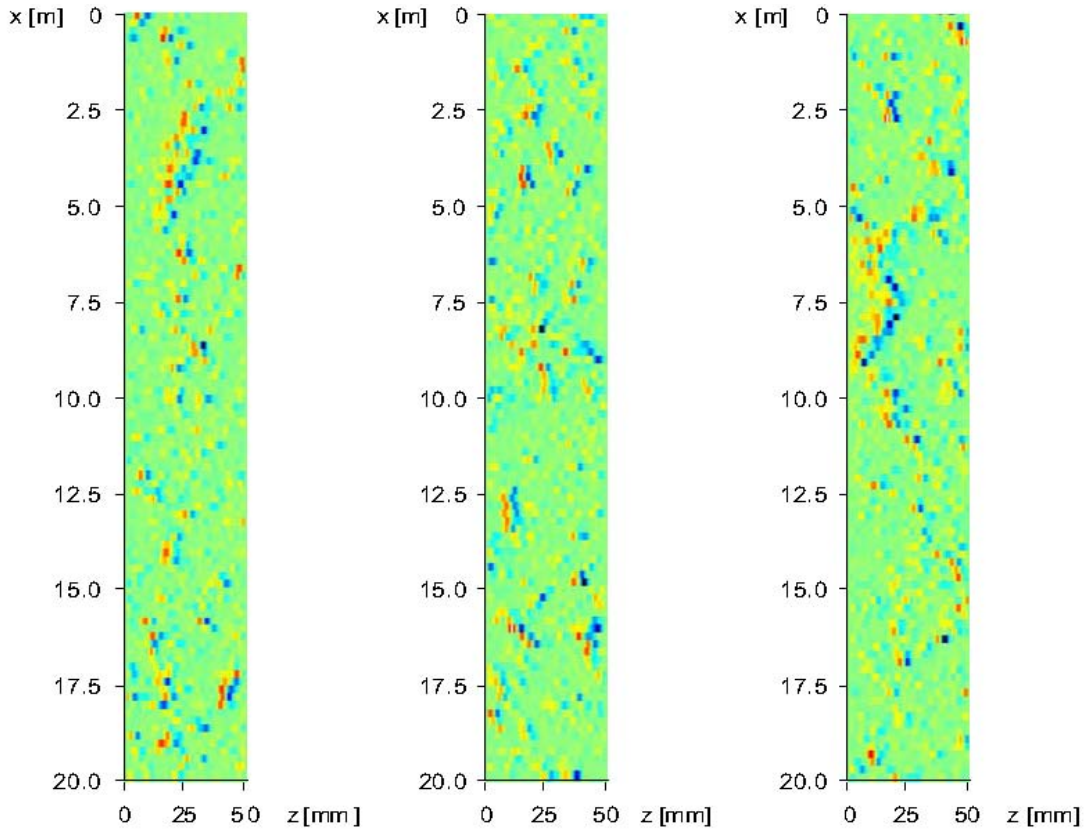

Figure 25. Three vorticity time-sequences in the step shear layer.

The important questions that originally motivated the present study is, what kind of interaction there is between the step shear layer and bottom wall boundary layer. The principal mode of interaction is naturally the acceleration due to the sudden contraction. But in addition to the mean flow pattern other modes of interaction are conceivable. The appearance of strong vortex pair close to the step might create a disturbance, which would affect the flow on the bottom wall. To study if this kind of mechanism could be found in the present case, conditional averaging is utilized to reveal if the occurrence of strong vortex pair in the shear layer induces something typical on the opposite wall. In each instantaneous field the magnitude of wall-normal velocity component is threshold along a spanwise line just under the step. Strong negative values signify down wash of fluid towards the bottom wall, which typically occurs due to streamwise vortex pairs. Using strong negative wall-normal velocity as the condition for averaging, a mean flow pattern presented on top the figure 26 is achieved. This flow field is established by cropping and storing a window with a size of 25x10mm^2 centred to the location of maximum down wash and averaging over the collected samples. Every time a sample is cropped, the flow pattern on the opposite wall is stored too. This way the conditional average- and rms-fields for the boundary layer can be established. Conditional average of the boundary layer flow pattern is presented also in the figure 26.

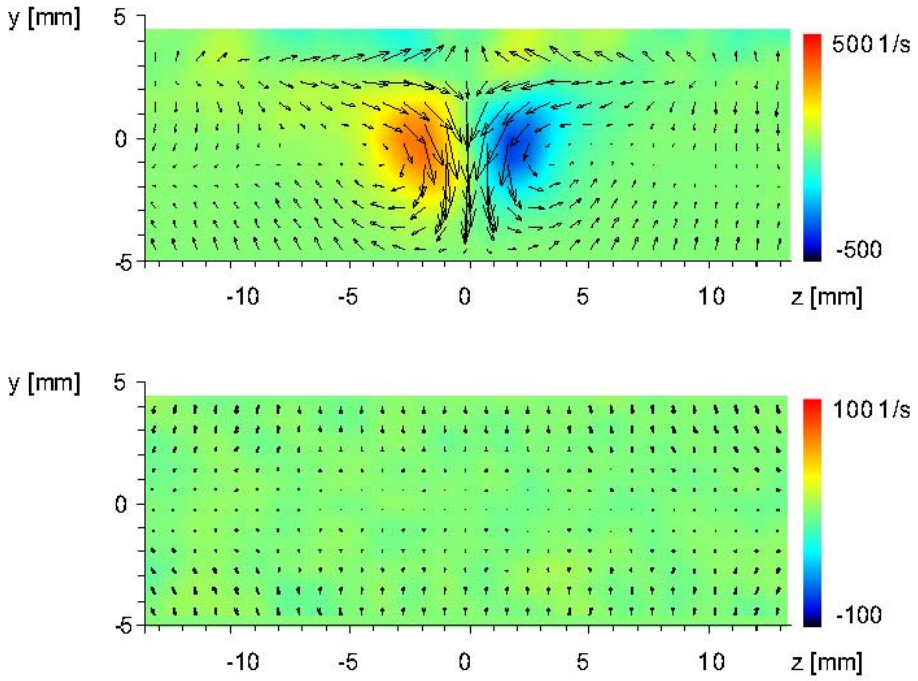

Figure 26. Conditionally averaged flow patterns related to a strong negative velocity under the step.

This analysis does not bring forward any secondary flow structure or even increased turbulence energy compared to randomly sampled locations. To further verify this result some sequences, in which streamwise vortex pair remains at a constant location over several frames are analysed by visually inspecting the vorticity fields close to the bottom wall. The results from this study do not either reveal any characteristic structure related to long streamwise vortex pairs on the opposite wall.

3.6.7 References

[1] Kataja, M., Luukkainen V.-M. & Saarenrinne, P. Monifaasivirtausten mittaukset. Esiselvitys. VTT tutkimusraportti, ENE22/T0096/99.

[2] Frey, A. Lasikanavamittauslaitteiston käyttöönotto ja testimittauksia. TTKK, Energia- ja prosessitekniikka, Raportti. 18 p., 2001.

[3] Pärssinen, T. Vesikiertolaitteiston käyttöönotto ja testimittauksia. TTKK, Energia- ja prosessitekniikka, Raportti. 20 p., 2001.

[4] Honkanen, M., Stoor, T., Saarenrinne, P. & Niinimäki, J. Turbulent bubbly flow in the outlet pipe of a centrifugal pump. Int. Journal of Multiphase Flow, 2004b. (Submitted)

[5] Honkanen, M. Turbulent Multiphase Flow Measurements with Particle Image Velocimetry: Application to Bubbly Flows. MSc thesis, Tampere University of Technology, Finland, 2002a.

[6] Honkanen, M. & Saarenrinne, P. Turbulent bubbly flow measurements in a mixing vessel with PIV. 11th Symp. on Applications of Laser Techniques to Fluid Mechanics, 7–10 July 2002, Lisbon, Portugal, 2002b.

[7] Lahti, M. PIV-kuvien kuvankäsittely. ProMoni-projektiraportti TTY, Mittaus- ja informaatiotekniikka. 21 p., 2001.

[8] Honkanen, M. & Saarenrinne, P. Calibration of PIV to measure local void-fractions in bubbly flows. Pivnet 2/ ERCOFTAC workshop, Lisbon, 5.–6. July, 2002c.

[9] Honkanen, M., Saarenrinne, P. & Larjo, J. PIV methods for turbulent bubbly flow measurements. The Particle Image Velocimetry: Recent improvements. Proceedings of the EUROPIV 2 Workshop on PIV. Stanislas, M, Westerweel, J. 6 Kompenhans, J. (Eds.). Springer Verlag. 2003c. (In print)

[10] Laakkonen, M., Honkanen, M., Saarenrinne, P., Keskinen, K. & Aittamaa, J. Local bubble size distributions, gas-liquid interfacial areas and gas holdups in a stirred vessel with Particle Image Velocimetry (PIV) technique. Chem. Eng. Sci. Draft, 2003. (In review)

[11] Honkanen, M. Particle Recognition with Image Processing Methods. Final report of a joint project with LaVision GmbH, 2003b.

[12] Honkanen, M. & Saarenrinne, P. Multiphase PIV method with Digital Object Separation Methods. 5th International Symposium on Particle Image Velocimetry, Pusan, Korea, 23.–16.09.03, Paper 3249, 2003d.

[13] Honkanen, M., Saarenrinne, P. & Reunanen, J. Characterization of turbulent flow and floc morphology in a flocculation process: PIV/Digital imaging experiments. 3rd International Symposium on Two-Phase Flow Modelling and Experimentation Pisa, 22–24 September 2004, 2004a.

[14] Honkanen, M. PIV-tekniikan laajennus turbulenttisen monifaasivirtauksen mittauksiin ja sen sovellus kuplavirtauksiin. ProMoni-vuosiraportti 2002, TTY, Energia- ja prosessitekniikka, 2003a.

[15] Eloranta, H. Kuitujen ja turbulenssin välinen vuorovaikutus virtauksessa – kirjallisuusselvitys. Promoni-projektiraportti, TTY, Energia- ja prosessitekniikka. 16 p., 2004.

[16] Eloranta, H., Saarenrinne, P. & Pärssinen, T. Estimation of Fiber Orientation in Pulp-suspension Flow In: the Proc of The 3rd International Symposium on Two-Phase Flow Modelling and Experimentation, Pisa, Italy, September 22th – 24th, 2004, 2004.

[17] Eloranta, H., Hsu, T.Y., Wei, T. & Saarenrinne, P. A PIV study on the interaction between a forward-facing step and turbulent boundary layer; Application to a papermaking machine. Presented in the Application of Laser techniques to Fluid Mechanics, Lisbon, Portugal, July 10th – 13th, 2003, 2002.

[18] Eloranta, H., Hsu, T.Y., Wei, T. & Saarenrinne, P. On the interaction between a forward-facing step and turbulent boundary layer. Presented in the Third International Symposium on Turbulence and Shear Flow Phenomena, Sendai, Japan, June 25–27, 2003, 2003.

[19] Pärssinen, T., Eloranta, H. & Saarenrinne, P. Analysis of vortex shedding in a splitter plate wake by DPIV. Advances in Turbulence X. Andersson, H.I. & Krogstad, P.-A. (Eds.). CIMNE, 2004.

[20] Pärssinen, T., Eloranta, H. & Saarenrinne, P. Formation of streamwise vortices in a flat-plate wake. Pivnet T5/ERCOFTAC SIG 32 5th Workshop on PIV, Lisbon July 5–2002, 2002.

[21] Saarenrinne, P., Honkanen, M., Eloranta, H. & Pärssinen, T. Multiphase flow measurement with PIV and Digital Imaging, Final report of the ProMoni-project. TUT Energy and Process Engineering, Report 175. Tampere. 80 p., 2004. (Available at: http://www.tut.fi, from which to >Yksiköt>Laitokset>Energia- ja prosessitekniikka >Tutkimus> Virtaustekniikka)

3.7 Fast pressure measurement in a free jet

Janne Poranen, Antti Koponen, Pasi Selenius and Juha Salmela
VTT Processes, Pulp and Paper Industry

3.7.1 Background

In a papermaking process the fluidisation level of fiber suspension at filtration stage is known to have direct influence on final paper quality. To understand the basic mechanisms how a fluidisation level is achieved and how it affects on the paper properties both theoretical and experimental research is needed. At the present, there are very few measurement techniques available that could provide useful information on the fluidisation level in realistic process conditions. Therefore, new measurement techniques are needed in order to gain better understanding of the connection between fluid flow conditions and final paper structure. The work done in this project is based on the assumption that, for a fibre suspension at a consistency exceeding the sedimentation consistency, intensity of pressure fluctuations is indicative of fluidization level of the suspension. In this project, a new device for measuring fast pressure fluctuations and thereby to characterize the fluidization state of fibre suspensions has been developed. Of special interest is the measurement of pressure fluctuations in a free jet.

3.7.2 Methods

There are several challenching designing principles that a measurement system and probe geometry for fast pressure measurement for fibre suspensions should fullfill. The flow field should not be excessively disturbed and the sensing area should not be blocked by fibres. The sensor should be small, fast and sensitive enough to resolve the relevant frequency band of pressure fluctuations. To fulfill these requirements, a fast piezoresistive pressure sensor (Entran, EPIH-111-1B-1Z2/V10/L1M) was installed at the tip of a fin-like probe such that the sensing area of diameter 1.4 mm could be positioned normal to the direction of the fluid flow (see Fig. 1). Such an assembly makes it possible to use very sensitive sensors required for measuring very small pressure fluctuations. The electronics (pre- and main amplifier) was particularly designed for measuring pressure fluctuations, i.e. it cuts out the static pressure level of the measurement signal.

In particular, we aim in measuring and analysing quantitatively the pressure fluctuations in the free jet in different process conditions. Such an analysis necessitates a very robust and repeatable measurement procedure. One of the key issues for accurate

measurements is the ability to set the position of the sensor accurately. With the developed sensor controlling unit the position of the sensor can be controlled in X,Y and Z direction with an accuracy of 0.1 mm. The controlling and measurement software is highly automated and based on the LabView-software.

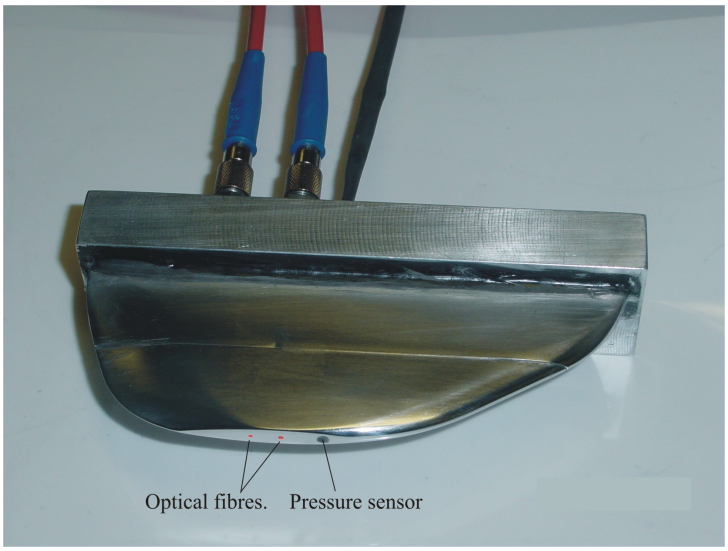

Figure 1. The fast pressure sensor mounted in a fin shaped probe. Also shown are the optical fibres assembled in the same probe.

3.7.3 Results and applications

The developed measurement technique was first tested in a free planar jet produced by a slice channel nozzle with a slit outlet of height 14 mm (see Fig. 2). The sensor was used to through-scan the jet in the vertical z direction in steps of 0.5. At each z position, 10^6 pressure readings were collected using a sample rate of 100 kHz. The pressure sensor was located 100 mm downstream of the slice opening. The velocity of the free jet was varied from 15 m/s to 33 m/s. Inside the flow channel divider plates of different length were used.

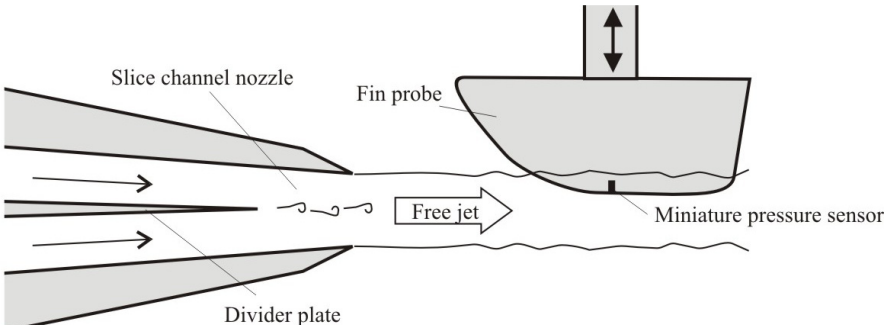

Figure 2. Schematic illustration of the setup for measurement of pressure fluctuations in a two-dimensional free jet.

Figure 3 shows the measured power spectra of fluctuating pressure for jet speeds of 18, 25 and 33 m/s. These measurements were done in the surface layer of the jet where the flucutuations appear to be maximal. A clear peak corresponding to about 20 mm wavelengths with the used jet speeds can be seen in every spectrum. This size scale coincides with the results of independent measurements of the vortex structures shed by the trailing edge of the divider plate inside a similar slice channel.

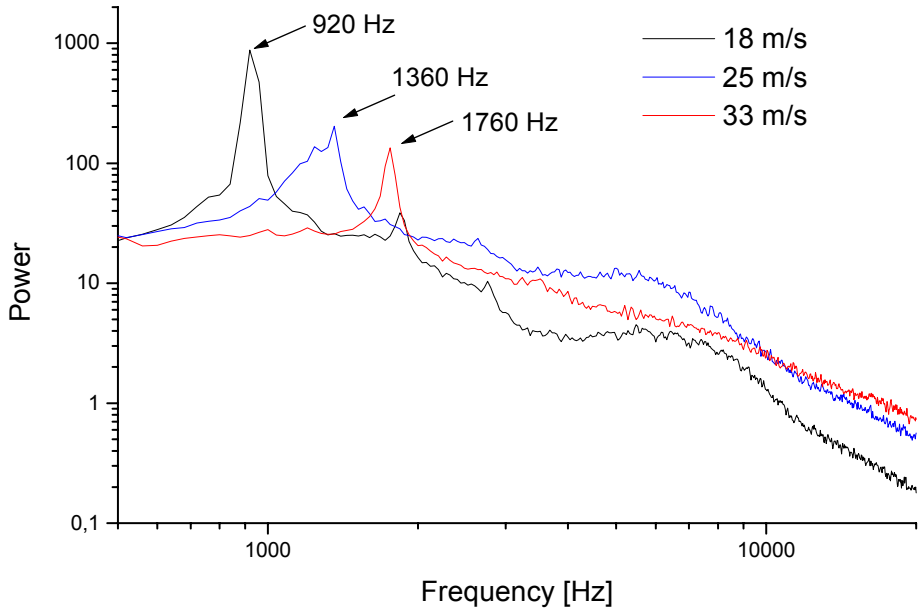

Figure 3. Measured power spectra within the surface layer of a planar jet at three different jet speeds.

Figure 4 shows the total (integrated) power as a function of z -directional position across the jet for the three jet speeds. The first measurement point is located well above the jet surface, the sensor not in contact with the flow. The pressure fluctuations (sound within air) are very weak in that area, z ~ 0–5.0 mm. The highest intensity of the signal is found at the surface region, z ~ 5.0–15.0 mm depending on the flow speed. This behaviour arises mainly due to the rough surface structure of the jet whereby the probe is only intermittently in contact with the jet. The up-stream turbulence generated by the boundaries of the slice channel may, in principle, add to fluctuations in this region as well. This contribution is assumed to be small in the present case, however. In the inner part of the jet the probe is in continuous contact with the fluid and the measured signal reflects the turbulent state of the jet. The increase of total intensity of fluctuations and the thickness of the rough surface layer with increasing jet speed is clearly visible in Fig. 4. Notice that the measurement is not extended here down to the lower surface of the jet and no corresponding surface peak is visible. The preliminary tests indicate that measurement in conditions where the probe tip approaches the bottom surface may be disturbed by increased deflection of the flow downwards by the fin geometry, and even by flow separation.

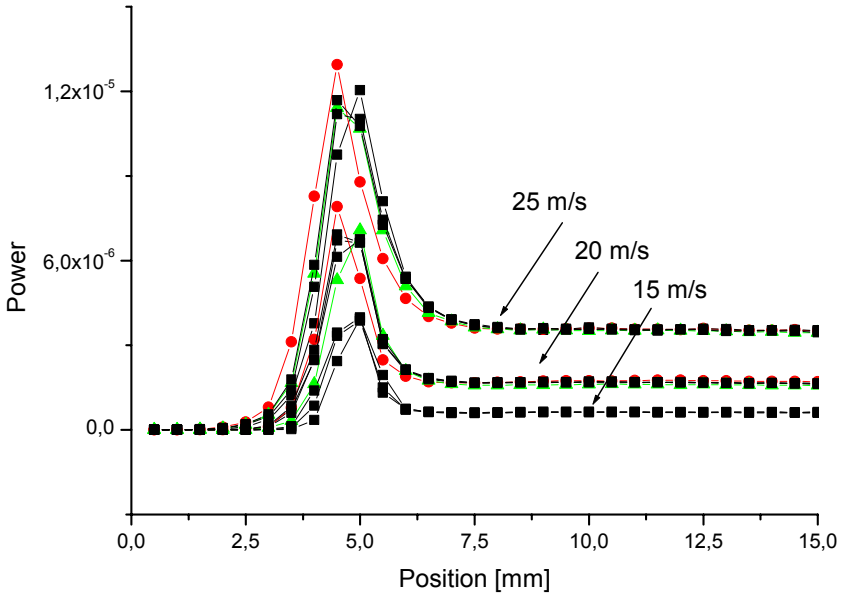

Figure 4. Pressure intensity profiles as a function of position in z-direction (vertically across the planar jet) at three different jet speeds. For each speed, shown are results from three independent measurements.

The effect on the measured intensity of the consistency (solids mass fraction) of fiber suspension is shown in Fig. 5. As expected, the overall intensity degreases with increasing consistency – obviously a consequence of enhanced dissipation, and perhaps also of attenuated production, of turbulence due to the presence of fibres. The origin of the intensity minimum just after the surface peak, visible in the results for the lower consistencies, is not fully understood. One possible explanation is incipient flow separation at the probe surface just upstream of the pressure sensor, which may happen especially in the absence of fibres and lead to an erroneous increase of pressure fluctuations in conditions where the probe is well inside the jet. No confirmation for this assumption has been found so far.

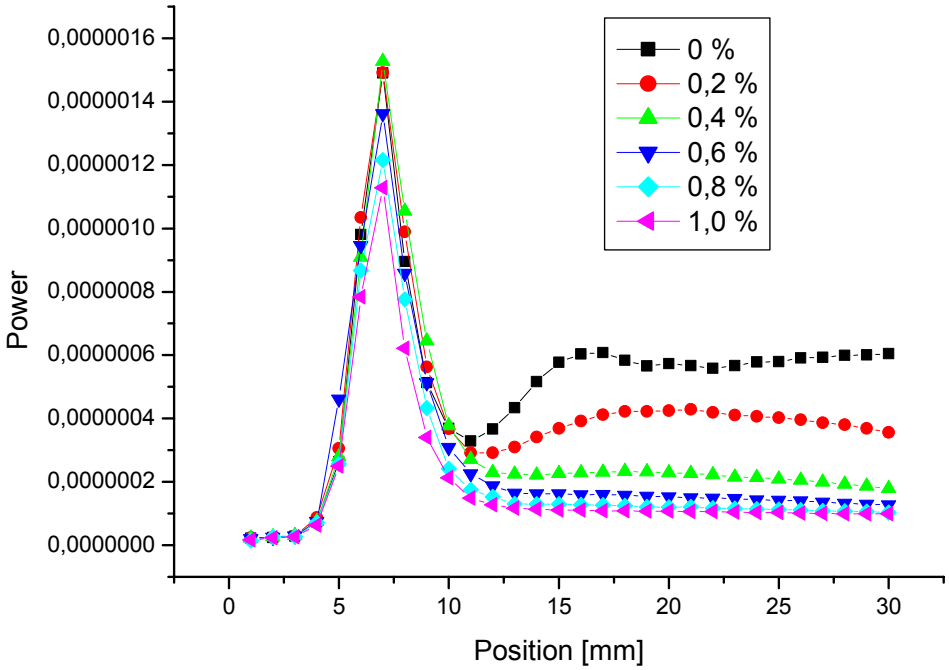

Figure 5. Measured intensity profiles as a function of measurement position in z-direction at fiber consistencies of 0, 0.2, 0.4, 0.6, 0.8 and 1.0 %.

3.7.4 Conclusions

During this project a novel technique for measuring fast pressure fluctuations of fibre suspension in closed channels and in free jets was developed. The technique has been tested in planar high-speed jets. In spite of the fact that disturbance caused to the flow by the probe can not be fully avoided, the method has proven useful in characterizing the turbulent state and the degree of fluidization of the suspension. The technique has already been used in several industrial projects. It provides new possibilities for studying details of e.g. paper-making process, in particular, the effect of flow condition in a free jet entering the former section on the structure of the final paper.

3.8 Fin probe for measuring stratified flows

Pasi Selenius, Antti Koponen and Markku Kataja
VTT Processes, Pulp and Paper Industry

The main goal of this part of the project was to develop a generic probe for studying details of stratified multiphase flows. In particular, applications would include stratified planar free jet of fibre suspension. To this end, a fin shaped probe with a specific symmetrical airfoil profile was constructed. The probe was equipped for three different measuring techniques, namely conductivity measurement, light back scattering measurement and close range imaging of the flow at the stagnation point (see Fig. 1).

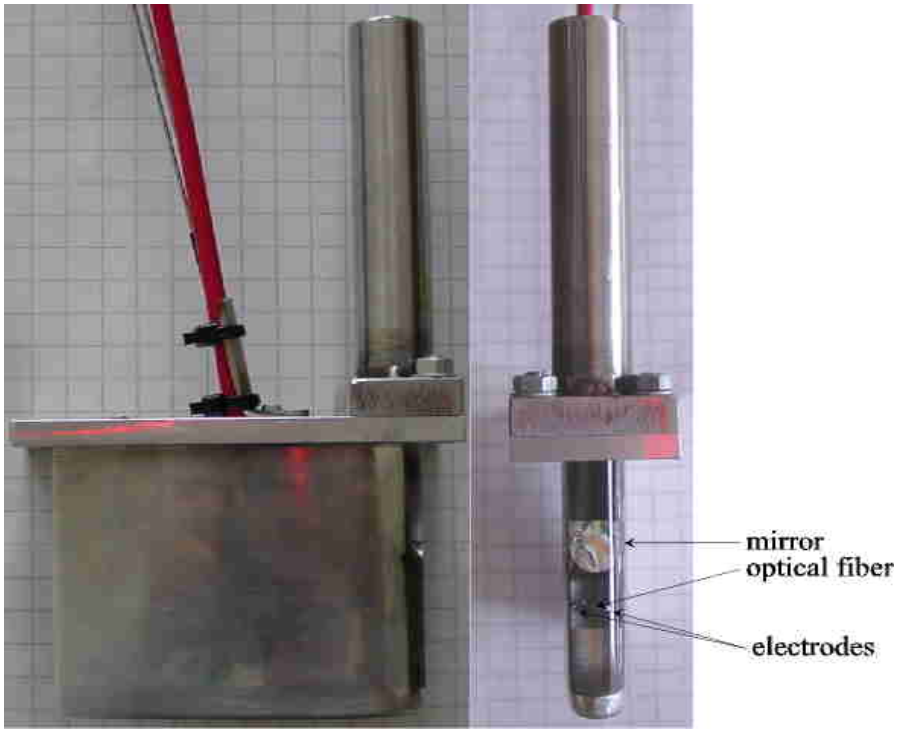

Figure 1. The fin probe constructed for stratified flow measurements. Also shown are the 45° degree mirror, two metal electrodes and an optical fibre embedded in the leading edge rod made of quarz glass.

The body of the probe was made of aluminium and machined in the shape of symmetric airfoil profile with maximum thickness of 12 mm. The leading edge was made of a quarz glass rod of diameter 10 mm, including a 45° mirror in the middle. The rod extends well beyond the probe body and was equipped with a special mount for illumination system and a CCD camera (see Fig. 2). The device thus allows imaging through the glass rod and mirror of the flow entering the leading edge stagnation point. In addition, two metal electrodes and an optical fibre were mounted on the leading edge just below the mirror. The horizontal distance between the electrodes is 4 mm and the

tip of the optical fibre is located in the middle of the electrodes (see Fig. 1). The single optical fibre is used to transport both incident and scattered light. Special electronics and an optical device including a 20 mW diode laser, beam splitting optics and a sensitive light detector were constructed to allow for fast, simultaneous conductivity and back scattering measurements.

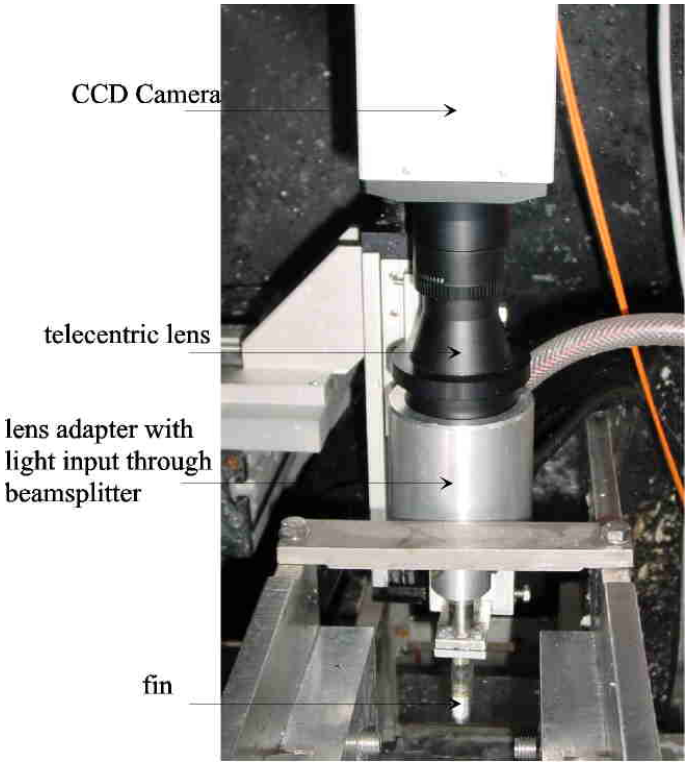

Figure 2. Fast CCD camera and telecentric lens adapted to the leading edge glass rod of the fin probe. The measuring system is mounted here on a travelling table in front of a slice channel nozzle producing a planar free jet (to emerge towards the probe from the nozzle slit located near the lower end of the image).

The probe geometry was tested using a planar free jet of pure water and of dilute fibre suspension. The assembly of the equipment is shown in Fig. 2. The geometry of the probe was found satisfactory in the sense that the flow remains attached to the fin close to the trailing edge and up to the maximum speed of 10 m/s available with the used flow line. Although fibre flocs intermittently hit the leading edge stagnation point, no long lasting blocking of the electrodes and optical fibre tip was observed. While some vertical flow appears along the leading edge, the fin probe geometry seems to disturb the flow mainly by deflecting it in the horizontal direction. Concerning the intended use of the probe in studying horizontally stratified flows, no exessive errors due to vertical mixing induced by the probe are to be expected.

The first scattering and conductivity measurement for calibration purposes were made using the setup show in Fig. 2, but without camera installed. Here, macroscopically homogeneous jet was used (i.e. no stratified structures present) . The thickness of the planar jet in the measuring point was approximately 15 mm and the probe was positioned such that the electrodes and the tip of the optical fibre were located in the middle of the jet in z direction.

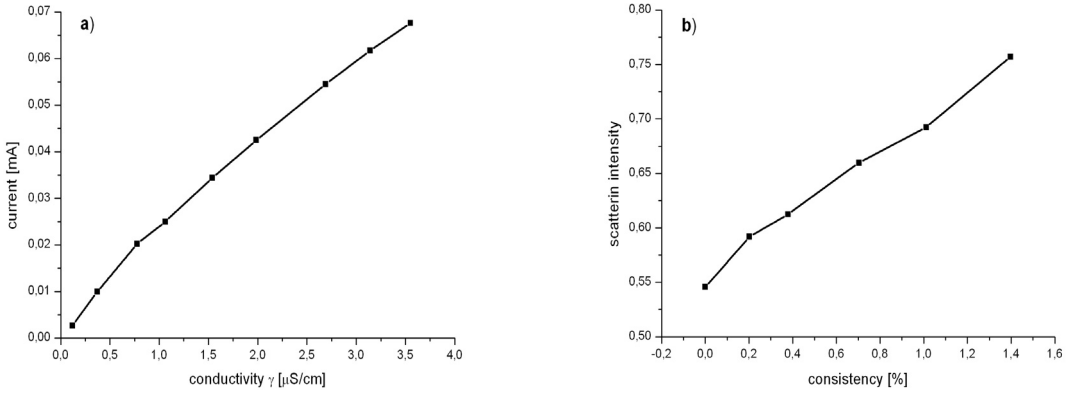

Figure 3. a) Measured current between conduction electrodes as a function of conductivity of the liquid. b) Intensity of ligh scattered from fibre suspension as a function of fibre consistency (in arbitrary units). Both measurements are done well inside a homogeneous planar jet of water salt solution (a) and fibre suspension (b) at jet speed 7 m/s.

Figure 3 a) shows the measured current between the electrodes at the leading edge of the fin probe (at a constant voltage) as a function of the conductivity of the liquid. The conductivity was altered by adding salt in the circulation and measured by a laboratory conductivity meter. Figure 3 b) shows the measured intensity of scattered light as a function of consistency of fibre suspension. The consistency is measured by weighing the amount of fibres added and mixed in the flow circulation. The result indicate nearly linear response of the measured conduction current and back scattering intensity to conductivity and fibre consistency of the fluid, respectively.

The second test measurement was done using a stratified jet produced by leading fibre suspension with added salt in the middle layer of the slice channel nozzle and pure water in top and bottom layers. Inside the slice channel, the layers were kept separated by lamellae extending close to the outlet slit. Figure 4 shows the measured profiles of time averaged conduction current and back scattering intensity across the jet at different jet speeds. The measurement was done approximately 100 mm downstream of the outlet. The position of the probe in the z direction was measured by an ultrasound displacement sensor. All the measured profiles indicate clearly layered structure of the

jet at measurement location. The conductivity profiles are somewhat wider than the scattering intensity profiles. This can be interpreted as an indication of higher dispersion of the liquid phase as compared to fibre phase. Slight widening of profiles indicating enhanced mixing with increasing velocity can also be observed. The results measured near the upper and lower surface of the jet may be affected by errors induced by vertical flow along the leading edge of the probe.

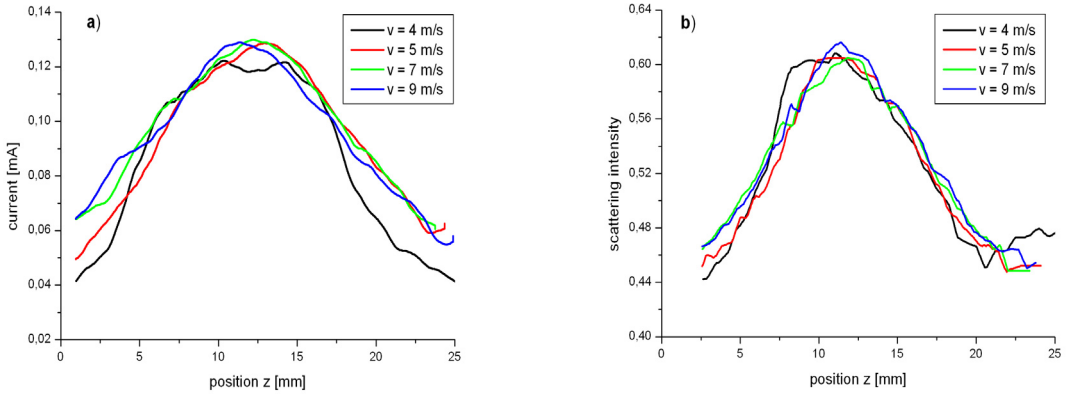

Figure 4. Filtered and averaged conductivity (current at constant voltage) and scattering intensity profiles across a planar stratified jet with fibres and salt added in the middle layer and pure water in outer layers.

The analysis of images obtained through the leading edge mirror was hampered by the very irregular illumination conditions caused by reflections from the fluctuating surface of the jet. Using this techniques requires further research and results from the preliminary measurements are not reported here.

3.9 Optical methods for fibre suspension flows 1: Mixing

Antti Koponen, Markku Kataja and Juha Salmela
VTT Processes

3.9.1 Introduction

Mixing in flow channels is a major activity for the chemical industry, and there is a wide variety of mixers available for mixing of liquids. One important option is jet mixing. Here one fluid, called *primary fluid*, is sprayed into *secondary fluid* from a small tube with high flow velocity. The analysis of the effectiveness of the mixing process is often tedious. Sampling is difficult, and although a transparent flow channel would be available, the interpretation of the images is not a straight forward task.

In this work we will show how light absorption can be utilized to solve the average concentration profiles in effectively 2D mixing processes. The new algorithm presented in this report makes this possible also for jet mixing.

3.9.2 Lambert-Beer law

According to the Lambert-Beer law, the intensity of monochromatic light decays in a dilute homogeneous solution of light absorbents and scatterers as

$$I(x) = I_0 \exp(\alpha c x). \tag{1}$$

Above, I_0 and I are the ingoing and out coming light intensities, x is the distance light has traveled in the solution, and c (unit $\mathrm{kg/m^3}$) and α (unit $\mathrm{m^2/kg}$) are the concentration and the absorption coefficient of the absorbents or scatterers. In the experiments presented below these are either birch pulp or blue food dye.

Absorption coefficients are constant for low concentrations. When concentrations increase, light usually starts to behave diffusively, and the validity of the equation (1) decreases. In practice, this is seen in the decrease of the absorption coefficients. Absorption coefficient depends often strongly on the light wavelength. In Figure 1 we show as an example the absorption coefficient of blue food dye produced by Roberts Ltd. The wavelength dependence of the absorption coefficient is not always significant. Pulp, for example, scatters and absorbs light approximately equally for the whole spectrum of visible light.

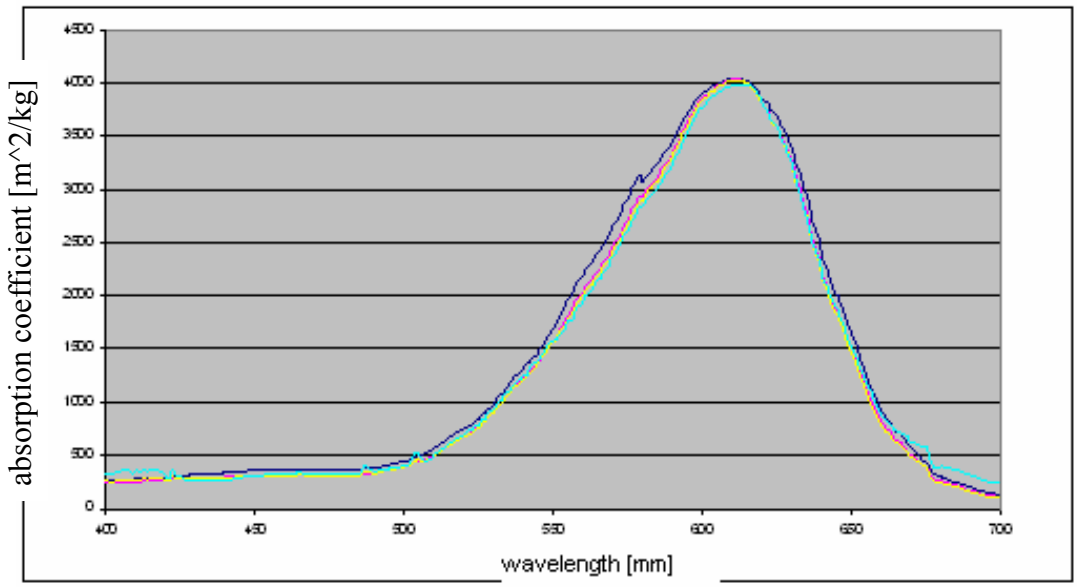

Figure 1. The absorption coefficient as a function of wavelength for blue food dye produced by Roberts Ltd. Four concentrations c = 0.10, 0.050, 0.0250 and 0.010 kg/m3 have been used. We see that the effect of concentration on the absorption coefficient is small with the given concentrations.

In practical applications the light intensity distribution should be taken into account. Then, we can define the *effective absorption coefficient* (see reference [1] for the details):

$$\alpha_{eff} = -\frac{1}{\xi}\log\left(\frac{1}{I_0}\int_0^\infty i\exp(-\alpha\xi)d\lambda\right), \tag{2}$$

where $id\lambda$ gives the intensity of the incoming light for the interval $[\lambda, \lambda + d\lambda]$, $\alpha = \alpha(\lambda)$, I_0 is the total intensity of the incoming light and $\xi = cx$ is the grammage of the absorbent. So, α_{eff} depends both on the grammage and the intensity spectrum of the incoming light. In this work, however, we will simplify our analysis by using directly Eq. (1). This approach works well, when ξ is small, or when α and the intensity of the incoming light i vary only slightly as a function light wavelength.

3.9.3 Determination of concentration profiles by light absorption

Equation (1) can also be used in a case in which concentration is a function of position x. Then, c in Equation (1) represents the average concentration of the absorbent or scatterer. We get

$$c_{ave}(y,z) \equiv \frac{1}{L}\int_0^L c(x,y,z)dx = \frac{1}{\alpha L}\log\frac{I_0(y,z)}{I(y,z)} \tag{3}$$

where L is the thickness of the medium (see also Figure 2).

The use of Equation (3) was tried in an experiment, where water and 1.0% birch pulp were mixed in an effectively 2D geometry. The experimental setup is shown in Figure 3. The intensity image $I(y,z)$ (constructed from several images taken from different positions) is shown in Figure 4. The concentration profile $c_{ave}(y,z)$ calculated from this image is shown in Figure 5.

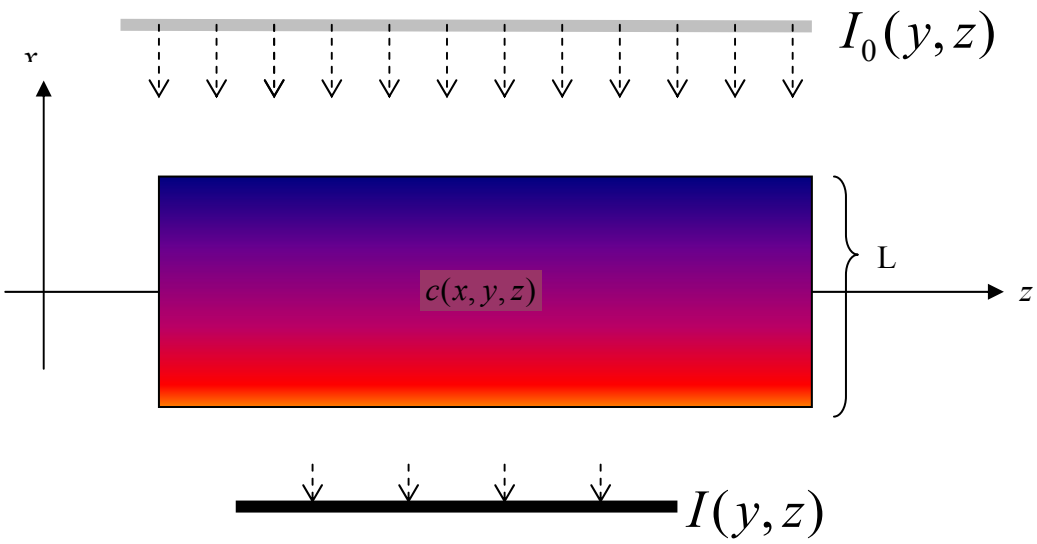

Figure 2. The basic experimental setup for determining the average concentration field $c_{ave}(y,z)$. The absorbent concentration profile is c(x,y,z), and the ingoing and out coming intensity profiles are $I_0(y,z)$ and I(y,z), respectively.

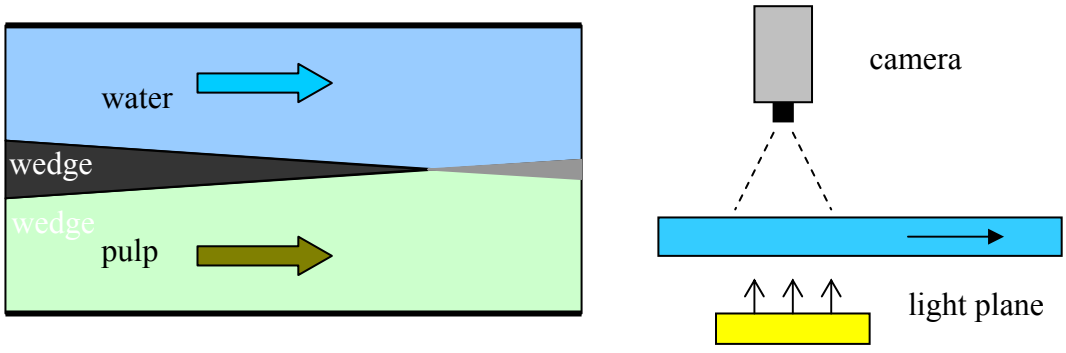

Figure 3. 2D mixing experiment of water and 1.0% birch pulp. The tube cross section is rectangular.

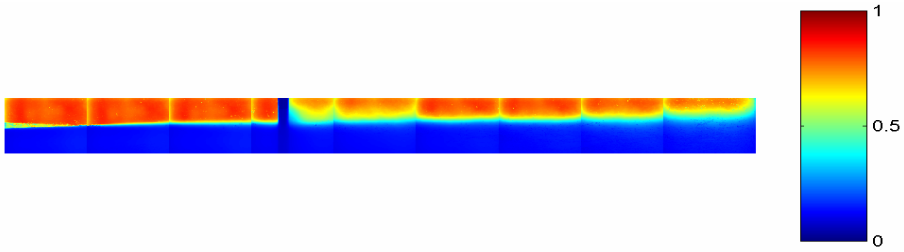

Figure 4. Average light intensity profile $I(y,z)$ of the 2D mixing experiment. The image has been composed of several smaller images. The width of the light plane has been a little too small, which is seen in the low light intensity areas between these images. The blue horizontal rectangular area in the middle of the tube is an ultrasound transmitter, which is seen to disturb the concentration profile. The image width is 30 mm and length 300 mm.

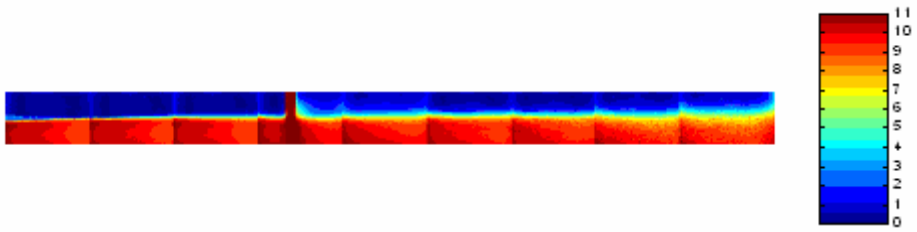

Figure 5. Concentration profile $c_{ave}(y,z)$ (expressed in kg/m^3) of the pulp in the 2D mixing experiment. The initial pulp consistency was 10 kg/m^3. The profile has been calculated from Figure 4 using Eq. (3).

The use of light absorption for determination of 2D consistency profiles was also demonstrated with measurements of the response of the headbox dilution system. Here, the fluid concentration was diluted locally, and the free jet was imaged with a similar setup to the one shown in Figure 3. The sensitivity of the measurements was studied by varying the average consistency of the pulp. From this data one could get a calibration coefficient which can be used to transform the gray levels of the ccd-images into true consistencies (see Figure 6). We see from Figure 6, that the sensitivity of the consistency measurement is about 0.05%.

In the actual dilution measurements the average consistency was 1.0%. The cd consistency profile was disturbed by opening one dilution tube. The streak thus created was so wide that it had to be imaged by using two camera positions. The final results after removal of the illumination profile are shown in Figure 7. The dilution effect is clearly seen in the grayscale profiles, and the two profiles obtained from different camera positions are seen to match very well with each other.

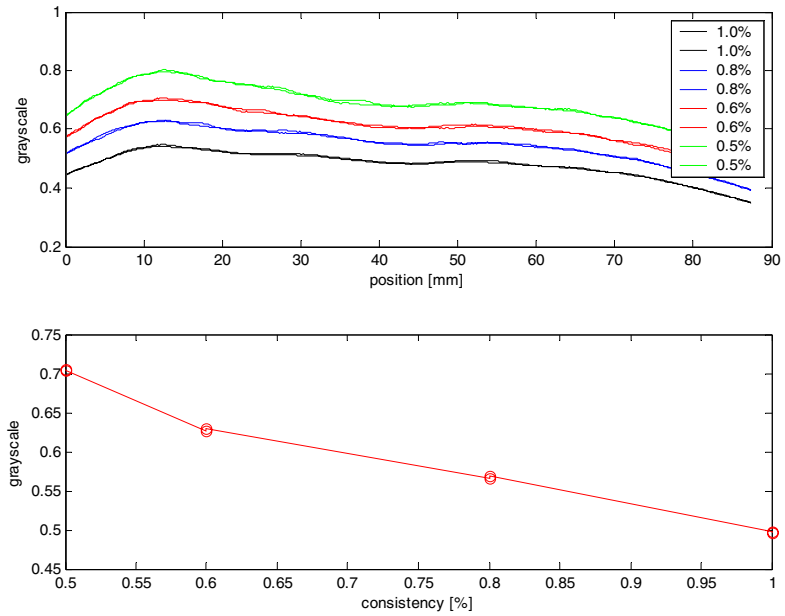

Figure 6. Above: Grayscale levels of the free jet in the cd-direction with various pulp consistencies. (Two measurements have been performed for each consistency.) Below: The calibration curve of the gray levels.

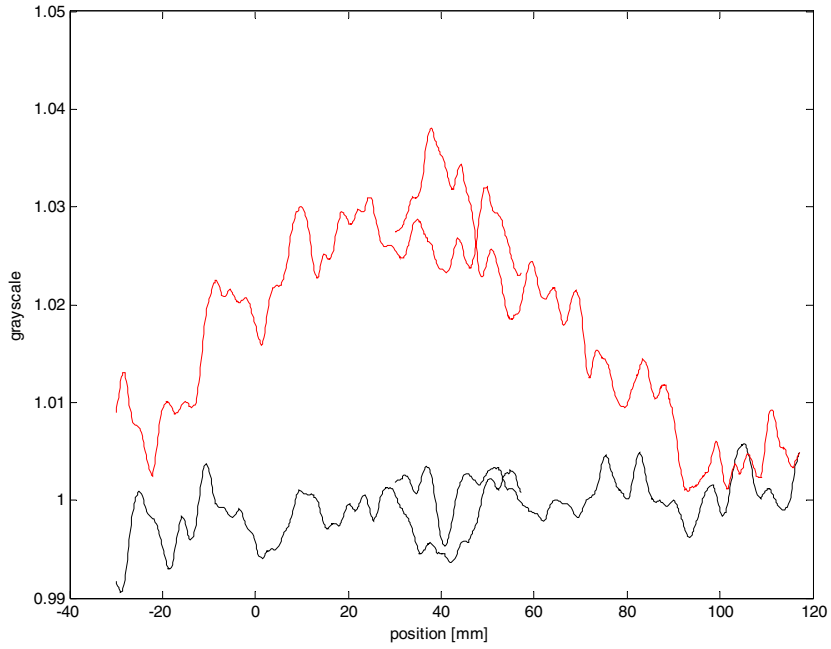

Figure 7. The cd grayscale profiles of the free jet with (red) and without dilution (black).

3.9.4 Determination of the concentration profile for cylindrically symmetric mixing

In many industrial processes, two fluids are mixed using jet mixing. Here one fluid, *primary fluid*, is sprayed into *secondary fluid* from a small tube with higher flow velocity. The average mixing area is cylindrically symmetric. (See Figures 8 and 9)

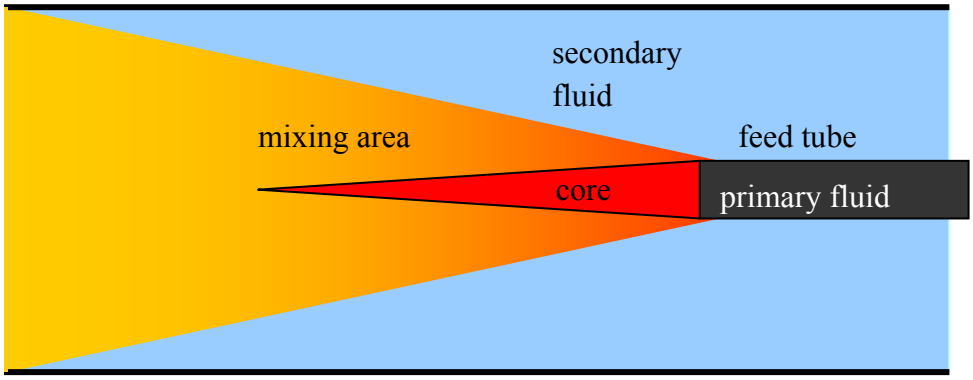

Figure 8. In jet mixing, primary fluid is sprayed into secondary fluid from a small tube with higher flow velocity. The average mixing area is cylindrically symmetric.

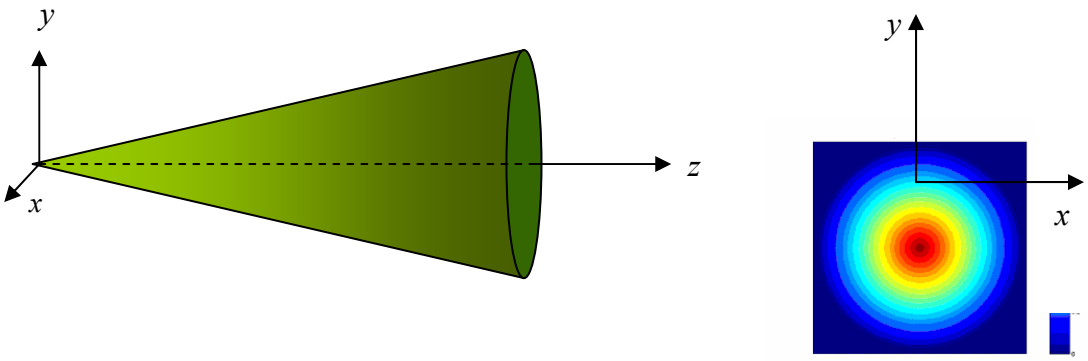

Figure 9. Cylindrically symmetric jet. The feed tube is located in the origin and flow direction is to the positive z-direction. The average concentration of the primary fluid is $c = c(r,z)$.

One can use an experimental setup analogous to Figure 2 for getting the average concentration profile $c_{ave}(y,z)$ of the primary fluid in jet mixing. However, if one utilizes the cylindrical symmetry, the real average concentration profile $c = c(r,z)$ can also be obtained. The numerical algorithm that was developed for this purpose is rather complicated. It is presented in detail in Ref. [1]. The basic idea is to divide each cross section of the mixing area into small circles (see Figure 10). Now, rays of light travel

through a different number of these circles, and one can solve the concentration profile by using Eg. (1) in each of these circles separately.

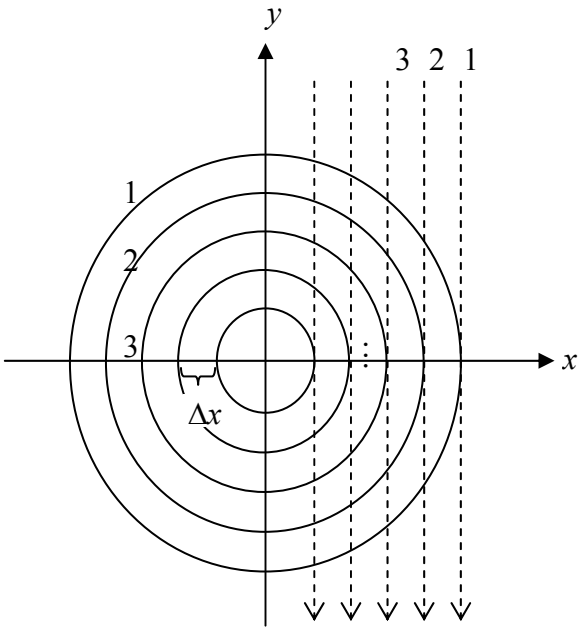

Figure 10. Each cross section of the jet mixing area is divided into small circles. Rays of light travel through a different number of these circles.

The algorithm was written into a Matlab code. It was tested by generating various theoretical concentration profiles, calculating the corresponding intensity images, and using the Matlab code for recalculating the original profile. The algorithm was found to work well. The errors in the concentration profiles were found to be typically only a few percent.

3.9.5 Experiments on determining concentration profiles for cylindrically symmetric mixing

The numerical algorithm for determining the concentration profile of cylindrically symmetric mixing was tested with blue food colour and birch pulp. The experimental setup for mixing of colour is shown in Figure 11. The details are presented in Ref. [1].

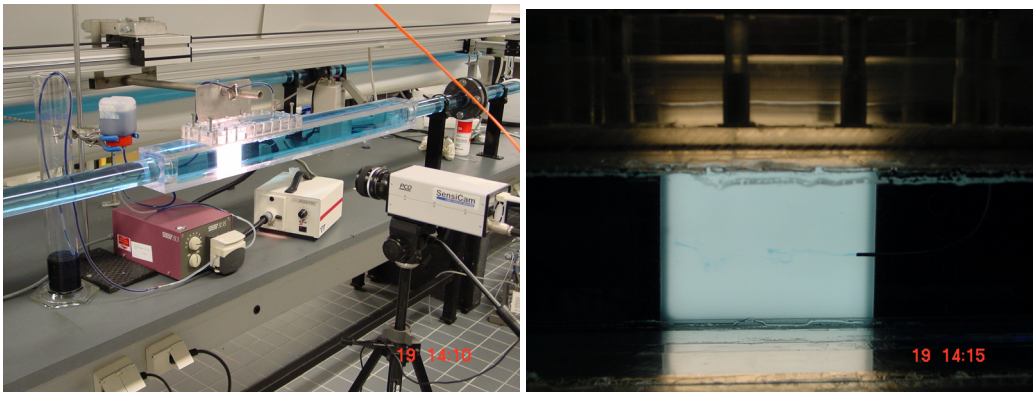

Figure 11. The experimental setup for jet mixing of blue food colour.

a)

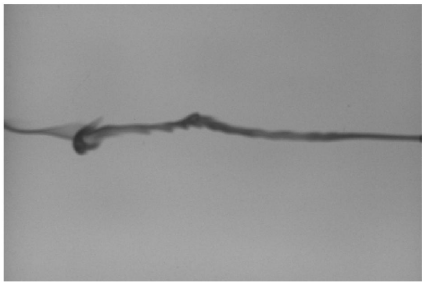

b)

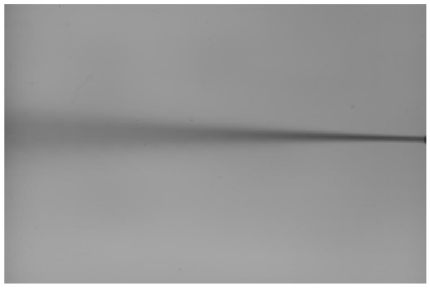

Figure 12. a) An instantaneous intensity image of jet mixing of food colour. B) An average of 200 instantaneous images.

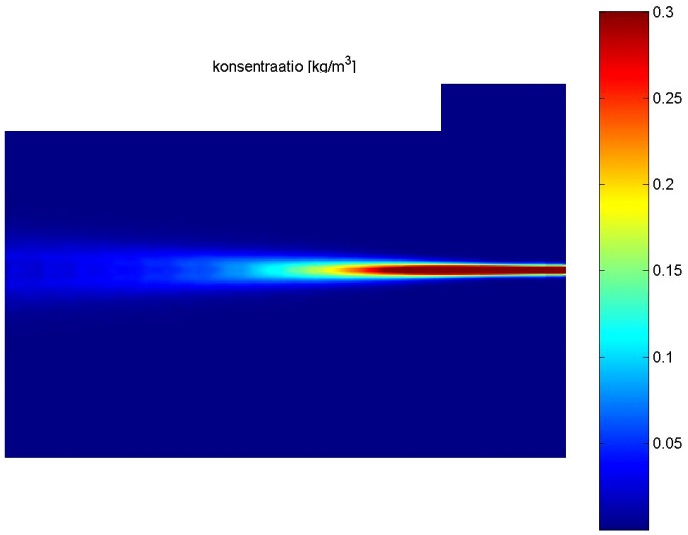

Figure 13. The calculated radial concentration profile of jet mixing of food colour. The colour concentration was 1.0 kg/m^3 in the primary fluid. The numbers are expressed in kg/m^3. The image size is 40x60 mm.

Figure 12 shows an instantaneous intensity image of jet mixing of food colour, and an average image of 200 instantaneous images. In Figure 13, the calculated radial concentration profile is shown. The algorithm is found to work very well here: the average colour flux calculated from the concentration profile is within 20% of the real value. Figures 14 and 15 show corresponding images of jet mixing experiment of 0.5% birch pulp. Here also, the analysis works pretty well.

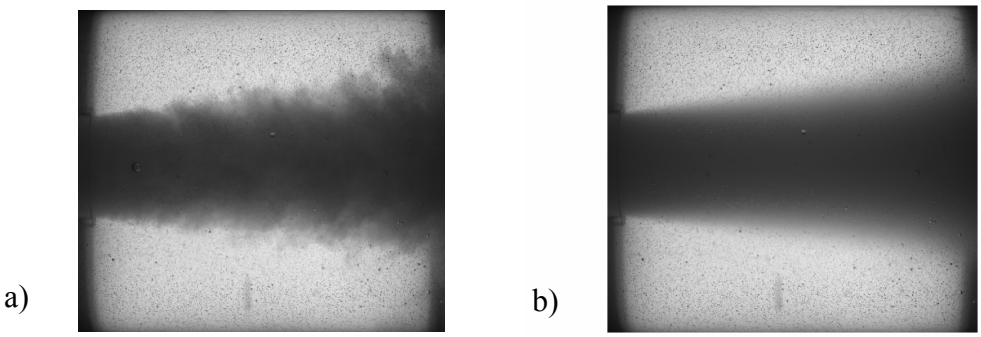

Figure 14. a) An instantaneous intensity image of jet mixing of 0.5% birch pulp. b) An average of 200 instantaneous images.

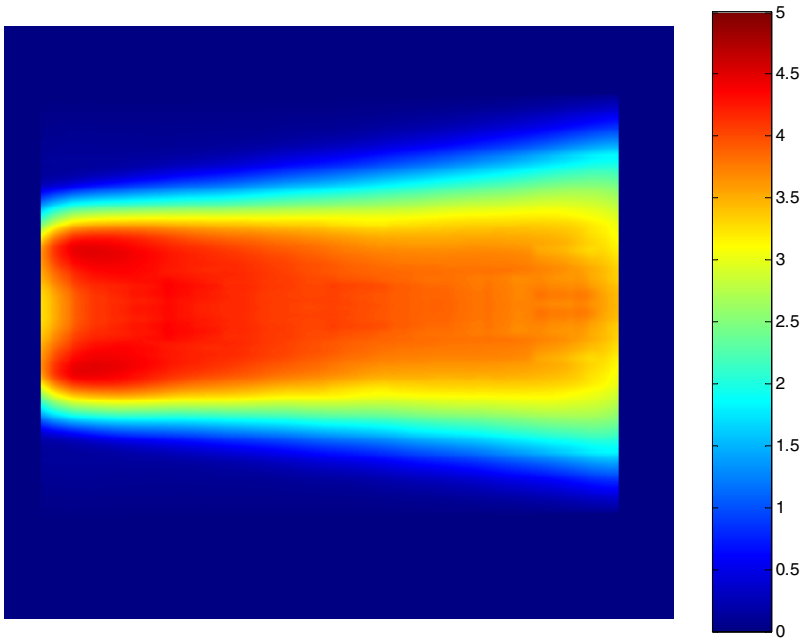

Figure 15 The calculated radial concentration profile of jet mixing of 0.5% birch pulp. The boundaries of the image have been omitted from the analysis. The numbers are expressed in kg/m^3. The image size is 95x108 mm.

3.9.6 Conclusions

Light absorption can be utilized to solve the average concentration profiles in effectively 2D mixing processes. The new algorithm presented in this report, makes this possible also for jet mixing. Accurate analysis necessitates the following conditions: The grammage of the absorbent must be relatively small, so that the light does not behave diffusively. The absorption coefficient should not vary too much as a function of light wavelength. The intensity of the illumination light should not vary too much for different wavelengths. Also, the camera should be equally sensitive to the whole spectrum of the illumination light. These requirements sound rather tight. In practical studies, however, violation of some of them does not mean, that the analysis is totally prevented. Also then, the process can often be analysed to good qualitative level.

For practical measurements one usually needs a transparent flow channel, but free jets can also be analysed. The method suits well e.g. to the analysis of turbulent jet mixing, if light diffusion is not very strong in the primary fluid. If light absorption is too weak, some extra dye can be mixed with the primary fluid.

3.9.7 References

[1] Koponen A. & Kataja, M. Konsentraatioprofiilin määrittäminen sylinterisymmetrisessä sekoittumisessa. Tutkimusselostus PRO/T6048/02, VTT Prosessit, Jyväskylä, 2002.

3.10 Optical methods for fibre suspension flows 2: Free jet surface topography

Antti Koponen, Pasi Selenius, Juha Salmela and Markku Kataja
VTT Processes

3.10.1 Introduction

Laser scanning is a commonly used method in pattern recognition and machine vision systems. The technique is known under a variety of names such as sheet of-light, range imaging, laser profiling, structured lighting or light-stripe ranging. In this method, the target is illuminated with one or several laser lines, that are imaged with a ccd-camera. The shape of the target can be obtained from the ccd-image by analysing the deviations of the laser lines. (See Figure 1.) Previously structured lighting has mainly been used for rigid objects. In this study, we apply the method to get the surface topography of a free jet.

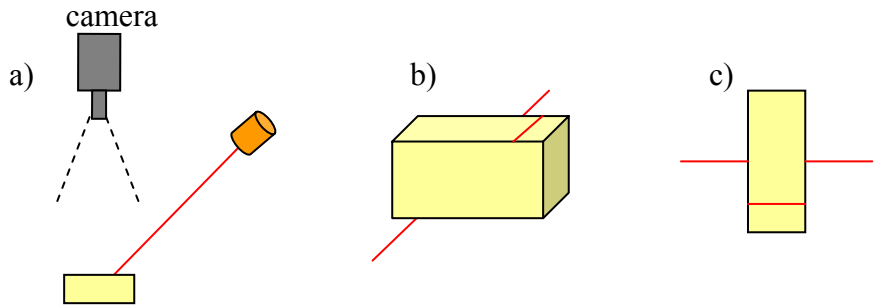

Figure 1. The principles of structured lighting. The target is illuminated with a laser line, which is imaged from another angle with a ccd-camera. The observed deviations of the laser line can be used to calculate the shape of the object. a) The overall arrangement of the measurement. b) The side view of the object and the laser line. c) The view of the ccd-camera.

In Figure 2, the principle of structured lighting has been show in more detail. The laser beam lays on the yz-plane. The light spot, that is originally on the basic plane (point A), moves to A' or A'', if the new surface level is higher or lower, respectively. From Figure 2 ones gets the following formula for the vertical deviation of the surface

$$\Delta z = \Delta y \tan \beta \,. \tag{1}$$

Notice, that this formula gives the surface height at $y+\Delta y$, not at the original location y of the light spot.

Here we will not consider the detailed analysis and technical problems related to the structured lighting method. Problems met in practice, such as the perspective correction of the ccd-images, the effects of the opening angle of the laser beam, and the effects of the camera optics, have been discussed in more detail in reference [1].

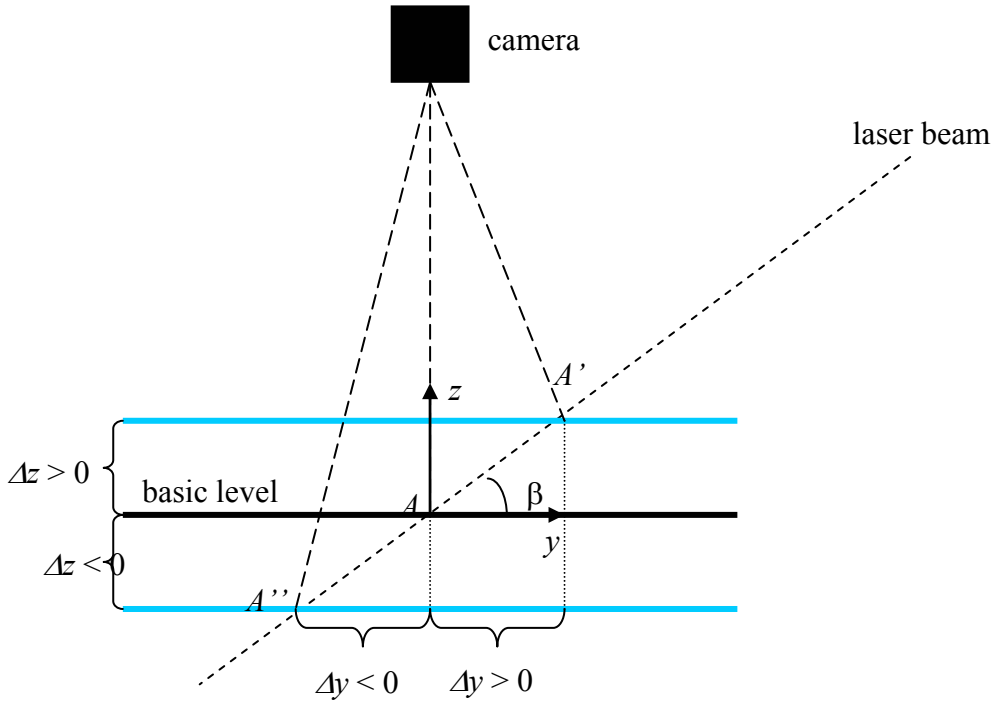

Figure 2. The horizontal (y-direction) deviation of the light spot depends on the surface height Δz. The black thick line shows the original location of the surface (basic level), and the blue line a new location.

3.10.2 Experimental studies at VTT

The free jet imaging experiments were performed at VTT Jyväskylä pilot scale flow line using 1.0% eucalyptus pulp. Here PCO Sensicam 12bit ccd-camera was used, and the laser lines were created with a diffraction lattice made by Nanocomp Oy. A schematic picture of the experimental setup and a photograph of the jet are shown in Figures 3 and 4, respectively. The exact locations of the lines were detected from the ccd-images by a sophisticated Matlab-software specifically written for this purpose.

Before the actual experiments were performed, the correctness of the experimental setup and the analysis software were checked with several experiments. Here, e.g., solid calibration plates, still latex solutions and free jets of latex solution (see Figures 5 and 6) were used.

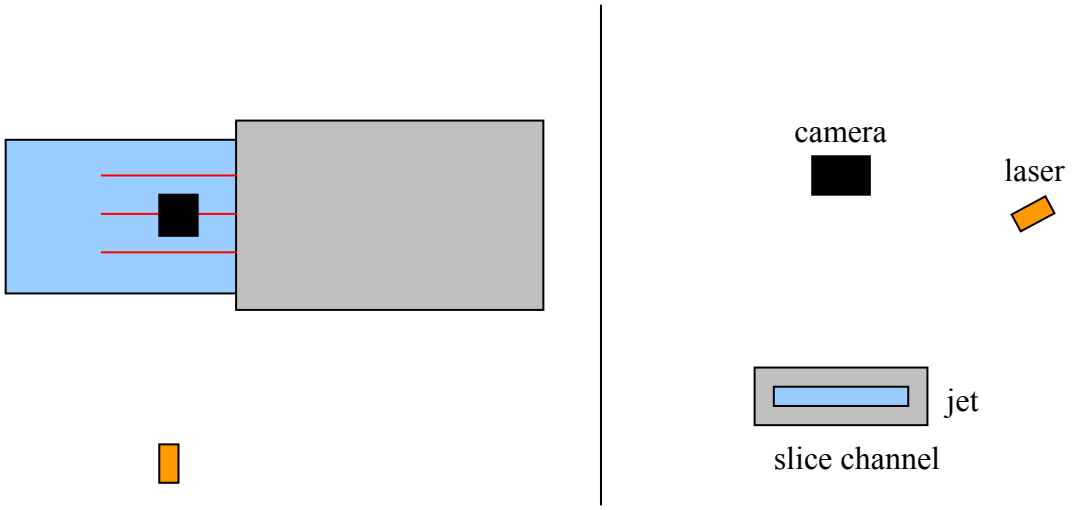

Figure 3. A schematic picture of the experimental setup for analysing MD-structures of the free jet. The red lines indicate the laser lines on the surface.

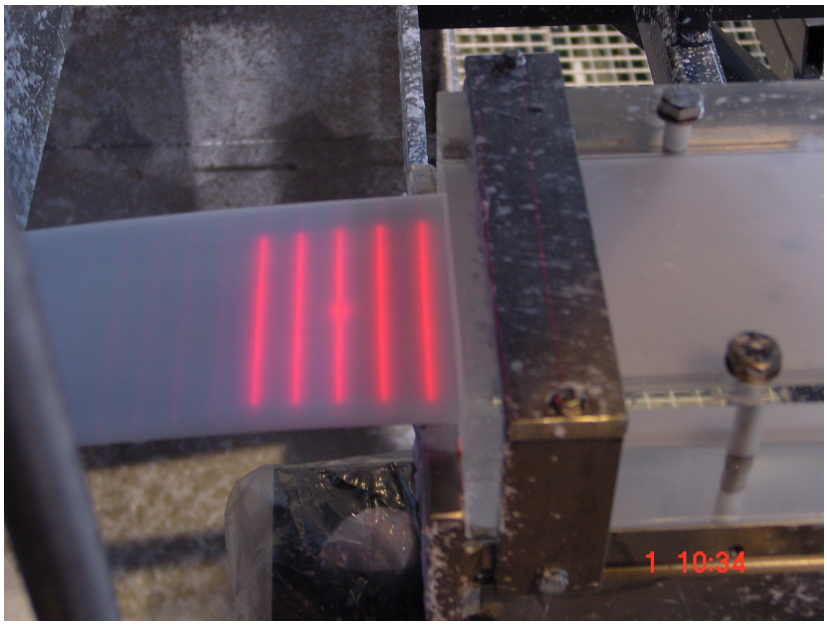

Figure 4. Laser lines on the surface of the free jet.

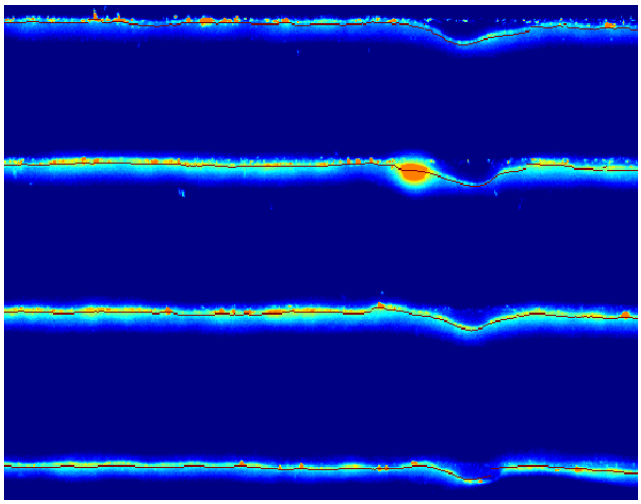

Figure 5. An intensity image of four laser lines on the surface of free jet. Bright colours indicate high light intensity. MD-direction is from bottom to top. The jet has been perturbed with a small stylus tip. This is seen in the depression of the jet. The dark red lines show the exact locations of the laser lines given by the analysis software. The quality of the lines is very good due to latex, that acts as a very efficient diffuser of light.

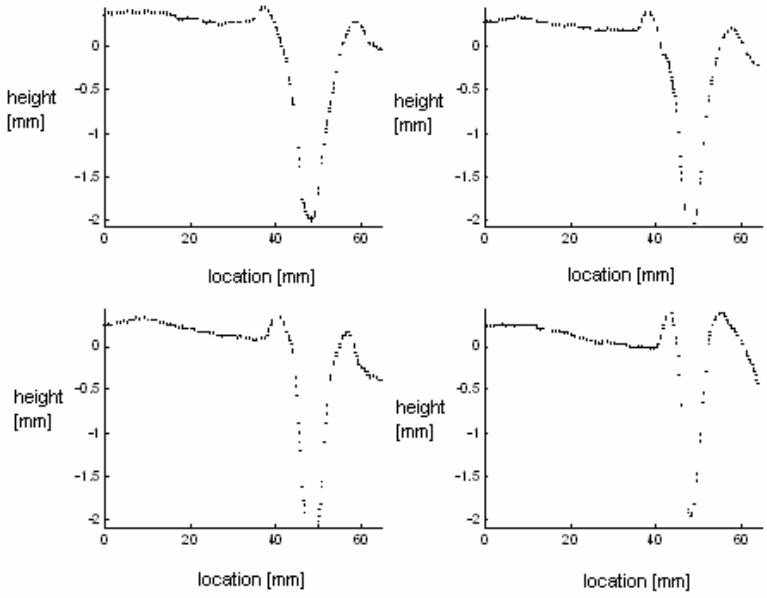

Figure 6. The average heights of the laser lines shown in Figure 5. The upper line is on the top left and the lowest line on the right bottom.

In Figure 7, an instantaneous intensity image of three laser lines on the surface of free jet of eucalyptus pulp is shown (MD-direction is from left to right). In Figure 8, the local intensity maxima of this image are shown. Contrary to the Figure 5, the lines in Figure 8 are now very noisy. Some extra analysis is required for filling the holes and

removing the duplicate points (created usually by reflections) before the final lines are obtained for closer mathematical analysis.

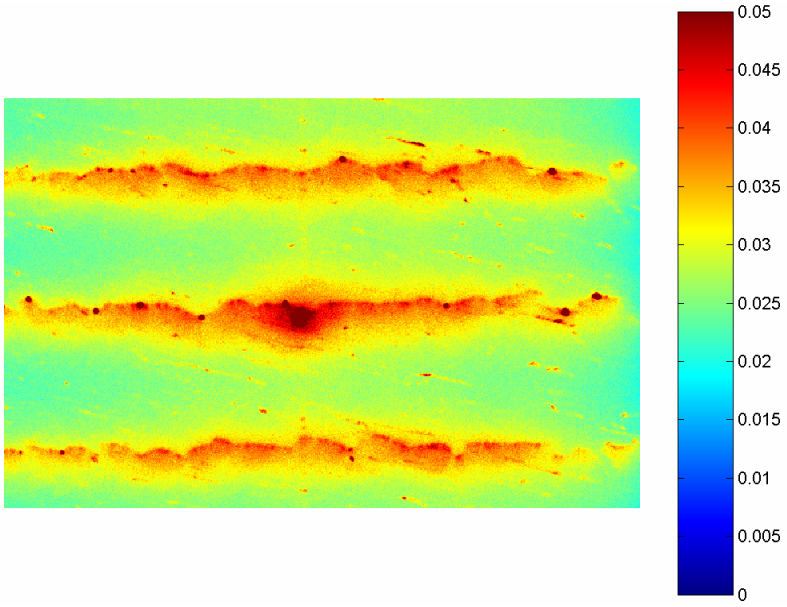

Figure 7. An instantaneous intensity image of three laser lines on the surface of free jet of eucalyptus pulp. MD-direction is from left to right. The image size is 61 mm x 94 mm.

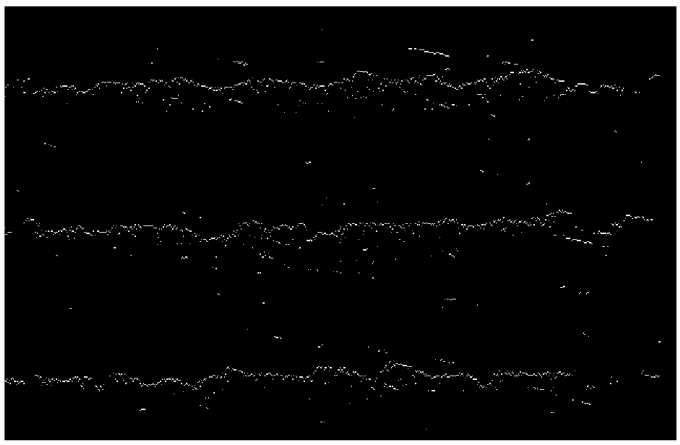

Figure 8. The local maxima of the intensity image shown in Figure 7. The final lines used in the mathematical analysis are determined from images of this kind after some extra analysis including filling of holes and removal of duplicate points.

In Figures 9, 10 and 11, the averaged fourier power spectrum, the autocorrelation function and the wavelet power spectrum of the laser lines are shown. We see from these figures, that the jet surface is not totally random, but includes structures, which have a typical length between 10–20 mm. We also see from Figure 11, that the amplitude of these structures increases in the MD-direction.

Similar analysis was also performed in the CD-direction. In this case no clear structures could be found.

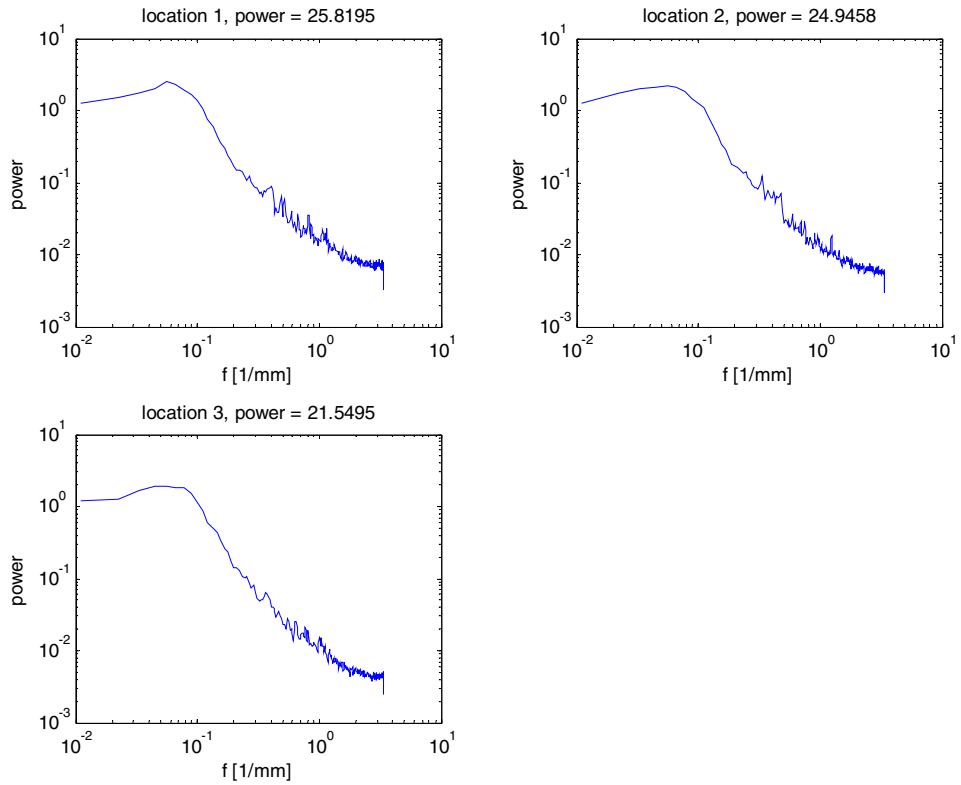

Figure 9. Averaged Fourier power spectra of 200 laser lines on three locations (numbering from top to bottom). All spectra are seen to be very similar. A rather wide peak is found around $f \approx 6\times10^{-2}\,\frac{1}{mm}$. *The typical length scale is thus* $\lambda \approx 17$ mm.

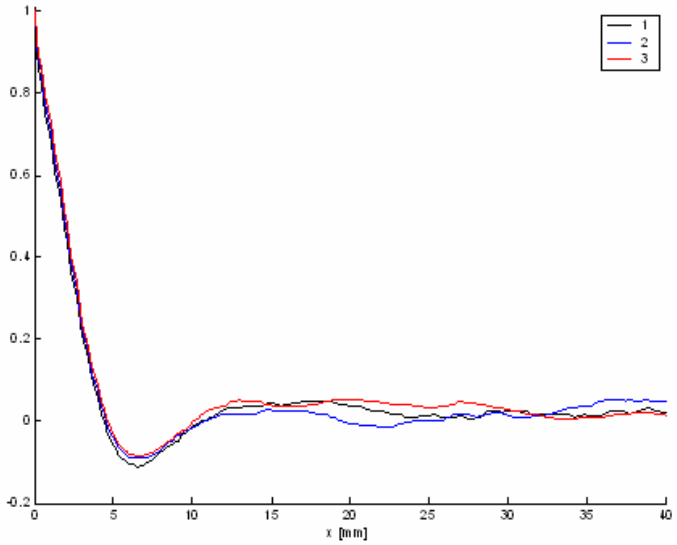

Figure 10. Averaged autocorrelation function of 200 laser lines on three locations (numbering from top to bottom). The typical length scale is about 14 mm (two times the location of the maximum autocorrelation.)

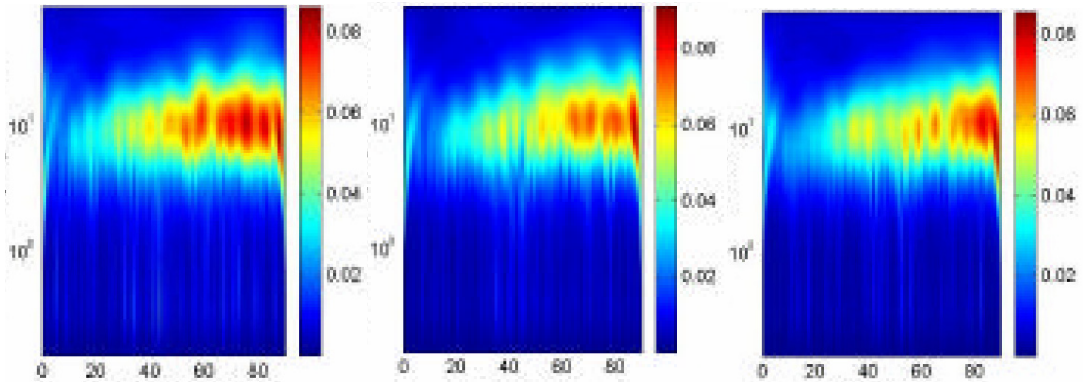

Figure 11. Averaged wavelet power spectra of 200 laser lines on three locations. The horizontal and the vertical axes show in millimetres the location and the wavelength, respectively. The colours indicate the power intensity. The typical length scale is seen to be about 10 mm. We also see, that the power increases in the MD-direction.

Encouraged by the relatively good results reported above, a commercial development environment for range profiling, IVP Ranger SAH5, was purchased to VTT Jyväskylä.

The systems includes a laser, a very powerful CMOS-camera and an analysis software. The equipment was found to be very handy for detecting e.g. static defects in free jets. In Figure 12, we show an example of the analysis result given by the system. The jet has once again perturbed with a small stylus tip. The vane thus created is seen very well in this image.

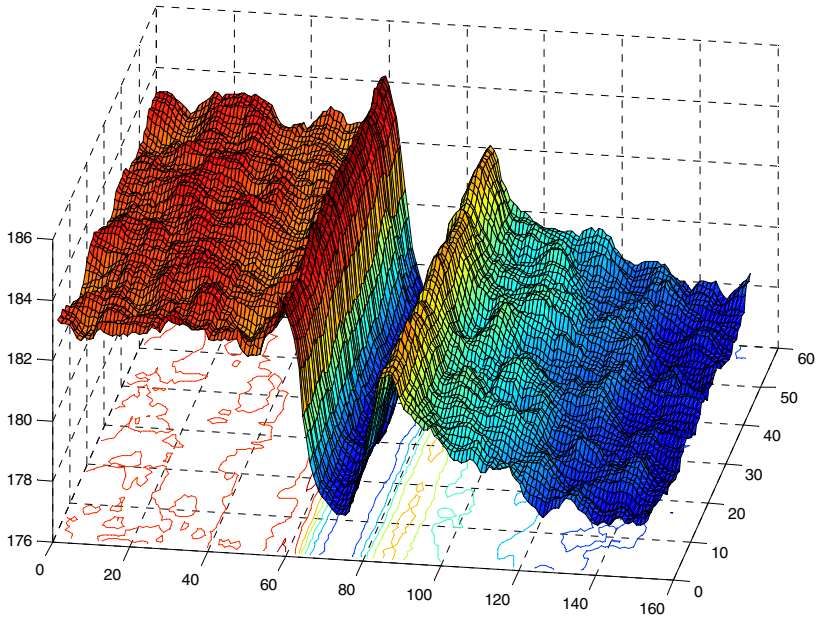

Figure 12. An analysis result of a free jet perturbed with a small stylus tip given by IVP Ranger SAH5 system. Here z-axis gives the height (in pixels), y-axis gives time-index and x-axis gives the CD-location (in pixels). The image has been filtered somewhat to eliminate fluctuations.

3.10.3 Conclusions

Use of structured lighting necessitates, that the target surface is diffusive for light. In pulp flow, this task is well performed by the fibers and the filler particles. So, structured lighting can well be applied to the analysis of free jets. Sometimes the images can be noisy, and extra numerical analysis is needed before they can be used. However, when used properly, the method can give valuable information on temporal and spatial behaviour of the surface. E.g. fourier, autocorrelation or wavelet analysis can be used to obtain typical size of the surface structures.

3.10.4 References

[1] Koponen, A., Selenius, P., Salmela, J. & Kataja, M. Huulisuihkun pintatopografian laserskannaus. Tutkimusselostus PRO/T6058/02, VTT Prosessit, Jyväskylä, 2002.

3.11 Image correlation techniques for measuring 2D velocity fields of fibre suspension flows

Juha Salmela and Markku Kataja
VTT Processes, Pulp and Paper Industry, Multiphase Flows

3.11.1 Background

The research of fibre suspension flows at VTT Processes is heavily based on various imaging and image processing methods. Here, we have combined and developed further two distinct imaging methods, namely flock size analysis and 2D velocity field measurement by image correlation techniques. The former method was originally developed as a part of the National Technology Programme of Computational Fluid Dynamics [1]. The development of the latter method was initiated within the project 'Novel experimental methods for fibre suspension flows (KUITU)', and completed here. Both methods are best suited for two-dimensional flows and for analysing flows near the surface of a three-dimensional flow.

3.11.2 Method

The basics of experimental techniques and the computational algorithm for flock size analysis based on image analysis is fully covered in ref. [1] and will not be repeated here. The method for measuring 2D velocity field, developed in the KUITU -project, is based on the analysis of two gray-scale images taken at short intervals in the same position of flow in a transparent channel or in a free jet. The original image correlation algorithm, 'Oflow 1', that was used to find the velocity field was based on comparing small rectangular subelements of the two full images to identify local translation of fibre flock structures between the images. Given the time interval between exposures, the velocity field can be calculated from the resulting 'deformation field' similarly to the standard PIV -methods. The drawback of this method was that only translational motion of image subelements was considered. Therefore *e.g.* rotational flow, or 3D flows where sources or sinks appear in a 2D image plane were not appropriately resolved.

The more advanced agorithm (Oflow 2) developed here is based on an iterative method where a discretized deformation field of the entire first image is optimized to give a maximum correlation with the second image. The initial guess for the deformation field is given by the Oflow 1 -algorithm. The method thus allows for a general (rate of) strain at the 2D imaging plane. Combined, the two methods can be used to simultaneous

measurement of flock size and velocity field and thus to gain new information on *e.g.* dispersion and flocculation mechanisms of fibre network in various flow conditions.

The experimental techniques involved in velocity field measurement requires a fast double exposure camera and a well synchronized pulse light source. A high speed video camera with a DC light source was also tested in preliminary experiments. However, the former techniques was found more suitable for the present purposes. This is mainly due to the better dynamics of the double exposure CCD camera as compared to the high speed video camera available for the present experiments. A simple device including an array of ultra bright LED:s was built att VTT to provide fast pulsed through illumination necessary for the double exposure CCD camera techniques.

3.11.3 Devices

The experimental setup for flow measurements utilizing the new methods is shown in Figs. 1 and 2. The equipment consists of a PCO Sensicam fast double shutter gray scale CCD camera with a telecentric optics, and an LCD illuminating device. The resolution of the camera is 1280 x 1024 bytes with 12 bit dynamics. The exposure time is 100 ns – 10 ms. The camera is connected to a computer by a fiber optical link and operated by a Lab View interfeace. The imaging equipment is mounted on an x-y manipulator assembly which is used to move the camera and light source along the acrylic tube section. The entire apparatus is computer controlled and even very complicated measuring sequences with camera motions and syncronized lighting/exposure events can be pre-programmed and executed. Extensive amount of data can thus be collected and analysed automatically.

Figure 1. PCO SensiCam mounted on a flow line at VTT flow research laboratory.

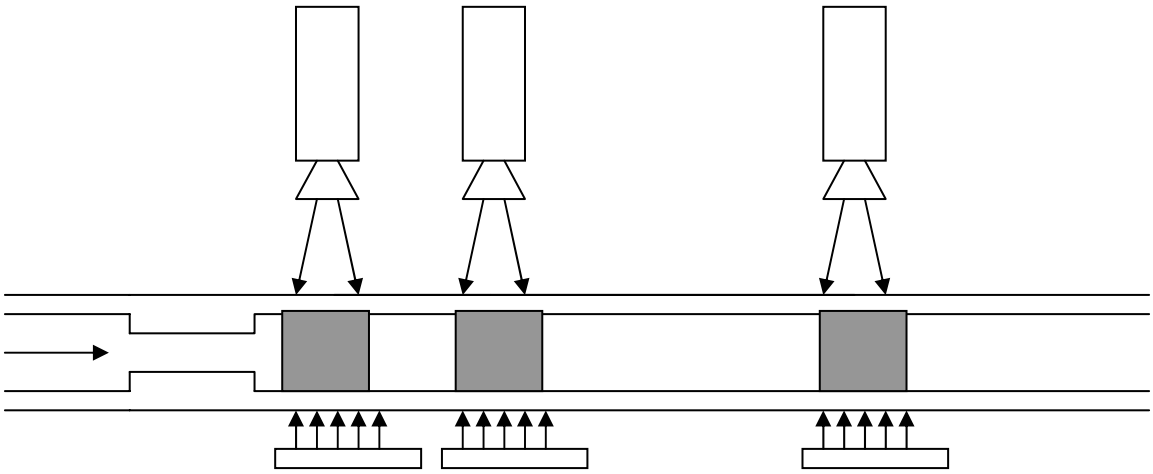

Figure 2. Experimental setup with different imaging positions along a test tube section.

The illumination device including an array of 40 white ultra bright LEDs is shown in Fig. 3. the brightness of each LED is 8000 mcd, the minimum duration of light pulses is 10 µs and the minimum delay between flashes is 10 µs. The device is syncronized with camera exposures using timing pulses generated by the computer that is controls the entire measurement procedure. The device was found to be very suitable for the present

purpose. It is easily controllable and provides sufficiently homogeneous illumination with constant intensity of light pulses.

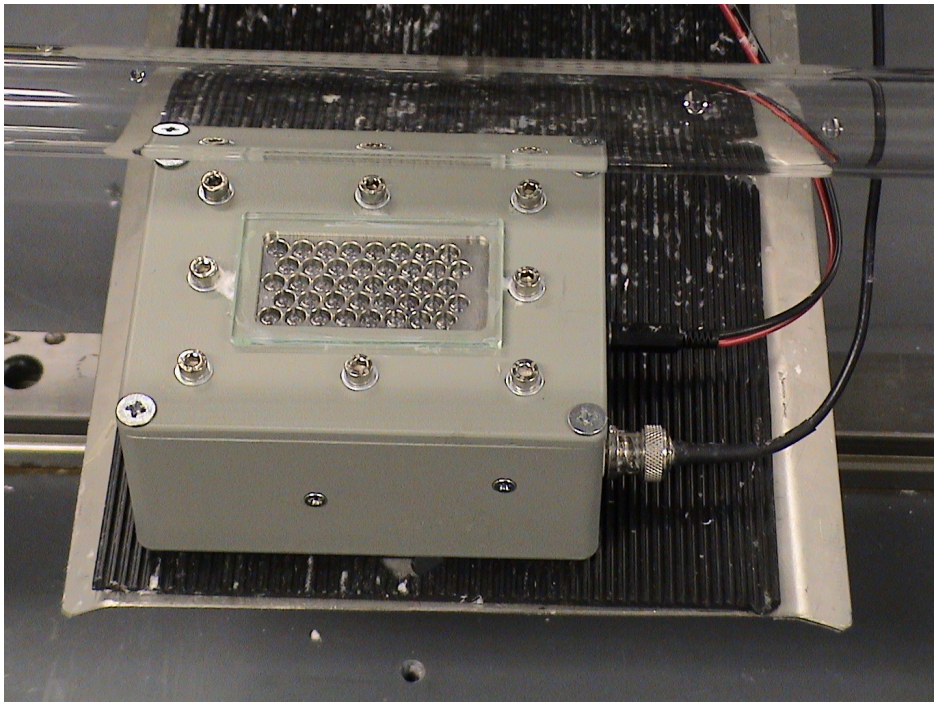

Figure 3. Pulsed Ulta bright LED illumination system developed at VTT flow laboratory. The device is shown the without the dispersing screen (white glass plate) which can be used to further increase homogeneity of emitted light.

3.11.4 Application examples

Flow in a sudden expansion after a converging channel: The Oflow techniques was tested in a 2D flow channel that consists of a step expansion after a converging channel section (see Fig. 4). The measured mean velocity field computed as an average of 200 individual flow fields near the step is shown in Fig. 5 for 1.0% birch fibre suspension. The back flow eddies after the step are easily detected. Notice the 'spontaneous' asymmetry of the flow pattern that is often found in pulp flows in apparently symmetric flow geometries.

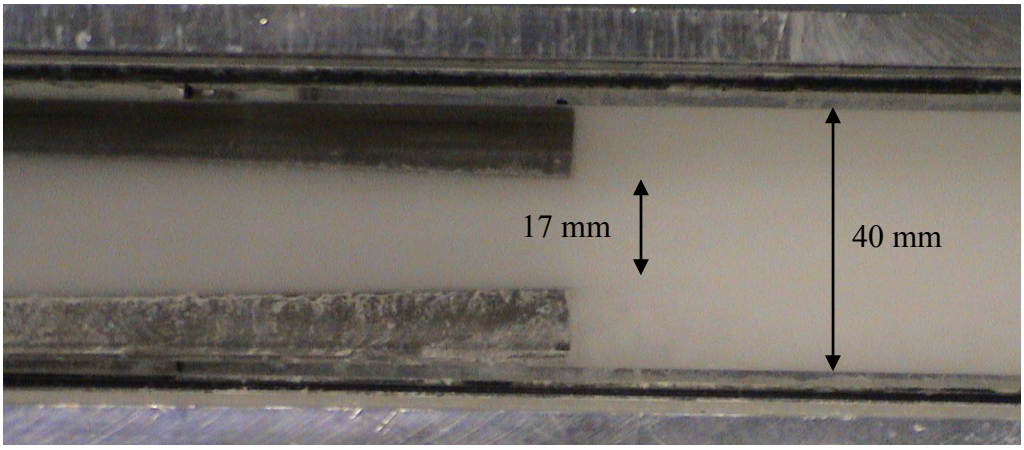

Figure 4. Fibre suspension flow in a 2D converging channel with a sudden expansion. the depth of the channel is 30 mm in direction transverse to the plane of the image.

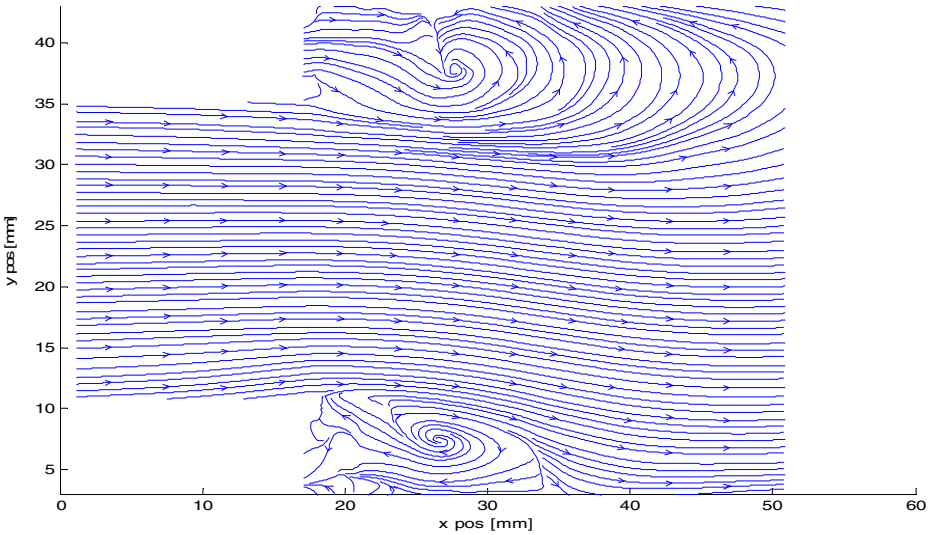

Figure 5. The mean velocity field of accelerated flow and backward facing step measured by Oflow techniques.

In addition to mean flow, the individual measured fields can be used to calculate quantities associated with fluctuating velocity. An example of such a result is given in Fig. 6, which shows the mean turbulent intensity at cross sections along a channel with step expansion. Also shown is the evolution of the average flock size along the same channel. The turbulent intensity and flock size analysis are both based on same images.

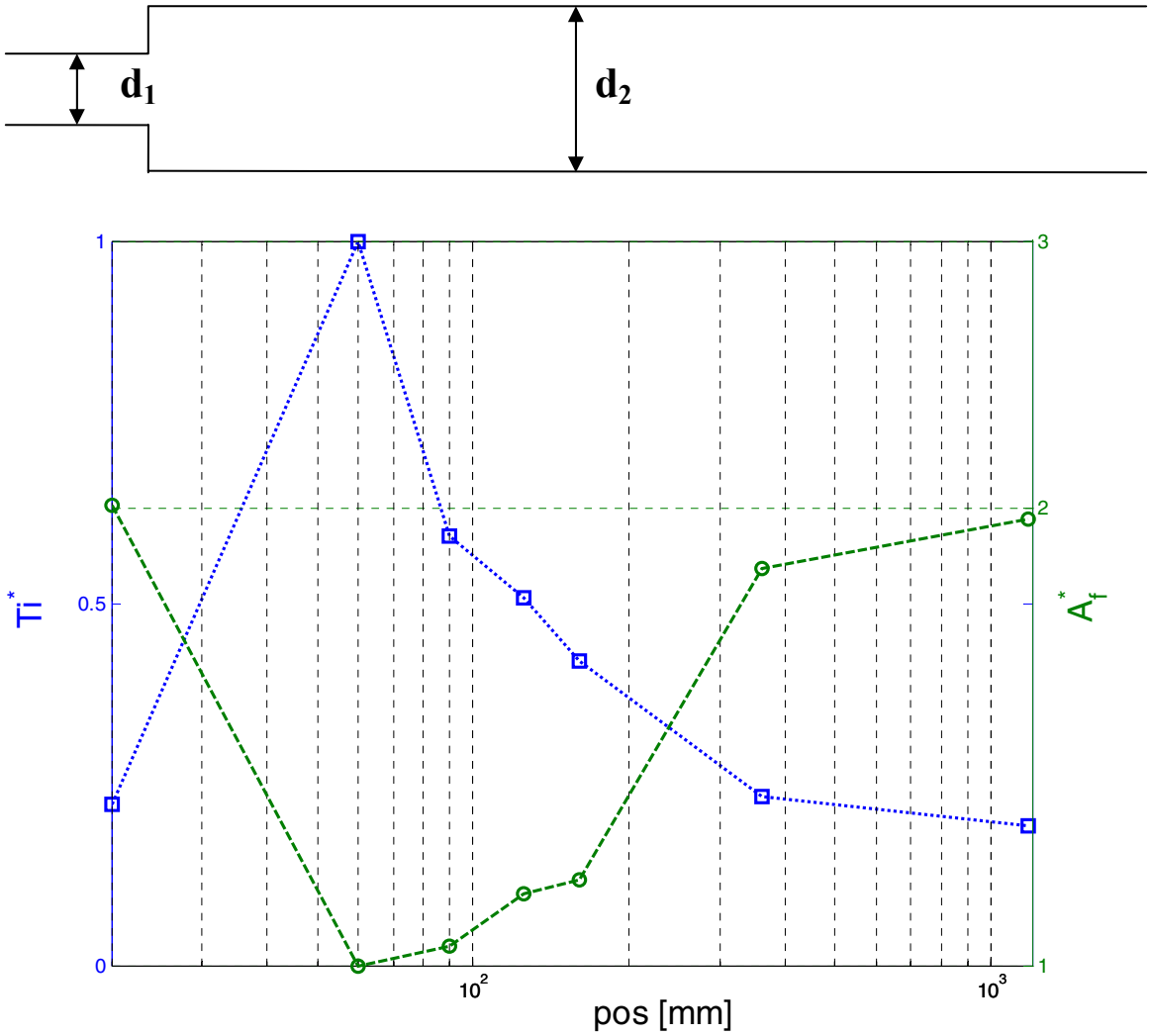

Figure 6. Measured relative Turbulence intensity (Ti^*) (scaled by maximum intensity) and relative Flock size (A^*_{flock}) (scaled by minimum flock size) on pipe geometry after sudden expansion (1.0% birch suspension, 2.0 l/s, d_1 = 16 mm and d_2 =21 mm).

As can be expected, a strong anticorrelation between turbulent intensity and flock size is found. The maximum turbulent intensity corresponds to minimum flock size, and reflocculation occurs in the region of decaying turbulence. Notice, that the value of 'turbulent intensity' found by the present techniques may include errors that arise from noise inherent to the method. At the least, it can, however, be used as a useful relative measure of the fluctuating state of the fibre phase in 2D flow geometries.

Length of the backflow eddy after a cylindrically symmetric step: Although the present method is most suitable for measuring fibre flow velocity in 2D geometries, *i.e.* in channels that are relatively narrow in the direction perpendicular to the average flow, it can be applied in 3D flows where the velocity field near the surface of the transparent channel is of interest. An example of such an application is given by a measurement of

the length of the backflow eddy produced by a step in cylindrical tube. Figure 7 shows the measured flow field birch fibre suspension near the outer surface of the 3D cylindrically symmetric eddy. The main flow is in the positive x direction (i.e. from left to right) and the step is located at x = 0. The length of the eddy is clearly indicated by the stagnation line located at tube surface near x = 29 mm where the measured (2D) velocity vanishes, and changes its overall direction.

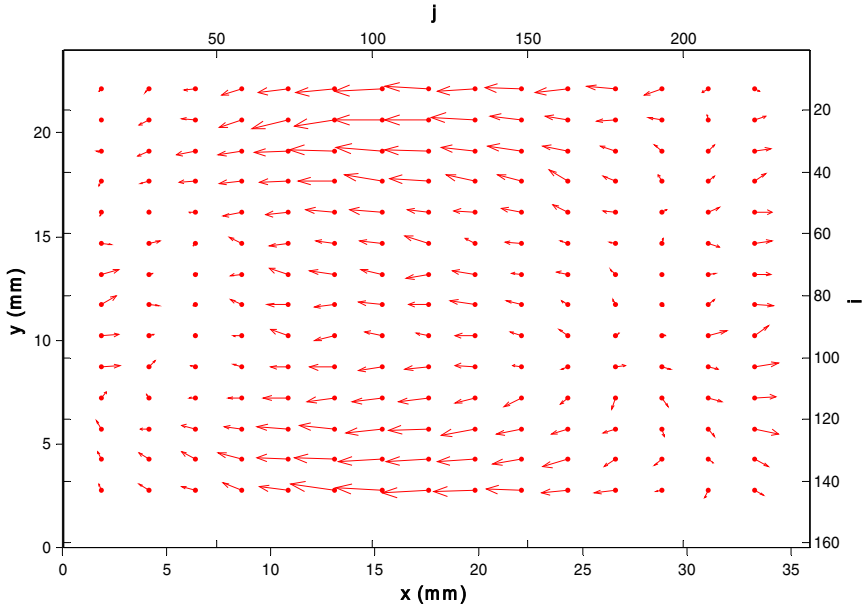

Figure 7. Mean flow field for 1.0% birch suspension after a backward facing step of sudden pipe expansion.

Figure 8 shows the measured backflow eddy length L_e as a function of the step height H = (d_2 -d_1) / 2 for 1.0% birch suspension. Also shown are typical correlations found in the literature for lower and upper bounds for pure water.

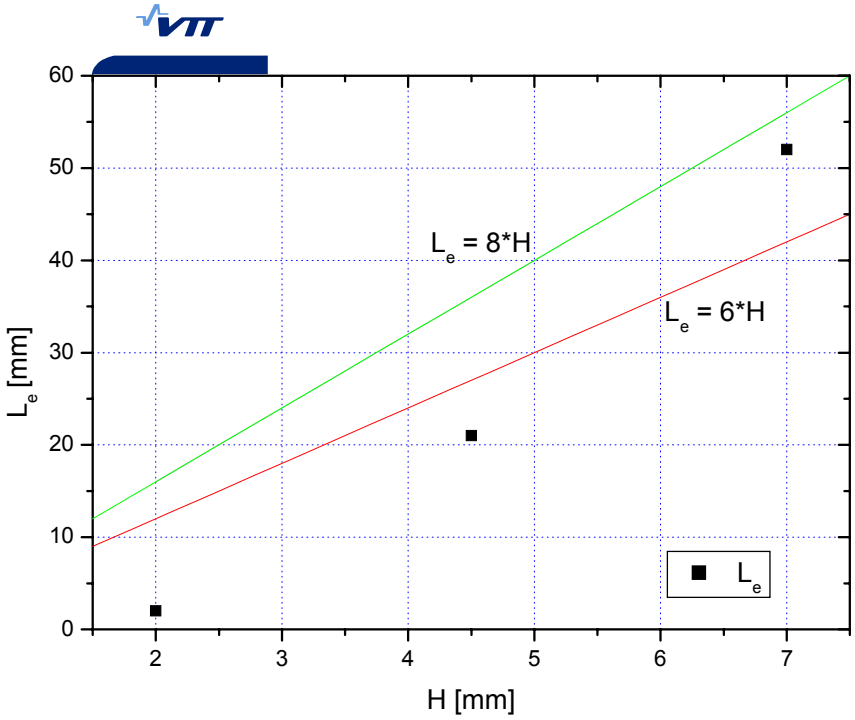

Figure 8. Comparison between measured eddy lengths L_e of 1.0% birch pulp suspension (solid symbols) and the limiting values of back flow eddy lengths for water (solid lines).

3.11.5 Conclusions

The two experimental methods based on image analysis, namely flock size analysis and 2D velocity field measurement provide a very useful tools for the study of flow behaviour of fibre suspensions. In particular, simultaneous measurement of flock size evolution and turbulent state of the flow can provide invaluable new information on the flocculation mechanisms in such flows. At the present, the two methods are used in various industrial research projects at VTT flow laboratory.

3.11.6 References

[1] Computational Fluid Dynamics Technology Programme 1995–1999. Final Report. Järvinen, E. (Ed.). Technology Program Report 8/2000, TEKES, Helsinki, 2000. (In Finnish)

3.12 Flow rate measurement of fiber suspensions

Veli-Matti Luukkainen
VTT Processes, Pulp and Paper Industry

3.12.1 Introduction

Flow meters used to measure the flow rate of also multiphase flows in many process industries are normally tested and calibrated using pure water or, in some cases, using radioactive tracers. In order to facilitate such testing in conditions and with fluids closer to those met in industrial processes, a specific flow loop including accurate mass and volume measurement was constructed at VTT Processes flow laboratory. The equipment is primarily designed for pulp slurries, but is not limited to those. It also enables studying the effect of various process factors such as consistency and air content on the operation and accuracy of flow meters.

In this preliminary study, the flow loop was used to compare the accuracy of four magnetic flow meters made by different manufacturers. In these tests, the parameters were the consistency and velocity of fiber suspension. Also, the effect of the position of the flow meter (on a long straight pipe vs. immediately after a 90° bend) was studied. Some preliminary tests concerning the effects of air content of fiber suspension were carried out as well.

3.12.2 Experimental arrangements

3.12.2.1 Equipment

The loop for flow rate measurements was constructed in connection to the flow research environment at VTT. The main component is a 6.5 m^3 tank, into which the fluid is pumped through the flow meters by a conventional impeller pump. The reference method for the flow meters is provided by a precision weighing of the tank. To this end, the tank is installed on three high-precision weighing appliances supplied by Raute Precision Oy. The weighing system is annually calibrated by the supplier.

The volume of the tank has been calibrated by Inspecta Oy. The cross section of the tank is uniform between volume content of 1 000–6 500 l. Within that range, the volume of the fluid in the tank (i.e. the surface level) can be measured by two ultrasonic transmitters.

The flow rate can be controlled by adjusting the rpm's of the pump by frequency converter, and/or by a control valve.

In this study, the effect of consistency and velocity of fiber suspension was measured with four magnetic flow meters. At a time, three of them were installed on a straight pipeline 3 215 mm apart from each other. The first one was installed immediately after a 90° bend (Fig. 1). By switching the position of the meters, also the effect of the bend could thus be estimated. The nominal size of the pipe and the flow meters was DN150 (ID 164.3 mm).

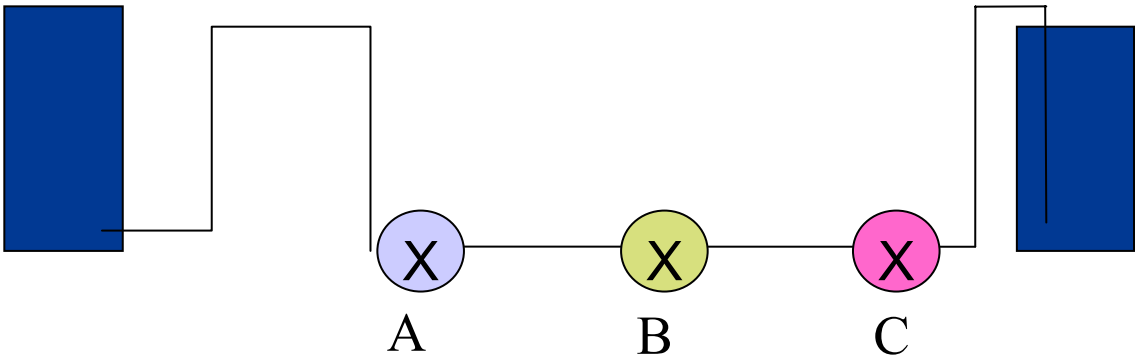

Figure 1. Schematic diagram of the assembly of the three flow meters. (Flow from left to right.) The rightmost tank includes precision mass and volume measurements

Control of the measurements and data logging were carried out by LabView 6.1-software. The hardware used was a National Instruments MegaPac.

The signals were read at a frequency of 10 kHz and from these the averages of each 2000 samples were calculated. Thus, the averaged data was recorded at a frequency of 5 Hz including the analogl signals from the weighing device and the level transmitters, as well as the digital pulses and analog signals from the magnetic flow meters. The intrinsic time constants and filterings of the magnetic flow meters were minimized.

Air could be added into the pulp by supplying compressed air either into the pipe flow or alternatively into the 8 m^3 tank from where the pulp was pumped. Feeding into the pipe was carried out through one porous sintered metal element installed in the middle of the vertical pipe. The feeding point was about 60 cm before the 90° bend preceding the first flow meter. The pore size of the sintered element was approximately 10 – 20 μm. The air into the tank was conducted through five porous ceramic plates, having a pore size of about 1 μm. The plates were installed on the bottom of the tank and their total surface area was about 0.28 m^2. The air flow rate supplied was measured and adjusted by rotameters.

3.12.2.2 Suspensions used in the tests

Comparative measurements were carried out with tap water and with chemical softwood pulp. The pulp was made by slushing the dried pine pulp sheets (from Äänekoski pulp mill) in a pulper at VTT. The consistencies of the pulp suspensions used were 5%, 3.3% and 1.5%.

In the first air content tests, softwood pulp was used, prepared as described above. Here, the consistencies were 3.1%, 2.1% and 1%. The second trial was made with chemical pulp including 2/3's of birch 1/3 of pine. Carbonate (PCC) was added to simulate fine paper pulp. In these tests, the consistency was 1% of which 16% was carbonate.

3.12.2.3 Experimental procedure

After turning on pumping, the flow was allowed to stabilize and the fluid level in the weighed tank to reach the calibrated range of the equipment. The data acquisition was then initiated at a pre-set trigger mass value, typically in the range from 2000 to 2500 kg. Correspondingly, data logging was terminated at a trigger value typically set between 4000 and 5000 kg.

Comparative measurements were made using 4–5 different flow rates between 10 and 100 l/s (corresponding to flow velocity between 0.5 and 4.7 m/s). At every flow rate, double measurements were carried out. The time of data logging varied from 20 seconds on high flow rates to few minutes on low flow rates. The air content tests were done using two different flow rates.

3.12.3 Results

The summary of the accuracy of the four flow meters, A, B, C, and D is shown in Table 1. Measurements were made using tap water and softwood pulp at different consistencies. The values are expressed as percents of relative error compared to weighing and they are the averages of measurements at 4–5 different flow rates. The error values obtained from both digital and analog signals, available with all the four devices, are shown separately. Prior to measurements at VTT, the same flow meters were also tested by Inspecta Oy using pure water. The results of these measurements, provided by Inspecta Oy, are also included in Table 1 for comparison.

The same results are presented also in Fig. 2, where the relative error is shown as a function of pulp consistency (only digital signals used here).

The magnetic flow meters give the flow rates in l/s. In order to compare with mass flow results obtained by weighing, these values have been converted to mass flow rate by using the tabulated values for the density of water. The actual density of pulp suspension was not known and it has been assumed to be 1000 kg/m^3. If the actual density is smaller than this, the negative error will be higher, correspondingly.

In Figures 3–6, the accuracy of the four flow meters is presented as a function of flow rate as calculated from digital output signals. Also shown is the effect of meter position, i.e. whether installed in a straight pipe or immediately after a 90° bend (for meters A and B only). Measurements were again made with water and with softwood pulp at three different consistencies.

Table 1. Accuracy of the flow meters expressed as percentage relative error as compared to precision weighing (each value is the average of measurements at 4–5 different flow rates).

Digital pulses	**"A"**	**"A" after bend**	**"B"**	**"B" after bend**	**"C"**	**"D"**
pulp C ≈ 5%	-7.37	-6.94	-2.88	-4.25	-3.20	-2.32
pulp C ≈ 3.3%	-6.21	-6.00	-1.39	-1.32	-2.66	-1.84
pulp C ≈ 1.5%	-5.31	-5.21	-0.95	-1.18	-1.86	-0.87
water	-4.22	-5.00	-0.50	0.05	-1.11	-0.56
water by Inspecta	-3.28		-0.40		0.15	-0.02
Analog signal						
pulp C ≈ 5%	-8.18	-8.03	-3.89	-5.00	-4.14	-2.83
pulp C ≈ 3.3%	-7.07	-7.13	-2.36	-2.12	-3.46	-2.25
pulp C ≈ 1.5%	-6.37	-6.30	-1.91	-1.95	-2.65	-1.33
water	-5.37	-5.89	-1.58	-1.04	-2.04	-1.03
water by Inspecta	-3.17		-0.67		-0.21	-0.05

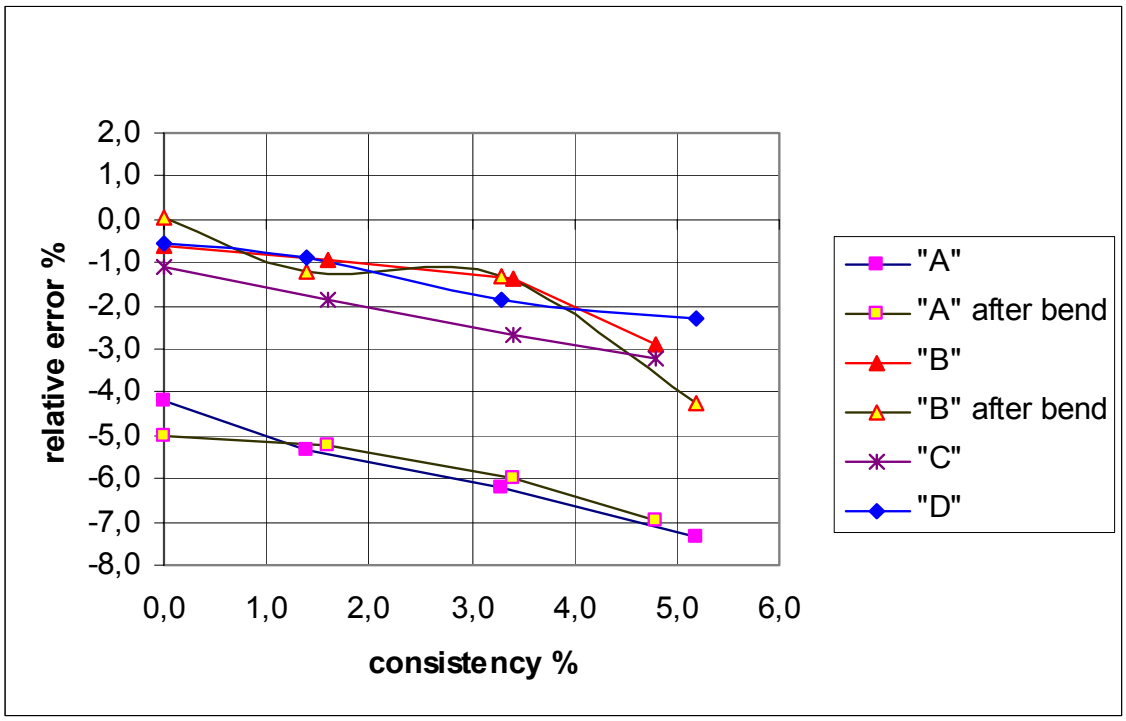

Figure 2. Accuracy of the four flow meters A, B, C and D as a function of pulp consistency (flow rate registered using digital output of the flow meters).

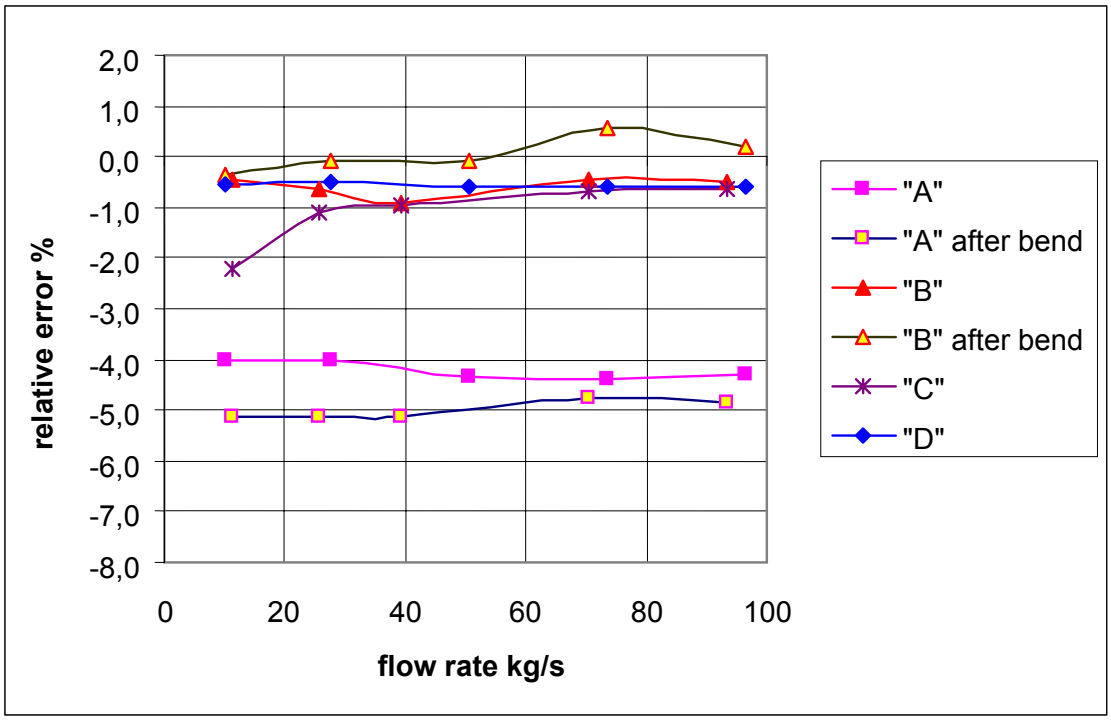

Figure 3. Accuracy of four flow meters A, B, C and D as a function of flow rate for water. Also shown are the results for the meters A and B installed immediately after a 90° bend.

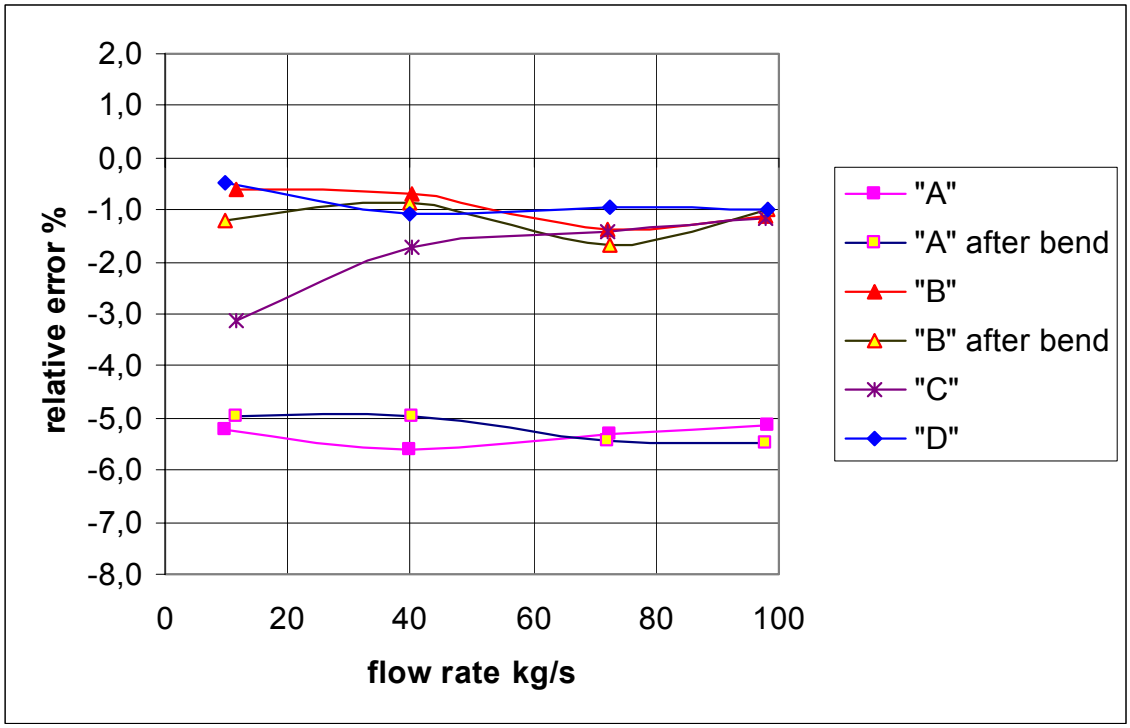

Figure 4. As Fig. 3 but for softwood pulp of consistency 1.5%.

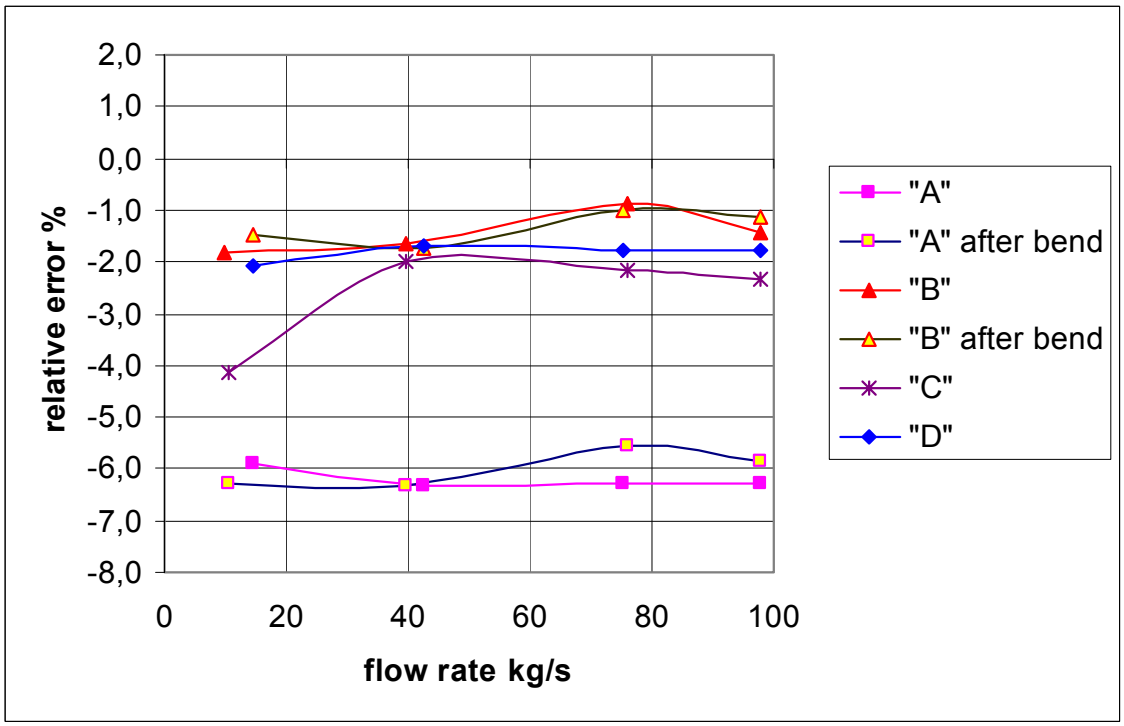

Figure 5. As Fig. 3 but for softwood pulp at consistency 3.3%.

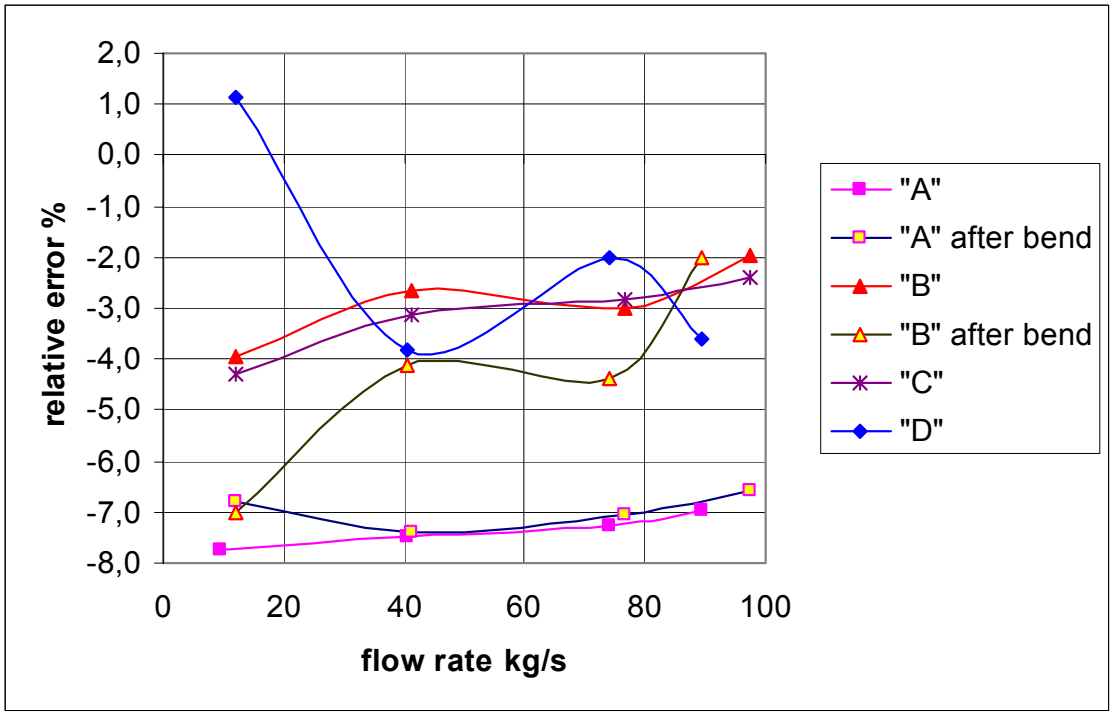

Figure 6. As Fig. 3 but for softwood pulp at consistency 5%.

All the flow meters gave systematically somewhat smaller values than weighing. There were no significant difference between the flow meters B, C and D. The meter A showed a clear deviation (3.5–5%) compared to the others. All meters had a 0.5–1 percentage unit difference between the digital and analogical signals.

As shown by the results listed in Table 1, the relative error measured with water at VTT was slightly higher than that measured at Inspecta Oy for all the flow meters. The difference was between 0.2 and 1.2 percent units with digital signals and 0.9–1.8 percent units with analog signals. One explanation for this is that at equipment used by Inspecta, the flow may be more fully developed than at VTT's equipment with shorter straight pipe segment. On the other hand, the flow conditions at VTT's equipment are closer to those found in many industrial processes.

Generally, the relative error grew with the increasing consistency of the pulp. The flow velocity, i.e. the flow rate did not have marked effect on the accuracy. For one of the meters, C, the error slightly grew at low flow rates. The position of the meter immediately after a 90° bend had some effect, but only with pure water.

In the first air content tests, chemical softwood pulp with consistencies about 3.1%, 2.1% and 1% was used. When air was fed into the pipe (about 0.5–1.4 percents by volume), the indicated flow rate increased about the equal amount at 3.1% consistency. At lower consistencies, the flow rate increased from 1.5 to 4 times the actual increase due to the added air volume (1–3 percent units).

The most significant effect could be seen in the first meter after feeding point and, correspondingly, the smallest effect in the meter located at longest distance from the feeding point. Presumably, the air in the pipe gathered on the upper part of the pipe during the horizontal pipe section. The sensor electrodes in flow meters are situated horizontally at the opposite walls of the pipe. Consequently, a small amount of air on the upper part of the pipe may not disturb the measurement very much.

An another air trial was made with chemical pulp and PCC added, simulating the pulp for making fine paper. The purpose of adding carbonate was to increase the ability of the pulp to retain air. The fibre consistency was 1%.

In these tests, more air was fed into the pipe (1–5 percent by volume). As can be seen from Fig. 7, there is a significant effect when air content exceeds 2%. The presumed gathering of the air on the upper part of the pipe is again supported by the fact that significant effect of air on the last meter is seen only with the largest air contents.

Feeding the air into the tank through five porous ceramic plates did not prove to be very effective, as the amount of air captured in the pulp was not enough to be seen in flow meters. In addition to this mechanical feeding, some preliminary tests were made to chemically disperse carbonate to carbon dioxide. Lowering the pH from 8.3 to 7.3 with sulphuric acid should have started the reaction, but it did not create enough gas in the pulp either.

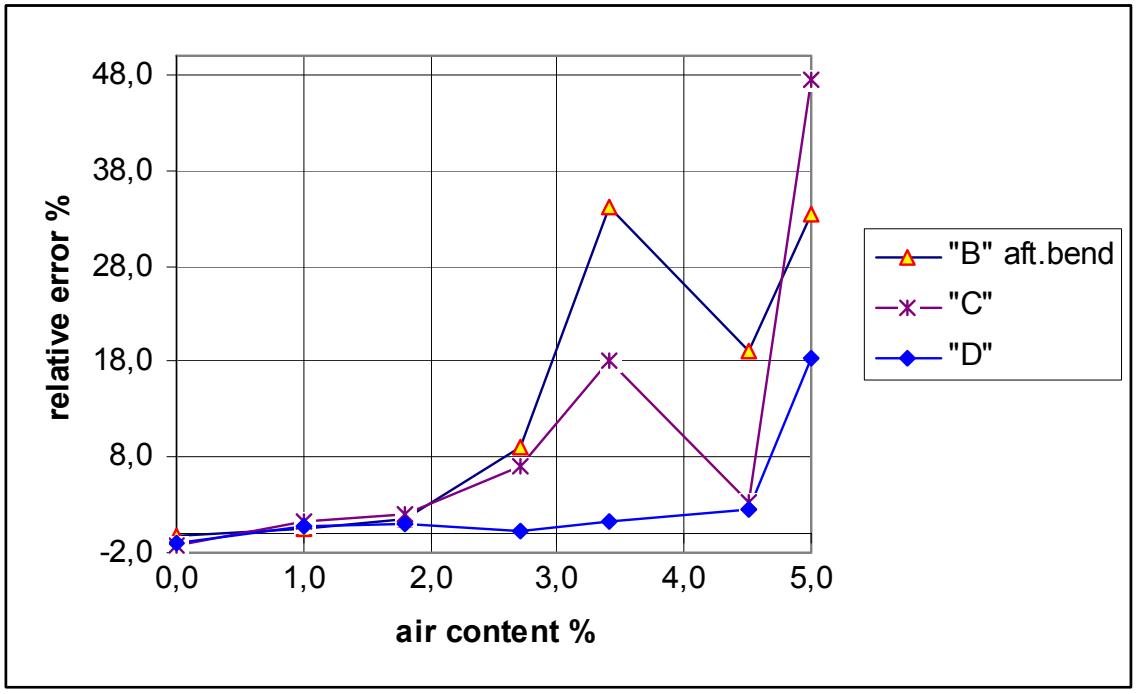

Figure 7. The effect of air on the accuracy of flow meters B, C and D at flow rate 30 l/s.

3.12.4 Conclusions

A flow loop constructed at VTT Processes flow laboratory was used to compare the accuracy of four magnetic flow meters made by different manufacturers. The parameters varied within these tests were the consistency and the velocity of fiber suspension. In addition, the effect of the position of the flow meter (on a straight pipe vs. immediately after a 90° bend) was studied. Some preliminary tests concerning the effects of air content of fiber suspension were also carried out.

According to the measured results, the flow meters gave systematically somewhat lower values of flow rate than those obtained by precision weighing. There were no significant difference between three of the meters. One meter showed a clear deviation (3.5–5%) as compared to the others. All meters had a 0.5–1 percentage unit difference between the readings obtained from the digital and analog signals available with all the devices.

Generally, the relative error grew up with the increasing consistency of the pulp. The flow velocity, i.e. the flow rate did not have very much effect on the accuracy. Only with one meter, the error increase slightly with decreasing flow rate. The position of the meter immediately after a 90° bend had moderate effect but only with water. With fibre suspension, no effect could be found.

The air contained in the pulp had significant effect on meters when the air content exeeded 2% by volume. Even 2–4% air content in a horizontal pipe seems not to disturb the meters very much, provided that the air is concentrated on the upper part of the pipe. With large air contents (>5%), the effect is always significant.

In conclusion, the effects of different parameters on the accuracy of magnetic flow meters can be estimated quite reliably with the present device. These parameters include flow velocity and consistency of the pulp, as well as the position of the flow meter. However, further research on the effect of air content and pulp type as well as of the chemical properties of the pulp is needed.

4 Current research profile of the participating groups. Impacts of the ProMoni project

This section shortly summarizes the current status and research activities of the participating groups at the time of ending of the ProMoni project. Also given is a brief statement of the particular significance and impacts of the ProMoni project on their applied research related to industrial multiphase flows.

***VTT Processes, Multiphase Flows**:* The primary field of activity of the Multiphase Flows group at VTT Processes is experimental research of flows found in various industrial processes. At the present, the group consists of 15 research scientists and technical personnel. The experimental facilities available for the group at VTT flow laboratory include several research platforms for different purposes, ranging from well equipped laboratory flow loop up to a fully automated pilot scale short circulation facility[1)]. The total investments in the currently operational experimental facilities and devices has been considerable in the past few years. During the years 2000–2003 the group was involved in about 30 separate multiphase flow research projects of which 20 was funded primarily by the industry. Of the total income, approximately 65% comes from private sector.

Development of new experimental methods and research facilities has been a central issue within the multiphase flows group since 1995 when it was established. In addition to the resources provided by the ProMoni project, significant amount of also internally budgeted funds have been devoted to this purpose during the last three years. Most of the results from this development have already been extensively utilized in industrial projects, many of which would not have been even possible without such efforts. Some of the results will allow the group to enter new research topics that are within the interest of even wider field of industry. In accordance with its original goal, ProMoni project has also considerably enhanced productive cooperation between multiphase flows group and the other participating groups. With regard to the goals stated in the original research plan, the project can be considered successful and has served its planned purpose.

***VTT Processes, Process simulation*:** The Process simulation group at VTT Processes develops and utilizes CFD and process models related to design and operation of power plants and equipment of process industry. Important research areas are simulation of combustion and emissions, modelling of multiphase flows, and development of simulation software for design and optimisation of power plants. Currently, 21 researcher

---

[1)] See *e.g.* the web site:
http://www.paperrc.com/index.php?page=specialities&subpage=facilities&subpage2=flow

scientists are employed in the group. The external income is roughly 70% of the turnover, consisting of income from the private sector (62%) and public sector (38%).

The development and testing of fluidized bed CFD models have been carried out in the Process simulation group since 1996. The research work done in the ProMoni project is a continuation for the bubbling bed simulation modelling started in the CODE technology programme. Validation of the models has been done for bubbling fluidized beds, but the same models are applicable also to circulating fluidized beds. Therefore the results of the project have wider significance.

The experiences from the studies in the ProMoni project have already been utilised in industrial research projects, carried out in the Process simulation group. In 2004, the fluidized bed modelling continues in several research projects and applied industrial projects. These include both bubbling beds and circulating beds. For the latter application, the simulations of turbulent bed, carried out in the ProMoni project, are especially valuable. The activities in the research area of fluidized bed modelling constitute about 2.5 man years in 2004.

The validation studies performed in the ProMoni project consist of comparisons of the basic models for gas-particle flows. Owing to long computing times, these models are currently not appropriate for modelling large size fluidized bed boilers, for example. In the forthcoming projects, results of the modelling of laboratory scale experiments will be utilized in developing approximate models for simulating practical applications.

***Tampere University of Technology, Measurement and Information Technology*:** The research in the Institute of Measurement and Information Technology (MIT) concentrates on sensor technology and measurement information technology. Cooperation with pulp and paper industry has continued for more than twenty years. During recent years research cooperation in the area of telecommunication and other IT applications has increased. Other growing research areas are measurements based on images and wireless physiological measurements.

Research in the area of sensor technology includes

- sensor applications: process sensors, especially flow sensors
- microsensors: modelling and simulation tools, photolithography, clean room facilities
- wireless sensors: wireless bioelectrodes, implantable sensors
- biosensors: miniaturized transducers, microflow systems, magnetic labels
- polymer sensors: electret material (EMFi), sensing chair (heart rate, breathing), ultrasonic applications.

Research in the area of measurement information technology includes

- methodology for selection of data analysis methods
- analysis of non-stationary data
- decision support systems based on measurements
- measurements based on images.

In the institute there are three professors and approximately 30 researchers and research assistants. External funding in 2004 will be approximately 65% of the total budget of the institute.

The electrical impedance tomography (EIT), which has been the technology of our institute in the ProMoni-project, has a wide range of applications. Our application is mainly directed to non-newtonian fluid flows (e.g. pulp suspension flows) and there to the measurement of consistency profile and flow rate. This application is in direct connection with the projects, which have been carried out in the institute concerning velocity profile effects in single phase flows. The other connections are in the projects carried out with consistency measurement in pulp and paper processes. This includes both the projects with on-line analyzers and sampling. The analysis of the images generated by the EIT using the methods developed in the projects of measurements based on images will be the next step to gain more information on the EIT results.

The institute has not yet had industrial application projects in the area of process tomography, but now we have quite good possibilities to develop further the equipment so that application projects are possible. But in any case, further basic research is needed.

The ProMoni-project has been the starting point in the institute to use process tomography. In the beginning of the project our knowledge in this area was almost zero. Now we have basic equipment and basic knowledge how to direct the research. Process tomography has many possible applications e.g. in the research of flow, mixing and separation.

Tampere University of Technology, Fluid Dynamics: Experimental Fluid Dynamics Group at TUT includes six persons yearly. It conducts fundamental and applied fluid mechanical research, develops measurement methods and educates specialists in the field of experimental fluid dynamics. The aim of the group is to produce profitable information both in the fields of fundamental research and applied, industrially important problems by combining the thorough knowledge of the measurement methods and fluid dynamics theory. The research is based on versatile use of optical measurement methods and variety of research environments. The results are transferred

to the use of industry and society through education and close cooperation with customers. The vision of the group is to be the most advanced fluid measurement expert in Finland and internationally competent research unit in the field of multiphase flows. The contribution of the external funding is 85% of the budget.

ProMoni-project is a successor of a former project in which measurement and analysis methods for turbulent flow in single phase were developed. It appended methods of measurement and analysis for turbulent structures and multiphase flows. The resulting analysis methods have already been used in a number of projects in internal industrial flows. Examples of successful applications include those to water purification process for flocculation and precipitation analysis, gas-fluid reactors for bubbling flows, dissolute air analysis in pumping system and fiber suspension flow analysis. Up to the present, the estimated total volume of applied research rendered possible by the results from ProMoni project is five man-years. A part of the multiphase analysis software developed during the project has been sold to LaVision GMbH.

The project has been essential for the development of the group's abilities to confront the demands of basic and applied industrial research. In the future the developed methods will be used in applied industrial research in the analysis of fluid turbulence and dispersed phase of interaction. Also the tasks considering turbulence structure analysis will be met. New projects have already been initiated in areas of flocculation, polymer drag reduction, active turbulence control and turbulence-structure interaction.

Åbo Akademi University: The Heat Engineering Laboratory at Åbo Akademi University gives education in thermodynamics, heat and mass transfer, process simulation and optimization, fluid mechanics and dynamics and neural networks, and carries out research on international level in fields relating to the above mentioned items. Research topics include modeling of bioengineering processes, modeling of fluidized beds, blast furnace modeling and automation, applications of neural networks, reactor simulations with special emphasis on interaction between chemistry and turbulence, thermal modeling of steel plants, timber drying and process optimization. The number of people participating in research varies between 10 and 15. About 70% of the financing of the laboratory is obtained from external sources.

The research activities in Promoni were related to fluidized bed research. Heat Engineering Laboratory has cooperated with other laboratories at Åbo Akademi University (Laboratories of Inorganic Chemistry and Industrial Chemistry) and with VTT in fluidized bed combustion projects over the past years. This cooperation still continues and includes both research projects and industrially financed projects. The cooperation with VTT continues in Tekes- and industry-financed ModCher project and is conducted in close cooperation with the industrial partners Foster Wheeler Energia

Oy and Fortum Oyj. The experiences from measurements and experimental activities and the models developed in Promoni will be utilized in ModCher project.

Promoni project gave the Laboratory valuable experience in experimental studies of multiphase flows, in measurement techniques and in image processing. In addition to ModCher project, this experience is now used in another project, where a similar cold model of a metallurgical process is being built. Better understanding of multiphase flows and experiences in CFD modeling are utilized both in teaching and in research.

University of Kuopio, Department of Applied Physics: Inverse problems group. The main research interests of the group are in different types of inverse problems, including computational methods and in some cases development of measurement systems. The main applications are electrical impedance tomography, optical tomography, ultrasound therapy, radiation therapy treatment planning and ultrasound diagnostics. The research group directed by Professor Jari Kaipio includes one research director (associate professor) with Ph.D. degree, four researchers with Ph.D. degree, one lecturer with Ph.D. degree and ten researches with M.Sc. degree. Four of the group members are funded by the University of Kuopio and the rest are funded by other sources. These include TEKES, Academy of Finland and private foundations' funding, total of (approx. 1996–2003) 176 000 €/y.

The computational methods for optical tomography is a collaboration project with Jyväskylä group, who develops a measurement system for optical tomography. Our project has enabled image reconstructions from real measurements carried out in test phantoms and in a test laboratory in VTT, Jyväskylä. Final applications in industry are yet to be tested.

The main aim in our project was to develop new computational approaches for optical tomography. During the project we have developed three novel approaches for optical tomography that can be utilized in many applications. These methods are the dynamical imaging approach, computational calibration of measurement systems and new hybrid forward models for fast and accurate forward computations. These can directly be applied in optical tomography but can also be utilized in other inverse problems investigated by the group. One example is the new forward model which is utilized in radiation therapy treatment planning with small modifications. Also the computational calibration idea could be modified for other imaging modalities for measurement system calibration.

University of Jyväskylä, Flow Dynamics**:** The research group in the Department of Physics at the University of Jyväskylä comprises two senior staff at the professor level (one of them part time), one tenure lecturer, three post doctoral scientists, and nine post graduate students. The main research areas where the group has current activities are

experiments and ab initio numerical simulations in multiphase fluid dynamics and related topics, dynamics of interfaces, and elasticity and fracture of materials (including fibre networks). About 80 percent of all research efforts of the group are funded by external sources (national graduate schools (Ministry of Education), Academy of Finland (Center of Excellence Programme), Tekes and industry) The role of Tekes in this external funding is significant, and Tekes funding has also promoted the availability of other funding agents.

The activities and results of the ProMoni project have already made an impact on the other activities of the group. Up to the present, it has given rise to two direct industrial projects which have been carried out alongside the Tekes funded activities. One important channel through which results achieved are assimilated to practical use in industry is master's thesis projects. After the year 2000 eighteen (18) such projects have successfully been carried out, and additional four projects will be completed this summer. Many of these projects have been directly or indirectly connected with Tekes funded projects, and they have mostly been funded by industry, directly or through e.g. VTT.

The results obtained within the ProMoni project have made a significant contribution to the fluid dynamical applications of the research group. They have helped us to further develop the simulation methods towards more challenging (realistic) applications, and directed in particular the experimental efforts of the group towards novel experimental techniques applicable for suspension flows. Both these directions are strategically important for our future activities, and play and will continue to play a central role in the current and planned research projects. There are a number of new applications of these methods which are now possible. In particular, development of tomographic methods, based on laser optics as well as x-rays, will be a central task of the group in the near future as interesting applications of both these methods are available. Another aspect of the research carried out in the ProMoni project is that it has increased our possibilities for international collaboration, which possibility we already have used and will increasingly be using.

5 Conclusions

As demonstrated in previous sections, flows found in industrial processes are typically multiphase flows. Compared to flows of more simple fluids, multiphase flows are poorly understood. The most important reason for this is the limited applicability to multiphase flows of many of the conventional experimental and numerical methods and devices, originally developed for pure, single phase fluids. Up to the present, development of new methods and techniques has therefore been an important part of the everyday practice of multiphase flows research. It can not be over emphasized that, in order to facilitate effective applied research and support to industrial research characterized by rapidly shortening development cycles, such development is still imperative for all research groups working within this dicipline. In accordance with the general goals stated in its original research plan ProMoni project has served as an important platform for such a continual development within the participating seven research groups. From the point of view of the five research institutes involved in the ProMoni consortium, it may well be termed as an R&D project producing new advanced research facilities and services to be utilized in industrial applications.

The total volume of the ProMoni project was approximately 25 person years during the three-year project period 2001–2004. It covered a comprehensive cross-section of the topical issues of theoretical, numerical and experimental multiphase flows research as motivated by the participating process industry. The total amount of particular results obtained during the project is extensive. Among the most important general results are the following:

- Bubble interaction and gas and solids mixing in a 2D bubbling fluidized bed were measured and used in comparisons with CFD simulations. The kinetic Eulerian models for granular two-phase flows predict qualitatively correct bubble shapes and interactions, but quantitative agreement with measurements is difficult to achieve. In turbulent conditions, the modelling produces the bed behaviour realistically and the simulations can be used in developing approximative macroscopic two-phase models. A new correlation for gas-solid drag was developed, implemented in Fluent and used successfully to simulate the typical flow structures in a circulating fluidized bed riser.

- Several new or newly adapted experimental methods for fibre suspension flows were developed and brought in regular use in laboratory or pilot scale environments. These include various optical methods for stratified flows and free jets, fast pressure and conduction measurements, accurate flow rate measurement facility and an improved method for fibre suspension filtration measurements.

- Methods based on Particle Image Velocimetry and Digital Imaging measurement were developed for multiphase flows in order to measure fluid dynamical interaction of the phases and the morphology of the dispersed phase.

- An optical tomographic device and related image reconstruction algorithms were developed for non-intrusive measurement of consistency profiles in flows of diffusive fluids such as wood fibre suspensions. The device can be used for 2D and 3D imaging of static and of time varying objects. The method complies with the original planned specifications and is now ready for pilot trials.

- Equipment for electrical impedance tomography was constructed. Reconstruction methods for pulp consistency profile measurement and for flow velocity measurement were developed.

Many of these results now make an important contribution to the present capabilities of the participating groups and have already been successfully utilized in industrial research carried out parallel to the present project. Some of the results are expected to make similar contribution and benefit research and applications in the near future.

Based on the results and their estimated impacts discussed above, we conclude that the general goals of the ProMoni project, namely "to enhance the skills and capabilities of the participating research groups for their applied research, to support their ongoing and planned industry-related research projects and, ultimately, to advance and intensify the dicipline of industrial multiphase flow research in Finland", have been met.

Appendix A:

PROJECT ORGANIZATION

Project Committee

Hannu Lepomäki, (Chairman)
R&D Manager
Metso Paper Oy
Tel. +358-20 4825838
email: Hannu. Lepomaki@metso.com

Mikko Ylhäisi
Chief Technology Adviser
National Technology Agency of Finland (TEKES)
Tel. +358 10 521 5877
email: Mikko.Ylhaisi@tekes.fi

Timo Hyppänen,
Research Manager
Foster Wheeler Energia Oy
Tel. +358-10 3933310
email: timo-hyppanen@fwc.com

Kari Koskinen, (Member until 31.12.2002)
Research engineer
Fortum Oy
tel. +358 10 4534735
email: Kari.K.Koskinen@fortum.com

Jouko Halttunen
Professor
Tampere University of Technology
Tel. +358 3 3115 2485
email: jouko.halttunen@tut.fi

Jussi Manninen,
Group Manager
VTT Processes, Pulp and paper industry
Tel. +358 20 722 2723
email: Jussi.Manninen@vtt.fi

Mikko Manninen
Senior Research Scientist
VTT Processes, Pulp and Paper Industry
Tel. +358 20 722 5072
email: Mikko.Manninen@vtt.com

Sirpa Kallio,
Researcher,
Åbo Akademi University, Heat engineering laboratory,
Tel. +358 2 215 4440
email: Sirpa.Kallio@abo.fi

Jussi Timonen,
Professor
University of Jyväskylä, Department of Physics
Tel. +358 14 602376
email: Jussi.Timonen@phys.jyu.fi

Pentti Saarenrinne,
Laboratory Manager
Tampere University of Technology
Institute of Energy and Process Engineering
Tel. +358 3 3115 2255
email: saarenri@cc.tut.fi

Marko Vauhkonen
Research Director
University of Kuopio, Department of Applied Physics
Tel. +358 17 162035
email: Marko.Vauhkonen@uku.fi

Markku Kataja (Project manager, Secretary of the committee)
Professor
VTT Processes, Pulp and Paper Industry
Tel. +358 20 722 2568
email: Markku.Kataja@phys.jyu.fi

Research organization

Project Manager:
Markku Kataja, Professor
VTT Processes, Pulp and Paper Industry
Tel. +358 20 722 2568, email: Markku.Kataja@vtt.fi

Participating research groups.

1. VTT Processes / Multiphase flows
   Group Manager:
   Jussi Manninen,
   VTT Processes, Pulp and paper industry
   Tel. +358 20 722 2723, email: Jussi.Manninen@vtt.fi
   Group members:
   Antti Koponen, FT
   Janne Poranen, FT
   Veli-Matti Luukkainen, FM
   Simo Puikkonen, tutkimusavustaja

2. VTT Processes / Process simulation
   Group Manager
   Mikko Manninen
   VTT Processes, Pulp and Paper Industry
   Tel. +358 20 722 5072, email: Mikko.Manninen@vtt.com
   Group members:
   Ulla Ojaniemi, M.Sc.
   Timo Pättikangas, Dr.Tech.
   Pekka Raussi, M.Sc. (Tech.)
   Veikko Taivassalo, Lic. Sc.

3. University of Jyväskylä / Flow Dynamics
   Group Manager
   Markko Myllys
   University of Jyväskylä, Department of Physics
   Tel. +358 14 2602391, email: Markko.Myllys@phys.jyu.fi
   Group members:
   Esa Rehn
   Jani Maaranen

4. Tampere University of Technology / Energy and Process Engineering

Group Manager

Pentti Saarenrinne
Tampere University of Technology, Institute of Energy and Process Engineering
Tel. +358 3 3115 2255, email: saarenri@cc.tut.fi

Group members:

Tero Pärssinen
Markus Honkanen

5. Tampere University of Technology / Measurement and Information Technology

Group Manager

Jouko Halttunen
Tampere University of Technology, Inst. of Measurement and Information Technol.
Tel. +358 3 3115 2485, email: jouko.halttunen@tut.fi

Group members:

Shaomin Zhou

6. Åbo Akademi University / Heat Engineering

Group Manager

Sirpa Kallio
Åbo Akademi University, Heat engineering laboratory.
Tel. +358 2 215 4440, email: Sirpa.Kallio@abo.fi

Group members:

Alf Hermanson, Laboratory Manager

7. University of Kuopio / Inverse Problems

Group Manager

Marko Vauhkonen
University of Kuopio, Department of Applied Physics.
Tel. +358 17 162035, email: Marko.Vauhkonen@uku.fi

Group members:

Tanja Tarvainen
Ville Kolehmainen
Jari Kaipio
Antti Vanne
Katja Markkanen

Published by

Series title, number and report code of publication

VTT Research Notes 2286
VTT–TIED–2286

Author(s)
Kataja, Markku (ed.)

Title

Multiphase flows in process industry
ProMoni

Abstract

The project "Multiphase flows in process industry (ProMoni)" 1.1.2001–30.4.2004 was a research consortium carried out jointly by seven research groups from VTT, University of Jyväskylä, Tampere University of Technology, Åbo Akademi University and University of Kuopio. It included modeling, development and validation of numerical methods as well as development of new experimental techniques for multiphase flows found in process industry. The primary fields of application are in fluidized beds and in various processes found in the paper and pulp industry.

This extensive final report of the ProMoni project includes results from experimental and numerical research of bubbling fluidized beds indicating that modelling produces the bed behaviour realistically and the simulations can be used in developing approximative macroscopic two-phase models. A new gas-solid drag correlation model was successfully used within Fluent CFD code to simulate the typical flow structures in a circulating fluidized bed riser. Several new or newly adapted experimental methods and measuring devices for fibre suspension flows were developed and brought in regular use in laboratory or pilot scale environments. Particle Image Velocimetry and Digital Imaging measurement were developed and used in two-phase flows to measure hydrodynamical interaction and morphology of the dispersed phase. Optical and electrical impedance tomographic devices and related image reconstruction algorithms were developed for non-intrusive measurement of consistency profiles and flow velocity in flows of diffusive fluids such as wood fibre suspensions.

Keywords
process industry, process measurements, flow measurement, multiphase flow, fluidized bed reactors, bubbling fluidized beds, computational methods, fibre suspensions, particle image velocimetry, digital imaging

Activity unit
VTT Processes, Koivurannantie 1, P.O.Box 1603, FI–40101 JYVÄSKYLÄ, Finland

ISBN
951–38–6536–3 (soft back ed.)
951–38–6537–1 (URL: http://www.vtt.fi/inf/pdf/)

Project number

Date	Language	Pages	Price
March 2005	English	177 p. + app. 4 p	D

Name of project
ProMoni

Commissioned by
National Technology Agency of Finland (Tekes)
Foster Wheeler Energia Oy, Metso Oyj, Fortum Oyj

Series title and ISSN
VTT Tiedotteita – Research Notes
1235–0605 (soft back edition)
1455–0865 (URL: http://www.vtt.fi/inf/pdf/)

Sold by
VTT Information Service
P.O.Box 2000, FI–02044 VTT, Finland
Phone internat. +358 20 722 4404
Fax +358 20 722 4374

The project "Multiphase flows in process industry (ProMoni)" 1.1.2001-30.4.2004 was a research consortium carried out jointly by seven research groups from VTT, University of Jyväskylä, Tampere University of Technology, Åbo Akademi University and University of Kuopio. It included modeling, development and validation of numerical methods as well as development of new experimental techniques for multiphase flows found in process industry. The primary fields of application are in fluidized beds and in various processes found in the paper and pulp industry.

This extensive final report of the ProMoni project includes results from experimental and numerical research of bubbling fluidized beds indicating that modelling produces the bed behaviour realistically and the simulations can be used in developing approximative macroscopic two-phase models. A new gas-solid drag correlation model was successfully used within Fluent CFD code to simulate the typical flow structures in a circulating fluidized bed riser. Several new or newly adapted experimental methods and measuring devices for fibre suspension flows were developed and brought in regular use in laboratory or pilot scale environments. Particle Image Velocimetry and Digital Imaging measurement were developed and used in two-phase flows to measure hydrodynamical interaction and morphology of the dispersed phase. Optical and electrical impedance tomographic devices and related image reconstruction algorithms were developed for non-intrusive measurement of consistency profiles and flow velocity in flows of diffusive fluids such as wood fibre suspensions.

Tätä julkaisua myy
VTT TIETOPALVELU
PL 2000
02044 VTT
Puh. 020 722 4404
Faksi 020 722 4374

Denna publikation säljs av
VTT INFORMATIONSTJÄNST
PB 2000
02044 VTT
Tel. 020 722 4404
Fax 020 722 4374

This publication is available from
VTT INFORMATION SERVICE
P.O.Box 2000
FI–02044 VTT, Finland
Phone internat. + 358 20 722 4404
Fax + 358 20 7226 4374

ISBN 951-38-6536-3 (soft back ed.)
ISSN 1235-0605 (soft back ed.)

ISBN 951-38-6537-1 (URL: http://www.vtt.fi/inf/pdf/)
ISSN 1455-0865 (URL: http://www.vtt.fi/inf/pdf/)